Maximizing Storage Rate and Capacity and Insuring the Environmental Integrity of Carbon Dioxide Sequestration in Geological Reservoirs

Final Report
Project period: 10/02/2000-8/1/2004

L. A. Davis, A. L. Graham, H. W. Parker and J. R. Abbott
Departments of Chemical and Petroleum Engineering
Texas Tech University
Lubbock, Texas 79409-3121

M. S. Ingber and **A. A. Mammoli**
Department of Mechanical Engineering
University of New Mexico
Albuquerque, New Mexico 87131

L. A. Mondy
Energetic and Multiphase Processes Department
Sandia National Laboratories
Albuquerque, New Mexico 87185-0834

Quanxin Guo and **Ahmed Abou-Sayed**
Advantek International, Inc.
Houston, Texas 77063

Submitted December 7, 2005
DOE Award Number: DE-FC26-00NT40925

THIS REPORT WAS PREPARED AS AN ACCOUNT OF WORK SPONSORED BY AN AGENCY OF THE UNITED STATES GOVERNMENT. NEITHER THE UNITED STATES GOVERNMENT NOR ANY AGENCY THEREOF, NOR ANY OF THEIR EMPLOYEES, MAKES ANY WARRANTY, EXPRESS OR IMPLIED, OR ASSUMES ANY LEGAL LIABILITY OR RESPONSIBILITY FOR THE ACCURACY, COMPLETENESS, OR USEFULNESS OF ANY INFORMATION, APPARATUS, PRODUCT, OR PROCESS DISCLOSED, OR REPRESENTS THAT ITS USE WOULD NOT INFRINGE PRIVATELY OWNED RIGHTS. REFERENCE HEREIN TO ANY SPECIFIC COMMERCIAL PRODUCT, PROCESS, OR SERVICE BY TRADE NAME, TRADEMARK, MANUFACTURER, OR OTHERWISE DOES NOT NECESSARILY CONSTITUTE OR IMPLY ITS ENDORSEMENT, RECOMMENDATION, OR FAVORING BY THE UNITED STATES GOVERNMENT OR ANY AGENCY THEREOF. THE VIEWS AND OPINIONS OF AUTHORS EXPRESSED HEREIN DO NOT NECESSARILY STATE OR REFLECT THOSE OF THE UNITED STATES GOVERNMENT OR ANY AGENCY THEREOF.

Public Abstract

Maximizing Storage Rate and Capacity and Insuring the Environmental Integrity of Carbon Dioxide Sequestration in Geological Formations

The U.S. and other countries may enter into an agreement that will require a significant reduction in CO_2 emissions in the medium to long term. In order to achieve such goals without drastic reductions in fossil fuel usage, CO_2 must be removed from the atmosphere and be stored in acceptable reservoirs. The research outlined in this proposal deals with developing a methodology to determine the suitability of a particular geologic formation for the long-term storage of CO_2 and technologies for the economical transfer and storage of CO_2 in these formations.

A novel well-logging technique using nuclear-magnetic resonance (NMR) will be developed to characterize the geologic formation including the integrity and quality of the reservoir seal (cap rock). Well-logging using NMR does not require coring, and hence, can be performed much more quickly and efficiently. The key element in the economical transfer and storage of the CO_2 is hydraulic fracturing the formation to achieve greater lateral spreads and higher throughputs of CO_2. Transport, compression, and drilling represent the main costs in CO_2 sequestration. The combination of well-logging and hydraulic fracturing has the potential of minimizing these costs. It is possible through hydraulic fracturing to reduce the number of injection wells by an order of magnitude.

Many issues will be addressed as part of the proposed research to maximize the storage rate and capacity and insure the environmental integrity of CO_2 sequestration in geological formations. First, correlations between formation properties and NMR relaxation times will be firmly established. A detailed experimental program will be conducted to determine these correlations. Second, improved hydraulic fracturing models will be developed which are suitable for CO_2 sequestration as opposed to enhanced oil recovery (EOR). Although models that simulate the fracturing process exist, they can be significantly improved by extending the models to account for nonsymmetric, nonplanar fractures, coupling the models to more realistic reservoir simulators, and implementing advanced multiphase flow models for the transport of proppant. Third, it may be possible to deviate from current hydraulic fracturing technology by using different proppants (possibly waste materials that need to be disposed of, e.g., asbestos) combined with different hydraulic fracturing carrier fluids (possibly supercritical CO_2 itself). Because current technology is mainly aimed at enhanced oil recovery, it may not be ideally suited for the injection and storage of CO_2. Finally, advanced concepts such as increasing the injectivity of the fractured geologic formations through acidization with carbonated water will be investigated.

Saline formations are located through most of the continental United States. Generally, where saline formations are scarce, oil and gas reservoirs and coal beds abound. By developing the technology outlined here, it will be possible to remove CO_2 at the source (power plants, industry) and inject it directly into nearby geological formations, without releasing it into the atmosphere. The goal of the proposed research is to develop a technology capable of sequestering CO_2 in geologic formations at a cost of US $10 per ton.

TABLE OF CONTENTS

Introduction

This project examines the feasibility of CO_2 sequestration into subsurface geological formations. While the principal result was to determine the economic viability of this method, this required the development of new experimental and simulation techniques. This work was divided into five overall areas each with multiple tasks. Each of these tasks are presented in the following sections in the order they were given in the initial proposal.

The first area was to improve the modeling of hydraulic fracturing and proppant flow control. One of the first tasks to be initiated and completed was to evaluate and extend a current fracture simulator. In Task 1.1, it was found that the factors which have most impact on long-term injector performance include the formation leak-off, the chemical interaction of injectant and the rock formations, reservoir pressure build up and the compressibility of the injected CO_2 stream. Estimates for each of these factors are given in Task 1.1.

Task 1.2 looked at the interaction between fracture simulations and geological formation modeling. Base on these early simulation predictions, it was found that hydraulic fracturing would be necessary in certain types of formations to get significant CO_2 sequestration rate and storage capacity. Other site factors of importance were identified such as formation water salinity and permeability.

Because of the complex fluids that can be used in fracturing and enhancing geological formations, one of the more ambitious tasks was to measure normal stress differences in particle laden flows. While new techniques and methods were developed to both experimental measure and numerical model these effects as part of Task 1.7, no significant normal stress differences were observed.

Another ambitious goal, which was much more successful, was to incorporate various non-Newtonian effects into both channel-scale and continuum-level models. Adding these additional capabilities improved the fidelity of the simulations, and is discussed in Task 1.9.

Other tasks dealt with additional refinements to these models like incorporating wall slip and determining hindered settling correlations (Tasks 1.6 and 1.8 respectively). Also there was testing and evaluating model parameters (Tasks 1.4 and 1.5). The last two remaining tasks were parallelizing and porting codes to a variety of platforms (Task 1.4) and incorporating all these advances, plus some others from later tasks into a fracturing simulator (Task 1.10).

The second major area of interest was modeling the flow of CO_2 and additives into fractures. The major work here was in the multiphase modeling performed in Task 2.1. In support of this effort, the properties of CO_2 and solubilities of various chemical species were determined (Tasks 2.4 & 2.5) along with some validation experiments (Tasks 2.2 & 2.3).

The third major area was to determine the integrity and quality of the reservoir seal. The most import part of this task was to develop a new NMR technique using measured T_2 values and correlating this with properties of the geological formations of interest (Task 3.2). Also a site was identified and arrangements made for a possible field test of the methods developed within this project (Task 3.3).

The fourth area was to evaluate the acidization effect cause by injecting CO_2. Here the main area was Task 4.3, were extensive tests were performed on a series of cores using similar methods to Task 3.2. Cores evaluated included some taken from the site identified in Task 3.3.

The final area was to use this information to evaluate various alternatives (Task 5.1), perform a cost estimate (Task 5.2) and compare it with other proposed technologies for CO_2 sequestration (Task 5.3). Based on these results, the primary goal of estimating the cost of this method for CO_2 sequestration was accomplished even though several of the intermediate goals could not be accomplished.

The following sections give a more detailed description of the work done on each task. Finally, some overall results and conclusions are presented. For completeness, a large set of appendices cover the results from the characterization experiments performed as part of Task 3.2, which would be beneficial if a field trial was performed.

Task 1.1 Extending Fracture simulator

Leak-off and Injector Long-Term Performance

One of the important issues in CO_2 sequestration into subsurface geological formations, as in any large scale or long term injection operations, is the impact of long term injector performance. The factors which have great impact on long-term injector performance include the formation leak-off, the chemical interaction of injectant and the rock formations, reservoir pressure build up and the compressibility of the injected CO_2 stream.

Chemical Interaction: Reaction of CO_2 with limestone can dissolve limestone and improve injector performance, while reaction of CO_2 with sandstone, carbonate formations or steel pipe can produce scale and precipitation and thus damage the injector performance. Texas Tech University reviewed and reported results of the chemical interaction of CO_2 with different rock formations in the last Quarterly Report. Scaling, corrosion and precipitation issues need to be addressed both in injector *completion* and in injector *stimulation*.

Figure 1.1.1 shows a proven well completion technique for CO_2 injectors in enhanced oil recovery applications. In this case, high proppant concentration slurry with clear fracturing fluid is injected to create a wedged or gap fracture. The green region shown in the bottom of the fracture in Figure 1.1.1 is a propped region and the clear region shown in the top part of the fracture is a wedged or gap region. Field trials indicated this completion technique can increase CO_2 injectivity by a factor of over 2 from a number of injectors.

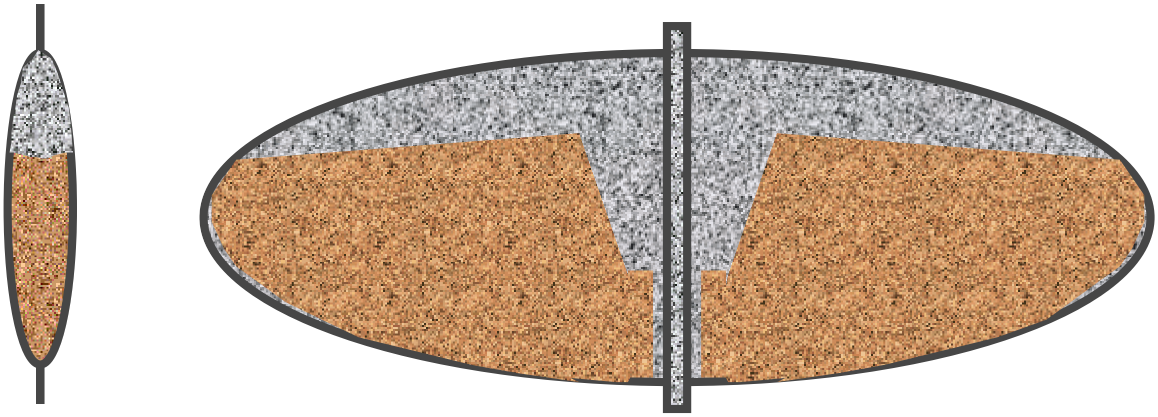

Figure 1.1.1. A schematic injector stimulation, showing a proven well completion technique in CO_2 injector completion.

We also worked on prediction of injector long-term performance. Specifically, we developed a method to estimate injectivity improvement and how long the improvement can last from injector acid stimulation to removed injector damages caused by scale, precipitation and other solid plugging. Field injector examples show that scale and precipitation due to CO_2 cause injectivity declines and acid stimulations can remove scales and thus improve injectivity. There is a cost associated with acid stimulations and one would like to estimate the injectivity improvement and how long the improvement will last. We have developed correlation to estimate both injector stimulation improvement after stimulation and how long the improvement can last from injector performance history data such as injection pressure and rate, reservoir pressure. These estimates are required in estimating whether a given amount of CO_2 can be sequestrated through a given number of wells during planned sequestration duration or extra injectors are necessary and when the new injectors are needed.

Fracture Pressure and Reservoir Pressure: Fracture closure pressure and reservoir pressure must be estimated for accurate simulations to be performed. Fracture closure and reservoir pressures change during long-term injection such as CO_2 sequestration, and are crucial to assess or to understand injector performance. The University of New Mexico has begun the development of a computation reservoir simulator for injector performance and reservoir pressure history prediction. However, it should be noted that fracture (as a function of injection history) must be incorporated in the reservoir simulator and that any reservoir simulator must be history matched with well testing data. Therefore, injector well testing for fracture closure pressure, fracture dimension and reservoir is crucial to understand and predict CO_2 sequestration. We reviewed a number of well testing methods that have potential to become the best practice guideline or recommended well testing methods in CO_2 sequestration design and operations. The following is a brief list and some or all the tests should be performed during CO_2 injector construction and operation:

- **Step Rate Test**: This is a test for obtaining fracture closure pressure. Step rate testing allows for determining when a fracture will propagate and when a pre-existing fracture will reopen. It can be run after a conventional falloff or a final falloff segment can be used in the test. Repeated falloff testing can also be used to assess if a reservoir has been altered by injection history in in-situ stresses or changes in permeability and leak-off.
- **Injectivity/Falloff Test**: This is a test for obtaining reservoir pressure history. An injectivity is similar to a drawdown test in a production well - the bottom hole pressure changes from a baseline value. Falloff testing is analogous to buildup testing in a production well - with time, the pressure falls off to a stabilized value from which the average reservoir pressure can be determined. Processing the injectivity and the falloff data can provide information on storage and diffusivity.
- **Conventional Leakoff Test**: This is a test for inferring fracture closure pressure. A Formation Integrity Test is carried out to evaluate the integrity of a casing shoe. Pressure in the wellbore is increased to a specified level. If the hydraulic seal around the shoe does not fail, the only information that can be determined is a minimum level of the breakdown pressure.

- **Extended Leakoff Test**: This is a test for obtaining fracture closure pressure and possible leakoff characteristics. After drilling ahead from the shoe a short distance, the openhole interval is pressurized until the formation breaks down.
- **Microhydraulic Fracturing Test**: This is a technique that is fundamentally similar to Extended Leakoff Testing. It differs in that it can be done in open or cased hole (through perforations) at any time during the life of the well. Isolation is a pre-requisite.
- **Hydraulic Impedance Test (HIT)**: This is a test for fracture height and length. The test is performed by sending a pressure pulse down the wellbore (from the wellhead), and then analyzing the frequency response of the consequent wave train. HIT has been successfully used to determine fractures in numerous injection wells and the method is reported to work in both poorly consolidated and more consolidated formations (Paige et al, 1992, Paige et al, 1993).
- **Tiltmeter Monitoring**: This is a technique for monitoring fracture size and orientation. Fracturing involves parting of rock and subsequent deformation. Tiltmeter fracture mapping infers hydraulic fracture geometry by measuring fracture-induced rock deformation (Wright et al, 1999). Measuring the gradient of the displacement field, or the tile field, is made. Tilt due to a fracture may be measured through tiltmeter arrays on the surface (known as surface tiltmeter) or through a wireline tiltmeter array in offset wellbores (known as down hole tiltmeter). A least-square fit of the measured tilt information with respect to the fracture geometry gives the location, orientation and dimension of the fracture.
- **Microseismic Monitoring**: This is a technique for monitoring fracturing process (Warpinski, 1998). Microseisms are generally seismic energy emitted by shear slippage along weakness planes in the earth. If you record the occurrence of these events and triangulate to find where they came from, it can be possible to outline the feature(s) causing these events. This technique has the potential for monitoring CO_2 sequestration front.

Leak-off: Leak-off characteristics for stimulation hydraulic fracturing (short period in minutes and hours) and long-term injector such as in CO_2 sequestration (in years and decades) are quite different. In stimulation fracturing, damage is modeled as filter buildup and leak-off is modeled as Carter's leak-off relation (proportional to the square-root of time). During long-term injection, leak-off changes with time. For long-term CO_2 sequestration operations, leak-off may be increased or decreased depending on whether reaction of CO_2 with rock stimulate injection or damage injection operation. Work has begun in changing the square-root leak-off relation in the current hydraulic fracturing simulator to leak-off relations that are realistic for long-term injection such as in CO_2 sequestration. This turns out to be more complicated than we originally estimated because change of leak-off can also change fracture propagation schemes. During modeling process, leak-off is calculated and fracture growth is estimated in the simulator by coupling with leak-off for the newly created fracture area, as well as with fracture volume reduction/increase with pressure reduction/increase.

Well bore Hydraulics

CO_2 rheology depends on pressure. Injection pressure at the surface dictates the requirement and economics of injection equipment (such as compressors, pumps, wellhead), while injection pressure down hole at the selected sequestration formation determined injection rate. The injection pressures at the surface and at the bottom hole are related through the following equation:

$$P_{BH} = P_{Surface} + P_{Hydrostatic} - P_{Friction} \qquad (1.1.1)$$

where:

P_{BH}	bottom hole pressure at the wellbore face (psia),
$P_{Surface}$	surface pressure (psia),
$P_{Hydrostatic}$	hydrostatic head due to the fluid column (psi), and,
$P_{Friction}$	frictional pressure drop through tubulars, completion hardware and perforations

The equations given below apply to single -phase fluid flow (either compressible or incompressible) along well bore. Although injection of CO_2 at bottom hole is under supercritical pressures, flow of CO_2 along well bore could be in foam and thus two-phase compressible CO_2 fluid flow needs to be considered, and work in this area is under progress.

Friction in the Injection String

The pressure drop per unit length (for friction effects only) under single phase fluid flow is:

$$\begin{aligned} \frac{dP\ (psi)}{dL\ (feet)} &= 0.3813\,\frac{f\rho\ (lbm/ft^3)q^2\ (BPM^2)}{D^5\ (inches^5)} \\ \frac{dP\ (psi)}{dL\ (feet)} &= 1.295\times10^{-3}\,\frac{f\rho\ (lbm/ft^3)v^2\ (ft^2/second^2)}{D\ (inches)} \end{aligned} \qquad (1.1.2)$$

where:

dP	pressure change (psi),
dL	length of the segment over which the pressure drop is calculated (feet),
ρ	density (specific gravity x 62.4) (lbm/ft^3),
f	Moody friction factor (dimensionless),
q	injection rate (BPM),
v	velocity (ft/s), and,
D	equivalent diameter (inches).

The term equivalent diameter is used to allow discrimination between pipe and annular flow. For conventional pipe flow, Equation (2) is used and D is the internal diameter of the pipe over the length being evaluated. For annular flow, the concept of effective diameter is used:

$$
\begin{aligned}
&\mathrm{D_{eff}} = \frac{4 \times \text{cross} - \text{sec tional area of flow}}{\text{wetted perimeter}} \\
&\text{For an annulus:} \qquad\qquad\qquad\qquad\qquad\qquad\qquad\qquad (1.1.3) \\
&\mathrm{D_{eff}} = \mathrm{D_{outer}} - \mathrm{D_{inner}}
\end{aligned}
$$

For annular flow, use D = D_{outer} - D_{inner} in the second form of Equation (1.1.2). In the first form of Equation (2) replace D^5 with $(D_{outer} - D_{inner})^3$ x $(D_{outer} + D_{inner})^2$.

The length term used is based on measured depth, since friction acts over the full length of the string (as opposed to hydrostatic head). If there are changes in string dimensions and/or inclination, it is common practice to divide the well up into individual increments and sum the friction over the individual discreet lengths. If compressible fluids are present, it is essential to discretize the well bore (divide the well bore into discreet lengths) if fundamental friction equations are used.

During flow, irreversible energy losses occur. With the exception of completely laminar flow, these energy losses cannot be predicted theoretically and are usually accounted for by using the friction factor [as shown in Equation (1.1.2)]. For consistency, only the Moody friction factor will be used (the Moody friction factor is four times the Fanning friction factor (f_F)). The friction factor, f, and the relative roughness (ε/D) are related to the Reynolds' Number. The Reynolds' Number is:

$$
\begin{aligned}
N_{\mathrm{Re}} &= \frac{D\,(feet) \times v\,(feet/\mathrm{sec}) \times \rho\,(lbm/ft^3)}{\mu\,(lbm/ft - \mathrm{sec})} \\
&= 1488.19\frac{D\,(feet) \times v\,(feet/\mathrm{sec}) \times \rho\,(lbm/ft^3)}{\mu\,(cP)} \qquad (1.1.4) \\
&= 7737.6\frac{D\,(inches) \times v\,(feet/\mathrm{sec}) \times S.G.}{\mu\,(cP)}
\end{aligned}
$$

where:

ε	absolute roughness (feet),
D	diameter (feet),
S.G.	specific gravity,
N_{re}	Reynolds Number, and,
μ	viscosity (lbm/ft-sec or cP).

The friction factor depends on the specific flow regime (Table 1.1.1). With the exception of laminar flow, there are many empirical representations of the friction factor in turbulent and transitional regimes.

Table 1.1.1 - Friction Factors

Flow Regime	Reynolds Number	Moody Friction Factor
Laminar	< 2000	$f = \frac{64}{N_{Re}}$
Critical	$2000 < N_{re} < 4000$	$f = \frac{0.5}{N_{Re}^{0.3}}$
Transition (Ikoku, 1980)	$4000 < N_{re} < (200D/\varepsilon)^{1.16}$	$\frac{1}{\sqrt{f}} = 1.14 - 2\log\left[\frac{\varepsilon}{D} + \frac{9.34}{N_{Re}\sqrt{f}}\right]$
Turbulent (Ikoku, 1980)	$N_{re} > (200D/\varepsilon)^{1.16}$	$\frac{1}{\sqrt{f}} = 1.14 - 2\log\left[\frac{\varepsilon}{D}\right]$
Transition	For a Reynolds number between 2100 and 4000	$\frac{1}{\sqrt{f}} = 2\log\frac{D}{e} + 1.14 -$ $-2\log\left(1 + 9.34\frac{D/e}{N_{Re}\sqrt{f}}\right)$
Turbulent (Katz, et al, 1959)	$N_{Re} > 4000$	$\frac{1}{\sqrt{f}} = 1.14 - 2\log\left[\frac{\varepsilon}{D}\right]$
Turbulent		$f = a + bN_{Re}^{-c}$ $a = 0.026\left(\frac{\varepsilon}{D}\right)^{0.225} + 0.133\left(\frac{\varepsilon}{D}\right)$ $b = 22\left(\frac{\varepsilon}{D}\right)^{0.44}$ $c = 1.62\left(\frac{\varepsilon}{D}\right)^{0.134}$

Frictional Factor and Pipe Roughness: Most of these formulations give approximately the same results (refer to Figure 1.1.2 - for a relative roughness of 0.0006 - the relative roughness is the ratio of the absolute roughness of a particular tubular to the internal diameter). For purposes of consistency, the following formulae are suggested. Figure 1.1.3 is an example. With a selected value of roughness, frictional pressure loss can be estimated using Equations (1.1.2) and (1.1.4) and Table 1.1.2. It is usually appropriate to discretize the flow path and solve over various increments, using the previous increment to provide an "upstream" boundary condition. Tools have been developed to compute frictional pressure drops during water or CO_2 injection.

Table 1.1.2 - Friction Factors

Flow Regime	Reynolds Number	Moody Friction Factor	Comments
Laminar	< 2100	$f = \frac{64}{N_{Re}}$	Independent of roughness
Non-laminar	For a Reynolds number greater than 2100	$\frac{1}{\sqrt{f}} = 2\log\frac{D}{e} + 1.14 -$ $-2\log\left(1 + 9.34\frac{D/e}{N_{Re}\sqrt{f}}\right)$	

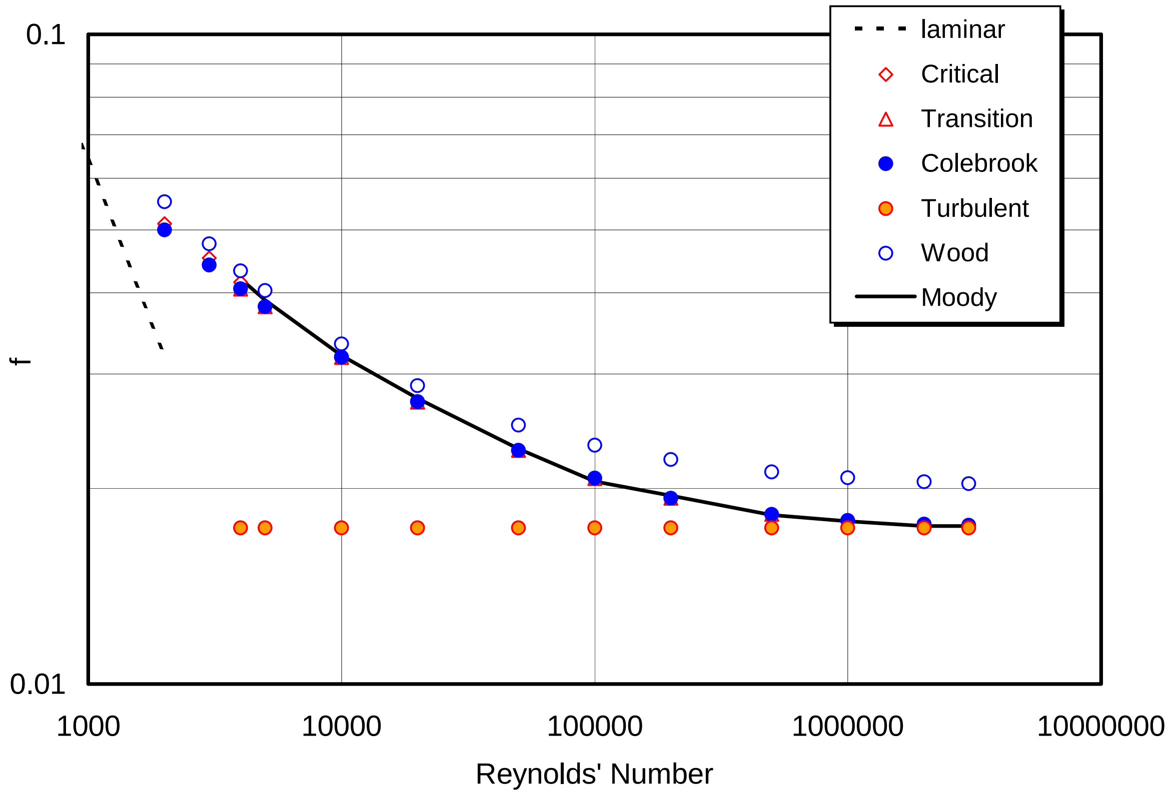

Figure 1.1.2. Comparison of Moody friction factors for various calculation methods for a relative roughness of 0.0006.

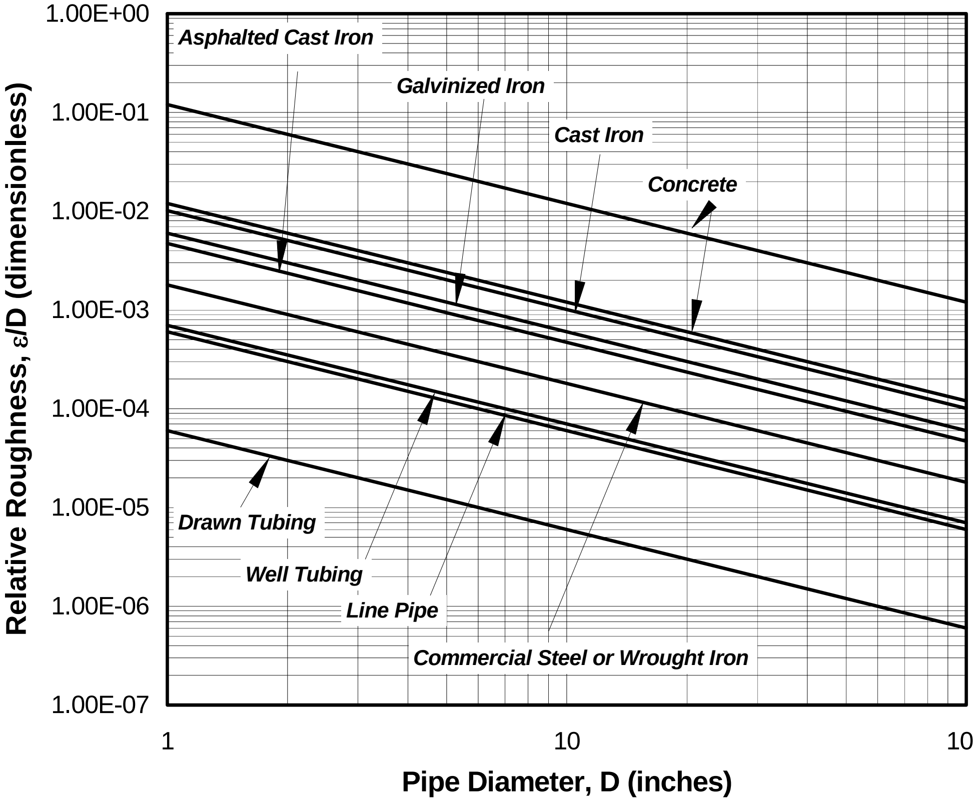

Figure 1.1.3. Relative roughness of various pipes.

Roughness is particularly difficult to determine, particularly for tubulars that have been in service for some time and for CO_2 sequestration operations, as CO_2 sequestration injection can cause pipe corrosion. With scale, corrosion and age, determining pipe roughness is one of the greatest challenge in inferring bottom hole pressures. In fact, periodic flow calibrations should be used to infer changes in roughness over time. Table lists general pipe roughness data and a database for CO_2 injection experience need to collected so that the table can be updated for CO_2 sequestration operations.

Table 1.1.3. Pipe Roughness Data

Roughness (feet)	Pipe
0.000027	New Plastic Coated Tubing
0.00015	New Carbon Steel with 1% Cr (per manufacturer)
0.00024	New Carbon Steel with 1% Cr (field measurements)
0.00075	2 year old Carbon Steel with 1%Cr (field data)
0.015	An actual field measurement (source anon.). Pipe was not specified. It merely indicates that roughness can increase dramatically during service life.
Rule of Thumb: **Roughness will increase by a factor of five over ten years.**	

CO_2 Density and Viscosity: Roughness is one of the parameters that needs to be used for calculating friction in the injection string. In addition, density and viscosity are required. In the previous quarterly report, the PVT (pressure-volume-temperature) properties of CO_2 have been developed and reported. Figure 1.1.4a shows density, and Figure 1.1.4b shows the viscosity, respectively, as a function of pressure and temperature for pure of CO_2 under supercritical conditions. In the use of Equation (1.1.2) to calculate frictional pressure the CO_2 density and viscosity as a function of pressure from Figure 1.1.4 should be used to integrate the pressure drop over the well bore. Although CO_2 injection at bottom hole is under supercritical condition, flow of CO_2 along the well bore could be in foam flow (Reidenbach 1986, Harris & Pippin 2000). Frictional pressure under two-phase pipe flow can be very complex.

Hydrostatic Head: To convert surface pressure to bottom hole pressure, the friction is calculated first. Then the hydrostatic head is determined. The hydrostatic head is determined by integrating the supercritical CO_2 or compressible two-phase foam gradient over the true vertical depth.

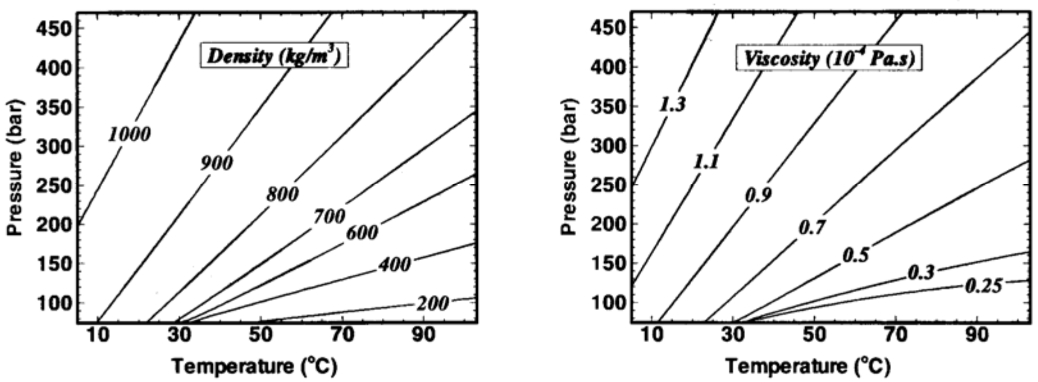

(a) (b)

Figure 1.1.4: Density of CO_2 (a) and Viscosity of CO_2 (b), under supercritical conditions, as a function of temperature and pressure.

Task 1.2 Coupling of fracture simulation with geologic formation modeling to predict injector performance

The objectives of this study are to investigate:

- Fracture length (no fracture, short fracture and long fracture) effects on CO_2 sequestration rate and storage capacity.
- Formation permeability (low permeability versus high permeability, coupled with fracture of different conductivity) effects on CO_2 sequestration rate and storage capacity.
- Salinity effects and other factors such as gravity on CO_2 sequestration rate and storage capacity.

A two-phase flow (gas and water) numerical reservoir simulator was used in this study. The main focus was to determine the impact of fractures on well injectivity. Accordingly, proper simulation of fluid flow through the fracture and into the reservoir was critical for this investigation. The fluid flow around the wellbore was primarily radial and the fracture was simplified as having a constant width. To properly simulate fracture and geological formation interaction during CO_2 sequestration, the fracture and the wellbore were modeled as grid cells and the cells were assigned data in order to calculate multi-phase fluid flow through them. For this reason, it was decided to use a three-dimensional Cartesian model and use fine grid cell sizes around the wellbore to represent as closely as possible an approximately radial flow regime. The model represented a well in 300-foot thick reservoir, 61500 feet in radius to represent infinite acting reservoir. The wellbore is assumed to be 6 inches in diameter with a zero skin factor. Table 1.2.1 shows the model parameters used in this study.

Table 1.2.1. Model Description

Reservoir Top Depth (ft)	5200
Reservoir Porosity	15%
Reservoir Permeability (milli-darcies)	15 and 150
Reservoir Thickness (ft)	300
Fracture Width (in)	1.0
Fracture Length (ft)	0.0, 600 and 1500
Fracture Porosity	32%
Fracture Permeability (darcies)	60, 120 and 600

Petrophysical Properties

The formation simulated had a porosity of 15%. The porosity of the propped fracture was assumed to be is 32% and the fracture was approximated has having a constant width of 1 inch and extending vertically through the entire pay (in fact, the one-inch width is very generous, compared to what would likely occur in reality). Simulation runs were made with fracture lengths of 0, 600 and 1500 ft, with formation absolute permeabilities of 15 and 150 md, with fracture absolute permeability of 60, 120, and 600 darcies (the upper end of this fracture permeability is likely extreme), and with water salinities of 10,000 and 30,000 ppm.

A critical gas saturation of 5% and irreducible water saturation of 20% were used. Corey's equation (Corey, 1954) for relative permeability to CO_2 gas was used in all cases. Relative permeability data used in this study to both CO_2 (gas) and water are shown in Figure 1.2.1.

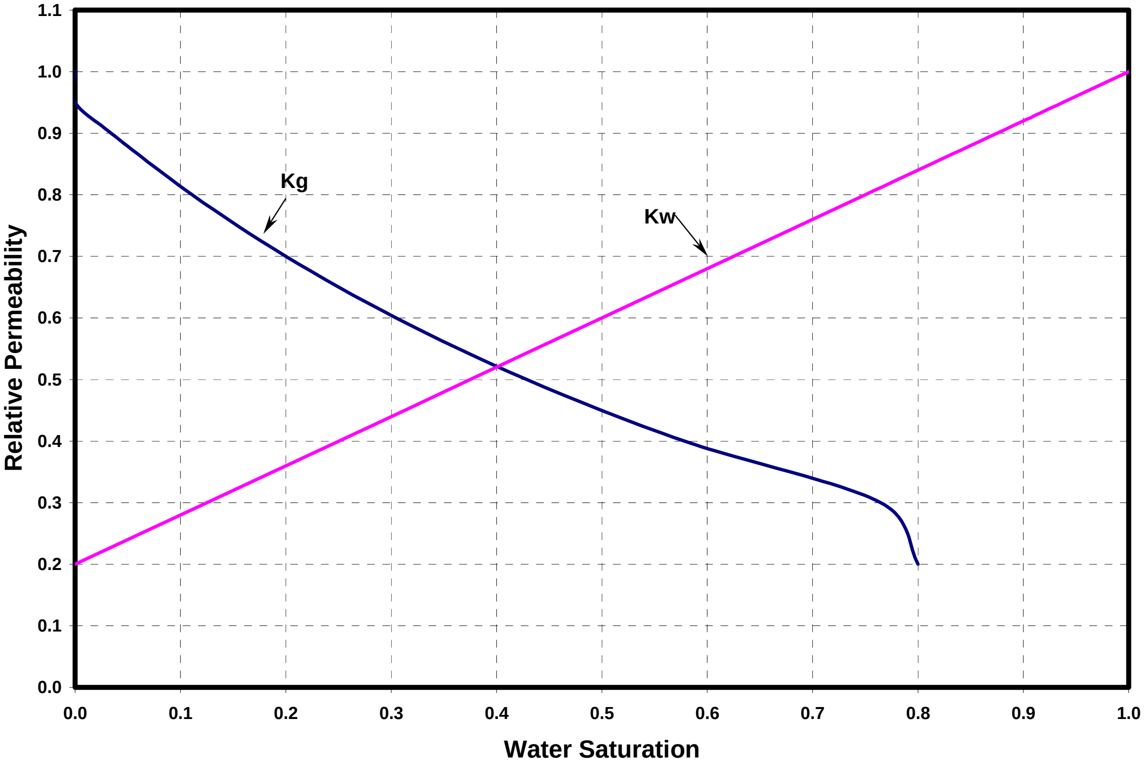

Figure 1.2.1. Relative permeability of CO_2 and water as a function of water saturation.

Fluid Properties

The following correlations were used to generate the fluids, CO_2 and water, properties:

- Equation of State (EOS) for the CO_2, see for example, Progress Report November 2001, (Davis *et al.,* 2001).
- Correlations for water density, compressibility and viscosity at different pressures, temperatures and salinity (see Table 1.2.2).
- Correlations for water- CO_2 mixtures that include CO_2 solubility and formation volume factors at different pressures, temperatures and salinity (see Tables 2 and 3).
- It was reported in the literature (e.g., Pruess, Xu and Garcia, 2001) that sequestration of CO_2 by precipitation of secondary minerals can consume as much

as CO_2 storage in the gas phase and in the simulations it was assumed that 35% of injected CO_2 was consumed by minerals. To account for this phenomenon, the solubility of CO_2 in water was increased by 35% without a corresponding change to water viscosity or formation volume factor.

- Effect of CO_2 solubility on water viscosity was neglected.

The fluid data used in the numerical model are listed in Table 1.2.2. The CO_2 properties used in the model are listed in Table 1.2.3.

Table 1.2.2. Water- Co_2 Mixture Properties

Pressure (psi)	Water Salinity = 10000 ppm			Water Salinity = 30000 ppm		
	CO_2 Solubility (Mscf/stb)	FVF (rb/stb)	Viscosity (cP)	CO_2 Solubility (Mscf/stb)	FVF (rb/stb)	Viscosity (cP)
15.000	0.00001	1.0001	0.5494	0.00001	1.0001	1.1794
50.000	0.00020	1.0002	0.5493	0.00020	1.0002	1.1793
500.000	0.04237	1.0352	0.5492	0.02070	1.0283	1.1792
1000.000	0.06990	1.0439	0.5491	0.03430	1.0320	1.1791
1500.000	0.08819	1.0497	0.5490	0.04340	1.0345	1.1790
2000.000	0.10066	1.0536	0.5489	0.04966	1.0362	1.1789
2500.000	0.10942	1.0564	0.5488	0.05407	1.0375	1.1788
3000.000	0.11576	1.0584	0.5487	0.05729	1.0383	1.1787
3500.000	0.12052	1.0599	0.5486	0.05971	1.0390	1.1786
4000.000	0.12424	1.0610	0.5485	0.06160	1.0395	1.1785
4500.000	0.12728	1.0620	0.5484	0.06315	1.0399	1.1784
5000.000	0.12988	1.0628	0.5483	0.06446	1.0403	1.1783
5500.000	0.13219	1.0635	0.5482	0.06563	1.0406	1.1782
6000.000	0.13434	1.0642	0.5481	0.06670	1.0409	1.1781
6500.000	0.13641	1.0649	0.5480	0.06773	1.0412	1.1780

Table 1.2.3. Co_2 Properties

Pressure (psi)	FVF (rb/mscf)	Viscosity (cP)
15.000	207.53000	0.02000
500.000	5.49120	0.02252
1000.000	2.36580	0.02474
2000.000	0.077510	0.03300
3000.000	0.49810	0.05200
4000.000	0.42800	0.06600
5000.000	0.40610	0.07600
6000.000	0.38130	0.08400
6500.000	0.37360	0.08750

Simulation Results

Simulations were performed to compute the CO_2 sequestration rate as a function of operation time *when the bottom hole injection pressure is fixed at 3640 psi*, which represents 70% of the overburden stress. As expected, the sequestration rate decreases with time and the simulation results give the expected sequestration rate under different conditions. Effects of fracture (no, short and long fracture), formation permeability and salinity were investigated. Simulation runs were performed to investigate the coupling effects between fracture and geological formation modeling. Table 1 lists the ranges of the study parameters. Preliminary results are as follows.

Figure 2 shows the fracture effect on CO_2 sequestration rate per unit reservoir thickness. As expected, fracture improves the injection rate. However, the difference in the results between the 600 feet and 1500 feet is not significant. It should be pointed out that this conclusion is obtained when no formation damage is considered. Should formation have been considered, fracture length effect on injectivity would have become significant.

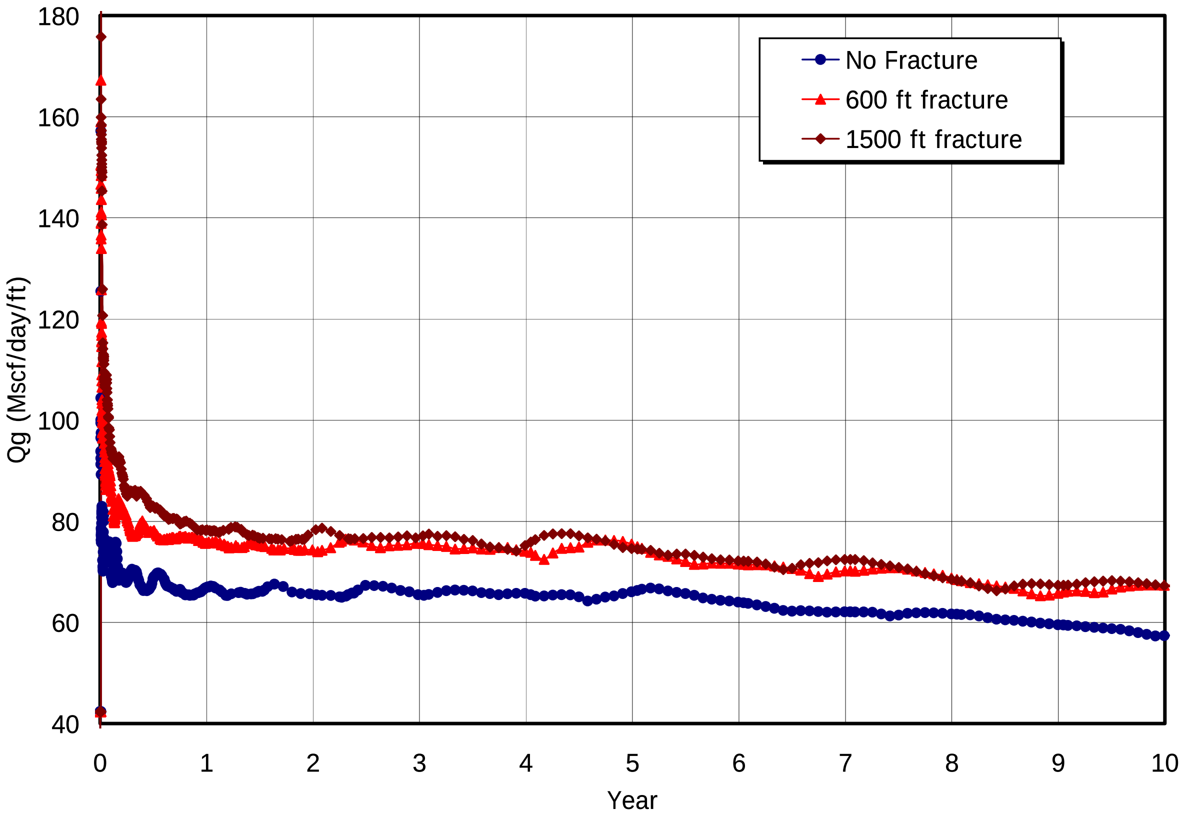

Figure 1.2.2. Fracture effect on CO_2 sequestration rate (per unit aquifer thickness) as a function of time.

Figure 1.2.3 shows the influence of formation permeability on the CO_2 sequestration rate. Note that a maximum injection rate was fixed in the simulation and this was maintained for over 3 years. The figure indicates that the injection rate for the high permeability aquifer is much higher than for the low permeability formation, at least for the first few years. The sequestration rate for injection into the high permeability aquifer declines rapidly during late stage when the injected volume approaches the sequestration capacity. Based on the results presented here, it can be hypothesized that a suitable geological formation should, unsurprisingly, have a high permeability, preferably over 100 md.

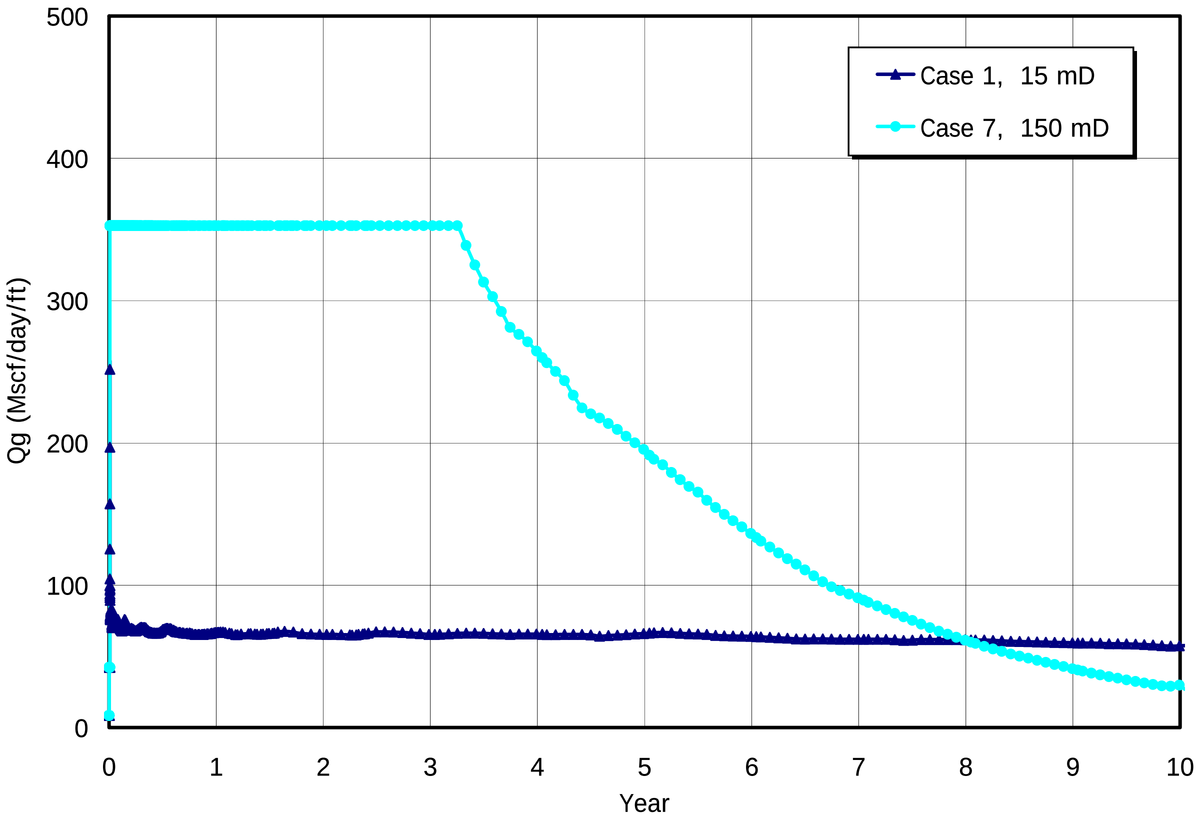

Figure 1.2.3. Formation permeability effect on CO_2 sequestration rate (per unit aquifer thickness) as a function of time.

Figure 1.2.4 suggests the impact of water salinity on the performance of the injection well. Increasing the salinity from 10,000 ppm to 30,000 ppm reduced the injectivity by almost 40 %. Therefore, suitable geological formations should have a low salinity.

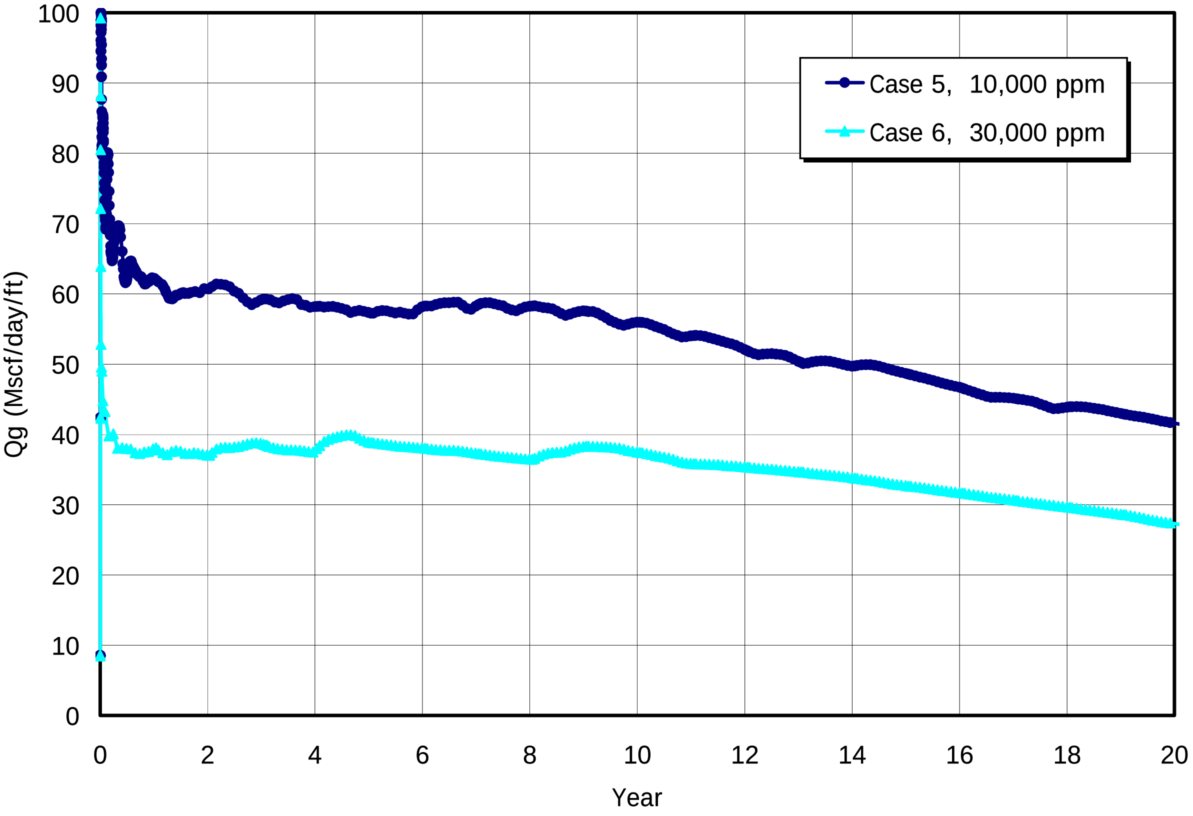

Figure 1.2.4: Impact of water salinity on CO2 sequestration rate (per unit aquifer thickness) of the injection well.

Task 1.3 Parallelize and port to a variety of parallel computer platforms

This part of the project was to take new and/or improved codes that were developed in other parts of the project and get them running on massively parallel computers. This consisted both of making some of the codes parallel and port the parallel codes to machines with different architectures.

The four codes used in this project that required massively parallel computers to execute were two boundary element codes BEAVIS and BEAST, a finite element code GOMA and a Stoke's flow code STOKES 2D. The main focus of this work was to modify the GOMA code with the correct particle and multiphase flow physics. Part of this could be derived from experimental observations, but the more detailed information from direct numerical simulations of discrete particles could have resolved the uncertainties seen in the experiments.

The boundary element codes were used to simulate the dynamics of individual particles in a suspension flow. To solve these systems for the large number of particles required, the codes would need both new solution methods and massively parallel implementations. After each improvement was added, the resulting algorithms were parallelized and the codes ported to the various parallel machines available to this project. These machines consisted of two machines at UNM (Los Lobos and Vista Azul) and two at Sandia National Laboratories (Cplant and Janus). The various characteristics of these machines are given in the table below.

Machine	Architecture	Processors	Interconnects
Los Lobos	733 Pentium III	512	Myrinet
Vista Azul	IBM RS6000	32	GigE
Cplant	Dec Alpha	1536	Myrinet
Janus	Intel Xeon	1166	Ethernet

Table 1.3.1: Characteristics of various parallel machines used.

The GOMA code received the most modifications. Details of the various features added, parallel algorithms used, and platforms ported to have been given in earlier progress reports. The chief features added to the GOMA code were flow-aligned tensor, diffusive flux and suspensions balance models.

Task 1.4 Test and evaluate flow-aligned tensor suspension constitutive models

In the context of modeling suspension flows through porous media the number of suspended particles involved may be too large for direct simulation to be possible and a macroscopic constitutive model may be required. Of particular interest is the correct modeling of particle migration and accumulation. Until recently constitutive models were only partially successful in correctly predicting particle concentration fields that resulted from various viscometric flows. These shortcomings were thought to be due to the incorrect treatment of normal stress differences that arise due to flow induced particle structure.

Models to describe the transport of particles in suspension flows have progressed considerably during the last decade. In one class of models, designated as suspension balance models (Nott & Brady 1994, Fang et al. 2001), the stress in the particle phase is described by a constitutive equation, and particle transport is driven by gradients in this stress.

In another class of models, designated as diffusive flux models (Leighton & Acrivos 1987, Phillips et al. 1992) as used in Task 1.8, the motion of particles within the suspension is described through a diffusion equation based on shear rate and effective viscosity gradients.

Original implementations of both classes of models lacked a complete description of the anisotropy of the particle interactions. Because of this, the prediction of particle concentration in torsional flows in parallel plate and cone-and-and plate geometries did not match experimental data for either class of models. In this work, the normal stress differences for the suspension balance formulation are modeled using a frame-invariant flow-aligned tensor. By analogy, the diffusive flux model is reformulated using the same flow-aligned tensor, which allows separate scaling arguments for the magnitude of the diffusive flux to be implemented in the three principal directions of flow. Using these flow-aligned tensor formulations, the main shortcomings of the original models are eliminated in a unified manner. Steady-state and transient simulations are performed on various one-dimensional and two-dimensional flows for which experimental data are available, using finite-difference and finite-element schemes, respectively. The results obtained are in good agreement with experimental data for consistent sets of empirical constants, without the need for *ad hoc* additional terms.

Two types of model have been considered, the suspension balance model and the diffusive flux model. In the suspension balance model, the suspension stress consists of contributions from both the fluid and the particle phases,

$$\langle \Sigma \rangle = -\langle p \rangle_f \mathbf{I} + \mathbf{2}\eta_s \langle \mathbf{e} \rangle + \langle \Sigma \rangle_p ,$$

where the particle phase contribution Σ_p is given by,

$$\langle \Sigma \rangle_p = -\Pi \mathbf{I} + \mathbf{2}\eta_s \eta_p(\phi)\langle \mathbf{e} \rangle + \eta_s \langle \chi \rangle ,$$

where Π is the particle pressure, η_p is the particle-phase relative viscosity and χ is the normal stress difference. It can be argued that normal stresses are linear in the shear rate and furthermore they have the same microstructural origin as the particle phase pressure. Therefore the particle stress can be expressed as:

$$\langle \Sigma \rangle_p = -\Pi \mathbf{Z} + \mathbf{2}\eta_s \eta_p(\phi)\langle \mathbf{e} \rangle ,$$

where **Z** is a tensor that represents the flow induced anisotropic nature of the suspension. Because it is flow induced, the tensor is a local function of the flow field. Based on a set of experiments the tensor components were determined. The results of the research have been published the article by Fang *et al.* The predictions made using the flow aligned tensor models were compared with all available experimental results and were shown to be in very good agreement. In particular, for the cone and plate geometry the anisotropic models predicted no particle migration, in contrast with available experimental data. On the other hand the flow aligned tensor model predicts steady-state particle concentrations, which are in close agreement with the experimental data, as shown in the figure. Similarly, a flow aligned tensor formulation was implemented in the diffusive flux model that gives similar improvements to those observed with the suspension balance model.

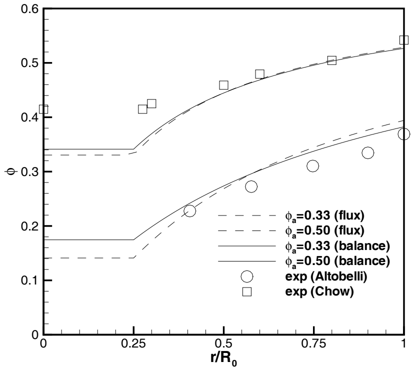

Comparison of predicted concentration profiles [lines] with experimental data [symbols] in a truncated cone and plate geometry.

Task 1.5 Determine diffusion coefficients – experiments

A review of the available literature was used to give best estimates for the diffusion coefficients used in task 1.4. As shown there, these values needed to be corrected to account for the correct physics. The diffusion coefficients obtained in the first year of this project were done assuming that the normal forces were not appreciable. In certain flow geometries normal forces dominate and it is unclear whether the same diffusion coefficients can be used. In Task 1.7, the normal forces in the experimental fluids and suspensions were not significant, so the values of the diffusion coefficient were not adjusted for use in subsequent numerical experiments.

Task 1.6 Incorporating wall slip models

Rheological models for the flow of concentrated suspensions based on the volume-averaged velocity of suspended particles in a viscous fluid have been developed. The so-called diffusive-flux and suspension-balance models are employed in this research to investigate the de-mixing rate of neutrally buoyant suspensions in CO_2 sequestration applications. Both models employ empirically determined (diffusion) coefficients which govern the rates and magnitudes of particle migration caused by gradients in the particle interaction frequency and suspension viscosity. The tuning parameters were originally sized based on no-slip boundary conditions. However, because the models are based on the suspension velocity, which is volume-averaged over the fluid and solid phases, slip exists at the walls. The effects of wall slip have been studied as part of Task 1.4

The slip boundary condition can be written as:

$$\beta a \dot{\gamma} = (\mathbf{u}_p - \mathbf{u}_f) \cdot \mathbf{t},$$

where α is the particle radius and $\mathbf{u}_p$ and $\mathbf{u}_f$ are the velocity of the particle and fluid respectively and $\mathbf{t}$ is the unit tangent vector to the boundary in the direction of slip.

The slip coefficient β governs the amount of slip at the wall. The case of no slip at the wall is given by $\beta = 0$ and the case of perfect slip is given by $\beta = \infty$. In general, the slip coefficient is a function of both the particle radius and solid-phase concentration. In particular, it has been found that β increases with both solid-phase concentration and particle radius.

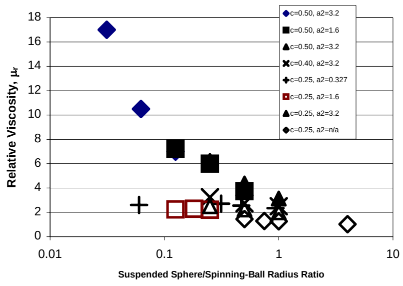

Relative viscosity of the suspension measured as a function of the suspended sphere to spinning ball radius ratio

Spinning ball rheometer physical and numerical experiments have been performed to determine quantitative values for β. To show the effect of slip, a plot of the relatively viscosity of a suspension as a function suspended sphere/spinning-ball radius ratio is shown in the figure. As the suspended sphere radius is increased, the apparent relative viscosity of the suspension is reduced. This is an indication that slip is increasing with increasing suspended sphere radius. It can also be inferred from the figure that slip increases with increasing volume fraction of the suspension. Although the numerical and experimental results at 25% volume fraction are qualitatively the same, the numerical results indicate more slip. This is probably caused by the fact that only 220 suspended spheres are contained in the numerical experiments whereas thousands are contained in the physical experiments.

The overall effect of slip is to reduce the migration rate. This is shown in the figure below for a numerical simulation based on the diffusive-flux model with slip boundary conditions. The simulation is performed in a Couette device with the initial conditions being uniform concentration of 50%. The simulations are run until steady state is achieved. For convenience, an alternative slip coefficient, C_β, is defined by:

$$C_\beta = \beta / \eta_r ,$$

where η_r is the relative viscosity.

The figure shows a plot of a difference measure as a function of time. The difference measure integrates the difference from a given concentration profile with the concentration profile at steady state, and hence, quantifies how far the simulation is from steady state at any given instant in time. Steady state is achieved when the difference measure is zero. As can be seen in the figure when the slip coefficient $C_\beta = 1/8$, steady state is achieved in approximately 8 dimensionless seconds. For no slip conditions, steady state is achieved in less than 4 seconds.

Reservoir Modeling

The reservoir will be modeled as a zoned homogenous region with different permeabilities in different zones. Certainly, the proppant-laden hydraulic fracture will be one zone but additional zones can be modeled representing strata in the porous media. Initially, all zones will be assumed to be fully saturated with brine. Supercritical CO_2 will be introduced at the wellhead.

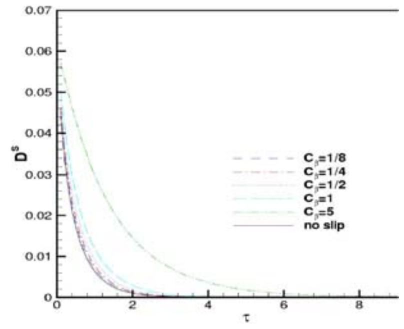

The difference measure as a function of nondimensional time t for no-slip and slip boundary condition for e = 0.0589 and a bulk solid-phase concentration of 50%.

The numerical simulation of the reservoir model will be based on a fully three-dimensional boundary element method. The viscosity variation at the advancing front between the brine and CO_2 can be modeled, in part, as a discrete jump in the permeabilties between zones (Hadavinia et al 1995). An advanced interfacial-tracking algorithm will be implemented so that viscous fingering can be studied.

Task 1.7 Normal Stress Differences: Numerical and Experimental

The normal stress difference is an important parameter in the suspension balance model for two-phase flows in porous media. In fact, it is believed that the $\sigma_{33}-\sigma_{11}$ and $\sigma_{22}-\sigma_{11}$ components are responsible for the nonisotropy of the flow field. The normal stress differences in a flowing suspension are known to be a function of the spatial distribution of the particles. The normal stress differences are of primary importance in the macroscopic simulation of suspension flow (Fang *et al*. 2002). Although it is possible to measure the normal stress differences in some cases (Zarraga *et al*. 2000), in the general case the direct measurement is very difficult. The approach used in this study was to experimentally measure the spatial distributions of particles in a suspension and then use numerical methods to calculate the viscous properties of such distributions. However, this method did not display any significant flow induced anisotropy with the result that no normal stress differences were observed numerically. Below are details of the experimental and numerical methods used.

Experimental Procedure

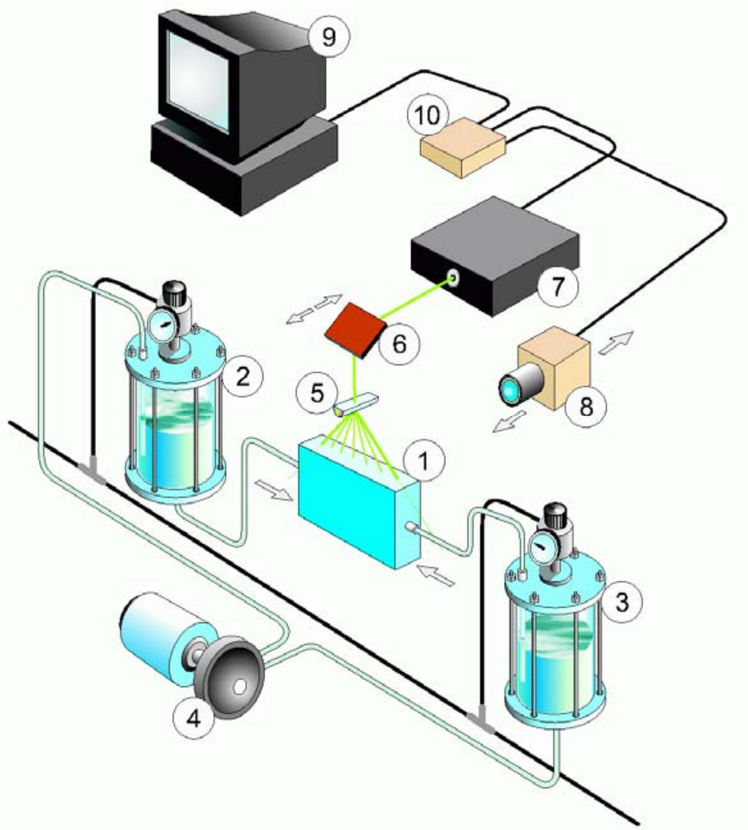

Figure 1.7.1: Schematic of flow loop: 1: visualization cell; 2,3: reservoirs; 4: recirculating pump; 5: cylindrical lens; 6: mirror; 7: Nd-YAG laser; 8: digital camera; 9: acquisition computer; 10: camera control interface.

The experimental procedure that will be used to make such measurements uses a similar apparatus to that which would be used in PIV measurements. In fact, PIV measurements were made (Task 2.3). The apparatus that has been built for this purpose is shown in Figure 1.7.1. It consists of two reservoirs, kept at a constant pressure differential, a visualization cell, a peristaltic pump for recirculating the suspension, a digital camera for image acquisition and a pulsed laser to illuminate a cross-section of the flow.

The phase distribution for a particular flow can be measured by halting the flow and acquiring a series of images at closely spaced cross-sections within the visualization cell. A voxel map of the suspension is generated by assembling the cross-sectional images. The acquisition of a cross-sectional image requires an optically clear suspension, in which the refractive index of the suspended particles matches the refractive index of the fluid.

The suspended particles are polystyrene-divynylbenzene particles, with a density of 1050 kg/m^3 and a refractive index of 1.59. Both the density and the refractive index can be matched using a combination of three components:

1-Chloronaphthalene (1.194/1.632)
1-Methylnaphthalene (1.001/1.615)
Paraffin oil (0.867/1.474)

The proportions of fluid that result in the optimal match are (by weight):

40.6% 1-Chloronaphthalene
43.4% 1-Methylnaphthalene
16% Mineral oil

Although the refractive index of the fluid can be carefully controlled, the particles' properties are not perfectly homogeneous. As a result, a loss of clarity occurs with increasing depth of the object under observation. To assess the error that arises from this, it is necessary to measure the error induced by the imperfect refractive index match.

To this end, a container was fabricated which allows the accurate location of a precision optical target, as shown in Figure 1.7.2.

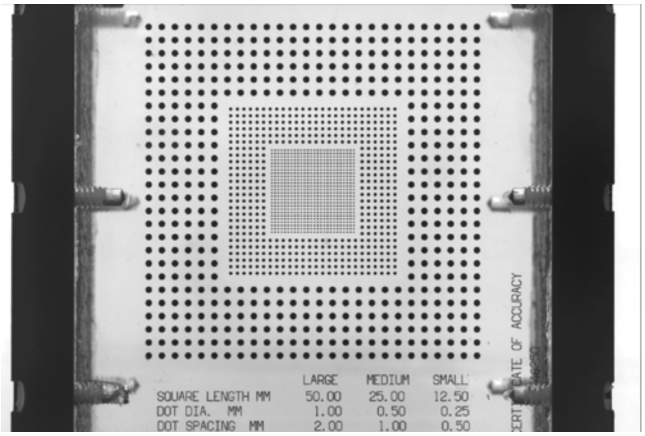

Figure 1.7.2: Image of an optical target in a calibration container (in air).

Images were acquired with the target located at depths ranging from 5mm to 25mm, at intervals of 5mm. The resulting images, with a suspension of 0.5mm diameter beads of 20% volume fraction, are shown below in Figure 1.7.3:

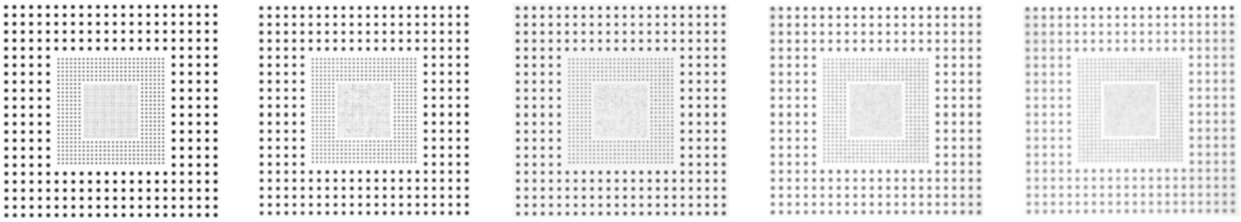
5mm 10mm 15mm 20mm 25mm

Figure 1.7.3: Images acquired with the target located at depths ranging from 5mm to 25 mm.

Eosin, a fluorescent dye that responds to the wavelength emitted by an Nd-YAG laser, was dissolved in the fluid. Illumination of the suspension with a sheet of laser light results in an image where particles show as dark areas, as shown in Figure 1.7.4. By scanning a suspension with a series of parallel laser sheets, it is possible to reconstruct a 3-D voxel map of the particles. Subsequently, via cross-correlation techniques, the 3-D particle positions can be extracted. While the flow-induced anisotropy of the particle distribution is another likely cause for non-Newtonian suspension rheology, no significant differences were observed.

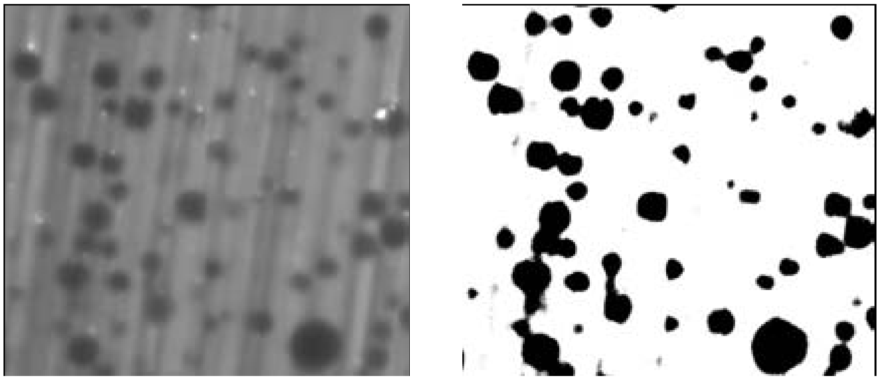

Figure 1.7.4: Image of polystyrene beads suspended in fluorescent density and refractive index matched fluid.

Numerical Procedure

The first measurements of the normal stress difference through numerical experiment have been performed. These simulations were run on Janus, the teraflop ASCI computer at Sandia National Laboratories, and represented some of the largest mesoscopic (particle-level) simulations ever performed. These normal-stress calculations are based on determining the volume-average stress tensor in post-processing of the numerical simulation. The numerical algorithm is based on a parallel boundary element method. 222 particles were suspended between counter-rotating parallel plates. The plates were rotating for 40 revolutions and the evolution of the volume averaged stress tensor was measured. We evaluated the pair-distribution function both before and after. No significant differences were seen. If the flow changes the pair distribution function in actual experiments, we are missing some physically important process. The most likely explanation is that any difference that occurred is too small for us to resolve with our current numerical methods.

Task 1.8 Determine hindered-settling correlation

Task 1.8 involved determining the appropriate way to model hindered settling in a non-neutrally buoyant suspension of particles in liquid. The diffusive flux model (Leighton and Acrivos, *J. Fluid Mech., 1987,* and Phillips et al., *Phys. Fluids A*, 1992) was implemented in a general purpose, Sandia developed, finite element computational program, GOMA. The momentum transport, continuity, and diffusive flux equations are solved simultaneously. The formulation is fully three-dimensional and can be run on a parallel computer platform. Gravity effects are added in an approach similar to that of Zhang and Acrivos (*Int. J. Multiphase Flow*, 1994).

The model results are compared with laboratory data on batch sedimentation obtained with Nuclear Magnetic Resonance (NMR) and x-ray imaging of evolving particle concentration profiles in complex flows. The x-ray images are produced after a polymerizing system cures, while the NMR images are obtained in near real time. Both experimental techniques give us particle volume fraction as a function of position, which is then used to validate our numerical results. Results compared well for three different flow fields: sedimentation in a cylinder with a contraction, sedimentation around a horizontal rod (Fig. 1.8.1), and sedimentation around a complex three-dimensional shape. As can be seen in the figure, the hindered settling is modeled adequately.

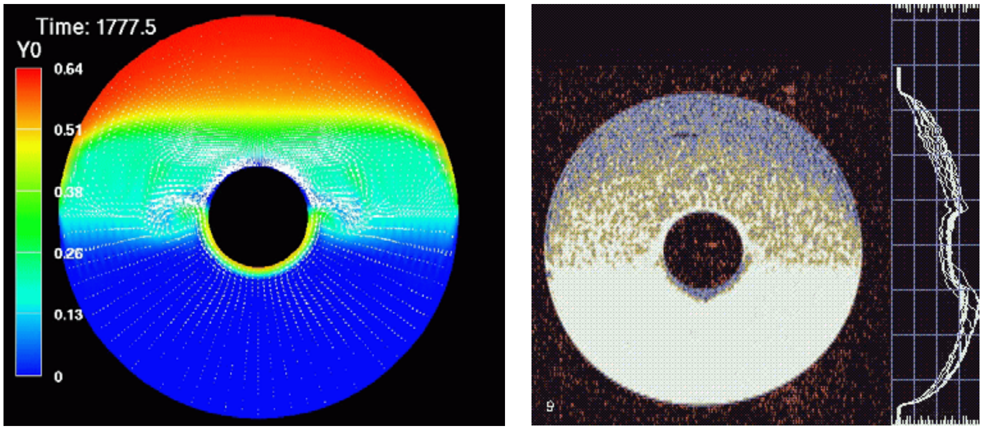

Figure 1.8.1: GOMA calculations of the flotation of particles vs. NMR measurements.

Task 1.9 Incorporation of non-Newtonian effects

BEM code

A new technique for treating non-Newtonian fluid behavior with a BEM simulation has been implemented and tested in 2-D. This technique is based on the ability to represent complex multiply connected geometries using boolean operations between a set of simple geometries. The technique allows the evaluation of domain integrals (necessary for the treatment of non-linear behavior with the BEM) much more efficiently than with conventional methods when combined with fast multipole acceleration. These microscale simulations will eventually lead to macroscopic models for non-linear suspensions.

Non-Newtonian behavior in a suspension is a result of irreversible inter-particle interactions. The extent of the irreversibility can be calculated by calculating the trajectory of two particles interacting in a shear field. The analytical solution of this is available, allowing the quantification of irreversibilities due to surface to surface interactions. Irreversible interactions can lead to the formation of a particle structure, which in turn can result in non-Newtonian macroscopic effects such as the presence of normal stress differences, shear thickening or memory effects.

When flowing through a contraction, particles can accumulate at the contraction, in such a way that Darcy's law is no longer applicable at the macroscopic scale (i.e. in a reservoir simulator). This effect is likely to be a function of the ratio of particle size to contraction minimum size. Particle level studies of this type are very large and require parallel platforms. A typical initial geometry is shown below:

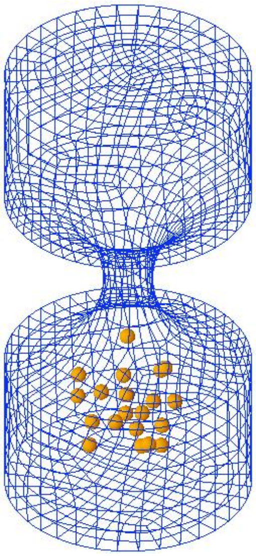

Fig.1.9.1: A typical initial geometry

The local increase in concentration at the throat is being studied as a function of initial particle concentration, ratio of particle size to pore size and interparticle forces. The results will be used in macroscopic models for flow through porous media.

The BEM formulation for non-Newtonian (non-linear) fluids generally results in a domain term in the integral equation. Of the many methods for dealing with this, the direct cell-based evaluation of the integral appears to be the most accurate, as demonstrated by Ingber et al. (2001). The multipole algorithm can be applied to the domain integration, resulting in significant reductions in calculation times. The speed advantage over comparable methods ranged from 10 to 100 times for the problems considered. Larger problems result in better speedup.

The main difficulty with the cell-based domain integration is that it is difficult to mesh complex three-dimensional multiply connected domains. A novel method to overcome this problem was devised by Mammoli (2002). It consists of evaluating the integral over a complex domain by Boolean operations involving integrals over simpler domains. The method was applied successfully to several 2-D and 3-D benchmarks in Mammoli (2002) and Hsiao et al. (2003), respectively.

A nonlinear capability has been added to the boundary element formulation in that small but finite Reynolds number effects can be included in numerical simulations. This capability was added as a prelude to adding nonlinear material properties associated with non-Newtonian fluids. As proof of concept, lateral migration of nonneutrally-buoyant spheres in Poiseuille flow have been investigated. The numerical results have been compared to experimental data as shown in Figs. 1.9.2 and 1.9.3.

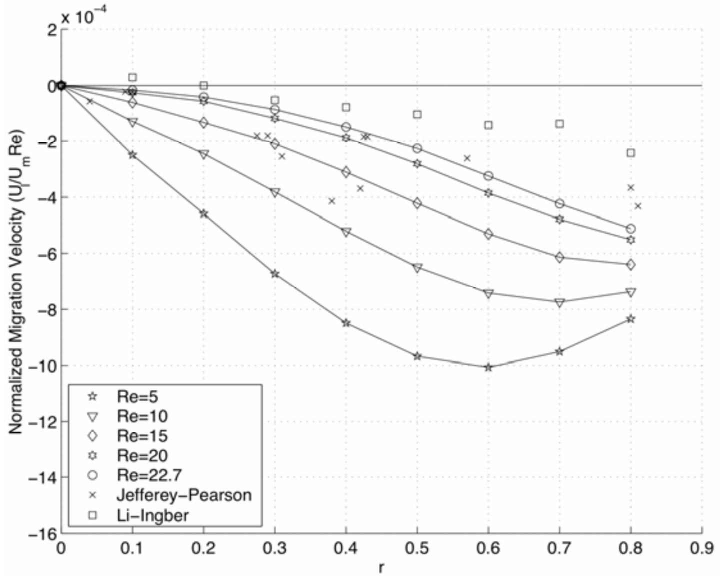

Fig. 1.9.2: The normalized lateral migration velocity as a function of the eccentric position *r* for the case in which the sphere lags the mean flow.

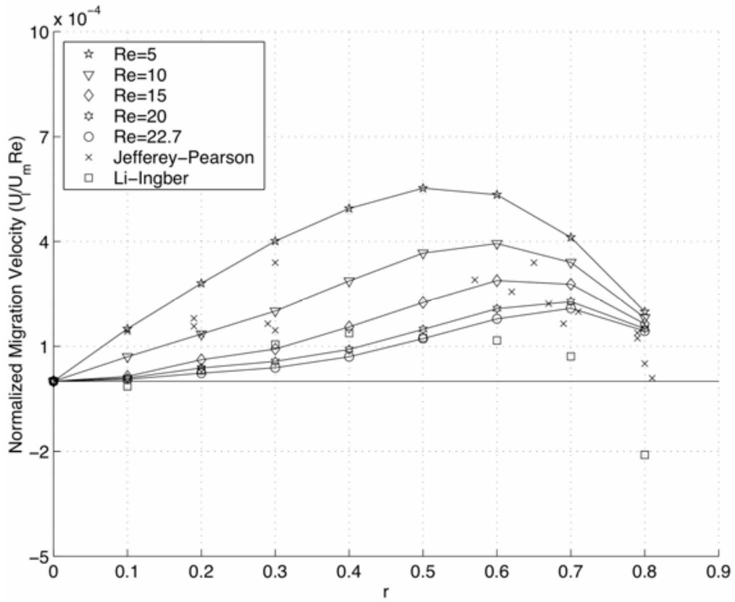

Fig. 1.9.3: The normalized lateral migration velocity as a function of the eccentric position *r* for the case in which the sphere leads the mean flow.

Continuum models

Shear-induced migration of particles was studied during the slow flow of suspensions of neutrally buoyant spheres, at 50% particle volume fraction, in an inelastic but shear-thinning, suspending fluid (Rao et al. 2002). The suspension was flowing in between a rotating inner cylinder and a stationary outer cylinder. The conditions were such that nonhydrodynamic effects are negligible. Nuclear magnetic resonance (NMR) imaging demonstrated that the movement of particles away from the high shear rate region is more pronounced than for a Newtonian suspending liquid. We tested a continuum constitutive model for the evolution of particle concentration in a flowing suspension proposed by Phillips et al. but extended to shear-thinning, suspending fluids. The fluid constitutive equation is Carreau-like in its shear-thinning behavior but also varies with the local particle concentration. The model captures many of the trends found in the experimental data, but does not yet agree quantitatively. In fact, quantitative agreement with a diffusive flux constitutive equation would be impossible without the addition of another fitting parameter that may depend on the shear-thinning nature of the suspending fluid. Because of this, we feel that the Phillips model may be fundamentally inadequate for simulating flows of particles in non-Newtonian suspending fluids without the introduction of a normal stress correction or other augmenting terms.

Numerical simulations for the macroscopic modeling of particles in non-Newtonian flows are based on the finite element method. Shear induced migration of particles has been studied during the slow flow of suspensions of spheres (particle volume fraction ϕ=0.50) in an inelastic but shear thinning suspending fluid in flow between counter rotating concentric cylinders. The movement of particles away from the high shear rate region was more pronounced than in a Newtonian suspending liquid. Previously, we tested a continuum constitutive model for the evolution of particle concentration in a flowing suspension proposed by Phillips et al. (1992), which works well in this geometry for Newtonian suspending fluids. The fluid constitutive equation in our model was Carreau-like in its shear-thinning behavior, but also varied with the local particle concentration. The original model was compared with the experimental data gathered with nuclear magnetic resonance (NMR) imaging and shown to be deficient (Rao et al. 2002). In fact, for a highly shear-thinning suspending fluid, the Phillips model could predict that the particles migrated in the opposite direction as shown in the experimental data.

The Phillips, or diffusive flux, model may be fundamentally inadequate for simulating flows of particles in non-Newtonian suspending fluids without the introduction of a normal stress correction or other augmenting terms. A modified suspension balance model and a modified diffusive flux model were developed in which a flow-aligned tensor has been added to capture the effects of normal forces on particle migration (Fang et al. 2002). A similar model to Fang's, but based primarily on work by Morris and Boulay (1999), has been tested for suspensions with non-Newtonian suspending liquids. Preliminary results show that this approach can capture the appropriate trends in the concentration profiles (Morris, 2003).

This approach, while giving initially promising results, has shown other problems when applied to certain types of problems. In particular, when particles become very close, strong nonlinear effects may become dominant. A similar effect was observed in the case of Newtonian rheology, where lubrication forces between neighboring particles are incorporated into the simulation using an approach described in previous reports and in several publications (Morris & Boulay 1999, Morris 2003, Phillips et al 1992). To resolve this issue definitively would require running a simulation with 3.6 million unknowns. This would require a computer with 10 TB of RAM and nine months on a terascale computing resource.

Task 1.10 Incorporate an advanced suspension flow into fracturing stimulation

Success of injectivity enhancement through hydraulic fracturing depends on placement of proppants during hydraulic fracturing. Simulation of proppant placement involves modeling of suspension flow of solid particles in fracturing fluids. Recent advances in modeling of suspension flow make it is possible for incorporating suspension flow model into hydraulic fracturing models for accurate simulation of proppant placement. Using a modified Philips et al. model[1], an advanced suspension flow model[1] was incorporated into an advanced fully three-dimensional hydraulic fracturing code.

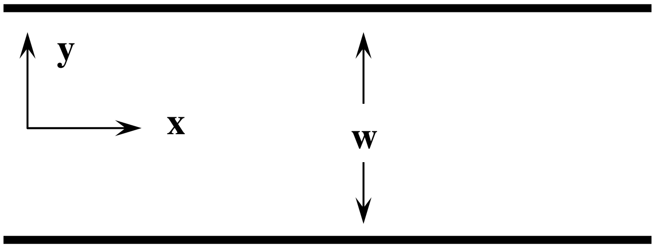

Figure 1.10.1. Schematic of suspension flow between fracture surfaces.

Let us consider a suspension flow of average solid or proppant concentration ϕ_a between fracture surfaces of width w, as shown in Figure 1.10.1. From fluid flow between parallel plates, one can obtain:

For a Newtonian suspension fluid flow:

$$\bar{u} = -\frac{dp}{dx}\frac{w^2}{12\mu_R}\Gamma \tag{1.10.1}$$

where

$$\bar{u} = \frac{2}{w}\int_0^{w/2} u dy \tag{1.10.2}$$

is the average suspension flow or slurry velocity, and

$$\Gamma = 3\int_0^1 \zeta^2 \frac{\mu_R}{\mu(\phi)} d\zeta \tag{1.10.3}$$

is a modification factor because of non-uniform distribution of particle concentration across the fracture width, μ_R is the viscosity of the fracturing fluid at zero particle concentration, $\mu(\phi)$ is the slurry viscosity at particle concentration ϕ, and $\zeta = y/(w/2)$ is integration variable.

For a power-law fluid, instead of Eqn. (1.10.1) we have

$$\bar{u} = -\frac{dp}{dx}\left(\frac{w}{2}\right)^{1+\frac{1}{n'}} \frac{\left(\frac{dp}{dx}\right)^{\frac{1}{n'}-1}}{(K_R^{'})^{\frac{1}{n'}}} \frac{\Gamma}{2+\frac{1}{n'}} \qquad (1.10.4)$$

where n' is the power-law fluid exponent and

$$\Gamma = \left(2+\frac{1}{n'}\right)\int_0^1 \zeta^{1+\frac{1}{n'}} \left(\frac{K_R^{'}}{K^{'}(\phi)}\right)^{\frac{1}{n'}} d\zeta \qquad (1.10.5)$$

K_R' is the fluid consistency coefficient at zero particle concentration and K'(ϕ) is the slurry consistency coefficient at solid concentration ϕ.

Since ϕ is a function of y, in order to get Γ from equation (1.10.3) or (1.10.5), one needs the relationship between suspension fluid viscosity and particle concentration. Slurry viscosity $\mu(\phi)$ is higher than the base fracturing fluid viscosity μ_R by the following correlation

$$\frac{\mu(\phi)}{\mu_R} = \left(1-\frac{\phi}{\phi_m}\right)^{-1.82} \qquad (1.10.6)$$

in which $\phi_m = 0.68$ is the maximum solid volume fracture for which the suspension or slurry exhibits fluid behavior.

Progress has been made in solving particle concentration ϕ at different distance from the wall and the results have reported recently[1]. For fully developed steady-state pressure-driven flow between fracture surfaces, the concentration profile for the modified diffusive flux model has the following form:

$$\frac{y}{w/2} = \frac{\phi_w}{\phi}\left(\frac{\phi_m - \phi}{\phi_m - \phi_w}\right)^{\zeta(K_\eta/K_c - 1)} \qquad (1.10.7)$$

where ϕ_w is the solid concentration at the wall, $\phi_m = 0.68$ is the maximum solid volume, $\zeta=1.5$ and $K_c = 0.41$, $K_\eta = 0.62$ are suspension flow model parameters[1].

As can be seen from equation (1.10.7), particle concentration across the fracture width is known once its value ϕ_w at the fracture wall is known. One can relate the ϕ_w to the average concentration ϕ_a. This can be done using the definition of the average volume fraction, written here in terms of z=y/(w/2)

$$\phi_a = \int_0^1 \phi(\zeta, \phi_w) d\zeta \qquad (1.10.8)$$

where, again, ζ=y/(w/2) is the integration variable. Numerical results between average particle concentration ϕ_a and the concentration ϕ_w at the fracture wall can be obtained from equations (1.10.7) and (1.10.8). In fact, results for average particle concentration at 30% and 50% are given in Zhiwu et al. (2002).

Once the relationship between average particle concentration ϕ_a and the concentration ϕ_w at the fracture wall is known, suspension (slurry) flow models in hydraulic fracturing models can be modified according to equation (1.10.1) or (1.10.4) to simulate particle transport in hydraulic fracturing, based on an advanced suspension flow model.

Task 2.1: Mesoscale simulation of multiphase flow through porous media

The development of the boundary element code to study fingering in porous media (Task 2.1) is continuing. Fingering is important at two length scales. At the microscopic length scale (the scale of the pores), microfingering can result in in loss of volumetric efficiency, because the more viscous fluid (water) that is being displaced by the less viscous fluid (supercritical CO_2) remains ‘locked’ inside pores. At the macroscale, classical fingering instabilities are known to lead to loss of volumetric efficiency by generating dendrite-like growth of the CO_2 bubble. To counteract fingering, emulsification of the injected fluid with a different fluid phase (typically water) leads to increased viscosity of the injected fluid, reducing the tendency for macroscopic fingering, but also increasing the required injection pressure for a given injection rate. It is necessary to perform numerical simulation at the microscale to determine the behavior of the emulsion. A 2-dimensional Stokes code was implemented to study a problem of the type shown in Fig. 2.1.1. A similar geometry is used by Power and Wrobel (1995) to study viscous fingering in a Helishaw cell, however in our case the governing equation is not a potential law, but the 2-dimensional Stokes equation.

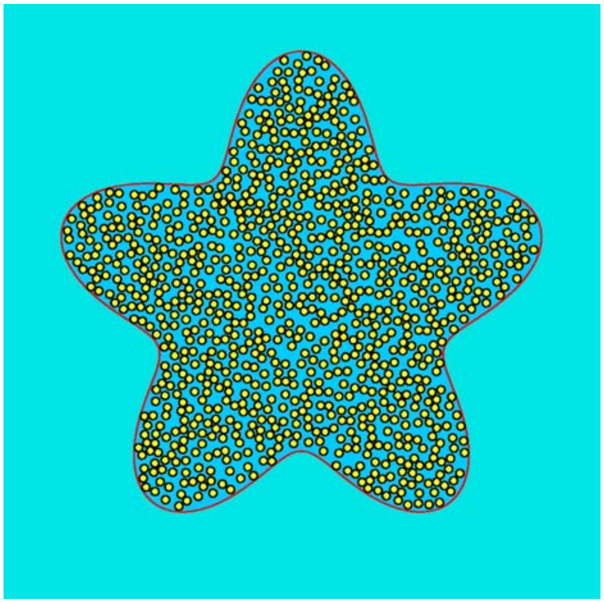

Figure 2.1.1: Schematic of the 2-dimensional simulation of viscous fingering of an emulsion in an unbounded fluid. The goal is to study the effect of adding a second phase (in yellow) to a growing bubble of less viscous fluid on the stability of its interface (red) with the displaced, more viscous fluid. The bubble grows because of a source at its center.

A two-phase Stokes code that uses C-1 continuous elements was initially developed to study this problem. C-1 continuous elements ensure that first derivative continuity between adjacent elements is preserved. This is a physical condition imposed by fluid interfaces with surface tension. C-0 continuous elements, such as quadratic elements, introduce artificial kinks at the joints of element. This leads to erroneous results.

The code was benchmarked against analytical solutions for the circular Couette flow shown below. The computational results are in excellent agreement with analytical results as shown in Figure 2.1.3.

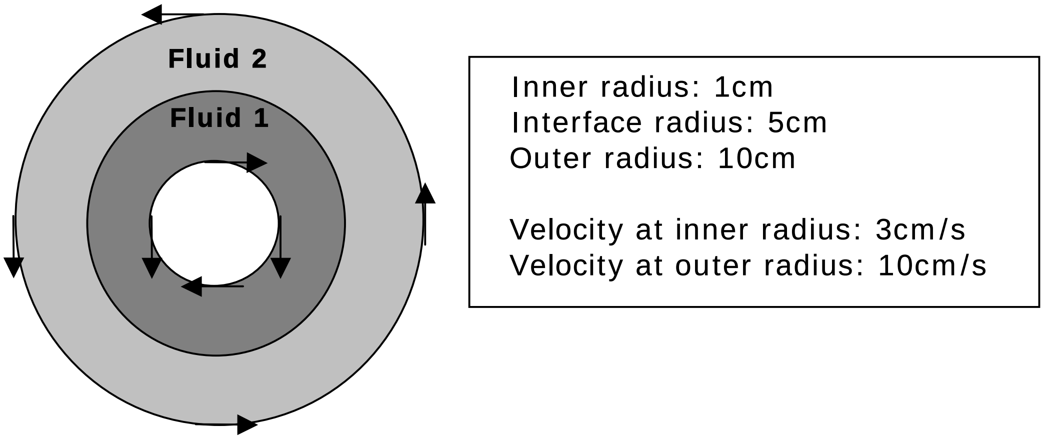

Figure 2.1.2: Benchmark of a two-phase circular Couette flow.

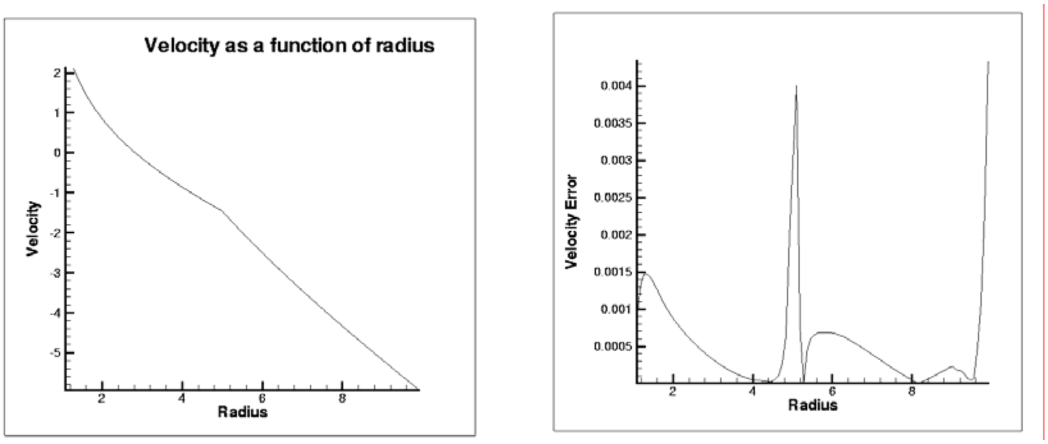

Figure 2.1.3: Velocity profile and error along the profile for a two-phase Couette flow. Analytical and computed velocities are shown on the left, however, the error is so small that the results cannot be distinguished. The error is shown on the right.

A forward Euler time stepping strategy was used to update the interface of the fluids. After each time step, surface nodes are re-distributed along the interface to prevent "bunching". "Bunching" occurs when nodes move closer and closer together in areas where the velocity field is converging to a small region and can lead to numerical inaccuracies.

We have simulated the effects of an inner fluid pushing an outer fluid in the presence of rigid obstacles, as is the case of injecting one fluid in a reservoir to displace another fluid. The initial configuration of the simulations is shown in Figure 2.1.4.

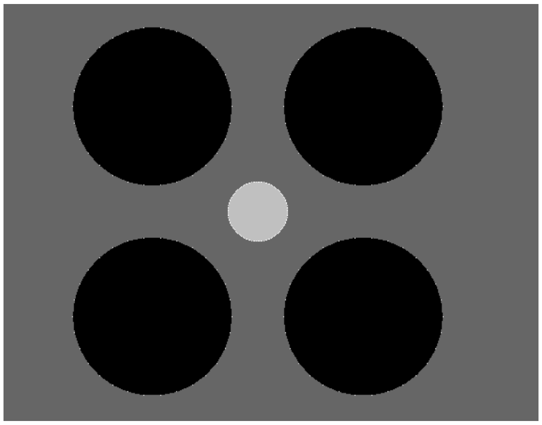

● Indicates a rigid obstacle the fluids must flow around.

○ Represents the inner fluid. A source present at the center drives both fluids radially outward.

◍ Represents the outer fluid. The pressure on the outer fluid very far from the source is zero.

Figure 2.1.4: Initial configuration of a two-phase fluid flow.

Two test cases indicate the effects of relative viscosity on fingering. When the viscosity of the inner fluid is larger than that of the outer fluid, fingering takes place. The amount of fingering increases when the viscosity of the inner fluid is smaller than that of the outer fluid. Simulation results for the two test cases are shown in Figure 2.1.5.

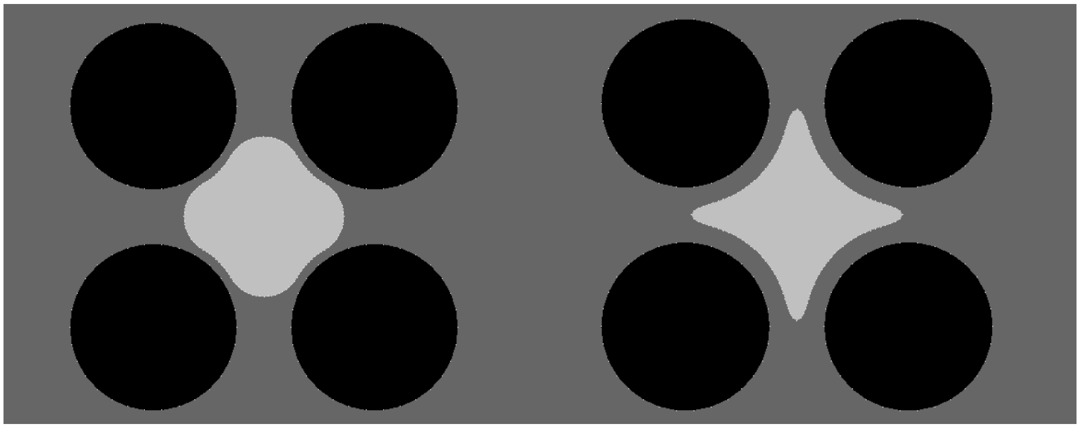

Figure 2.1.5: Two simulations of viscous fingering. On the left, the viscosity of the inner fluid is greater than that of the outer fluid. On the right, the viscosity of the inner fluid is smaller than that of the outer fluid.

We have also modeled, using our boundary element codes, the movement of a bubble of one fluid through a loosely packed bed filled with another fluid. We approximated the bubble as a solid sphere, which allowed us to validate the code with existing experimental data. The results compared very well with available data, even in the case where the ball is spinning. In the past, the torque on the sphere has proven to be a more difficult case to represent accurately.

A module was added to the code, which can accurately simulate surface tension forces. Simple test problems showed the problem with the earlier method and demonstrated that the new method was working properly. These tests reveled that C-2 continuity is a necessary for realistic simulation of surface tension forces. Surface tension forces are governed by the Young-Laplace equation. In two dimensions the equation for surface forces takes the following form,

$$\sigma = \gamma\kappa$$

where σ is the surface tension force, γ is the surface tension and κ is the curvature. The curvature can be computed from the parametric representation of an element and involves second derivatives. Functions, which are discontinuous in second derivatives may produce a discontinuous surface tension forces. One may think that by increasing the number of elements, the effects of these discontinuities may be diminished, but numerical simulations indicate that this is not the case. As the mesh is refined in these cases, the simulations do not converge quickly, if at all. Figure 2.1.6 below shows a simulation of a non-circular drop in a quiescent medium. Surface tension should cause the drop to deform to a circular shape. The discontinuous surface tension causes a pressure gradient, which induces a rotational flow.

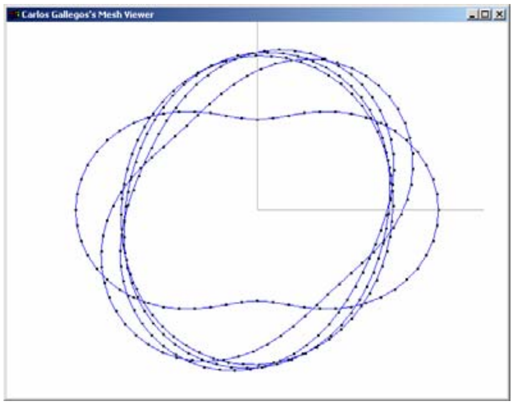

Figure 2.1.6: Deformation of a non-circular drop due to surface tension.

To circumvent this problem, we have resorted to a technique, which averages surface tension forces at coincident nodes in order to enforce C-2 continuity. Numerical results show vastly improved accuracy. The distorted drop does deform to a circle as shown in the figure below.

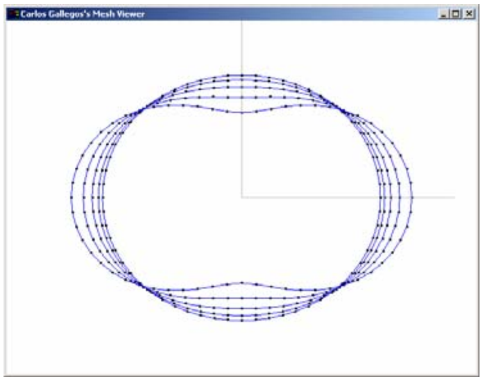

Figure 2.1.7: Deformation of a non-circular drop due to surface tension forces. The drop eventually deforms to a circular shape as expected.

Figure 2.1.8 shows simulations for these three design parameters. As can be seen, varying the viscosity ratio, as well as the porosity, has minimal effect on the finger shapes. However, the finger shapes change significantly with varying capillary number. The capillary number can be modified for typical flows by changing the rate of injection or adding surfactants to the fluids. Slowing down the rate of injection and increasing the surface tension would results in better storage efficiency.

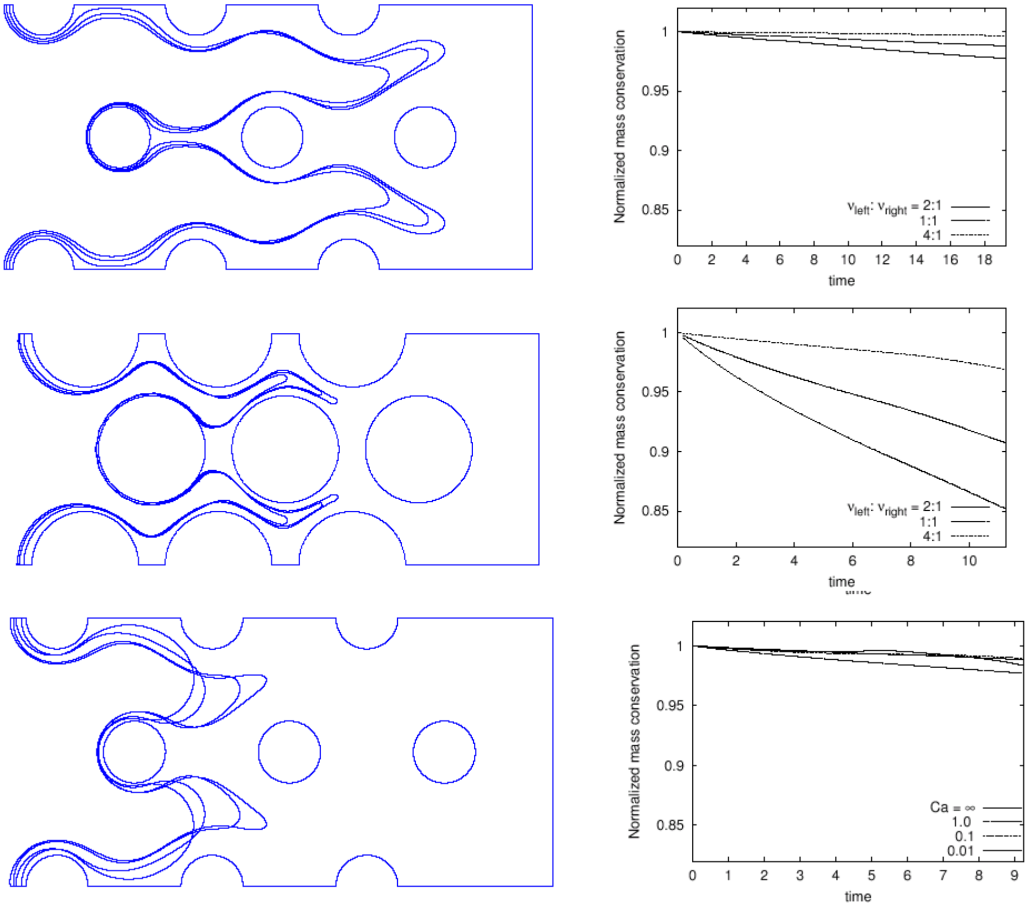

Figure 2.1.8: The top set of figures shows viscous fingering and normalized mass conservation as a function of viscosity ratio for a porosity of 85.4 % and capillary number of infinity. The middle set of figures shows viscous fingering as a function of viscosity ratio for a porosity of 42.0% and capillary number of infinity. The bottom set of figures shows viscous fingering as a function of capillary number for a fixed viscosity ratio of 1:2 (inner fluid to outer fluid).

Task 2.2 Determine appropriate geometries with NMR imaging

Initial experiments using the NMR facilities at Texas Tech University were used to establish acceptable apparatus geometries for imaging and characterization experiments. Several types of experimental apparatuses were designed and constructed. Concentric cylinder (Couette) and parallel plates were constructed of clear plastics so that both visual and NMR measurements could be performed.

The primary geometry used was concentric cylinder with at ratio of 4:1 of the outer cylinder to the inner rod. This gives a non-uniform shear field that is well defined. In these experiments the inner rod would be rotated while the outer cylinder was held fixed.

Task 2.3 PIV Validation of Simulation Results

Velocity maps of the flowing suspension in various flow geometries can be obtained with the same setup described in Task 1.7. The image processing software that is under development for measuring the phase distribution can also serve to measure particle velocities. In addition, it is possible to seed the flow with micron-sized particles, thus allowing the simultaneous measurement of the fluid velocity. If sufficiently accurate, the measurement of phase lag between the solid phase and the fluid phase will be possible.

Initial experiments used a refractive index matched suspensions of PMMA particles in Water/$ZnCl_2$/Triton suspending fluids. This choice was found to have properties that were very sensitive to water loss due to evaporation. A better mixture using methyl-chloronaphthalene, ethyl-chloronaphthalene and mineral oil was eventually used.

The transient numerical simulations discussed above from Task 1.7 are extremely time consuming taking several weeks to perform on large parallel computers. The reason that transient simulations are required as opposed to snapshots of random systems is that, in order to generate the appropriate features, flow induced structure needs to evolve. An alternative approach is to perform physical experiments and determine the particle distributions from PIV. Then a numerical snapshot can be performed to get the desired detailed information. An optical technique has been developed to determine particle positions using PIV. The technique involves illuminating a plane interior to the flow field using a laser sheet. Figure 1.7.4 is the result of one such experiment. One plane at a time can be illuminated to determine the deposition of particles everywhere in the field.

Task 2.4 PVT Properties of CO_2

All injection operations (either frictional pressure drops in injection strings) or pressure drops occurring in porous medium or fracturing flow) will be dependent on the compressibility (and viscosity) characteristics of the carbon dioxide stream. One of the first efforts in acquiring data relevant to simulations was to determine representative properties of non-cryogenic CO_2. The PVT (pressure-volume-temperature) properties of CO_2 are necessary for numerical modeling and engineering design studies of CO_2 sequestration.

Correlations have been developed in the literature to represent density and viscosity of pure CO_2 at different pressures and temperatures. Figure 2.4.1a shows density as a function of pressure and temperature under supercritical conditions. Figure 2.4.1b shows the viscosity as a function of pressure and temperature for pure CO_2 under supercritical conditions.

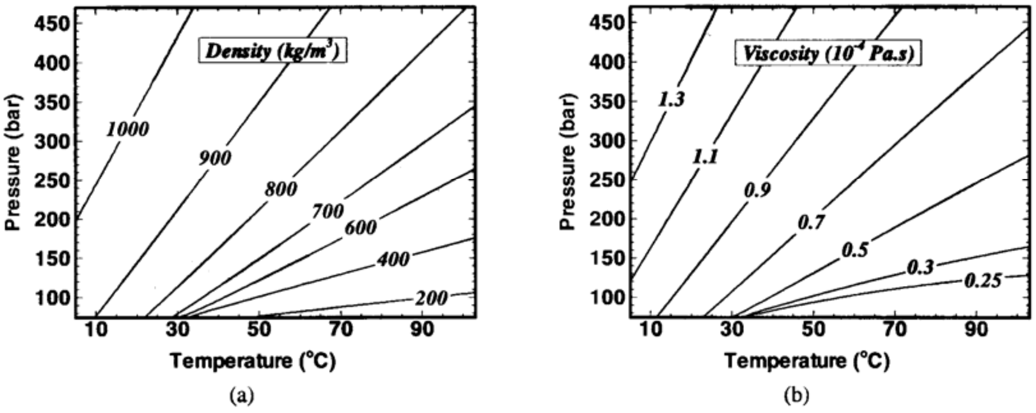

(a)

(b)

Figure 2.4.1: Density of CO_2 (a) and Viscosity of CO_2 (b), under supercritical conditions, as a function of temperature and pressure.

The system CO2, CaCO3 and H20 at 15 C and 18 MPa is used an example. Adding NaCl to the system and observing how the solubility of other ions changed is shown in Figure 2.4.2. As the salt concentration goes from zero to saturated, Ca++ solubility is decreased from 0.167 to 0.096 molal. Similarly the HCO3- ion concentration decreases from 0.335 to 0.19 molal. These decreases in solubility are significant, but acceptable since formation brines and injected will water will contain much lower concentrations of "inert" ions than saturated sodium chloride solutions. The pH and dissolved CO2 concentrations are much less changed by the addition of NaCl as shown in Figure 2.4/3. Figure 2.4.3 also indicates the solubility of NaCl in this solution is 5.88 molal. This compares favorably with reported solubility of NaCl in pure water of 6.11 molal, since the other ions in the example solution would suppress the solubility of NaCl.

The ChemCad simulations address equilibrium solubility matters, but not the rate at which dissolution takes place. Experimental measurements of dissolution rates are given as part of Task 4.3.

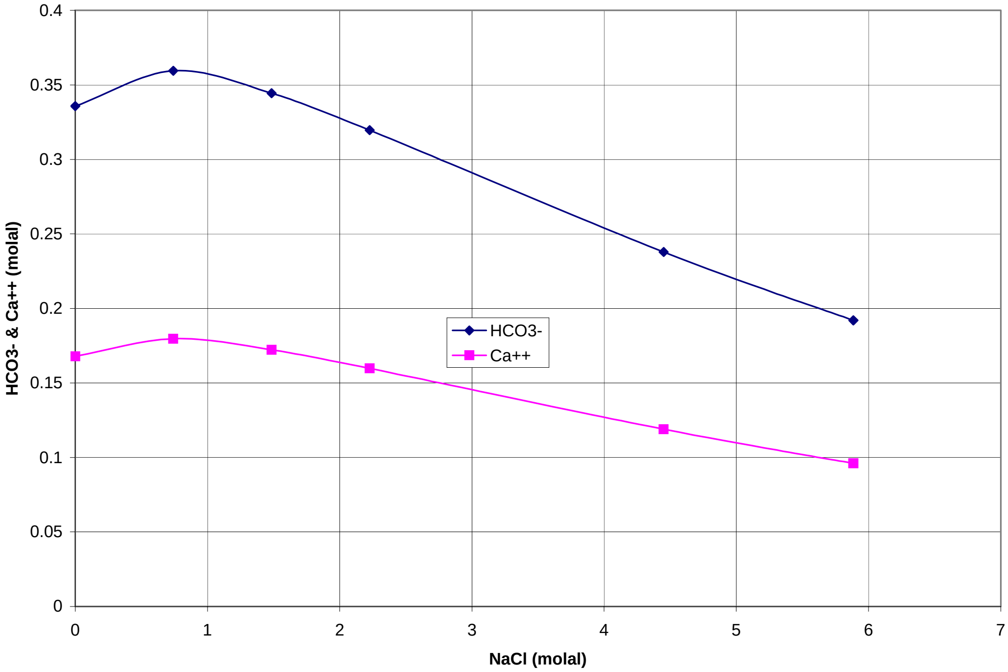

Figure 2.4.2 -Addition of NaCl to System Containing CO2, CaCO3 & H20 at 15C and 18 MPa

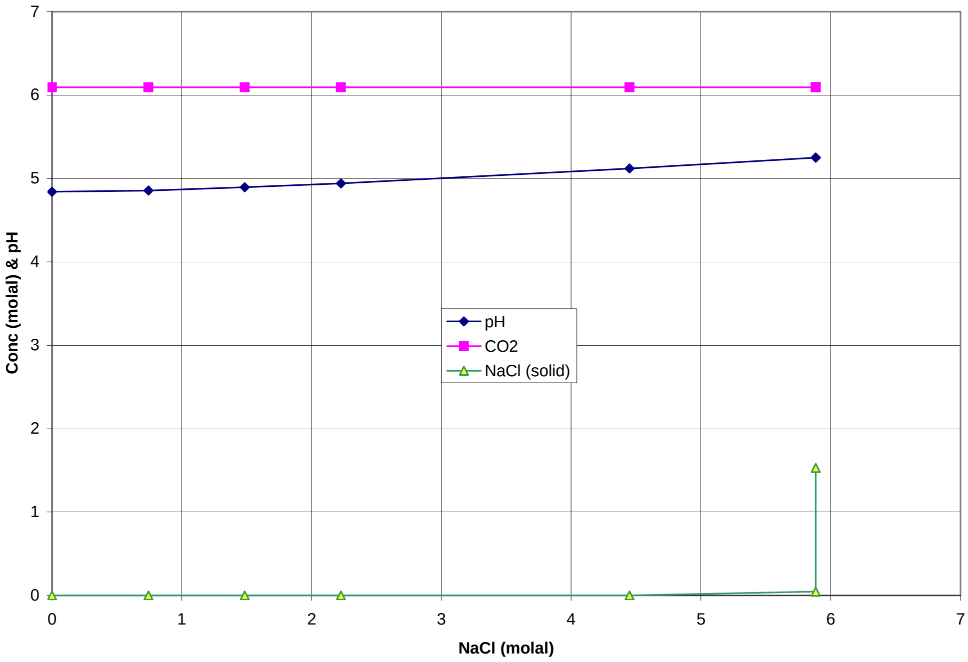

Figure 2.4.3 - Addition of NaCl to System Containing CO2, CaCO3 & H20 at 15C and 18 MPa

Task 2.5 Determine solubilities using chemical processing simulators

Several simulators were used to determine the solubilities of CO_2 in water and a variety of compounds in water/CO_2 solutions. The first, PHRQPITZ (USGS), is a modification of the geochemical modeling code, PHREEQE, to permit calculations of geochemical reactions in brines and other highly concentrated electrolyte solutions using the Pitzer virial-coefficient approach for activity-coefficient corrections. Reaction-modeling capabilities include calculation of (l) aqueous speciation and mineral-saturation index, (2) mineral solubility, (3) mixing and titration of aqueous solutions, (4) irreversible reactions and mineral-water mass transfer, and (5) reaction path. The computed results for each aqueous solution include the osmotic coefficient, water activity, mineral saturation indices, mean activity coefficients, total activity coefficients, and scale- dependent values of pH, individual-ion activities, and individual- ion activity coefficients. A data base of Pitzer interaction parameters is provided at 25 C (Celsius) for the system: Na-K-Mg-Ca-H-Cl-SO4-OH-HCO3-CO3-CO2-H2O; and it is extended to include largely untested literature data for Fe(II), Mn(II), Sr, Ba, Li, and Br with provision for calculations at temperatures other than 25 C. PHRQPITZ is accompanied by an interactive input code, PITZINPT.

The second, EQ6 (LLNL), is a computer program for reaction path modeling of aqueous geochemical systems. It calculates reaction paths in reacting water-rock and water-rock-waste systems. It models the chemical evolution of the system using thermodynamic and kinetic constraints.

In addition to these two models, ChemShare was also used. These predictions are comparable to those available in the literature.

Task 3.1 Determine T_2-cutoff value

NMR measurements on well-characterized synthetic core samples with known amounts of 30 nm Fe_2O_3 iron oxide added to the pore wall cement were performed. SEM and x-ray analysis was provided by Dr. Necip Guven, a noted clay mineralogist and geologist located at Texas Tech. As expected, the iron lowered the T_2 distribution values due to the additional paramagnetic interaction. In addition, the T_2 distribution was stretched and skewed as the iron concentration was increased. Moreover, the apparent total porosity measurement was reduced by as much as 15% from the ‘true’ value. We believe that this indicates that the NMR relaxation in the presence of clusters of strong paramagnetic particles is no longer in the fast diffusion limit.

Task 3.2 Test the hypothesis that the T_2 distribution of a shale can be correlated to its capillary pressure distribution curve

This research involves the study of shales, siltstone, tight fine sandstones, and synthetic samples, which will be used as standards. Texaco Inc. provided the rock samples from the Lewis Shale and the Shublick Formation. The Lewis Shale of south-central Wyoming accumulated within the Western Interior Seaway basin and represents the final transgression of the epicontinental sea during the Maastrichtian (Witton-Barnes et al., 2000). This unit is younger, and does not correlate to the Lewis Shale of southwestern Colorado (Weimer, 1960). In the Washakie and Great Divide basins, the Lewis Shale (Figure 12) overlies the Almond Formation and consists of 2,200 – 2,600 feet of shales, mudstones, siltstones, and sandstones (Witton-Barnes et al., 2000). The sandstones of the Lewis Shale and those of the upper Almond Formation contain productive oil and gas horizons (Asquith, 1970). Depositional environments of the Lewis Shale are highly variable from deep-water to shelf marine settings (Pyles and Slatt, 2000).

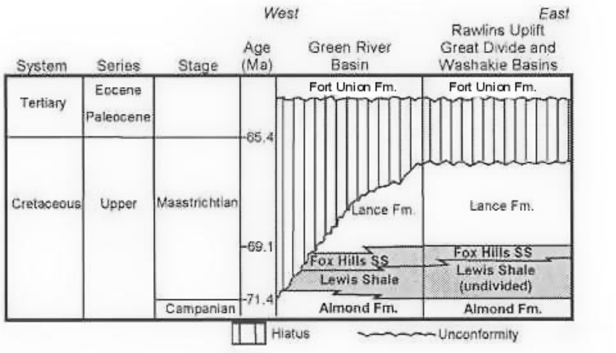

Figure 3.2.1: Chronostratigraphic chart of Upper Cretaceous in south-central Wyoming (modified from Pyles and Slatt, 2000).

The Triassic Shublik Formation is included in the Mississipian to Early Cretaceous Ellesmerian sequence of the North Slope of Alaska. This area is the most prolific of the oil producing regions in North America and the Ellesmerian system comprise 98% of the hydrocarbon discoveries in the North Slope (Bird, 1994). The Shublik Formation together with the Kingak Shale are considered to be the source rocks of the petroleum system. The Shublik Formation (Figure 13) is about 100 m thick and is composed of glauconitic, phosphatic, and fossiliferous shales, siltstones, mudstones, and limestones (Bird, 1994). They were deposited under upwelling conditions in a shallow marine environment under low sedimentation rate conditions (Bird, 1994).

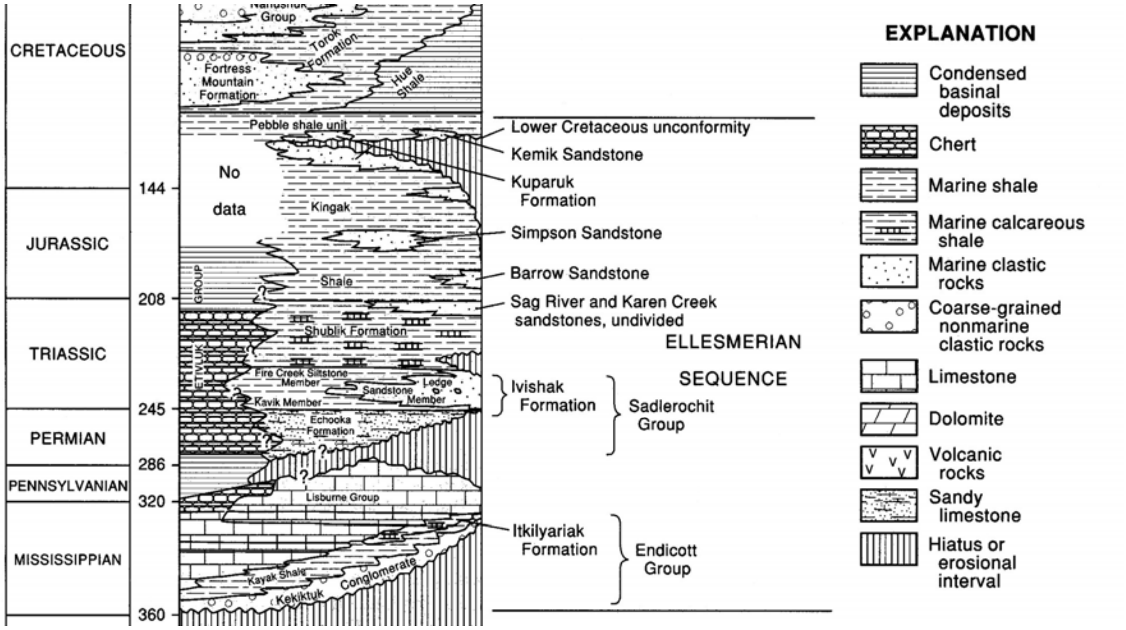

Figure 3.2.2: Stratigraphic column of the Ellesmerian sequence in the North Slope, Alaska (modified from Bird, 1994).

Transverse relaxation times, T_2, were obtained in a low field tabletop spectrometer by using Carr-Purcell-Meiboom-Gill, CPMG, sequences that have been designed to minimize the effects of diffusion processes. These sequences consist of an initial 90-degree pulse followed by a series of 180-degree pulses. The 180-degree pulses are separated from each other by a time called inter-echo spacing (TE in Figure 3.2.3). The purpose of the 180-degree pulses is to refocus the spins on the transverse plane; therefore, a short interecho time minimizes the effects of diffusion in a time-varying magnetic field.

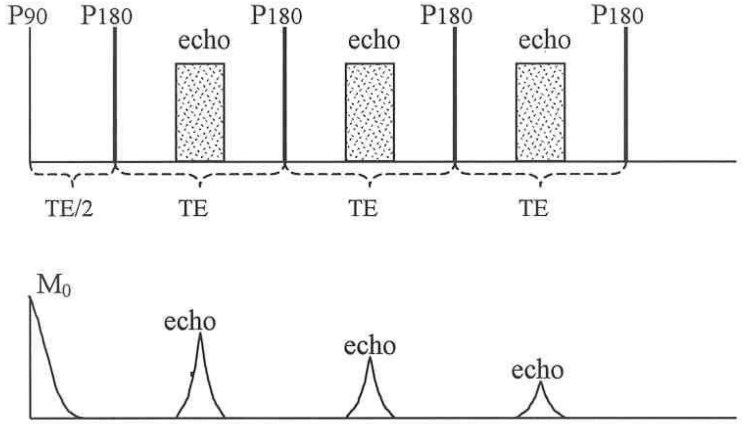

Figure 3.2.3: Schematic diagram of a CPMG sequence. Top diagram displays the arrangement of pulses and echoes. Bottom diagram shows the echo train.

Each 180-degree pulse produces an echo after half the time between the pulses (Figure 3.2.3); and the envelope of all those echoes is the result of the CPMG experiment.

The NMR spectrometer is a Maran 2 Ultra made by Resonance Instruments working at 2 MHz, which is the same magnetic field used by some logging tools. The Maran 2 has been audited to minimize the noise and improve the signal within the T_2 time range where the shales produce a signal. For this reason some modifications to the spectrometer, such as installation of magnetic shields and rerouting of cables, have been made. Also, it has been found that an appropriate T_2 will be obtained with an interecho time spacing of 166.67 microseconds. The Maran 2 Ultra spectrometer has been tested with solution samples of varying concentrations of Mn^{2+} to determine the shortest reliable T_2. This time has been determined to be 200 microseconds.

The T_2 response of all the samples was obtained at different saturation stages: as received (probably under-saturated), de-saturated, and fully saturated. Because NMR provides a measurement of the fluid content, total porosity is derived from the fully saturated samples. The T_2 data from the de-saturated samples represent the non-connected porosity, i.e. residual porosity; this will be subtracted from the total porosity to derive the capillary pressure curves of the samples. This property is fundamental in assessing the quality of a seal.

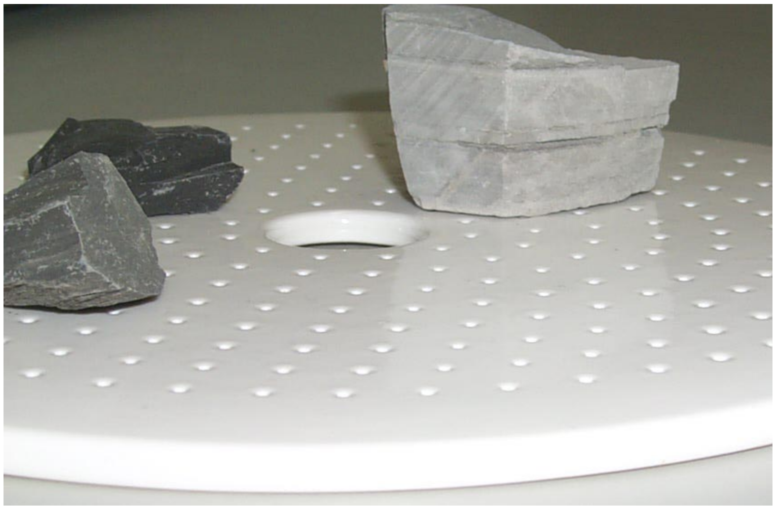

Figure 3.2.4: Photograph of Lewis Shale samples.

Hand specimen of the samples (Fig. 3.2.4) were analyzed and described by recording color, sedimentary structures, presence of organic matter and fossil remains (Tables 3.2.1-3.2.3). The organic matter was examined by monitoring the fluorescence of aqueous suspensions, which were prepared for X-ray diffraction analysis, using an UVP Inc. ultraviolet light model UVGL-25 with a multiband of UV-254/366 nm.

Table 3.2.1: Main characteristics of the pebble shale unit samples.

Sample	Lithology	Color	Sedimentary Structure	Organic Matter
PH 7647.55	Siltstone	Black	Massive	No

PH 7649.8	Siltstone	Dark gray	Massive	No
PH 7652.5	Siltstone	Dark gray	Massive	Yes
PH 7660.45	Shale	Black	Massive	No
PH 7666.4	Silty shale	Black	Massive	Yes
PH 7674.5	Silty shale	Medium gray	Massive	Yes
PH 7685.45	Silty shale	Dark gray	Massive	Yes
PH 7692.45	Silty shale	Dark gray	Finely laminated	Yes
PH 7695	Siltstone	Light brown	Finely laminated	No*
PH 7700.15	Very fine sandstone	Dark brown	Massive	Yes
PH 7702.35	Siltstone	Dark gray	Massive	No*

*PH 7695 and PH 7702.35 were treated with acid solutions that reacted with the organic matter if were present.

Table 3.2.2: Main characteristics of the Lewis Shale samples of the CSM core.

Sample	Lithology	Color	Sedimentary Structure
CSM 295.9	Mudstone-sandstone	Light gray	Beds are massive
CSM 307.6	Silty shale	Black	Fine laminations. Fossil remains
CSM 319	Mudstone-sandstone	Gray	Beds are finely laminated
CSM 433.3	Mudstone-sandstone	Gray	Mudstone is finely laminated. Fossil remains
CSM 440.1	Shale	Dark gray	Fine laminations. Fossils
CSM 447.2	Siltstone	Dark gray	Fine laminations
CSM 450	Mudstone-sandstone	Light gray	Fine laminations
CSM 915.5	Shale	Dark gray	Poorly defined laminations
CSM 918.3	Shale	Black	Fissile. Fossil remains. Fine laminations
CSM 920.9	Fine siltstone	Black	Fissile. Fine laminations
CSM 924.7	Fine siltstone	Dark gray	Fine laminations
CSM 927.6	Fine siltstone	Black	Wavy laminations. Fossils
CSM 930.2	Fine siltstone	Black	Massive. Fossils
CSM 930.4	Fine siltstone	Black	Poorly defined laminations. Fossils
CSM 931.7	Fine siltstone	Dark gray	Poorly defined laminations. Fossils
CSM 932.7	Shale	Black	Fissile. Fine laminations. Fossils
CSM 932.9	Shale	Black	Fissile. Deformed laminations. Fossils
CSM 934.1	Shale	Black	Lenticular bedding
CSM 1589	Very fine sandstone	Light gray	Massive
CSM 1605.8	Shale	Black	Massive

CSM 1621.5	Shale	Black	Massive

The samples representing the pebble shale unit are mainly dark gray to black massive siltstones (Table 3.2.1). These samples lack fossils and display a variable content of organic matter. Two of the samples, PH 7695 and PH 7702.35, exhibited more than 20% of siderite and dolomite respectively, which were removed with acid solutions to analyze the clay mineral content with X-ray diffraction. The acid treatment could have also removed any organic matter if present.

Table 3.2.3: Main characteristics of the Lewis Shale samples of the CH core.

Sample	Lithology	Color	Sedimentary Structure	Organic Matter
CH 8075	Shale	Black	Massive	Yes
CH 8098.5	Shale	Black	Massive	Yes
CH 8122.5	Shale	Black	Poorly defined fine laminations	Yes
CH 8112.5	Shale	Black	Poorly defined fine laminations	No*
CH 8131.6	Shale	Black	Massive	No*
CH 8155	Shale	Black	Massive. Fractures.	Yes
CH 8162.5	Shale	Black	Massive	Yes
CH 8168	Shale	Black	Massive	Yes
CH 8187.5	Shale	Black	Massive	Yes

*No aqueous suspension was available

Even though the NMR data of the desaturated shale samples displayed a low signal-to-noise ratio, all the NMR data were obtained with approximately the same SNR of about 70. All the NMR time datasets of the shales were inverted with the WinDXP software with 256 pruned points and 256 time constants to obtain the T_2 distributions. Note that only some of the results are presented here, but all the results are shown in the appendices. The resulting distributions were variable, depending mainly on their saturation state, and were generally characterized by more than one mode (Fig. 3.2.5). The T_2 distributions of the undersaturated samples were in general bimodal (Figs. C.1). The main modes of the Lewis Shale samples, CH core, corresponded to T_2 of a few milliseconds (Fig. C.1), while in the samples of the CSM core an increase of the main modes was observed. These modes ranged from 0.5 ms to 6.0 ms. The undersaturated siltstones of the Alaskan pebble shale unit also displayed main modes in the order of a few milliseconds. A different behavior was observed in the T_2 distributions of the saturated samples, which were characterized by unimodal distributions in the Lewis Shale (Figs. 3.2.6 A and B) and by bimodal distributions in the samples of the Alaskan PH core (Fig. 3.2.6 C). The T_2 distributions of the PH core had main modes between 0.6 ms and a few milliseconds, while the secondary modes were more variable and were generally on the order of a few tens milliseconds.

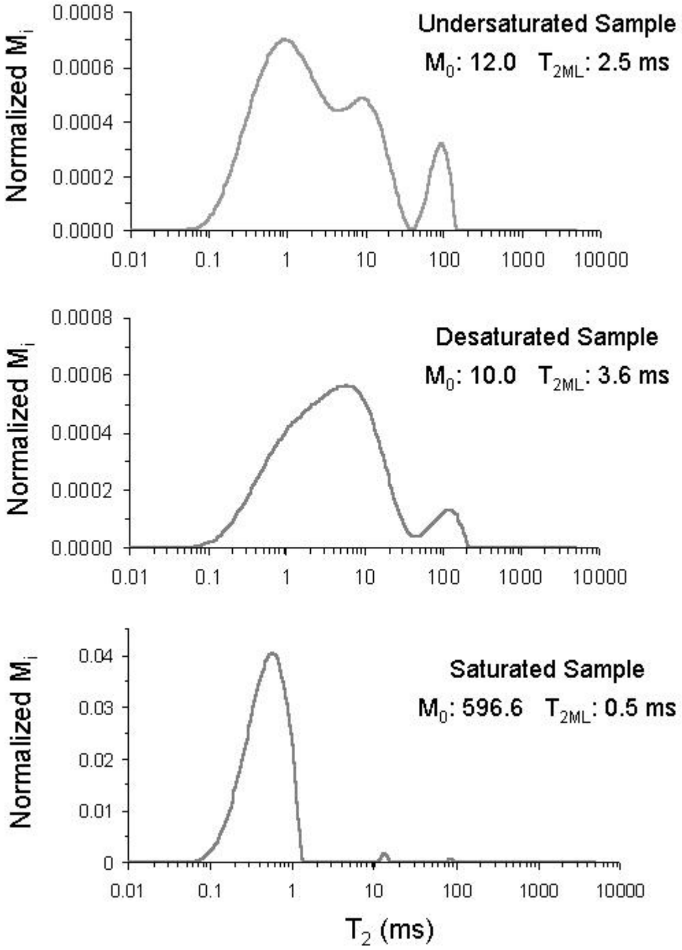

Figure 3.2.5: T_2 distributions of the sample CSM 450. Lewis Shale.

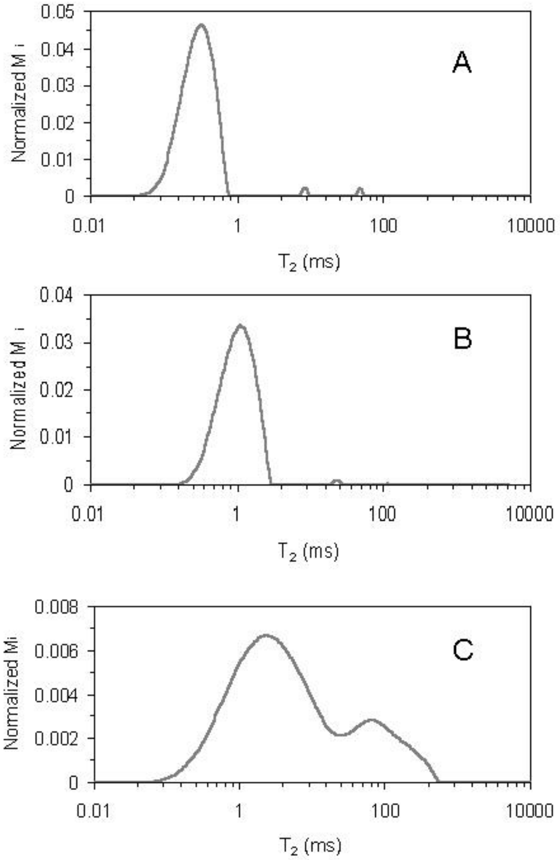

Figure 3.2.6: Characteristic T_2 distributions of the saturated samples. One sample of each core is represented, A: CH 8168; B: CSM 447.2; C: PH 7700.15.

The Lewis Shale samples consist of shales, siltstones, and interbedded mudstones with very fine sandstones were identified (Tables 3.2.2 and 3.2.3). Even though the samples of the CSM core displayed most of these different lithologies (Table 3.2.2), this was not reflected in the unimodal T_2 distributions of the saturated samples (Fig. 3.2.6 B). Special attention was paid to the T_2 distributions of the interbedded samples (CSM 307.6 to CSM 450 in Table 3.2.2; Fig. 3.2.6 B), which displayed a distinct unimodal character suggesting a transitional variation in pore sizes rather than a bimodal behavior. The pore size distributions obtained from the mercury injection tests, which were provided by Texaco, also displayed a unimodal character, confirming the transitional variation of the pore sizes (Fig. 3.2.7).

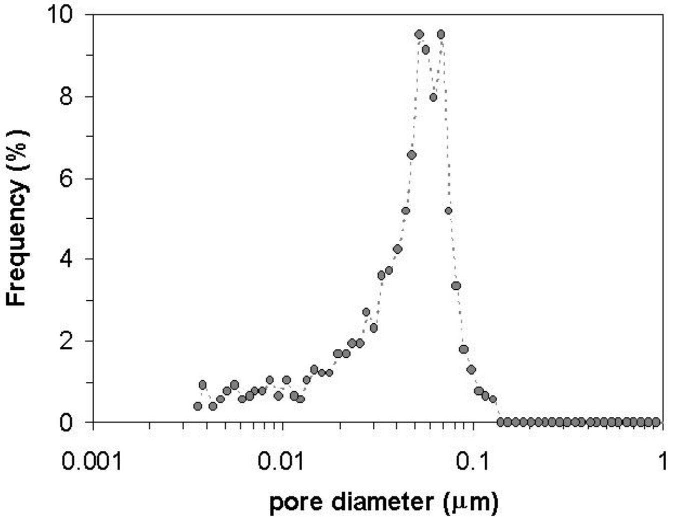

Figure 3.2.7: Pore size distribution of CSM 447.2. The pore diameters were derived from mercury injection tests.

One of the CH samples (CH 8187.5) was selected to evaluate the porosity underestimation of the MIP method. The CH 8187.5 shale had a MIP porosity of 4.28% and a NMR connected porosity of 7.63%. A histogram of pore volume as a function of pore throat diameter (Fig. 3.2.8) demonstrated that the smallest accessed diameter by mercury injection was 3.6 nm, which is, of course, twice the pore radius calculated above with equation [1.2]; i.e. 1.8 nm. The pore volume of the CH 8187.5 sample was calculated based on the MIP porosity (4.28%) and plotted on top of a histogram of NMR pore volume as a function of T_2 relaxation times (Fig. 3.2.9). The main purpose was to compare the relationship between the pore volumes derived from the MIP and NMR porosities. Mercury could penetrate only about half of the pore volume of the sample CH 8187.5 (Fig. 3.2.9). The missing pore volume represented an underestimated porosity of 3.35%. Similar results were found for the other Lewis Shale samples of the CH core (Table 3.2.4).

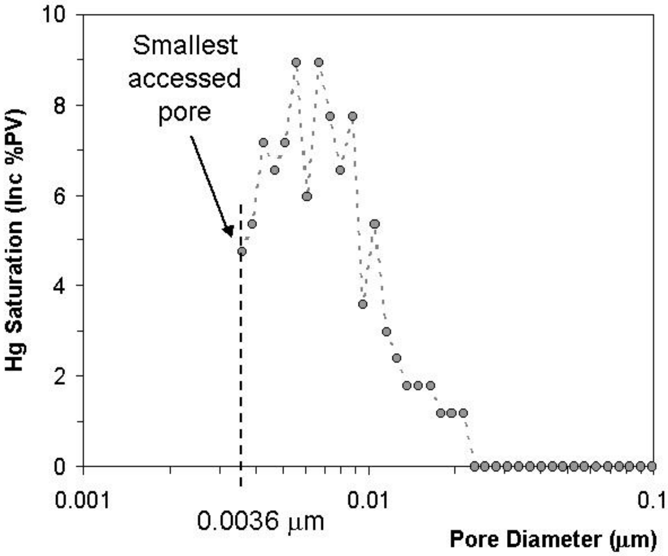

Figure 3.2.8: MIP pore volume as a function of pore diameter. Sample CH 8187.5. The smallest accessed pore at pressures of 60,000 psi is indicated.

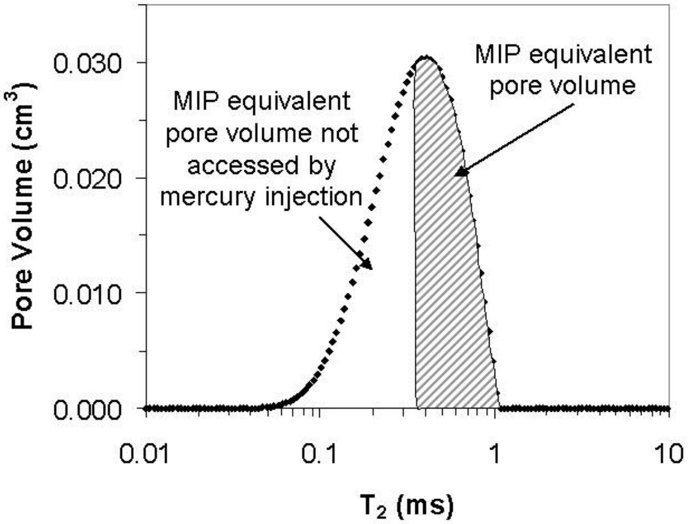

Figure 3.2.9: Comparison of MICP and NMR pore volumes. Sample CH 8187.5.

Table 3.2.4: Pore volume difference between the NMR and MIP porosities, CH core.

Sample	NMR Pore Volume (cm^3)	MIP Pore Volume (cm^3)	Pore Volume Difference* (%)
8075	0.647	0.308	52.4

8098.5	**1.142**	**0.609**	**57.8**
8112.5	**0.209**	**0.161**	**22.9**
8122.5	**1.303**	**0.790**	**39.4**
8131.6	**0.582**	**0.295**	**49.4**
8155	**1.656**	**0.683**	**58.7**
8162.5	**1.237**	**0.439**	**64.5**
8168	**1.904**	**0.889**	**53.3**
8187.5	**0.805**	**0.452**	**43.9**

* Pore volume of the sample not accessed by mercury, which corresponds to pore sizes of less than 1.8 nm (18 Å) equivalent to pressures greater than 60,000 psi.

The other Lewis Shale samples of the CSM core displayed higher NMR connected porosities than those of the CH core (Table 3.2.5) ranging from approximately 11.0% to approximately 24.0% with an average of 17.2% (Table 3.2.5). Similarly to the CH core, the CSM samples had a good agreement with the material balance porosities. The CSM core samples also exhibited good agreement with the mercury injection porosity suggesting that the smaller pores of the CH core samples represented a minimum proportion in the samples of the CSM core. The Lewis Shale samples of the CSM core had a more variable lithology and in general contained coarser grains than the black shales of the CH core. The upper portion of the CSM core was characterized by interbedded mudstones with very fine sandstones (samples CSM 307.6 to CSM 450 in Table 3.2.2). This portion of the core contained the minimum and maximum NMR connected porosities of the CSM samples, 10.98% and 23.86% respectively. The NMR porosities were close to the material balance porosities, however they did not present a good agreement with the mercury injection porosity (Table 3.2.5). The discrepancy of the porosities could have been related to the use of different samples during the NMR and MIP tests. The interbedded samples of this upper portion of the CSM core displayed high variability of the NMR porosity, suggesting that the porosity depended upon the relative proportions of mudstone and very fine sandstone in the sample. Since the samples analyzed with mercury injection slightly differed in depth with the samples examined for this research, the relative proportions between mudstone and sandstone could have been different, thus causing the MIP and NMR porosity disagreement.

The connected porosities in the middle portion of the CSM core ranged from 13.58% to 20.69% (Table 3.2.5) with an average porosity of 16.84%. The samples corresponded to fine siltstones and highly shaly siltstones with poorly-defined to well-defined fine laminations (CSM 915.5 to CSM 934.1 in Table 3.2.2). These samples displayed the best agreement with the material balance and MIP porosities among the CSM core samples (Table 3.2.5). A very-fine sandstone (CSM 1589) and two massive shales (CSM 1605.8 and CSM 1621.5) were the only samples received from the lower section of the CSM core. The NMR connected porosity of the CSM 1589 sandstone was close to the MIP porosity but it was lower than the material balance porosity (Table 3.2.5). This difference between the NMR and the material balance porosities was only observed in this sandstone. The general good agreement between the NMR connected and MIP porosities among the CSM samples could be due to the lack of large proportions of micro-pores. The pore size distributions of the MIP tests showed that micro-pores represented a minimal proportion of the samples (Fig. 3.2.10). Even the massive black shales of the lower sections of the CSM core (CSM 1605.8 and CSM 1621.5 in Table 3.2.2) presented different pore distributions from the black shales of the CH core (compare Figs. 3.2.8 and 3.2.10 bottom).

Table 3.2.5: Porosities of the CSM core, Lewis Shale.

Sample	NMR Connected Porosity (%)	Material Balance Porosity (%)	MIP Porosity (%)
295.9	17.23	18.01	16.9
307.6	19.60	18.21	19.7
319	10.98	9.52	18.0
433.3	14.76	14.86	20.2
440.1	20.02	19.15	17.5
447.2	15.69	14.48	17.1
450	23.86	18.87	17.4
915.5	20.69	20.57	16.6
918.3	16.48	17.89	15.1
920.9	13.58	13.02	17.7
927.6	16.29	15.24	14.5
930.2	15.02	15.87	13.3
930.4	19.96	19.82	Not available
931.7	15.36	14.39	13.4
932.7	14.82	15.60	15.3
932.9	15.69	16.37	16.4
934.1	18.53	15.26	15.1
1589	19.96	25.46	20.5
1605.8	17.23	16.25	13.3
1621.5	17.65	17.01	15.9

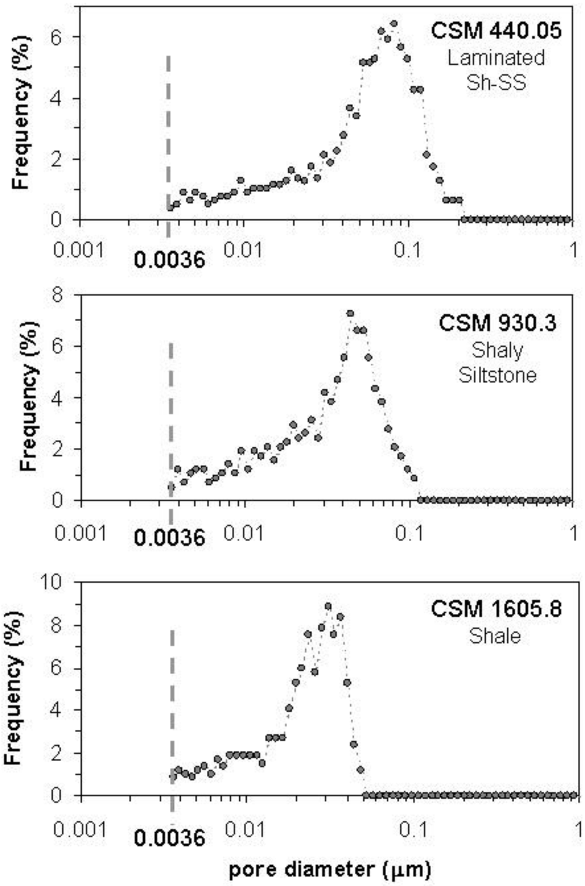

Figure 3.2.10: MIP pore volume as a function of pore diameter, CSM core. The identification of each sample is located at the upper right corner of each histogram.

The NMR connected porosities of the samples of the Alaskan CH core ranged between 2.33% to 10.98% with an average porosity of 6.49% (Table 3.2.6). As in the previously described samples the NMR and material balance porosities were in accordance among the PH samples (Fig. 3.2.11; Table 3.2.6). The MIP porosities were obtained from different samples placed at different depths in the core. In Figure 3.2.11 the MIP porosity of those samples that were separated by less than 2 feet were compared to the NMR connected porosity. A large discrepancy was generally observed between the NMR and MIP porosities (Fig. 3.2.11; Table 3.2.6). Among the possible causes of this disagreement, the use of samples from different depths could have been a factor. Another factor would have been related to the minimum pore throat (1.8 nm, 18 Å) that could be accessed by the mercury at a pressure of 60,000 psi. However, after examining the histograms of MIP pore volume as a function of pore diameter, it was determined that only one sample had appreciable micro-pore volume inaccessible by mercury (Fig. 3.2.12).

Table 3.2.6: Porosities of the PH core, pebble shale unit.

Sample	NMR Connected Porosity (%)	Material Balance Porosity (%)	MIP Porosity (%)
7647.55	8.05	7.35	6.44
7649.8	3.27	2.98	0.51
7652.5	10.93	9.75	Not available
7660.45	10.98	10.28	6.93
7666.4	6.89	5.89	7.61
7674.5	4.78	4.36	6.62
7685.45	4.61	4.26	Not available
7692.45	6.85	5.90	Not available
7695	2.33	2.74	15.3
7700.15	3.89	3.56	10.6
7702.35	8.77	8.64	4.41

Permeabilities

Two models are commonly used to estimate NMR permeability, Coates-Timur (Coates et al., 1999) and SDR models (Kenyon, 1997), both of which were originally developed for reservoir rocks. These models assume a direct correlation between permeability and porosity; consequently they imply that the porosity is mainly interparticle, which is true of the samples in this research. In order to apply the Coates-Timur model, the bound fluid volume of the samples must be known. This bound-fluid volume is commonly obtained by measuring the total magnetization (M_0) of a desaturated sample that was previously centrifuged at a specified air-brine capillary pressure (Coates et al., 1999). However, this centrifuging method could not be applied to the shale samples due to the high risk of breakage these samples posed. The desaturation procedure followed in this research preserved the sample integrity, but removed part of the bound-fluid volume (see earlier discussions). Therefore, the application of the Coates-Timur model required the use of a standard T_2 cutoff. For siliciclastic rocks this cutoff corresponds to 33 ms, which divides a T_2 distribution into a bound-fluid and a free-fluid portions associated with the T_2 relaxation times lower and higher than 33 ms respectively. The bound-fluid region of a T_2 distribution can be further subdivided into the clay-bound and capillary-bound pore volumes corresponding to the portions lower and higher than 3 ms, respectively. When comparing the T_2 distributions of Berea Sandstone and a massive black shale (CH 8098.5; Fig. 3.2.13), it became obvious that the major portion of the pore volume of the shale was associated with the clay-bound fluid and would not participate in the fluid transport. On the other hand, most of the pore volume of the Berea Sandstone (Fig. 3.2.13) contributed to the transport of fluids, which provides this rock with permeabilities of a few hundred millidarcies. The main portion of the pore volumes of almost all the saturated shale samples, especially the Lewis Shale samples, was identified as bound-fluid volume.

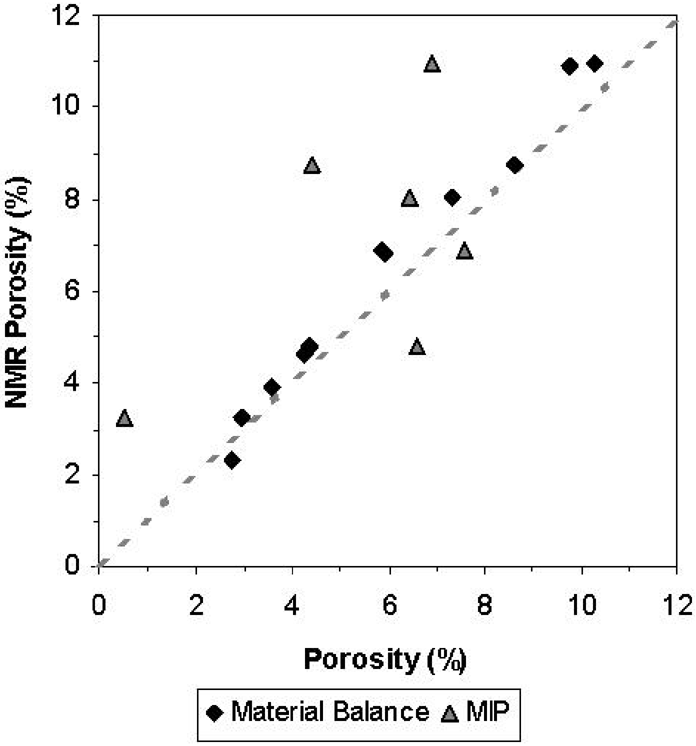

Figure 3.2.11: Porosities of the pebble shale unit samples, PH core. The porosities determined from MIP are the gray triangles; the material balance porosities are identified with black diamonds. A gray dashed line indicates the equality between the NMR porosities and the other porosities.

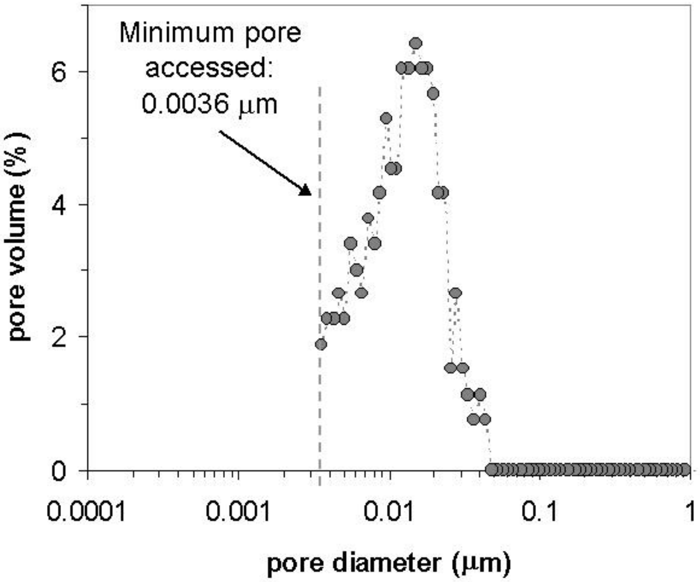

Figure 3.2.12: Pore size distribution PH 7647.55. The smallest accessed pore, corresponding to a pressure of 60,000 psi, is indicated.

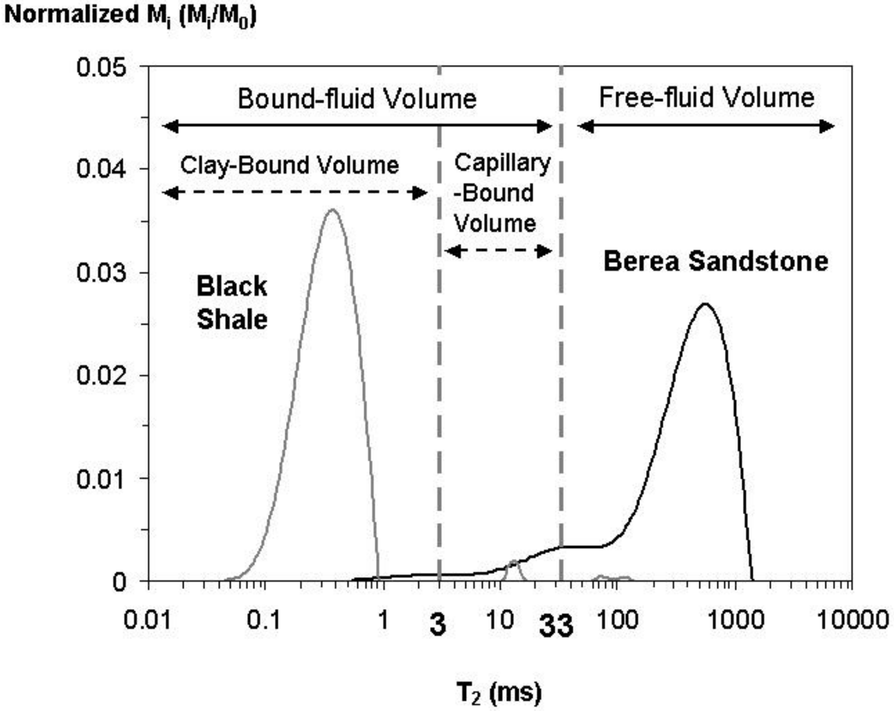

Figure 3.2.13: T_2 distributions of Berea Sandstone and CH 8098.5 black shale. The standard T_2 cutoffs are indicated as gray dashed lines at 3 ms and 33 ms. The T_2 distribution of the CH 8098.5 black shale is the gray solid line, while the T_2 distribution of the Berea Sandstone is the black solid line.

The free fluid index was calculated as the difference between the total porosity and the bound-fluid porosity (Akkurt and Cherry, 2000). Here, the bound-fluid porosity was assumed as the porosity given by the T_2 relaxation times lower than 33 ms (Fig. 3.2.13). Thus, the Coates-Timur (C-T) model can be written as:

$$k_{C-T} = \left(\frac{\phi_T}{C}\right)^4 \left(\frac{\phi_T}{\phi_{bnd}} - 1\right)^2 , \qquad [3.2.1]$$

where $k_{C\text{-}T}$ is the NMR permeability calculated with the Coates-Timur model in millidarcies; ϕ_T is the NMR total porosity in porosity units; C is a coefficient that depends on the formation and is expressed in porosity units (Akkurt and Cherry, 2000); ϕ_{bnd} is the porosity associated to the region of the T_2 distribution lower than 33 ms.

The NMR porosity was obtained by applying the definition of porosity:

$$\phi_{NMR} = \frac{V_{psh}}{V_B} = \frac{V_{Ni}}{V_B}\frac{M_{0sh}}{M_{0Ni}}100 , \qquad [3.2.2]$$

where ϕ_{NMR} is the porosity derived from the NMR data in percent; V_{psh} is the pore volume of a sample in milliliters; V_B is the bulk volume of a sample in milliliters; V_{Ni} is the volume of the calibration sample in milliliters; M_{0sh} is the total magnetization of the saturated samples; and M_{0Ni} is the total magnetization of the nickel sample.

Applying the definition of NMR porosity equation 3.2.2, to equation 3.2.1, the calculation of the NMR permeabilities with the Coates-Timur model was achieved with the following equation:

$$k_{C-T} = \left(\frac{\phi_T}{C}\right)^4 \left(\frac{M_{0-sh}}{M_{<33ms}} - 1\right)^2 , \qquad [3.2.3]$$

where $M_{0\text{-}sh}$ is the total magnetization of the saturated sample; and $M_{<33ms}$ is the sum of the magnetizations corresponding to T_2 relaxation times lower than 33 ms. The SDR model was easier to apply, since it only required the porosity and the logarithmic mean of the T_2 relaxation times of the saturated samples.

The obtained permeabilities ranged from $17\text{x}10^{-8}$ md to $88\text{x}10^{-4}$ md, which were in accordance with published data of very fine-grained rocks, especially shales. The permeabilities obtained with the Coates-Timur (C-T) model were in general lower than the permeabilities of the SDR model, in particular for the Lewis Shale samples of the CSM core. The NMR permeabilities were used to adjust the formation parameter C. A permeability obtained by a different method, such as air or mercury injection (MIP) permeability, is usually employed in the adjustment of the parameters. However it was interpreted that the air and MIP permeabilities of the samples had some problems as indicated below. For this reason, the C-T and SDR permeabilities were used instead. Assuming that the C-T and SDR permeabilities were equal and expressing the porosity in both models in fractional units:

$$\frac{M_{0-sh}}{M_{<33}} = \frac{\sqrt{C'}C^2}{100^2} T_{2ML} + 1 \qquad , \qquad [3.2.4]$$

where *C’* is the coefficient C of the SDR model. This coefficient was renamed to prevent mistakes and misunderstandings. The C’ and C parameters were recalculated for each of the cores using a non-linear fitting routine in Origin. The new parameters (Table 3.2.7) were applied to recalculate the C-T and SDR permeabilities. By applying the parameters C and C’ to fine-grained rocks, the validity of both models was extended to shales.

Table 3.2.7: Parameters of the C-T and SDR permeability models.

	SDR Model C’	C-T Model C
Default Values	4.5	10
CH core	2.77	9.08
CSM core	0.63	6.88
PH core	4.38	9.94

The permeabilities of the Lewis Shale samples were affected by the new parameters while the permeabilities of the siltstones of the PH core were unaffected, as indicated by the parameters (Table 3.2.6). The adjustment of the NMR permeabilities to the mercury injection derived (MIP) and the air permeabilities were also examined. Both air and MIP permeabilities were larger than the NMR permeabilities. In general, the traditional methods for determining permeabilities are performed on oriented samples, parallel to the bedding. On the other hand, it is impossible to make an oriented NMR measurement, unless images are being obtained, because all the hydrogen spins in the pore fluids are affected by the applied magnetic field. Therefore, the larger permeabilities obtained by the air and MIP could be caused by preferred orientations, while the NMR determinations corresponded to the whole sample. The air permeabilities were in general two orders of magnitude larger than the NMR permeabilities. The source of the discrepancy between the permeabilities could have also been caused by the Klinkenberg effect. This effect, also called the gas slippage effect, occurs when the diameter of the fluid-flow pathways approaches the mean free path of the gas (Amyx et al., 1960). Under these conditions the gas molecules slip along the capillary walls and behaves like a less viscous fluid. Consequently, the permeabilities measured while this effect takes place result in higher values. The gas slippage effect is a more notorious phenomenon in small capillaries such as those exhibited by these analyzed samples (Amyx et al., 1960). For reservoir rocks the air permeabilities are normally measured as a function of mean pressure of the air. The permeabilities are then plotted versus the inverse mean pressure, with the "true" Klinkenberg-corrected permeability being the intercept value at zero inverse pressure. Due to the extremely high pressures needed to perform this on shale samples, this technique is not used.

The relationship between NMR (SDR and C-T) permeabilities and the MIP permeabilities varied across the core samples. The NMR and MIP permeabilities of the Lewis Shale samples (CH core), which corresponded to the black massive shales (Table 3.2.3), were in the same order of magnitude with generally larger MIP permeabilities. This suggested that not all the pore volume was accessed during the mercury injection tests, which represented approximately half of the shale pore volume (Fig. 3.2.9; Table 3.2.4). The MIP and NMR permeabilities were similar; therefore, it appeared that the non-accessed pore volume (Fig. 3.2.9) did not participate in the transport of fluids. The samples of the CSM core of the Lewis Shale displayed the greatest discrepancies between the NMR and MIP permeabilities. The MIP permeabilities were one or two orders of magnitude larger than the NMR permeabilities. The cause of these differences could have been related to the laminated nature of the CSM samples (Table 3.2.2). The CSM samples could have been delaminated during the mercury injection tests generating a higher permeability parallel to the bedding. A large disagreement between the NMR and MIP permeabilities was also observed for the samples of the PH core. The use of samples from different depths could be the cause of these discrepancies.

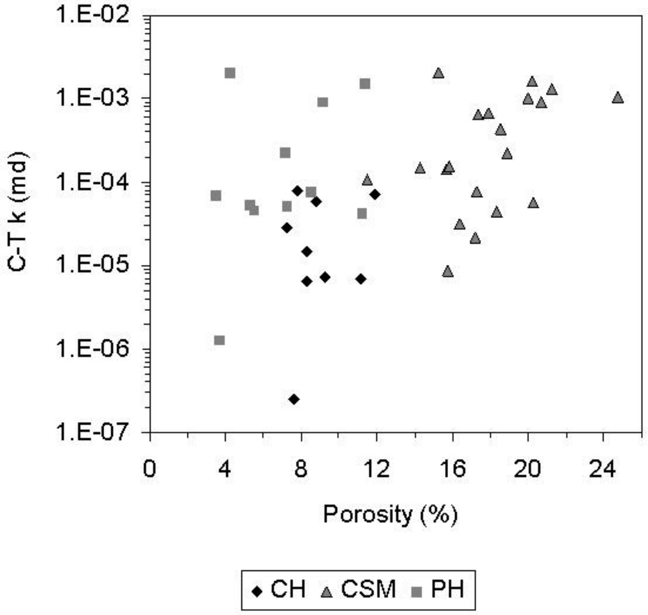

Figure 3.2.14: Relationship between the C-T permeability and porosity. The samples of all the cores were plotted, CH: black diamond; CSM: gray triangle; and PH: gray square.

To assess the quality of a seal rock, the entry pressure of that rock has to be known. However, once the entry pressure is exceeded, the transport of fluids is controlled by the permeability and relative permeability of the seal rock (Schlömer and Krooss, 1997). For this reason, the relationship between the NMR permeabilities and the porosities of the samples was evaluated. This type of analysis is generally used in reservoir rocks to determine the existence of flow paths. Both the recalculated Coates-Timur (C-T) and SDR permeabilities were evaluated (Figs. 3.2.14 and 3.2.15). A slight tendency of increasing permeability with increasing porosity was observed with both C-T and SDR permeabilities (Figs. 3.2.14 and 3.2.15). This relationship was expected, since the porosity was mainly interparticle. However, the relationship between the C-T permeability and the porosity was highly dispersed (Fig. 3.2.14). In the case of the SDR permeability, a better grouping of the samples was detected (Fig. 3.2.15). The black massive shales of the CH core, Lewis Shale, displayed a tight grouping, indicating a slight change in SDR permeability with increasing porosity (black diamonds in Fig. 3.2.15). Another grouping was also observed with the laminated silty shales and shaly siltstones of the Lewis Shale CSM core (Fig. 3.2.15). In contrast with the CH shales, the SDR permeability of the CSM shales and siltstones displayed a larger variation with porosity (Fig. 3.2.15). The siltstones of the Alaskan pebble shale unit exhibited great changes of permeabilities with small changes in porosities (Figs. 3.2.14 and 3.2.15). This tendency was better displayed with the SDR permeability (gray squares in Fig. 3.2.15). Among the analyzed samples, the CH black shales appear to have the best sealing properties because of their uniformly low permeabilities.

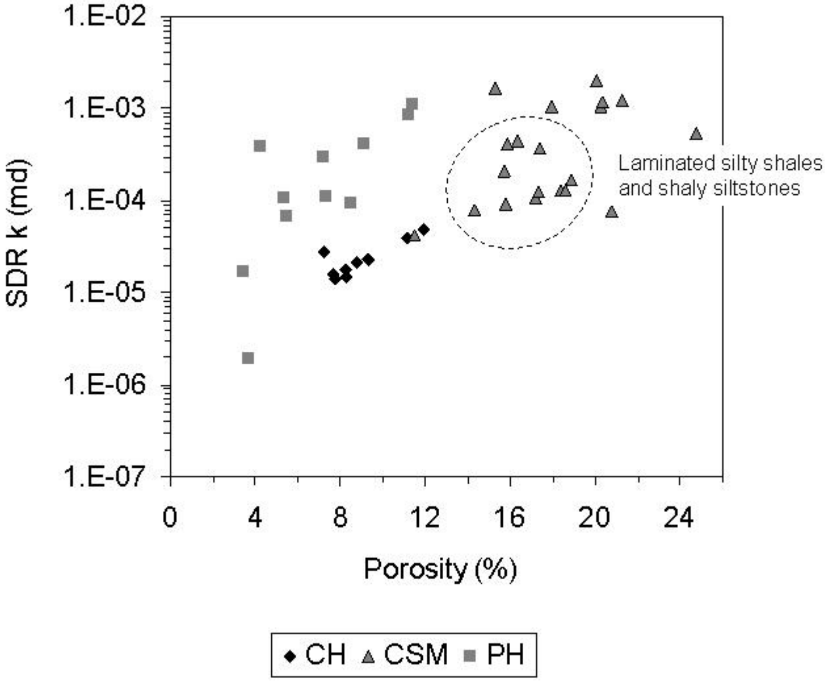

Figure 3.2.15: Relationship between the SDR permeability and porosity. The samples of all the cores were plotted, CH: black diamond; CSM: gray triangle; and PH: gray square.

<u>*NMR and Pore-Size Distribution*</u>

A pore-size distribution can be derived from a T_2 distribution if the surface relaxivity (ρ_2) is known. However, ρ_2 is difficult to obtain and generally is not uniform throughout a rock (Marschall et al., 1995; Kleinberg, 1996a & b). Therefore, the most commonly used methods for deriving the NMR pore-size distributions consist of comparing the T_2 distributions with the pore-size distributions derived from quantitative thin-section or image analyses (Kenyon et al., 1995; Basan et al., 1997) and from mercury injection data (Kenyon, 1997; Straley et al., 1997; Coates et al., 1999). Since one of the goals of this research is to evaluate the seal quality of the samples using NMR, and since no image analysis data is available, the pore-size distribution derived from mercury injection will be applied. It is frequently argued that because T_2 distributions provide pore body information while mercury injection capillary pressure (MICP) sense pore throats, a complete agreement between the pore-size and the pore-throat size distributions cannot be reached (Kenyon, 1997; Straley et al., 1997; Coates et al., 1999). However, the different nature of both measurements is generally overlooked. While pore-throat size distributions respond to a dynamic measurement (the intrusion of mercury into the pore space controlled by the sizes of pore throats), T_2 distributions represent a static measurement accounting for the pore volume at different T_2 relaxation times. Hence, the mercury injection measurement provides information on pore connectivity and transport flow, while a T_2 measurement is a porosity measurement. A hypothetical example can be analyzed to comprehend this fundamental difference between these two measurements. The pore space of the example is composed of three different pore-body sizes (circles 1 to 3 in Fig. 3.2.16) and three different pore-throat sizes, which are distinguished by solid colors (dark and light gray and black rectangles) in figure 3.2.16. In a mercury injection test, at the lowest applied pressure the largest pore throats allow the pore volume connected to them to fill first. That pore space corresponds to the diagonally shaded circles in figure 3.2.16. At a higher the pore volume connected to the black pore throats (Fig. 3.2.16) is filled. This pore space is the punctuated dark gray pore space in figure 3.2.16. Finally, at the highest applied pressures mercury intrudes the pore space (horizontally shaded pore space in Fig. 3.2.16) connected by the smallest pore throats (light gray rectangles in Fig. 3.2.16).

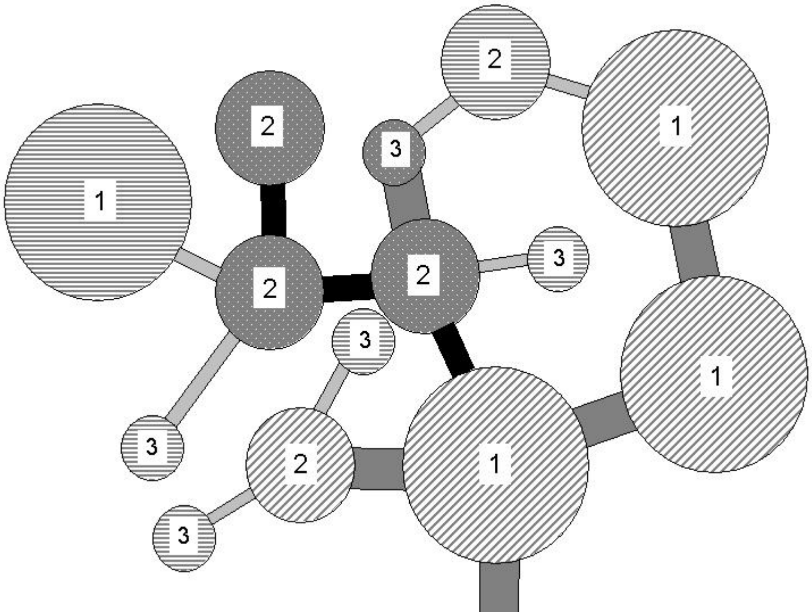

Figure 3.2.16: Hypothetical example of a pore network. The system contains three pore sizes (circles 1 to 3) and three pore-throat sizes (solid dark and light gray and solid black rectangles). The pore bodies are colored representing the different stages of a mercury injection. At the lowest pressure the diagonally shaded pore space is filled. The dark gray punctuated pore space is intruded at an intermediate pressure, and the horizontally shaded space is filled at the highest pressure.

The intruded pore volume at each of the applied pressures can be represented in a histogram where each of the columns characterizes the previously described intrusion (MICP in Fig. 3.2.17). The pore-throat sizes of that histogram are obtained by applying the Washburn equation (equation 3.2.9). However a T_2 distribution records the pore volume (1 to 3 in Fig. 3.2.16) without recording how the pore volume might be intruded (NMR in Fig. 3.2.17). To date the T_2 distribution data have been interpreted as a bundle of capillaries, in which all the pores of one particular size are connected among each other and are disconnected from pores of other sizes. As observed in this hypothetical example (Figs. 3.2.16 and 3.2.17), a perfect agreement between the pore-size distributions is difficult to reach.

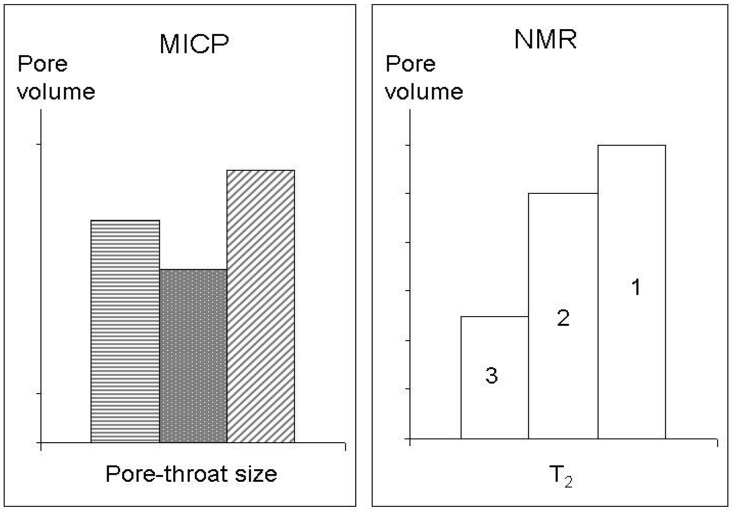

Figure 3.2.17: Histograms of pore-throat size and T_2 distributions. The histograms were constructed using the data of figure 3.2.16. MICP represents the pore-volume distribution as a function of the pore throat size, and NMR is a T_2 distribution.

In order to compare a T_2 distribution with a mercury injection pore-throat size distribution, the NMR data must be modeled into a pseudo-intrusion form. Davis (2003) developed a model that reshapes a T_2 distribution into an injection distribution. During a mercury injection smaller pores shield larger pores, such as the pore body "1" that is horizontally shaded in the hypothetical example of Figure 3.2.16. That largest pore body is filled only at the highest applied pressure, because it is connected to the smallest pore throat. This effect is considered in the pseudo-intrusion model by assuming a correlation volume over which a pore is connected to one like itself (Davis, 2003). The pseudo-injection model has the following general expression (Davis, 2003):

$$\Delta V_n = \frac{1}{M}\left[a_n + (M-1)\left\{a_n^2 + 2\sum_{l=1}^{n-1} a_l a_n\right\}\right] \quad , \qquad [3.2.5]$$

where $1 \leq n \leq N$ and N is the number of T_2 relaxation times (the samples analyzed in this research were fitted with a fixed number of 256 relaxation times); □V_n is the fraction of the normalized pore volume of the corresponding relaxation time n; a_n is the histogram amplitude of the n^{th} relaxation time; and *1/M* is a fraction of the pore volume connected to one similar pore size (i.e., if M is one all the pore bodies of a same size are filled at one pressure as if they were a bundle of capillaries; if M is two, half of the pore volume corresponding to a pore size is filled at one pressure; and so on).

The model was applied to the T_2 distribution histograms of T_2 relaxation times and normalized pore volumes. The expression 3.2.5 was used with an infinite value for *M*; for this limit equation 3.2.5 becomes (Davis, 2003):

$$\Delta V_n \rightarrow a_n^2 + 2\sum_{l=1}^{n-1} a_l a_n \quad . \qquad \mathbf{[3.2.6]}$$

An IDL routine was written with the new expression (equation 3.2.6; Davis, 2003), which was used to generate the pseudo-intrusion distributions. These histograms were skewed toward the lower T_2 relaxation times (Fig. 3.2.18), since the model included the shielding effect that small pores produced over large pores. During mercury intrusion tests some of the large pores are only intruded through small pore throats, which can be also associated to small pores. In order to compare the pseudo-intrusion T_2 histograms with the MICP pore-throat size histograms, the NMR data was converted into diameter, since that it is usually the manner the MICP pore-throat size distribution is presented. Functions were also generated for datasets, the NMR and MICP data. Even though histograms provide a good representation of such data, the magnitude of two different histograms cannot be compared if they have a different number of bins (i.e., if the data point spacing is different, bins are the numerical ranges or classes in which the histogram data are grouped). Probability density functions were used, since functions can be compared without such problems. The density function was computed as (Davis, 2003):

$$f(x_0) = \left(\frac{Y}{\Delta X} \right), \qquad \textbf{[3.2.7]}$$

where x_0 is the midpoint of a bin; Δx is the width of the bin and Y is the pore volume corresponding to that bin. If $f(r)$ is a porosity probability density function over pore radius, then the fractional porosity attributed to the range of radii between $r1$ and $r2$ is given by the integral of $f(r)$ over $r1$ and $r2$. To compare the unequally spaced datasets, the density functions were generated for both the pseudo-intrusion T_2 relaxation times and for the mercury injection pore-throat size distributions.

The NMR data was scaled to fit the MICP data (Figs. 3.2.19). The NMR data corresponded to the pore-body sizes, while the MICP data characterized the pore-throat sizes. Therefore, the scaling factor employed to fit the distributions involved the pore-throat-to-pore-body ratio, often referred as the aspect ratio. The scaling factor was visually adjusted trying to obtain the best possible agreement on the portion of the curves that corresponded to the largest pore and pore-throat sizes. That portion of the curve was selected since the initial entry pores are not shield by smaller pores. Also the larger pore data were complete for all the samples (the smallest pore sizes were not accessed by mercury in the majority of the Lewis Shale samples). It should be noted that this scale factor is a simple linear sliding adjustment along the horizontal log axis (T_2, pore throat radius). There is no vertical axis scaling.

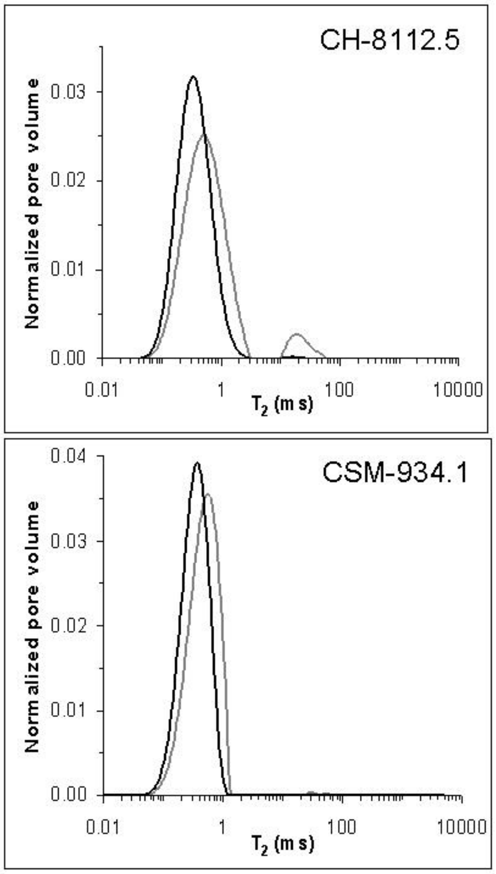

Figure 3.2.18: Comparison of the NMR distributions and the modeled distributions. The gray lines represent the T_2 distributions, and the pseudo-intrusion distribution is the black line. The sample is identified within each histogram.

The black shales of the CH core (Lewis Shale) displayed a general good agreement between the density functions of the NMR and MICP data. The pore-body porosity density functions (NMR data) of the CH shales required only one scaling factor, which suggested that the pore-throat-to-pore-body ratios were constant throughout the samples. This indicated that these samples were very well sorted. The scaling factors of the Lewis Shale samples ranged from 0.008 to 0.13. The scaling factors of the black shales of the CSM core corresponded to the lowest among the ratios of the Lewis Shale. The ratios ranged from 0.008 to 0.0125 and averaged 0.0105.

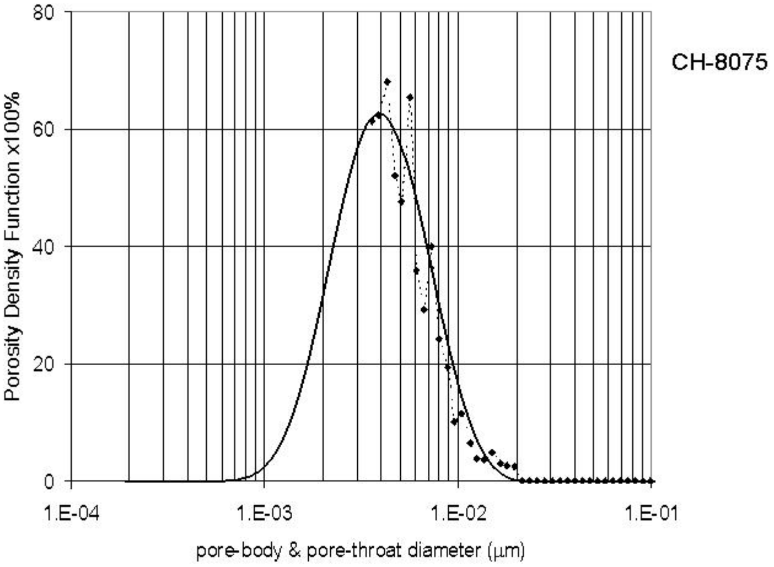

Figure 3.2.19: Density functions of the pore body and pore throat diameters. The solid black line identifies the NMR pore-body data and the dashed line represents the MICP pore-throat sizes. The diameters are in microns (μm).

The pseudo-intrusion pore-size distributions of the CSM samples (Lewis Shale) were difficult to fit. In some of the samples the portion of the distribution corresponding to the higher pore sizes was possible to fit, while in other samples the addition of another correction factor would be required (Fig. 3.2.20). A variation on the surface relaxivity of the samples can affect the T_2 relaxation time, and this effect can be interpreted as a change in pore size. An increase in the clay mineral content can produce the variation of the surface relaxivity. Nevertheless, the CSM samples displayed lower clay content than the CH samples. The presence of iron-rich minerals can also affect a T_2 distribution through dephasing of the spins via molecular diffusion in a heterogeneous magnetic field due to the increase in the magnetic susceptibility contrast (Hürliman, 1998). However, the content of iron-rich minerals in the CSM samples was lower. The other possible cause that could affect the fitting of the pseudo-intrusion NMR distributions was a variation of the aspect ratio within each sample. This effect was expected to occur especially in the interbedded very fine sandstones and shales (CSM 307 to 450 in Table 3.2.2). The use of different samples during the mercury injection tests could also produce a difference between the pore-throat size and pseudo-intrusion NMR distributions. The layers of the interbedded samples were thin (less than one inch thick); therefore, variations in the depth of more than the thickness of the layers can produce differences between the T_2 times and calculated pore-throat size distributions. Since the samples were different, the additional correction factor was not applied (CSM 319 in Fig. 3.2.20). The aspect ratios of the CSM samples of the Lewis Shale were in general higher than the aspect ratios of the CH samples. They ranged from 0.016 to 0.13. The laminated shaly siltstones and silty shales (CSM 918.3 to CSM 934.1 in Table 3.2.3) generally displayed higher aspect ratios than the interbedded sandstones and shales. The highest aspect ratio was observed for the only sandstone of the CSM samples, which contained rip-up clasts. Due to the high variability of the PH siltstones of the pebble shale unit, correlation between the NMR and the MICP dataset was not possible. Therefore pore-body and pore-throat size distributions of those samples were not analyzed.

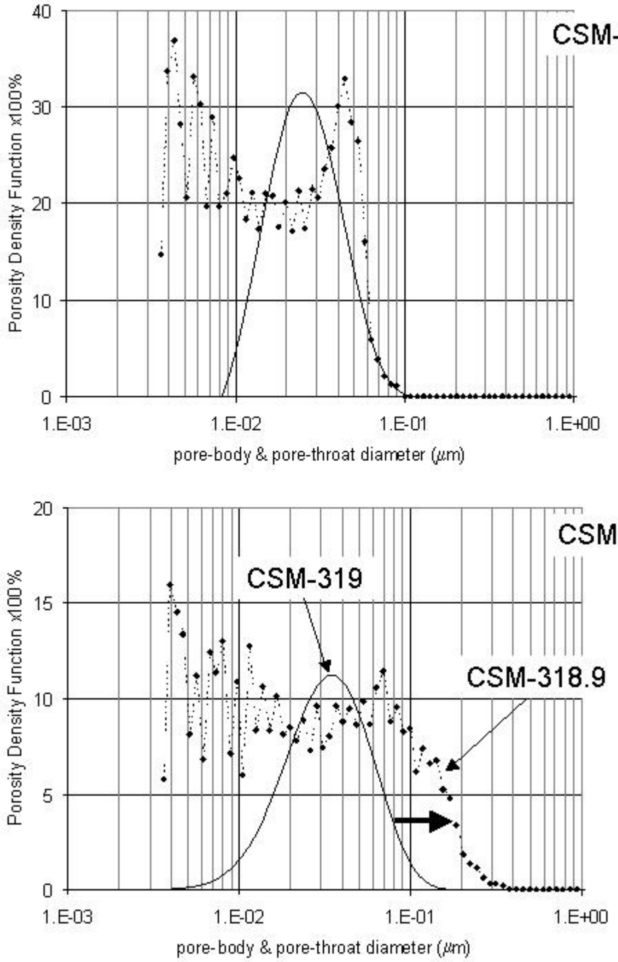

Figure 3.2.20: Examples of the porosity density functions of the CSM core. CSM 915.5 displayed a good fit of the first portion of the curve. CSM 319 required the addition of another factor indicated with a black arrow.

Pseudo-Capillary Pressure

Capillary pressure obtained from mercury injection (MICP) is a record of the pore volume occupied by mercury (the non-wetting phase) at certain pressure. The curves are generally plotted in a semi-log graph of capillary pressure as a function of the wetting phase saturation. These curves assumed that all the wetting phase (air) has been evacuated and that the whole pore volume has been occupied by the non-wetting phase (mercury). However, it has been demonstrated that the pore volume accessible by mercury is directly dependent upon the applied pressure. Among the analyzed samples, the black massive shales of the CH core displayed the largest inaccessible pore volumes (Table 3.2.4). In samples with a high proportion of microporosity, the non-wetting phase saturations are often underestimated, since the micro-pores are not accessed at the experimentally obtainable pressures.

The saturation of a fluid is defined as the relative proportion of that fluid with respect to the total pore volume of a rock. Therefore, all the saturations of the MICP data had to be corrected and adjusted with the measured NMR pore volume as follows:

$$S'_{NW} = \frac{S_{NW}}{F} \quad , \qquad [3.2.8]$$

where S'_{NW} is the correct saturation of the non-wetting phase; S_{NW} is the saturation of the non-wetting phase (mercury); and F is a proportional factor between the NMR and MICP porosities. All the MICP curves were recalculated and plotted with the corrected saturations (Figs. 3.2.21). The correction of the non-wetting phase saturation modified the slopes of the capillary pressure curves (Fig. 3.2.21); and consequently, affected the location of the pressures used for the assessment of the quality of a seal. These pressures are used in the calculation of the hydrocarbon column that a rock can hold without leaking. Entry, displacement, and percolation threshold pressures are the most frequently employed pressures in that calculation, and all these pressures are found at the lower-pressure portions of the MICP curves. Among the studied samples, the MICP curves of the Lewis Shale of the CH core were mainly affected by the correction of the saturation (CH 8168 in Fig. 3.2.21) due to the large proportion of micro-pore volume not accessed by mercury (Table 3.2.4).

The pseudo-intrusion NMR data were used to construct the pseudo-capillary pressure curves. The pore-body diameters, which corresponded to the fitted pseudo-intrusion T_2 distribution, were inverted as in the Washburn equation (Schowalter, 1979):

$$p_c = \frac{2\sigma \cos\theta}{r} \quad , \qquad [3.2.9]$$

where p_c is the capillary pressure in dynes cm^{-2} (1 psi=69,035 dynes cm^{-2}); σ is the interfacial tension between the two fluid components of the system and is expressed in dynes cm-^{1}; θ is the contact angle in degrees between the two phases; and r is the pore throat size in cm. The corresponding normalized pore volume was reprocessed in percent, and the cumulative pore volume was calculated. Since only one phase participated in the NMR measurements, the normalized pore volume was equal to the wetting phase saturation. These pseudo-capillary pressure curves were plotted together with the MICP curves. The pseudo-capillary curve was fitted with respect to the MICP curve by applying a scaling factor. Initially, these factors were twice the inverted aspect ratios (2x(R_{aspect})$^{-1}$). A factor 2 was included to convert the pseudo-intrusion T_2 diameters into radius as in the Washburn equation (3.2.9). These factors worked well with the CH samples of the Lewis Shale even though the good fit between the curves was not complete (CH 8098.5 in Figs. 3.2.22). The MICP curves were incomplete after the correction that was made to compensate for the mercury inaccessible pore space (Fig. 3.2.21). That pore volume corresponded to the pore throats smaller than 1.8 nm. Although the pseudo-capillary pressure and the MICP did not display a perfect agreement for the CH samples, the initial portion of the curves indicated a similar displacement pressure.

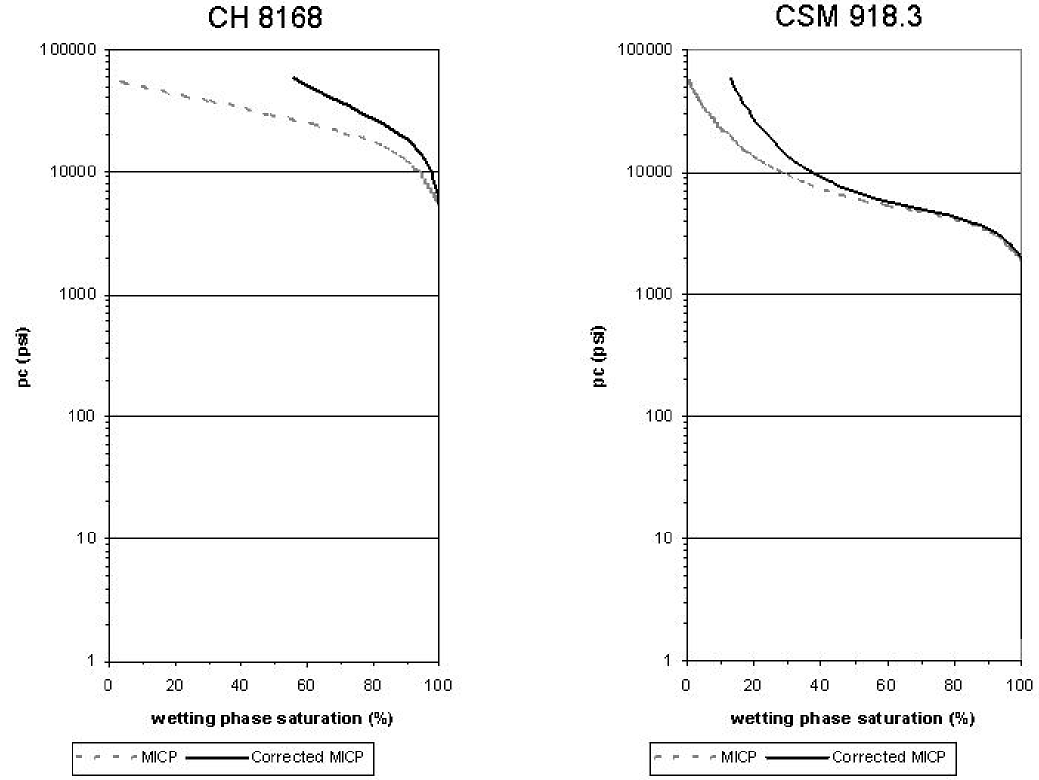

Figure 3.2.21: Correction of the capillary pressure curves. A dashed gray line represents the original MICP data and the corrected MICP data is the solid black line.

In the CSM samples of the Lewis Shale was not possible to apply the same scaling factors as in the CH samples ($2x(R_{aspect})^{-1}$). The fitting technique consisted of applying multipliers to the pseudo-capillary T_2 curve until a desirable fit of the curves was achieved (Fig. 3.2.23). In general, the scaling factors were in the same order of magnitude as the ones applied to the CH samples. The initial portions of the MICP and the pseudo-capillary pressure curves were similar among the CSM samples (CSM 920.9 in Fig. 3.2.22). As previously mentioned the pseudo-capillary pressure curves of the PH samples of the Alaskan pebble shale unit were not constructed due to the lack of correlation with the MICP data.

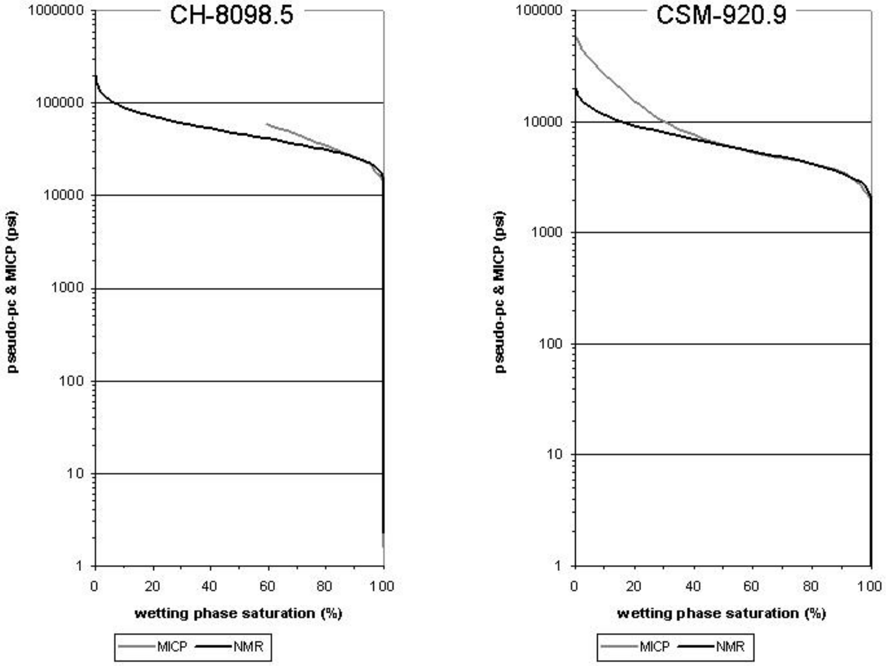

Figure 3.2.22: Examples of the pseudo-capillary pressure and MICP curves.

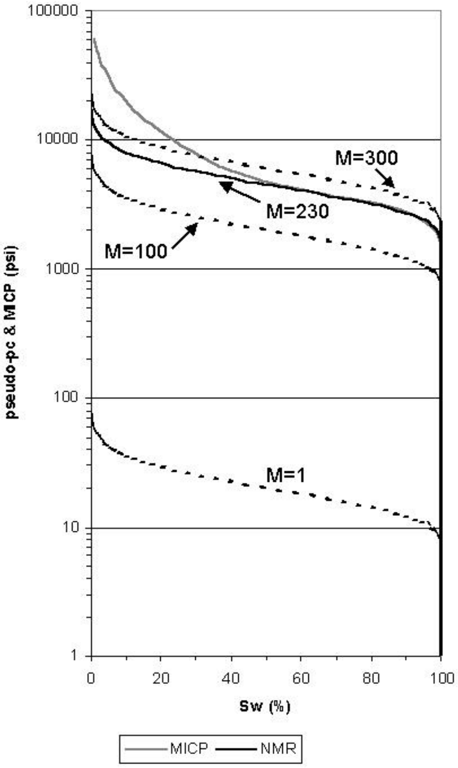

Figure 3.2.23: Fitting technique applied to the CSM samples. Sample CSM 1589, different multipliers (M) were applied to the pseudo-capillary pressure curve.

Seal Quality

The quality of a seal is established by the minimum pressure required to displace a fluid from pores allowing leakage (Downey, 1994). That minimum pressure is directly related to the height of the fluid column that a rock can hold above the free-water level which can be expressed by the following equation based on field units (Watts, 1987; Sneider et al., 1997):

$$h_{\max} = \frac{p_{cw/HC}}{(\rho_w - \rho_{HC})0.433} \quad , \qquad [3.2.10]$$

where $h_{\max}$ is the maximum height of the hydrocarbon column in feet that a seal can hold before leaking; p_c is the capillary pressure in psi of the water-hydrocarbon system; ρ_w and ρ_{HC} represent the densities of water and hydrocarbon respectively, which are measured in g cm^{-3}; and 0.433 is a conversion factor. The minimum pressure is found in the initial portions of a MICP curve for this reason the main goal was to obtain the best fit of the pore size distributions as well as of the pseudo-capillary pressure curves. The visual evaluation of the pseudo-capillary pressure curves was difficult. Therefore, the Schowalter (1979) approach was used to obtain the displacement pressure. This method consisted of obtaining the capillary pressure correspondent to the 10% saturation of the non-wetting phase. Since the displacement pressures were acquired for an air-mercury system (the wetting and non-wetting phases respectively) a correction was applied to convert the pressures into a brine-hydrocarbon system. For this correction the parameters summarized in Table 3.2.8 were applied. A hydrocarbon with a 32º API gravity was selected, which had a density of 0.865 g/cm^3. A density of 1.1 g/cm^3 was used for the brine in equation 3.2.10. The calculated maximum heights above the free-water level (p_c=0) of the hydrocarbon (Figs. 3.2.24 and 3.2.25) can hold indicated that the CH samples of the Lewis Shale constituted a better seal than the CSM samples. These heights were generally higher than 10,000 ft and were compatible with published data of good seal quality (Krushin, 1997). Among the CSM samples a tendency of an increasing seal quality with depth was observed. The laminated shaly siltstones and silty shales can hold higher hydrocarbon columns than the interbedded sandstones and shales (Fig. 3.2.25). The two shales of the CSM samples (CSM 1605.8 and CSM 1621.5) were the best seal rocks of the CSM samples; however the hydrocarbon columns that these shales can hold were lower than those of the CH samples (Figs. 3.2.24 and 3.2.25).

Table 3.2.8: Typical contact angle and interfacial tension values. (from Vavra et al., 1992; Sneider et al., 1997)

System	Contact angle (θ) (°)	Interfacial tension (□) (dynes cm^{-1})
air - mercury	140	480-485
methane - brine	0	70-72
crude oil – brine		
< 30° API	0	30
30 - 40° API	0	21
> 40° API	0	15

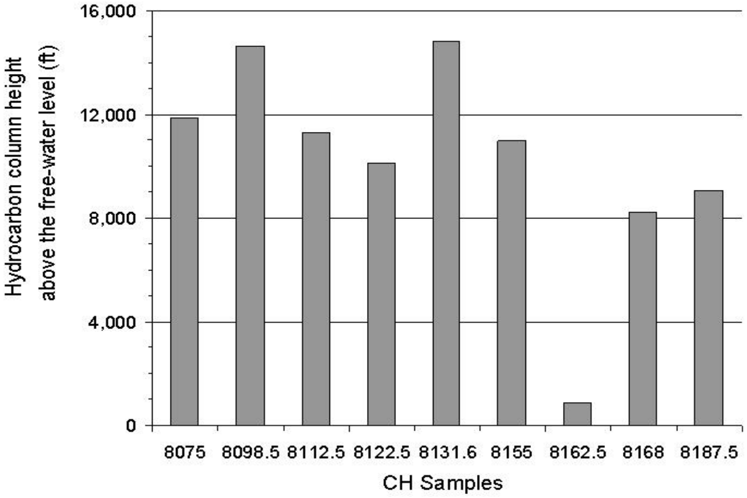

Figure 3.2.24: Maximum hydrocarbon columns of CH samples. The hydrocarbon column heights above the free-water level were plotted as a function of the sample depths, which corresponded to the sample number.

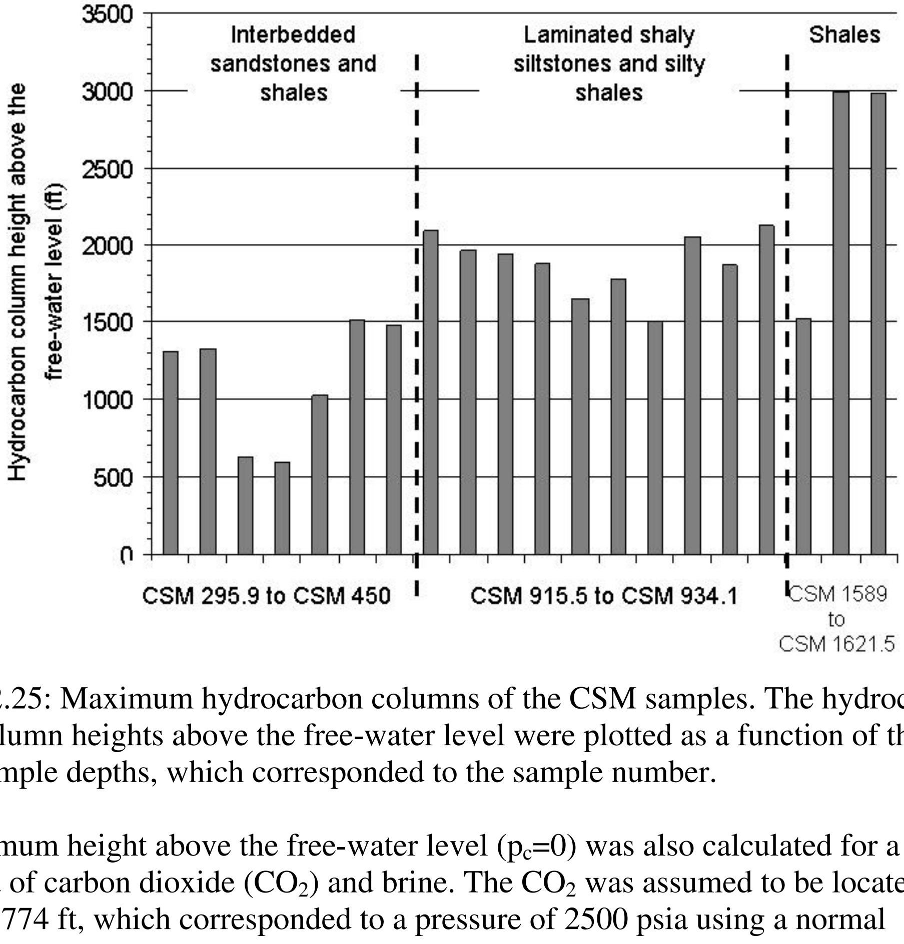

Figure 3.2.25: Maximum hydrocarbon columns of the CSM samples. The hydrocarbon column heights above the free-water level were plotted as a function of the sample depths, which corresponded to the sample number.

The maximum height above the free-water level (p_c=0) was also calculated for a system composed of carbon dioxide (CO_2) and brine. The CO_2 was assumed to be located a depth of 5774 ft, which corresponded to a pressure of 2500 psia using a normal hydrostatic gradient of 0.433 psi/ft and a temperature of 162° F under a normal geothermal gradient of 15°F/ft. Under these pressure and temperature conditions CO_2 was in a supercritical phase with a density of 0.58 g/cm^3 (Klins, 1984). The interfacial surface tension of a methane-brine system (Table 3.2.8) was employed, and its variation with pressure and temperature was not included. A similar pattern as the one observed for the hydrocarbon-brine system was obtained for the CO_2-brine system (Figs. 3.2.24 to 3.2.25). However, the maximum heights of CO_2 above the free-water level that the Lewis Shale samples could hold were approximately half of the hydrocarbon column.

Task 3.3 Plan and arrange with a logging service company a field trial on shale seal assessment

Task 3.3 is to plan and arrange with a logging service company a field trial of the shale seal assessment. To accomplish the objective of a future public test of this technology, since this particular grant does not continue forward into a field trial next year, we introduced parties that would have an interest in an open-access field trial in the future if funding were available. We have begun a dialog between Dr. T. S. Ramakrishnan of Schlumberger-Doll research Center and Dr. Roger M. Slatt, Director of the School of Geology and Geophysics at the University of Oklahoma. In turn, Dr. Slatt has contacted Bob Davis, the geologic supervisor at Schlumberger in Bakersfield, Ca., Schlumberger has suggested the possibility of discounted logging services for such a future project. Dr. T. S. Ramakrishnan of Schlumberger-Doll has suggested that the new Schlumberger ECS logging sonde be run to provide additional characterization of the clays in seals.

Dr. Slatt was Chair at the Colorado School of Mines when the CSM Strat Test #61 hole in the Lewis Shale of Wyoming was drilled. This is the test hole from which our Lewis Shale samples were taken and are being analyzed in the MRI Lab of Texas Tech University. Dr. Slatt is an active, leading expert in shale evaluation in the field and has worked with Schlumberger before on acquisition of public data for borehole imaging calibration. Dr. Slatt thinks that there is a possibility to cheaply reenter this plugged hole. The well was drilled to 1700 ft., of which about 900ft. were cored. A complete Baker-Hughes log suite was run including NMR.

The NMR log was run in 1999 with an old series “B” Numar tool, and the CPMG sequence interecho spacing used for the NMR pulses at that time would preclude reliable capture of a significant fraction of the shortest T_2 components which we observed in the lab. The latest generation of NMR logging tools uses interecho time delays nearly as short as those used in our lab (within 20%). Moreover, the latest generation also provides much better signal-to-noise ratio (SNR) by ‘stacking’ the data from more adjacent radial bands of formation. The SNR under standard operating conditions should now be large enough to generate a useable T_2 pore size distribution for seal capacity analysis with our techniques. The one critical feature is the logging speed, and that must be decided locally on the basis of the logging crew’s experience with the formation. If the tool sticks at slow speeds, the speed will have to be increased, thus degrading the SNR.

Task 4.1 Establish physical property correlations

Here the extensive literature on chemical interaction between CO_2 and the reservoir rock and their likely consequences on storage operations is investigated. The first approach has been developing is an extensive literature review aimed to investigate the fluid/rock interactions that are expected when CO_2 is used to enhanced oil recovery. The second one was a review of enhanced oil recovery studies. The third deals with a review of the chemical process developed when CO_2 in injected into deep aquifers in order to be sequestered, and the fourth one is focused on natural accumulations of CO_2 in sedimentary basins. Finally, the role of CO_2 in diagenesis alteration was also reviewed.

Of the few relevant researches, carbonate precipitation due to the action of H_2CO_3 formed when CO_2 reacts with the connate water (Patton, *et al* 1980). Also, Omole and Osoba, 1983 identify the reduction in permeability caused by carbonate precipitation. Also, studies led to determine the changes in total porosity of the reservoir (Mathis and Sears, 1984).

Other studies have observed reduced injectivity in some calcareous sandstone and carbonate formations (Henry, and Feather, 1981, Ross, *et al*. 1982, and Sayegh et al., 1990). Also, the tendency of scaling of production water during CO_2 injection has led some researchers to investigate the inorganic geochemical aspects of CO_2 reservoir interactions (Bowker and Shuler, 1991, Shuler *et a.*1991).

Also, simulation studies of the disposal of acidic waste fluid in carbonate and sandstone formation have been carried out by Liu and Ortovela, 1996.

The chemical alteration that could occur among the formation water, mineral assemblage of the rock and supercritical CO_2 is injected into geological formations could improve the technical feasibility of the underground storage of CO_2. The injectivity performance and storage capacity could be affected as a consequence of chemical reactions that could lead to precipitation of clay minerals and dissolution and precipitation of carbonates. Previous researches (Gunter 1993, Bachu *et al*. 1994, Gunter 1996, Gunter 1999) have suggested the main trapping mechanism to fix CO_2 underground is called “mineral trapping”, which involves geochemical reactions that sequesters CO_2 in the form of carbonates. Also, dissolution of authigenic feldspar grains, dolomite and anhydrate could lead to precipitate clays mostly kaolinite, illite and/or chlorite.

Additionally, it has been reported by some authors (Hutcheon *et al*, 1993, Czernichowsk-Laurion *et al*, 1996) that the pH is buffered at higher values in sandstone aquifers than in carbonate aquifers. It is shown that the amount of CO_2 trapped in a carbonate aquifer is lower than that calculated in a sandstone aquifer at the same conditions of temperature and pressure. Thus, the amount of CO_2 trapped was calculated to be 62 g of CO_2 per kg of water, while in a sandstone was 83 g of CO_2 per kg of water. In general, although sandstone and carbonate aquifers appear to be suitable for CO_2 sequestration, the widespread occurrence of sandstones makes them the initial choice for studies.

The third approach included the chemical interaction expected with CO_2 injected in the deep geosphere was related to the natural occurrence of carbon dioxide in sedimentary basins (Pearce, *et al*. 1995). Most of the CO_2 used as tertiary oil recovery operations comes from natural resources and the main reservoir are: Bravo Dome Unit (New Mexico), Sheep Mountain, Mc Dome and Bravo Canyon (Colorado), la Barge-Piney (Wyoming) and Jackson Dome (Mississippi).

Two natural occurrences of CO_2 have been described in depth. One such site is the Bravo Dome CO_2 field in the northeastern New Mexico. The main productive formation is Tubbs sandstone. This formation is sealed by 6 meters of the Cimarron anhydrate that has excellent seal characteristics.

Based on petrography studies, anhydrite, dolomite and detrital plagioclases were subjected to dissolution as consequence of early introduction of CO-rich formation waters. In addition, K-feldspar and gypsum cement are highly corroded and kaolinite, zeolite and gibbisite are the late stage cementing material in this sandstone. Hence, zone of high porosity grade into zones of reduced porosity and permeability as a consequence of these authigenic materials.

Another giant carbon dioxide accumulation is Jackson Dome. The CO_2 is concentrated in the Smackover, Buckner and Norphlet Formations. Dissolution of feldspars and precipitation of clays (kaolinite and illite) have been observed. The sediments had excellent original primary porosity that was estimated to be from 40 to 45%, but the average porosity is 12% now. The reduction in porosity and permeability is related to fibrous illite that completely fills the pore throats. It has been concluded that the introduction of CO_2 into the Jackson Dome did not directly result in extensive clay precipitation, since illite and chlorite also occur in most of the Norphlet formation, which has not been subjected to CO_2 migration. The fourth approach dealt with the role that carbon dioxide has played in diagenesis processes. Several authors (Meshri, 1986; Lundergard *et al.1986;* and Kharaka, *et al.* 1986 and Capuano, 1990,) have discussed the effects of CO_2 – rich fluids on reservoir rock in the development of secondary porosity in sandstone reservoirs. This phenomenon has been attributed to the dissolution of feldspars, kaolinites and carbonate minerals by carbonic acid. Additionally, it has been stated (Meshri, 1986) that thermal maturation of kerogen between 80^0C and 140^0C could be abundant in formations water giving generation a high amount of CO_2 that would have caused precipitation of carbonates and clays.

Published values have been selected with regard to the properties of CO_2, water, and their mixtures at supercritical conditions. Density and viscosity data were provided by Advantek in the 2nd quarter progress report. Mutual solubility data are limited (Gunter, et.al., 1993). The concern for this task is CO_2 solubility in water to acidize limestone and dolomite. This reference reports solubility at 15 MPa (2,176 psi) to be about 4 M which will be used in initial acidizing calculations. Some literature values for solubility of CO_2 in water are much lower, 0.6 M at 1,500 psi and may be in considerable error (Janda, et.al., 2001). More elaborate data bases computer codes are available (Johnson, et.al., 1992) and will be used as needed.

Task 4.2 Estimation of the diameter and length of a single flow channel

Material balances can provide an estimate of the volume of limestone dissolved for a given amount of water injected. Assuming a diameter for a wormhole the material balance then allows the estimation of a wormhole. This calculation does not consider the dynamics of CO_2 saturated water solubilizing limestone. These dynamics must consider many variables such as the following:

- Local pressures adjacent the injection well, as well as in fractures and wormholes.
- Porosity, permeability, and purity of the limestone.
- Mass transfer rates both to and from the limestone.
- Reaction rates

Due to the complexity of the above dynamics laboratory experiments were performed. Published literature has established that limestone dissolution in CO_2 saturated water at typical reservoir conditions is rather rapid (Ross, et.al., 1982). This reference tested calcareous sandstones, to the growth of wormholes in relatively pure limestone was not observed. Initially these experiments will be rather simple, 25 mm diameter x 75 mm cores. The front face of the core will have an axial hole drilled to serve as a known start for the wormhole. The hole may be 2mm in diameter and 5 to 15 mm deep.

An experimental apparatus was designed to evaluate the mass transfer between limestone and CO_2 saturated brines at supercritical conditions of CO_2. A schematic diagram of this experimental apparatus for flooding a limestone core simultaneously with brine and carbon dioxide is depicted in Figure 4.2.1.

Detailed petrophysical and petrographic studies, include X diffraction, SEM, electron microprobe and porosity and permeability measurements, have been performed both before and after core flooding in order to observe the mineralogical alteration and changes in rock texture (wormholes), porosity, and permeability as consequence of mineral dissolution and/or precipitation (see task 3.2).

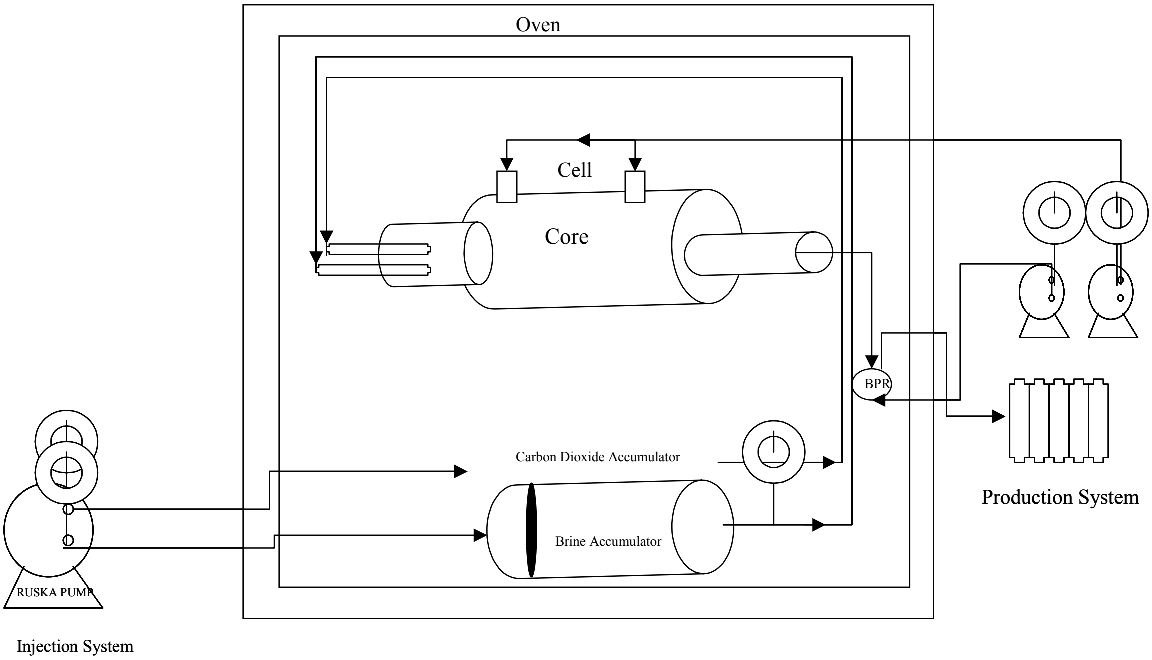

Figure 4.2.1: Schematic diagram of CO_2 coreflood experimental apparatus

The present research is aimed at investigating the water acidification in carbonate aquifers, in which the reactivity of the host formation is obviously controlled by carbonate minerals. Task 2.4 has established physical and chemical properties of the three-phase system CO_2, water and calcium carbonate.

Sample cores were recovered from two observation wells drilled in a tertiary CO_2 pilot in the Levelland field, Hockley County Texas, in 1979. The wells (Well-744 and Well-745) were cored from 4853 to 4885 feet; about 32 feet of reservoir and non-reservoir zone were recovered. Figures 4.2.2 and 4.2.3 show the cores to be used. Of the core from Well-744 (seven three-foot core boxes) 48% were preserved (cores in yellow wrap). Well-745 has five three-foot core boxes, of which 42% of the cores are preserved. The core was selected at the Bureau of Economic Geology's facilities in Midland, Texas, strictly on a visual basis. The preserved cores are available for plugging to characterize the representative zone of the reservoir to be tested. The San Andres formation is an active oil and gas reservoir under enhanced oil recovery with CO_2, and consequently there is core information and geophysical data available.

The San Andres formation was deposited in a marine environment in the Permian Basin of West Texas. This formation is dense with permeable dolomitic layers, which contain nodular anhydrite and anhydrite and gypsum cement. Also, it has been noticed that a rich bed of authigenic aluminosilicates such as quartz, feldspar, kaolinite, illite and mixed layer clays is a representative marker throughout the reservoir. Formation water in San Andres was brackish water at the time that the wells were cored and had a total dissolved solid concentration of about 100 g/L.

Based on the broad mineralogical composition of the San Andres formation and the work carried out by Gunter et al., in 1993, it can be speculated that carbonate formations associated with aluminosilicates could significantly increase CO_2 uptake. This is because there is a favorable environment for an artificial diagenesis - favored by pressure and temperature conditions of the reservoir to be tested. The chemical composition of the formation water will also be relevant to the dissolution of CO_2.

An integrated petrological, mineralogical, petrophysical and experimental study is being undertaken in order to evaluate the expected mineral–brine–CO_2 reactions in San Andres carbonate formation.

The expected mineral-brine – CO_2 reactions will be evaluated considering two different approaches:

1. Formation Characterization.
    a. Petrological and Mineralogical Studies. These studies will be aimed at identifying important components of the rock and recognizing the distribution of the potential authigenic aluminosilicates (clays, feldspar, plagioclases, etc.), which could react in presence of carbonic acid, formed after dissolution of carbon dioxide in the formation brine. Clay authigenic aluminosilicates identification will be performed under the supervision of Dr. Guven of Texas Tech Geosciences Department, who is internationally recognized for his contributions to applied and basic clay research. The clay identification will be performed in Texas Tech's clay laboratories that are fully equipped with X-ray diffractometer (XRD) and Scanning Electron Microscope interfaced with X-ray microanalyzer (SEM).
    b. Petrophysical Studies. These studies will allow determining the subsequent enhancement of porosity, permeability and injectivity as a consequence of CO_2-rock expected interactions. These studies will be performed before and after CO_2 injection in order to compare the petrophysical parameters. These studies will also be carried out using NMR petrophysical analysis, as well as conventional core analysis for comparison.
2. Experimental Displacements
    a. Representative San Andres formation core plugs and CO_2 saturated formation brine interaction tests will be carried out with core flow tests under temperature and pressure reservoir conditions. A sampling of brackish water produced after CO_2 injection will be performed in order to determine the pH and chemical composition or solids concentration in the produced brine.

.

Figure 4.2.2: Levelland Well #744 core.

Figure 4.2.3: Levelland Well #745 core.

The experimental apparatus to be used during CO_2 experimental flooding is shown below in the figure.

Two cores will be placed into rubber tubing. This core assemblage will place in the core holder (high pressure vessel- 10,000 psi). Distillated water will be introduced around the core to obtain an overburden pressure about 3000 psia. The distillated water will be injected using a Precision Syringe Isco pump. This overburden pressure ensures a tight fit between the rubber tubing and the outside of the cores, thus preventing solution from passing through the annulus between the rubber tubing and the outside of the cores.

The brine injection and CO_2 gas will be injected into the core holder from two accumulators one for brine (high pressure vessel- 3000 psi) and the other for CO_2 (high pressure vessel–5000 psi). After the temperature of the system will be reached 150^{o}F , the CO_2 pressure will set to 2000 psia by adjusting the position of the accumulators pistons. The equilibrium between CO_2 gas and the injection brine will be obtained maintaining the CO_2 injection pressure.

A Ruska pump will be used to inject mineral oil into the accumulators to maintain the injection. The injection rate of the brine will be determined based on the cores permeability and the capability to inject of the Ruska pump. A burst disk of 5000 psia has been installed into the Ruska pump.

During each test, the effluent solution will pass through a backpressure regulator (BPR) and then thought a separator in order to collect the brine continuously into an auto-sampler. The tubes of the auto-sampler will sifted the position at about min interval. CO_2 degassed out of brine solution will be measure using a wet test meter. All the connections and valves have made using Autoclaves Engineering Valves, which have a range of pressure between 10,000 and 35,000 psi.

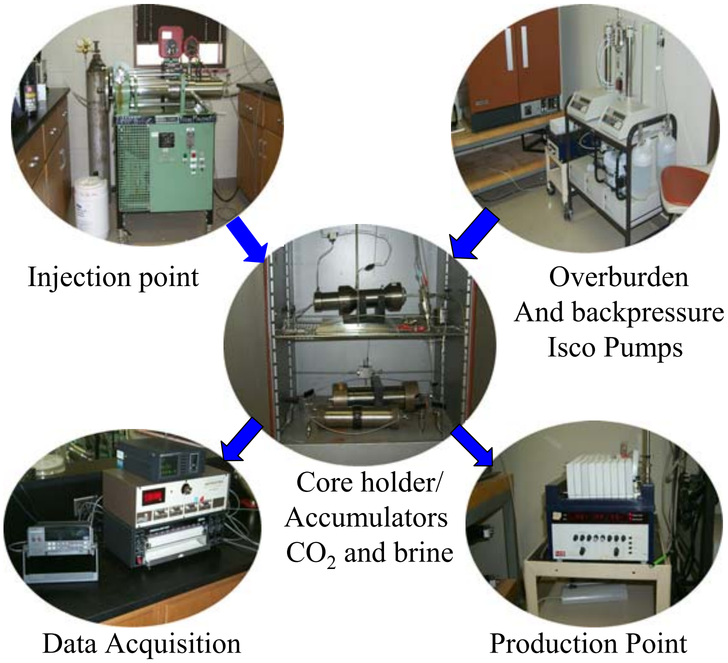

Figure 4.2.4: Setup to be used to evaluate the CO_2 flooding using San Andres Formation core plugs.

Task 4.3 Characterize 3-phase flow within an acid developed channel/Initial Results from CO2 Injection

The experimental laboratory work focused on injection rate, natural formation brine composition from the Permian Basin, dolomite core samples from San Andres Formation and CO_2 injection above supercritical conditions.

Two different injection rates were used: 2.696E-06 cubic feet/min (0.1613 cc/min-20 pore volumes injected) and 3.467E-02 cubic feet/min (0.982 cc/min-120 pore volumes injected). Dynamic displacement of CO_2 and brine was performed for about 167 hours (7 days). The ratio of CO_2 to formation brine was about 20% for all the tests. To better describe the phenomena during injection, laboratory tests were performed under reservoir conditions of pressure and temperature 2000 psia (140.64 atm) and 120˚F (62.2˚C), respectively.

The primary objective of these laboratory tests was to investigate the alteration of the petrophysical properties (permeability and porosity) as a consequence of a possible geochemistry alteration of porous medium. It has been pointed out that generation of new mineral species can be precipitated and deposited in the pore throats reducing the pore volume, porosity and permeability.

Rock-CO_2 - brine interactions

A total of fifteen (12) core samples were selected to be injected simultaneously with brine and CO_2. The injection tests were designed to detect the effect of CO_2/brine on the changes of rock petrophysical properties, and to identify the major mechanisms producing these changes.

Table 4.3.1 summarizes the results obtained before and after low injection rate of CO_2/brine. The absolute initial permeability ranges from 0.2 mD to 2.76 mD. After CO_2/ brine displacement, the samples were cleaned using methanol, and dried at 70°C for four days. Afterwards, permeability and porosity were measured. The final permeabilities ranged from 0.02 mD to 6.47 mD.

Table 4.3.1 Permeability results under low injection rate of CO_2/brine.

Run	Sample	Permeability, mD		PPA	Permeability Alteration, %
		Before CO_2	After CO_2		
1	4860(1)	3.00	0.02	$6x10^{-3}$	99.0
1	4861(1)	0.20	0.07	0.32	62.0
2	4868(1)	0.71	0.33	0.46	24.0
2	4878(2)	0.44	0.27	0.60	40.0
3	4827(4)	2.62	6.40	1.14	14.0
3	4872(1)	2.76	6.47	1.12	12.0
4	4827(1)	1.37	1.22	1.10	10.0
4	4871(3)	3.49	2.38	0.68	32.0

Table 4.3.2 summarizes the bulk, grain, pore volumes and porosities of the cores injected at a low rate, before and after injection of CO_2/brine. An increase of grain volume of about 6% in all the core samples represented a reduction in pore volumes and porosities of about 22%. It can be noted that all the samples showed a PPA average of 76%, indicating that the reduction in pore volume and porosity was 24%.

All eight core samples exhibited porosity alteration after CO_2/ brine injection. As mentioned above, low injection rate promotes mineral dissolution by weak carbonic acid. The dissolved minerals may have precipitated and occluded the pore throats of the pore spaces. It should be pointed out that a decreased in pore volume and porosity can lead to a decrease in permeabilities. This in turn produces a reduction of CO_2 injectivity.[26]

Table 4.3.2 Pore volume and porosity results under low injection rate of CO_2/brine.

Run	Sample	Bulk volume	Grain volume		Pore volume		PPA	Pore volume Reduction	Porosity	
			Before CO_2	After CO_2	Before CO_2	After CO_2			Before CO_2	After CO_2
1	4860(1)	82.6	64.6	67.1	17.2	13.1	0.72	22.0	21.3	16.0
1	4861(1)	82.1	66.3	70.0	11.4	8.1	0.71	29.0	14.1	9.9
2	4868(1)	82.9	77.0	78.4	2.9	4.2	0.76	24.0	7.1	2.4
2	4878(2)	82.9	67.1	71.6	14.6	10.1	0.69	31.0	17.8	12.3
3	4827(4)	81.7	60.2	62.2	23.7	20.4	0.86	14.0	28.7	24.7
3	4872(1)	74.2	28.2	63.3	24.7	19.6	0.79	21.0	29.8	23.6
4	4827(1)	82.1	64.6	67.1	20.2	12.4	0.76	24.0	23.9	18.3
4	4871(3)	84.3	66.3	70.0	16.0	12.0	0.77	23.0	21.6	16.2

Table 4.3.3 summarizes the main M_o and porosity values calculated on the T_2 distribution curves. A comparison between preflood and postflood results with CO_2 indicates that the M_o was reduced in all the samples that were displaced at very low injection rate or at low pore volumes. The petrophysical property alteration (PPA) related to NMR porosity was calculated to be from 0.03 to 0.89. This represents a reduction range in porosity from 97% to 13%. The highest reduction in porosity was calculated for samples 4868(1) and 4878(2).

Table 4.3.3. T_2 distribution results under low injection rate of CO_2/brine.

Run	Sample	M_o		Porosity $_{NMR}$		PPA	Porosity Reduction, %
		Before CO_2	After CO_2	Before CO_2	After CO_2		
1	4860(1)	936.84	672.00	7.34	2.27	0.72	28.0
1	4861(1)	1838.38	1229.01	14.20	12.06	0.83	17.0
2	4868(1)	1228.94	48.89	11.92	0.38	0.03	97.0
2	4878(2)	920.17	39.01	7.43	0.30	0.04	96.0
3	4827(4)	2006.83	1296.24	12.91	12.66	0.80	20.0
3	4872(1)	1926.22	1883.41	17.08	16.44	0.96	14.0
4	4827(1)	1873.42	1202.83	14.77	11.88	0.80	20.0
4	4871(3)	1848.683	1638.24	14.20	12.28	0.89	11.0

Table 4.3.4 shows the BVI (small pore sizes) and FFI (large pore sizes) values calculated for the samples injected under very low injection rate or under low pore volume. Significant increase in the small pores (increase in value of BVI) and consequent decrease in the large pores (decrease in value of FFI) were observed after injection of CO_2/ brine in the San Andres core samples. The distribution and size of the pore throats, which may be occluded by fine material reducing the porosity and permeability of the samples is an important feature to be considered during qualitative observations of the San Andre formation**.**

Table 4.3.4 Bound water volume and free fluid index values under low injection rate of CO_2/brine.

Run	Sample	BVI			FFI			
		Before CO_2	After CO_2	PPA	Before CO_2	After CO_2	PPA	Reduction FFI
1	4860(1)	17.74	39.00	2.20	82.26	61.00	0.74	26.0
1	4861(1)	33.87	20.14	1.20	66.13	49.86	0.72	22.0
2	4868(1)	44.29	91.20	2.10	22.41	8.8	0.16	84.0
2	4878(2)	78.01	89.00	1.14	21.99	11.00	0.20	20.0
3	4827(4)	27.87	42.39	1.63	72.13	24.61	0.76	24.0
3	4872(1)	19.20	23.10	1.19	80.2	76.90	0.96	4.0
4	4827(1)	32.47	47.20	1.33	64.23	22.80	0.82	18.0
4	4871(3)	36.28	62.10	1.79	63.72	34.90	0.22	42.0

The original structure of sample 4860 is illustrated in Fig. 4.3.1. It shows that fine calcite and dolomite fill the intergranular area of the sample. The framework of dolomite grain boundaries are difficult to differentiate. Micro-porosity is common within dolomite grains (see arrows).

Fig. 4.3.2 shows sample 4860 postflood with CO_2/brine injection. The framework grains are difficult to discern in this microphotograph because of the presence of abundant ultrafine material. Small scattered micro-pores are visible (see arrows in picture). Fig. 4.3.3 BSE of the original sample depicts a macro-pore visible in the framework of dolomite grains. Tiny particles of calcite coat the dolomite grains and also bridge the intergranular spaces. In Fig. 4.3.4 BSE image shows the sample after CO_2 injection. Calcite coats most of the dolomite framework. Calcite appears to overlay the dolomite grains and to bridge the pores.

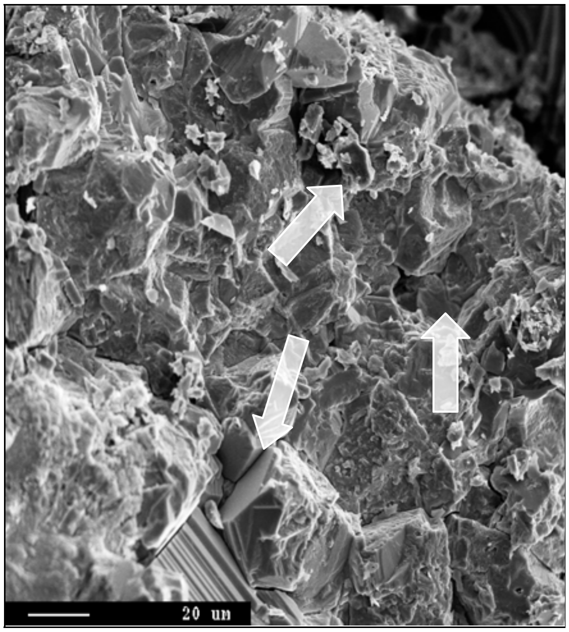

Figure 4.3.1. SEM image of original sample 4860 at 200X.

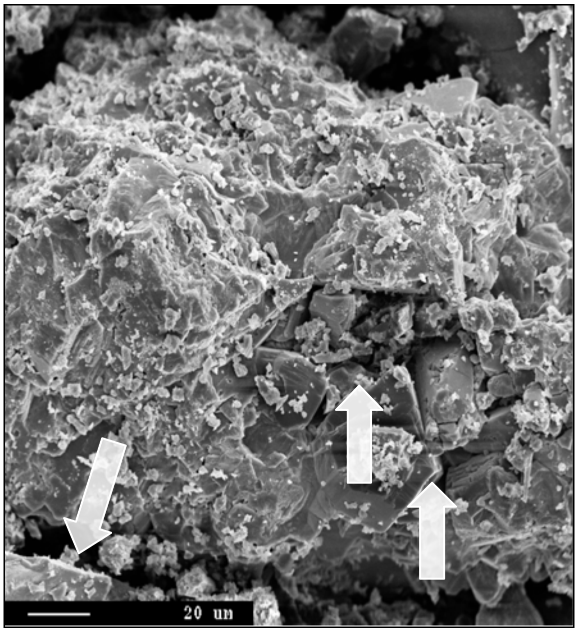

Figure 4.3.2. SEM image of sample 4860 treated with CO_2/brine at 200X.

Figure 4.3.3. BES image of original sample 4860 at 200X.

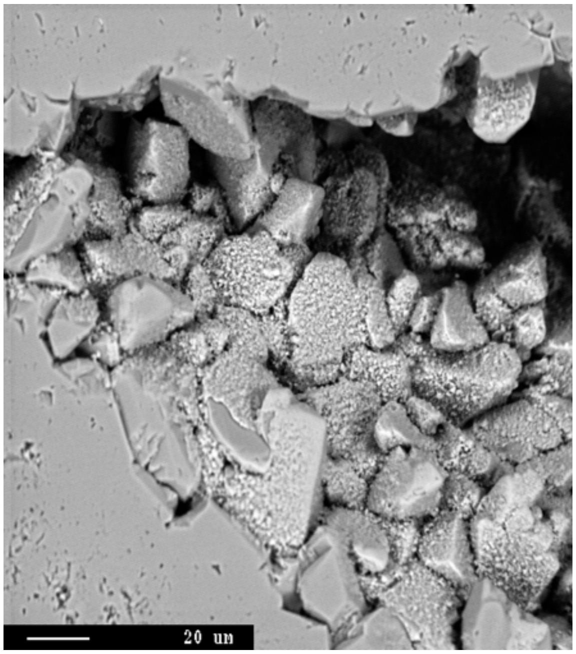

Figure 4.3.4. BSE image of sample 4860 treated with CO_2 at 200X.

Determining the chemical composition of the effluent brine to be in contact with supercritical CO_2 should, in principle, show the brine's tendency to react with CO_2 and form stable compounds. The objectives of these tests explore possible correlation with the chemical concentration of the brine, and the extent of formation damage due to precipitation of new material.

As a first step, the chemical concentration of the initial brine was found in order to evaluate any variation in the concentration of the main cations and anions after interaction with supercritical CO_2. The results obtained using ICP analyses for the cations and liquid chromatography for ions of the original brine are summarized in Table 3.3 section 3.2. The results of the laboratory analyses of the brine samples taken during the floods with CO_2 are summarized in Tables 4.3.5 and 4.3.6.

The chemical concentrations of the effluents collected during flooding of samples 4868-4878 are summarized in Table 4.3.5. TDS, chlorine and sodium concentrations did not change significantly after 167 hours of injection. The reduction in these concentrations was very small, about 3%.

Table 4.3.5 Chemical composition of the effluent brine after CO_2/brine flooding on samples 4868-4878 under low injection rate.

Time Hrs	TDS g/L	Na$^+$ g/L	Cl$^-$ g/L	Ca^{2+} g/L	SO_4^- g/L	Mg^{2+} g/L	K$^+$ g/L	HCO_3^- mg/L	pH
0.0	78.2	18.0	46.2	6.0	4.88	1.82	1.21	0.092	6.4
48.6	77.3	17.2	42.9	2.91	4.86	1.84	1.49	0.100	6.2
168.0	77.0	17.6	42.2	2.90	4.60	1.94	1.27	0.130	6.8

There was a slight decrease in sulfate ion content, and a slight the concentration of bicarbonate ions. The concentration of sulfate varied from 4.9 g/l to 4.6 g/l, a reduction of 6%. The concentration of carbonate was increased from 0.092 mg/L to 0.13 mg/L, an increase 37% over the original concentration.

The pH increased slightly. However, pH measurements were obtained under laboratory conditions. This value was not recorded during the test time; hence it is not conclusive about pH variation during the reactions.

Table 4.3.6 summarizes the chemical concentration of the ions obtained from analysis of the effluent brine collected during flooding of samples 4827 (1) and 4871 (3).

Table 4.3.6 Chemical composition of the effluent brine after CO_2/brine flooding on samples 4827(1)_4871(3) under low injection rate.

Time Hrs	TDS g/L	Cl$^-$ g/L	Na^{+-} g/L	Ca^{2+} g/L	SO_4^- g/L	Mg^{2+} g/L	K$^+$ g/L	HCO_3^- mg/L	pH
0	78.21	46.2	18.0	6.00	4.88	1.82	1.21	0.092	6.4
12	79.39	46.7	18.2	6.02	4.60	2.00	1.29	0.220	6.2
48	72.92	44.2	17.7	2.86	4.48	1.93	1.23	0.220	6.7
168	63.69	36.9	14.6	4.90	4.44	1.26	1.20	0.082	6.7

The calcium concentration decreased from 46.2 g/L to 36.9 g/L, a reduction of 19% from the original concentration. The magnesium concentration was decreased in 14 %, potassium decreased in 20%, and the sulfate ions decreased by 10%. The bicarbonates ions increased by about 220% after 48 hours of injection. At the end of the test, a reduction of 61% took place. The pH increased from 6.4 to 6.7.

The previous results do not explain how the concentrations of the ions changed at very low injection rate. However, an integration of the present results with those obtained from petrophysical analyses, NMR, XRD, and structural changes observed with SEM and BSE suggest that when the brine affected by CO_2 is displaced through porous media under a differential pressure, the suspended solids are able to precipitate as a result of any reduction in pressure or increase in temperature. These solids are very small. Consequently, they can be retained easily, bridging and coating the pore space and as a result decreasing the permeability and the porosity.

Table 4.3.7 Permeability results under high injection rate of CO_2/brine.

Run	Sample	Permeability, mD		PPA	Permeability alteration
		Before CO_2	After CO_2		
1	4860(3)	2.60	2.60	1.0	0.0
1	4872	0.20	0.62	1.3	30.0
1	4876(3)	12.89	16.60	1.3	30.0
2	4822(1)	0.167	0.22	1.2	20.0
2	4862(2)	0.200	0.23	1.2	20.0
3	4879(1)	0.400	0.43	1.1	10.0
3	4882(2)	0.220	0.27	1.1	10.0

On average (Table 4.3.7), the petrophysical property alteration related to permeability changed from 1.0 to 1.2, observing a little improvement in permeability after injection of 120 pore volumes of CO_2/brine.

From the previous observations, it can be concluded that there is not a defined trend in the permeability behavior. In general, a slight improvement in the petrophysical properties of permeability and porosity could be connected with rock dissolution, either anhydrite or dolomite or both minerals as result of carbonic acid reaction.

A notable improvement occurred in pore volume and porosity for all the samples injected under high pore volumes. An enhancement of pore volume was found from 0.2 cc to 3.3 cc. Thus, the porosity increased from 6 % to 36%.

The pore volume and porosity results before and after high pore volume injection of CO_2/brine is shown in Table 4.3.8.

Table 4.3.9 condenses the total equilibrium nuclear magnetization and porosity results before and after flooding with CO_2 of the samples injected at high pore volumes. A detailed evaluation of the M_o shows that, in general, the values were not extensively increased. The porosity values before and after CO_2/brine injection are almost the same.

Table 4.3.10 summarizes the most important peaks observed in the unimodal and bimodal T_2 distribution.

Table 4.3.8 Porosity results before and after high injection rate of CO_2/brine.

Run	Sample	Bulk Volume	Grain volume		Pore volume		PPA	Porosity,%		PPA
			Before CO_2	After CO_2	Before CO_2	After CO_2		Before CO_2	After CO_2	
1	4860 (3)	38.10	33.02	32.48	2.02	2.62	0.98	13	12	1.12
1	4872	67.86	28.02	24.80	9.81	13.06	1.33	14	19	1.36
1	4876 (3)	72.26	43.16	40.13	29.40	32.44	1.10	N/A	N/A	1.10
2	4822 (1)	83.46	69.29	68.79	14.17	14.67	1.04	17	18	1.06
2	4862 (2)	82.62	70.26	69.42	12.36	13.20	1.07	12	16	1.07
3	4879 (1)	82.39	66.68	62.36	12.72	17.03	1.08	19	21	1.10
3	4882 (2)**	82.70	74.24	71.09	8.16	11.61	1.42	10	14	1.4

N/A No available

**Abnormal increase in pore volume

Table 4.3.9 T_2 distribution results under high injection rate of CO_2/brine.

Run	Sample	M_o		Porosity NMR		PPA
		Before CO_2	After CO_2	Before CO_2	After CO_2	
1	4860(3)	1099.94	1087.00	18.7	18.2	1.0
1	4872	976.82	1021.92	4.7	4.8	1.0
1	4876(3)	1489.84	1477.84	29.6	29.6	1.0
2	4822(1)	1327.87	1327.87	23.1	23.1	1.0
2	4862(2)	1239.12	1316.287	23.1	23.1	1.0
3	4879(1)	1760.71	1778.82	31.4	31.4	1.0
3	4882(2)	1372.93	1187.40	24.1	21.0	0.9

Table 4.3.10 Main peaks in T_2 distribution

Run	Sample	Main Peaks, Milliseconds		Type of distribution
1	4860(3)	81.48		Unimodal
1	4872	143.21		Unimodal
1	4876(3)	422.88		Unimodal
2	4822(1)	23.70	707.20	Bimodal
2	4862(2)	208.21		Unimodal
3	4879(1)	48.70		Unimodal
3	4882(2)	29.83		Unimodal

Most of the cores tested under high pore volume injection showed a unimodal distribution with peaks from 49 milliseconds to 208 milliseconds, and with a long tails extending down to very short T_2 values. Modes less than 2 milliseconds could hide Sample 4822 (1) presents a bimodal distribution and its peaks are 23.7 milliseconds and 707.20 milliseconds. Two pore systems are defined in this sample.

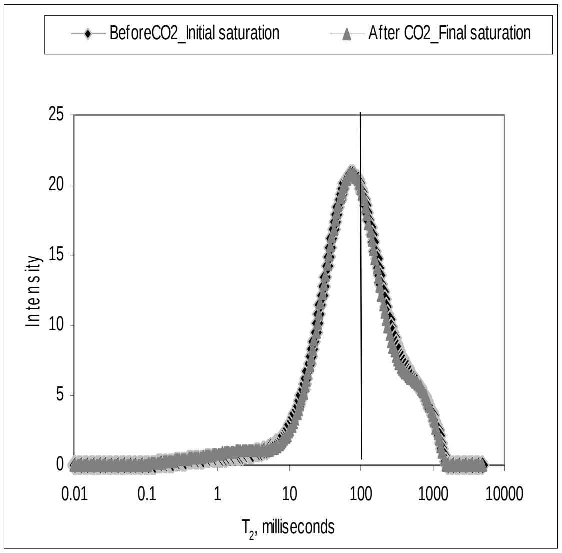

Figure 4.3.5. T_2 spectra before and after CO_2. High injection rate of sample 4860. (3). Upstream.

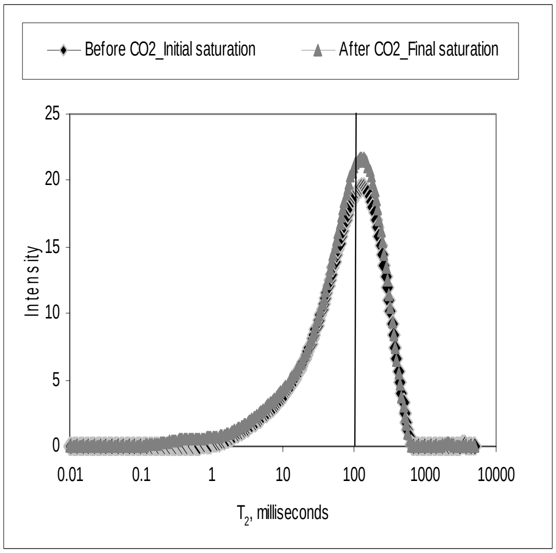

Figure 4.3.6. T_2 spectra before and after CO_2. High injection rate of sample 4872. Midstream.

The T_2 spectra behavior before and after CO_2/brine injection are detailed in Figs. 4.3.5 through 4.3.11. In these figures, a T_2 cut off of 100 milliseconds divides the spectra in BVI and FFI. Most of the samples show the same T_2 profile before and after CO_2/brine injection at high pore volumes. There is not substantial increment or reduction in the total equilibrium nuclear magnetization, and then the petrophysical properties did not present remarkable variation.

Simple observations of the T_2 distribution plots indicate that there is good agreement between the petrophysical properties before and after CO_2/ brine injection at high pore volumes. The (BVI) and (FFI) values seem to indicate no variation in pore size distribution.

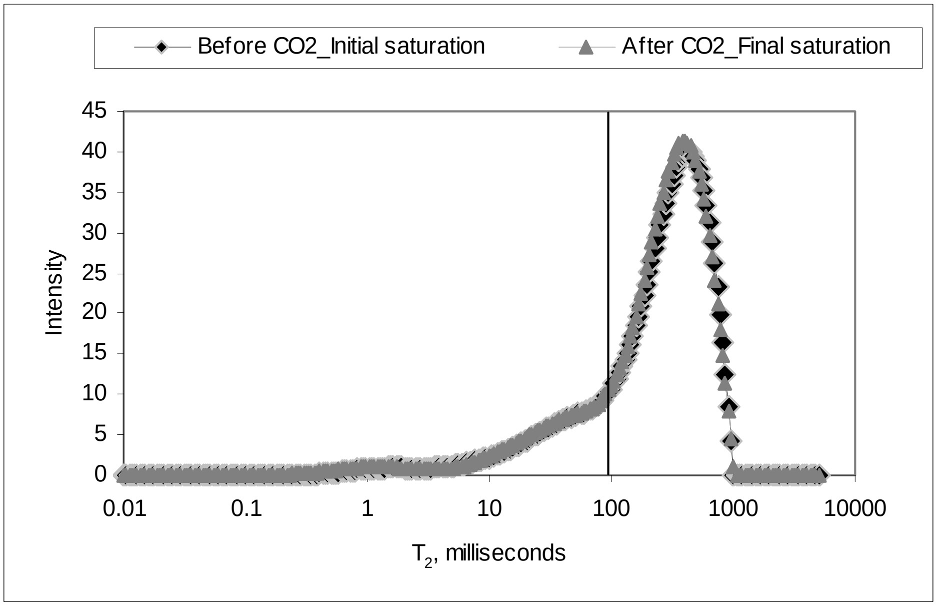

Figure 4.3.7 T_2 spectra before and after CO_2. High injection rate of sample 4876 (3). Downstream.

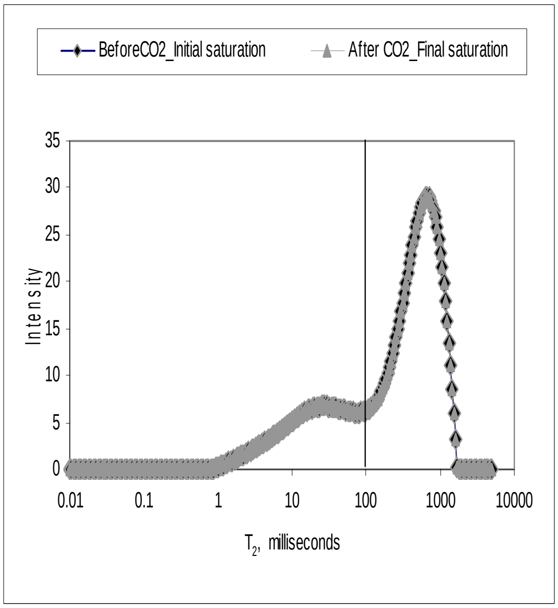

Figure 4.3.8 T_2 spectra before and after CO_2. High injection rate of sample 4822 (1). Upstream.

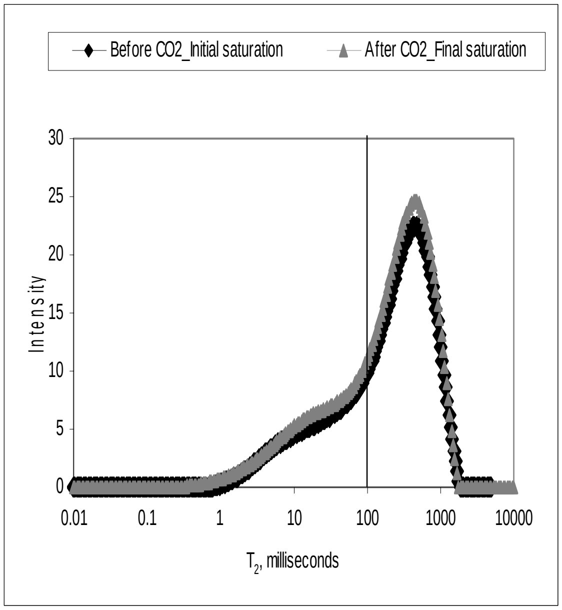

Figure 4.3.9 T_2 spectra before and after CO_2. High injection rate of sample 4862(2). Downstream.

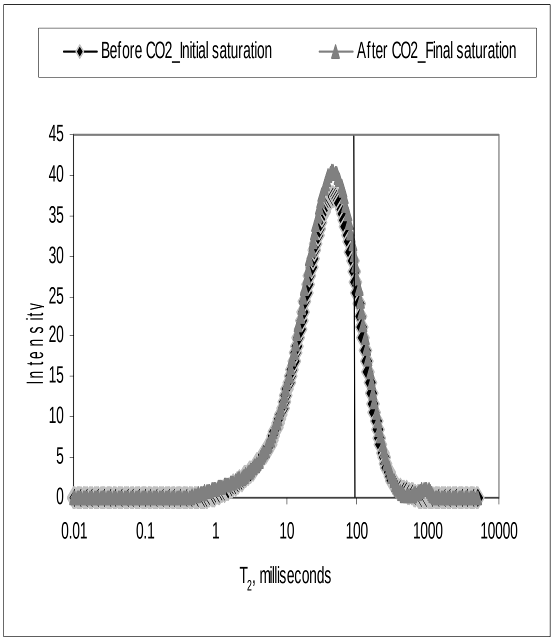

Figure 4.3.10 T_2 spectra before and after CO_2. High injection rate of sample 4879 (1). Upstream.

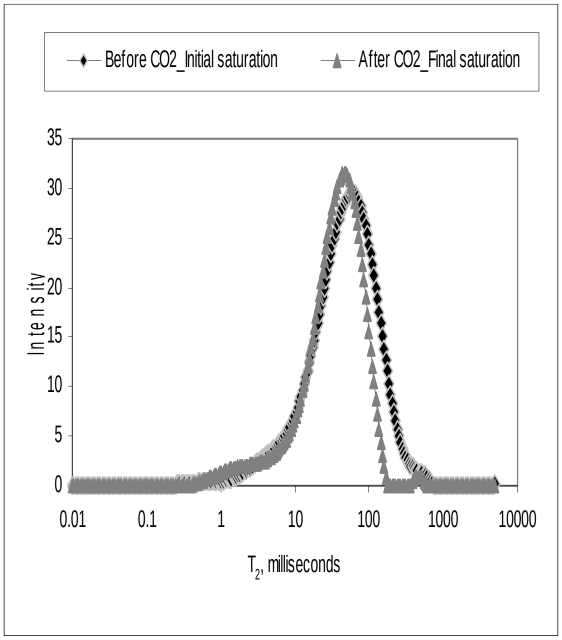

Figure 4.3.11 T_2 spectra before and after CO_2. High injection rate of sample 4882(2). Downstream.

XRD patterns of the original bulk sample confirmed that San Andres formation is formed mainly by dolomite, anhydrite and lesser amount of quartz. The fine material of the San Andres formation is mainly composed by anhydrite, quartz and some dolomites. XRD patterns of the postflood samples indicated that the dolomite and anhydrite peaks were very defined, indicating that dissolution of these two minerals did not occur. The fine material XRD patterns from samples injected under high injection rate suggest dissolution of silica and precipitation of gypsum.

Table 4.3.11 Bound water volume and free fluid index values under high injection rate of CO_2/brine.

Run	Sample	BVI		PPA	FFI		PPA
		Before CO_2	After CO_2		Before CO_2	After CO_2	
1	4860(3)	28.30	29.76	1.03	41.70	40.24	0.96
1	4872	24.90	29.26	1.08	49.10	40.44	0.82
1	4876(3)	22.20	23.20	0.97	77.80	76.80	0.99
2	4822(1)	29.22	29.22	1.00	70.42	70.42	1.0
2	4862(2)*	22.69	42.10	1.64	74.31	27.9	0.77
3	4879(1)	82.27	84.80	0.99	14.73	12.2	1.03
3	4882(2)*	79.23	93.72	1.18	20.47	6.22	0.30

*Abnormal behavior

Task 4.4 Estimate the relative costs for injection of CO_2 into aquifers

Work has been conducted to investigate hydraulic fracture effects in horizontal injectors. The objective is to predict horizontal injector performance (Task 1.1) and to forecast its impact on CO_2 injection economics (Task 4.4). Specifically, the objectives are to investigate:

- What can one expect from a horizontal injector?
- How should one predict injectivity or injector performance over time?
- What is the impact of multiple hydraulic fractures on horizontal injector performance?

The need for calculation (or prediction) of injectivity in horizontal injectors arises both from need for the analysis of performance and for planning a development. The tools and methods available for predicting the injectivity of horizontal injectors are summarized here. It covers both analytical and numerical methods.

Nomenclature

B	Formation volume factor
c_t	Compressibility
F_{cD}	Dimensionless fracture conductivity
h	Thickness
h_D	Dimensionless thickness
k	Permeability
k_f	Fracture permeability
p_i	Initial reservoir pressure
p_{wD}	Dimensionless pressure response at the wellbore
p_{wf}	Bottom hole injection pressure
q	Injection rate
r_f	Fracture radius
r_w	Well radius
r_{wD}	Dimensionless well radius
t	Time
t_{Df}	Dimensionless fracture time
s	Skin factor for pseudo-radial flow
s'	Skin factor for formation linear flow
w_f	Fracture width
φ	Porosity
η	Diffusivity
η_f	Fracture diffusivity
η_{fD}	Dimensionless fracture diffusivity
μ	Viscosity

This part of the report summarizes the methods for predicting injectivity index (II) for various configurations of horizontal wells. The purpose of this review is to establish a baseline of expected performance and to detect abnormal changes in injectivity due to chemical reaction, geomechanics, etc..

Analytical as well as numerical methods are available for predicting the performance of horizontal injectors. Virtually all of these have been developed for production wells and as such do not include injection considerations. Also, most analytical methods involve some approximations and there can be large differences between them.

There are a number of analytical methods available for calculating II of horizontal well. All methods assume a well located symmetrically in a rectangular reservoir volume, with uniform properties. The II is either in steady state (if pressure is maintained at the boundaries) or is pseudo-steady state (if the boundaries are no-flow). The methods most often used are:

Babu and Odeh (1989)
Goode and Kuchuk (1991)
Joshi (1988)

Comparison of these methods was presented by Kuppe and Settari (1998). The problem compared by Kuppe and Settari (1998) is a horizontal well of length=400 ft in a square reservoir of constant thickness. The well is located symmetrically in the “box”. Single phase, steady state or pseudo-steady state is considered. The problem was solved by analytical methods and by fine-grid simulation. Both isotropic and anisotropic permeability cases were considered. The comparison of the analytical methods is shown in Table 4.4.1.

Wall Length = 400 ft				Analytical Solutions			Simulation
Well Direction	kx	ky	Bdy cond	Babu & Odeh	Goode & Kuchuk	Joshi	
X	100	100	no flow	4.82	5.18	3.92	4.87
Y	100	100	Const P		7.13		7.36
X	10	100	no flow	2.21	2.49	1.6	2.37
Y	10	100	no flow	1.22	1.3	1.6	1.31
X	1	100	no flow	.42	0.47	0.6	0.48
Y	1	100	no flow	.22	0.23	0.6	0.27

Table 4.4.1. Calculated Injectivity Index By Various Methods

It is evident that the Babu and Odeh (1989) and Goode and Kuchuk (1991) methods are similar, with the latter giving somewhat higher results. Both are in reasonable agreement with the numerical answers. However, the Joshi (1988) method under-predicts as well as over-predicts II as shown in Table 4.4.1 and Figure 4.4.1, and should not be used for anisotropic permeability.

The results also illustrate that the analytical methods must be chosen with care.

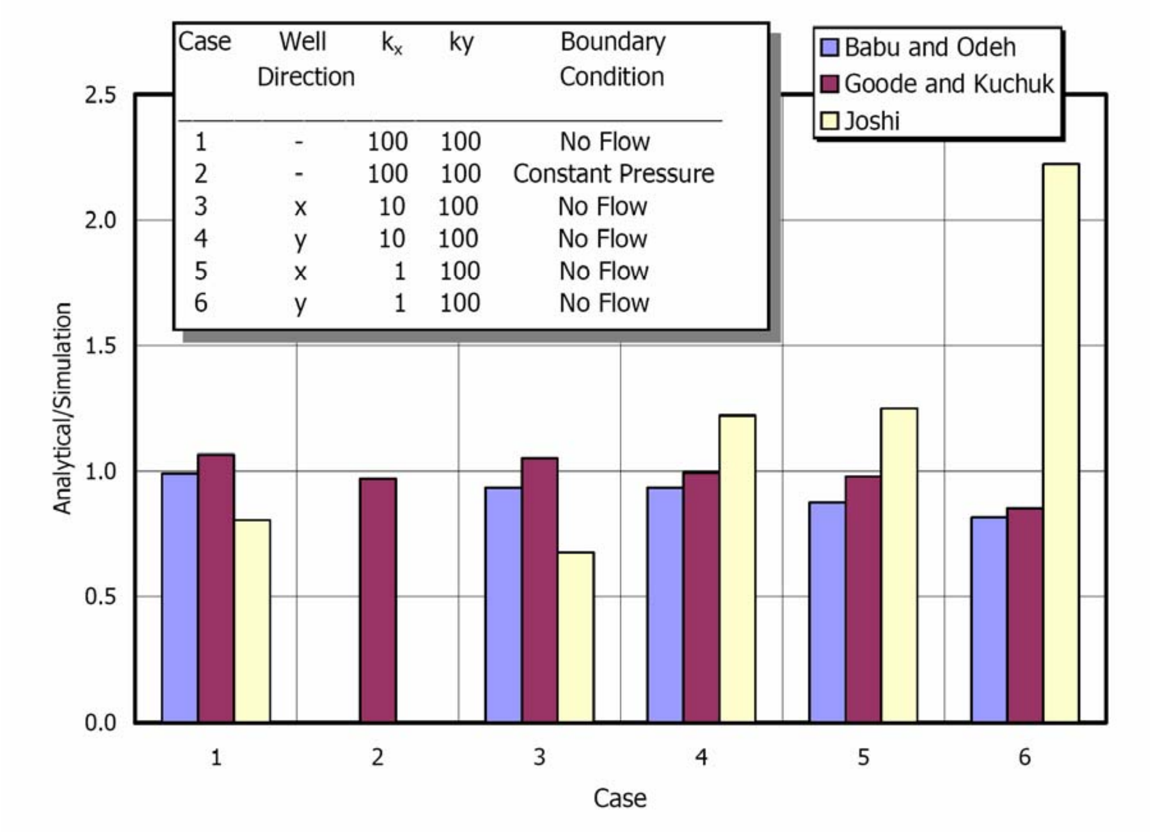

Figure 4.4.1: Comparison of analytical methods for calculation of the injectivity of horizontal injectors

Fractured horizontal injector

Single Fracture Perpendicular to a Horizontal Injector

The above considers an unfractured horizontal injector under steady-state flow condition. The following considers a single hydraulic fracture perpendicular to a horizontal well. Based on the solution given in Larsen and Hegre (1991), there are several flow periods, depending on the time frame:

- First, the flow is within the fracture - a fracture radial flow period. This is shown schematically in Figure 4.4.2.
- As injection continues, the flow evolves to a situation where it is from the fracture to the reservoir through the fracture surfaces. This is sometimes referred to as the radial-linear flow period. It is shown schematically in Figure 4.4.3.
- As injection continues further, the flow becomes formation linear flow, shown schematically in Figure 4.4.4.
- Finally, pseudo-radial flow is reached. This is shown schematically in Figure 4.4.5.

Each flow period is governed by different flow equations, which will be summarized next. In the following, we present the solution form Larsen and Hegre (1991), assuming that the horizontal permeability is the same as the vertical permeability. In order to generalize the results, the following dimensionless parameters are introduced and used, with each variable defined in the Nomenclature section at the beginning of this section:

$$p_{wD} = \frac{2\pi kh(p_i - p_{wf})}{qB\mu} \tag{4.4.1}$$

$$t_{Df} = \frac{kt}{\varphi\mu c_t r_f^2} \tag{4.4.2}$$

$$F_{cD} = \frac{k_f w_f}{kr_f} \tag{4.4.3}$$

$$\eta_{fD} = \frac{\eta_f}{\eta} \tag{4.4.4}$$

$$f_{wD} = \frac{r_w}{r_f} \tag{4.4.5}$$

$$h_D = \frac{h}{r_f} \tag{4.4.6}$$

The fracture radial flow period (Figure 4.4.2) is the first flow period in the injection life of a horizontal well with a single transverse fracture. This flow regime occurs at very small dimensionless time and has a very short life span ending within seconds or less of real time. The period is characterized by radial flow occurring within the fracture as fluid is injected into the fracture from a small entrance, the perforations, and moves radially outward to fill the fracture. The dimensionless pressure response at the wellbore is given by:

$$p_{wD} = \frac{h_d}{2F_{cD}}\left(\ln\frac{t_{Df}\eta_{fD}}{r_{wD}^2} + 0.80907\right) \tag{4.4.7}$$

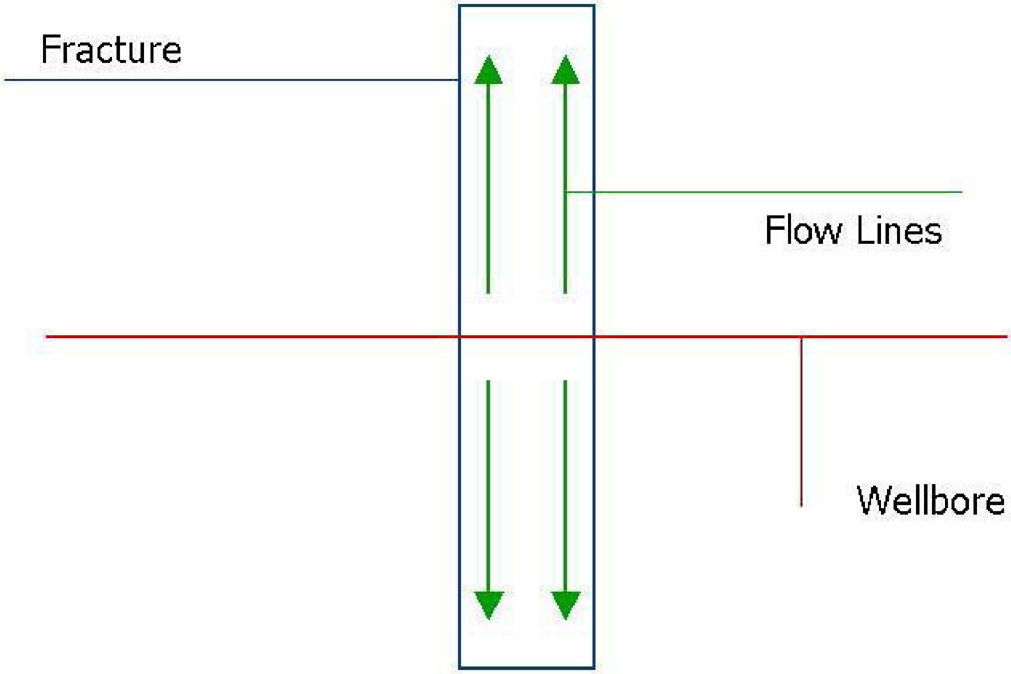

Figure 4.4.2: Fracture radial flow period for single transverse fracture.

The radial-linear flow period (Figure 4.4.3) is the second injection flow period in the life of a horizontal well with a single transverse fracture. This period is characterized by linear flow into the formation from the fracture and transient radial flow within the fracture. In this period linear flow is initiated to the formation from the fracture, this flow increases with time, while radial flow within the fracture decreases until it finally dies out. The duration of this period is strongly related to the fracture conductivity. For small fracture conductivity, this period is very long. As the fracture conductivity increases the length of this flow period decreases. For fractures with a dimensionless fracture conductivity greater than 100, there is no detectable radial-linear flow period. The pressure response at the wellbore during this period is given by:

$$p_{wD} = \frac{h_d}{4F_{cD}}\left(\ln t_{Df} + \ln\frac{F_{cD}^2}{4r_{wD}^4} + 1.0409\right) \tag{4.4.8}$$

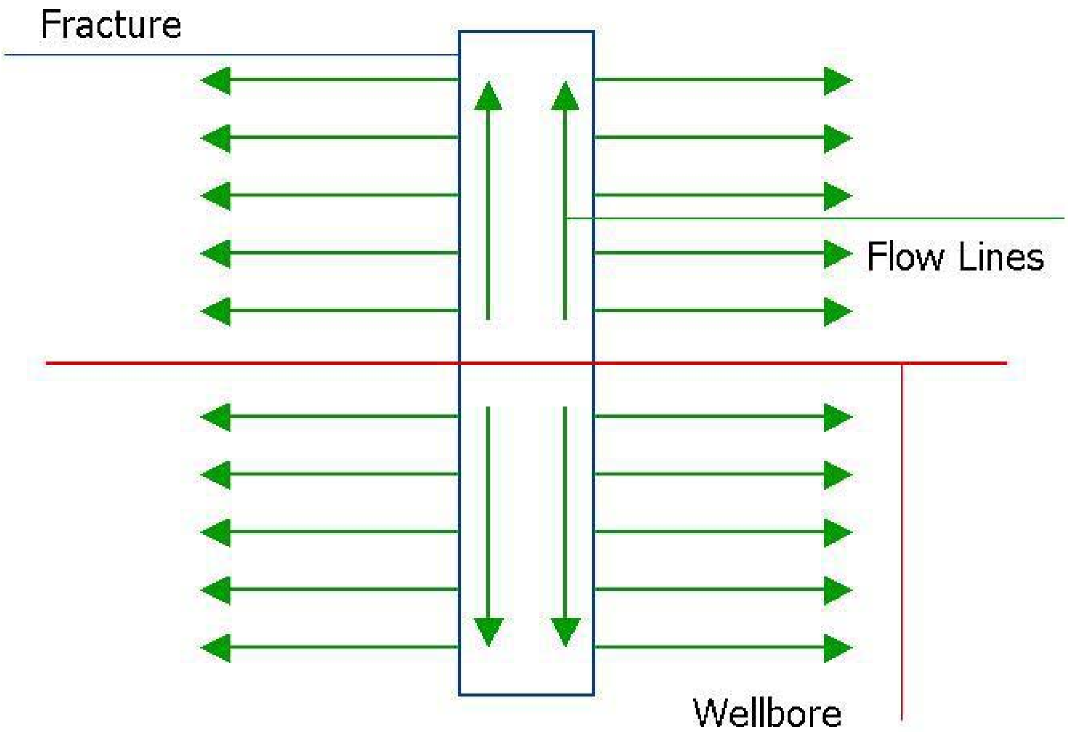

Figure 4.4.3: Radial-linear flow Period for single transverse fracture

Formation linear flow (Figure 4.4.4) is the third generic flow regime in the life of a horizontal injector with a single transverse fracture. This flow period is characterized by linear flow from the fracture into the formation. Again, this flow period is largely dependent on the fracture conductivity; the length of this flow period is directly proportional to the fracture conductivity. Formation linear flow is only exhibited by fractures with high conductivity. The pressure response at the wellbore for this flow period is given by:

$$p_{wD} = \frac{2h_d}{\sqrt{\pi}}\sqrt{t_{Df}} + s'(F_{cD}, r_{wD}) \tag{4.4.9}$$

where s' is a skin factor accounting for the extra pressure drop due to finite conductivity in the fracture and small communication interval between the wellbore and the fracture. The skin factor is directly proportional to the fracture conductivity.

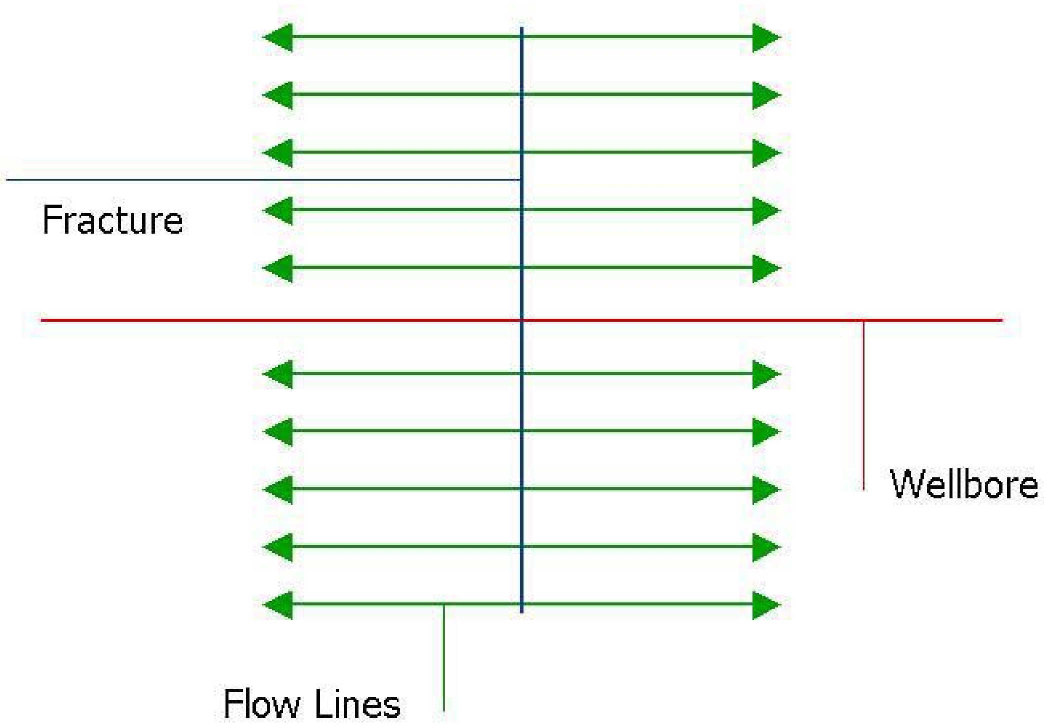

Figure 4.4.4: Formation linear flow period for single transverse fracture

The pseudo-radial flow period (Figure 4.4.5) is the fourth and final flow period in the life of horizontal injector with a single transverse fracture. This flow period is eventually reached provided that no flow barriers are encountered.

$$p_{wD} = \frac{h_d}{2F_{cD}} \left(\ln \frac{t_{Df} \eta_{fD}}{r_{wD}^2} + 0.80907 \right) + s(F_{cD}, r_{wD}, h_D) \qquad (4.4.10)$$

where s is the skin factor associated with the fracture conductivity, communication interval and thickness.

The above equations for a single fracture perpendicular to a horizontal injector have been implemented in spreadsheet program and they can be used for parametric studies for CO_2 sequestration via a horizontal well. Figure 4.4.6 shows an example of a horizontal injector with a single fracture. Comparing the injection pressure shown in blue for a horizontal injector without a fracture (or a fracture with low conductivity) with others, one can see that there is a significant injectivity improvement and thus injection economics from a single fracture.

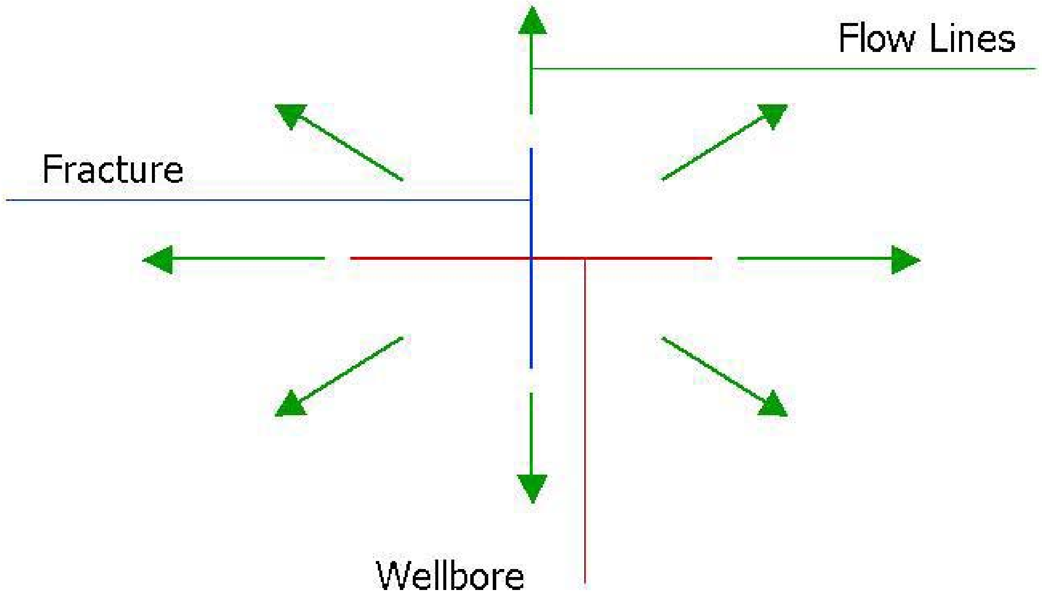

Figure 4.4.5: Pseudo-radial flow for single transverse fracture

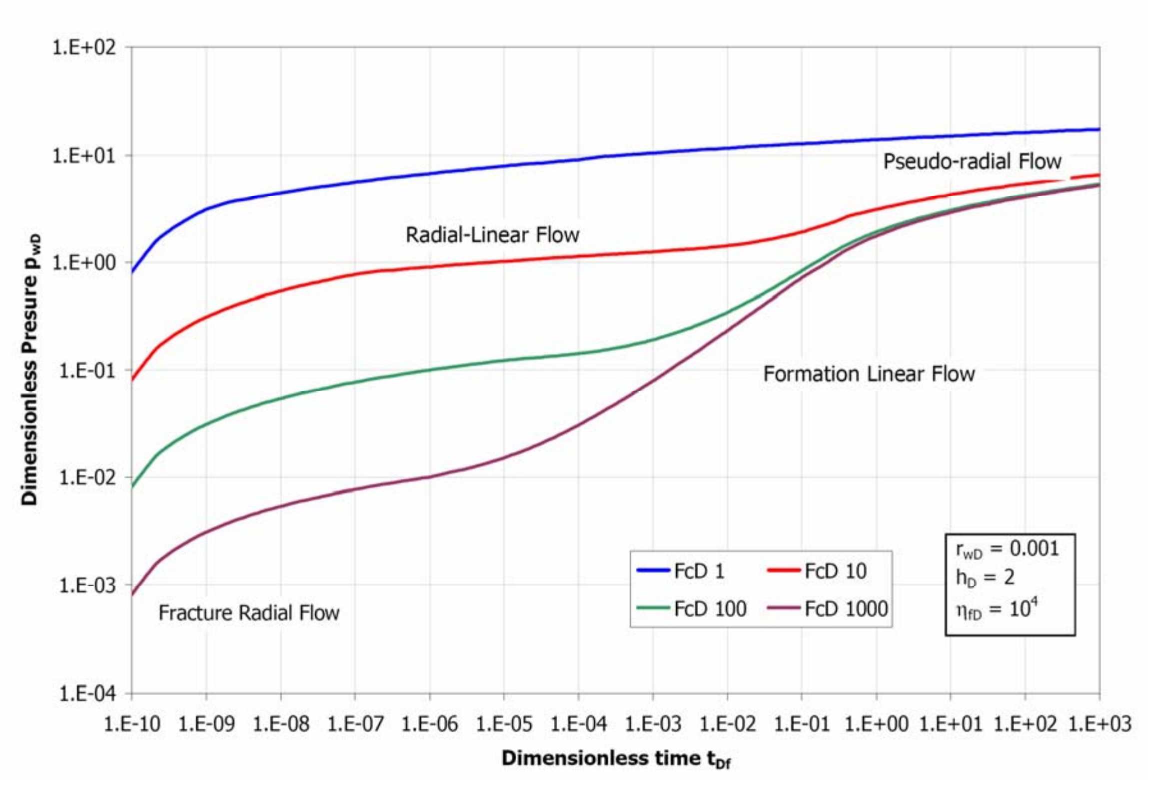

Figure 4.4.6:. Fundamental Flow Periods for Single Transverse Fracture

Injection performance for injection into a horizontal well with multiple transverse fractures (a transverse fracture cuts the wellbore, as opposed to a longitudinal fracture which strikes in the same direction as the well's azimuth) also consists of four injection periods, similar to those for a single fracture.

Like the single fracture scenario, radial flow initially occurs within the fracture as the fractured is filled. To compute the dimensionless pressure response, first calculate the response for a single fracture and then divide by the number of fractures – partitioning it equally – this presumes no frictional pressure drop along the length of the well. This also implicitly assumes that all fractures have the same properties (radius, width and conductivity) and there is no flow interference or communication between fractures.

The formation linear flow period will only be sensed if the fracture conductivity is high. The injection pressure response can be computed from the rate into a single fracture; i.e., the injection rate divided by the number of fractures. It is assumed here that there is no flow interference or communication between fractures.

Pseudo-radial flow may occur around all of the fracture in unison - as seen in Figure 4.4.7a, or around each fracture separately - as in Figure 4.4.7b. Start of the pseudo-radial flow period can be delayed by increasing the distance between each fracture. If the distance is sufficiently large, pseudo-radial flow may develop around each fracture separately. It is not the number of fractures but the horizontal distance (compared to the fracture length) between each fracture that is the controlling factor in the onset of interference.

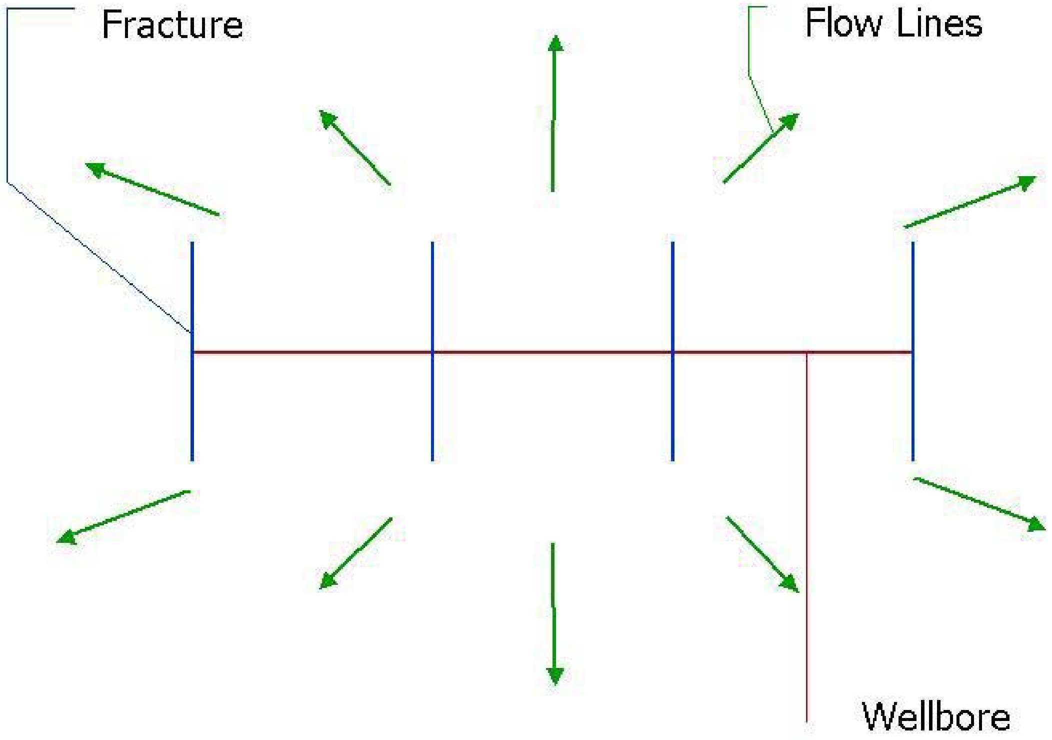

Figure 4.4.7a: Pseudo-radial flow for multiple transverse fractures.

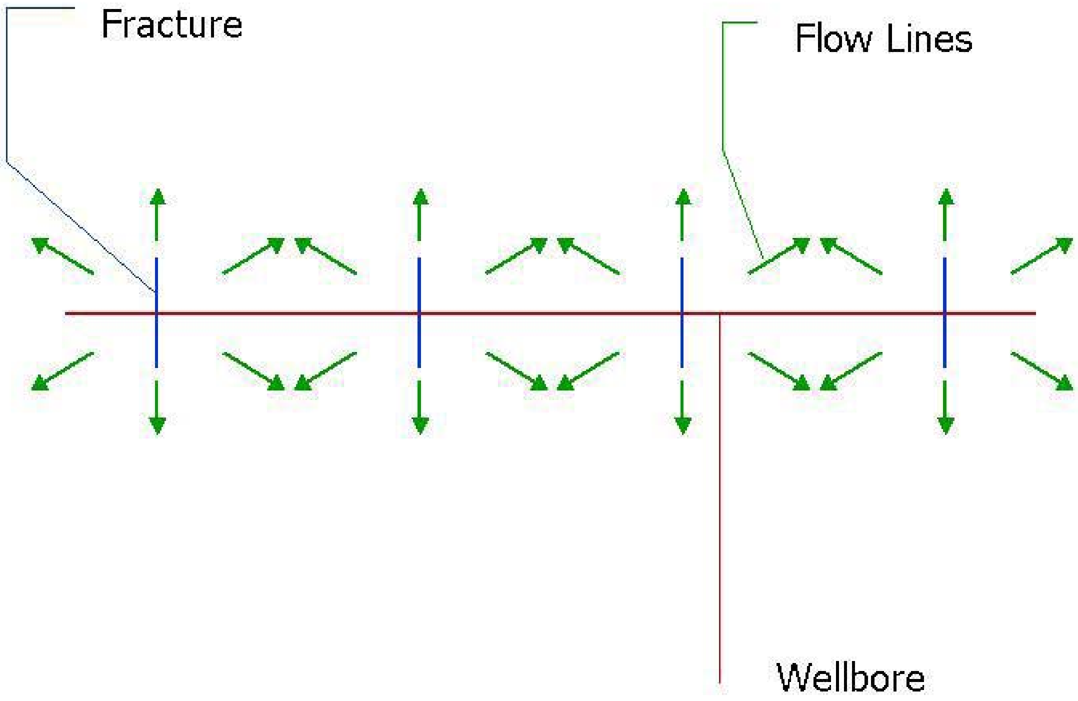

Figure 4.4.7b: Pseudo-radial flow for multiple transverse fractures.

The equations for multiple fractures perpendicular to a horizontal injector have also been implemented and they can be used for parametric studies for CO_2 sequestration through a horizontal well. Figure 4.4.8 is an example indicating how the number of fractures affects horizontal injector performance. However, it should be cautioned that the validity of the analytical solution for multiple fractures may be limited because the interaction between fractures and permeability anisotropy are not considered in obtaining the solution. Numerical methods are often required for horizontal wells with multiple fractures.

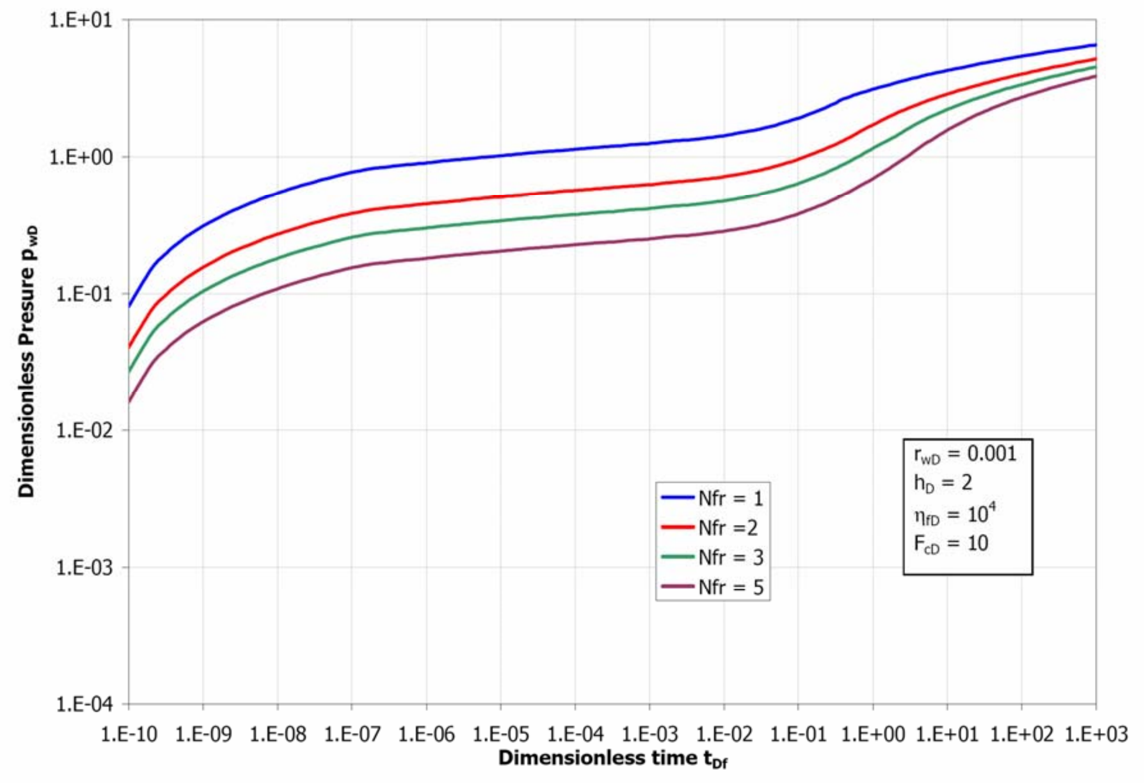

Figure 4.4.8 Impacts of number of fractures on the performance of a horizontal injector.

Numerical Methods

Numerical methods have a wider range of applicability and should be more accurate than the analytical methods if the grid is sufficiently fine. Their drawback is the larger effort required to set up the problem. Use of simulators for horizontal wells is now routine, but it is often done poorly. The important aspects include:

- The grid has to be sufficiently fine, such that the difference between the well pressure and the cell pressure is small. If large cells must be used, the relation between the cell pressure and wellbore injection pressure should be derived numerically.
- Accuracy will be decreased in problems where the permeability anisotropy (horizontal perm k_x versus vertical perm k_y) is not aligned with the coordinate axes, unless models with full permeability tensor treatment are used
- High angle and/or arbitrary trajectory wells pose conflicting requirements on gridding in layered reservoirs, which are very difficult to resolve
- Modeling of wellbore frictional pressure drop may be required in high rate injectors. This feature is also important for competition of fractures.
- Features for modeling operation of smart wells are not provided for in commercial models.

The following presents an example of multiple transverse fractures in a finite drainage area. The geometry of the system is shown on Figure 4.4.9. The well and the fractures are placed symmetrically in the reservoir. The solution was developed by Kuppe and Settari (1998) from computer runs in the range of permeability between 1 and 100 md and odd number of fractures between 1 and 7. Extension of the correlation for the range of k=0.1 to 1000 md and even number of fractures is shown in Figures. 4.4.10 and 4.4.11. The numerical results presented here can be applied to CO_2 injection by converting the CO_2 volume such as million standard cubic feet (mscf) to reservoir barrel (rb) at given bottom hole injection pressure using Table 4.2.

Table 2. CO2 Properties

CO_2 PROPERTIES

Pressure psia	FVF rb/mscf	Viscosity cp
15.000	207.53000	0.02000
500.000	5.49120	0.02252
1000.000	2.36580	0.02474
2000.000	0.077510	0.03300
3000.000	0.49810	0.05200
4000.000	0.42800	0.06600
5000.000	0.40610	0.07600
6000.000	0.38130	0.08400
6500.000	0.37360	0.08750

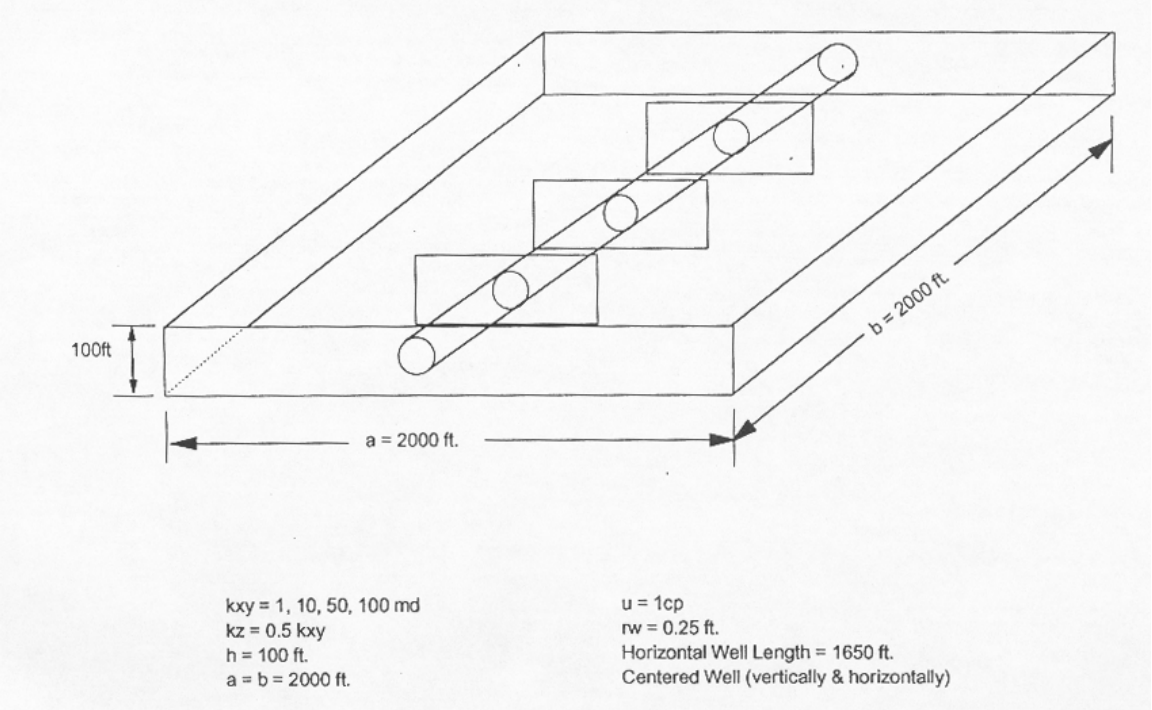

Figure 4.4.9: Multi-fractured well configuration.

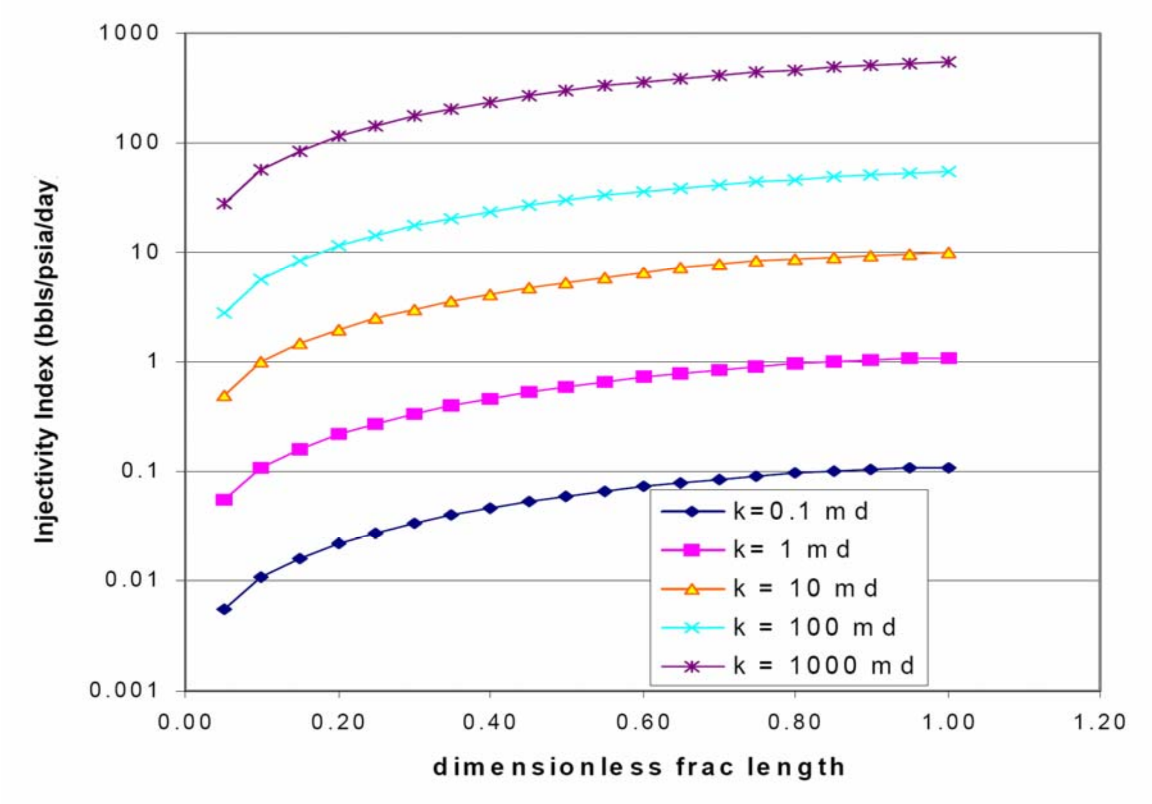

Figure 4.4.10: Permeability range effect on injectivity.

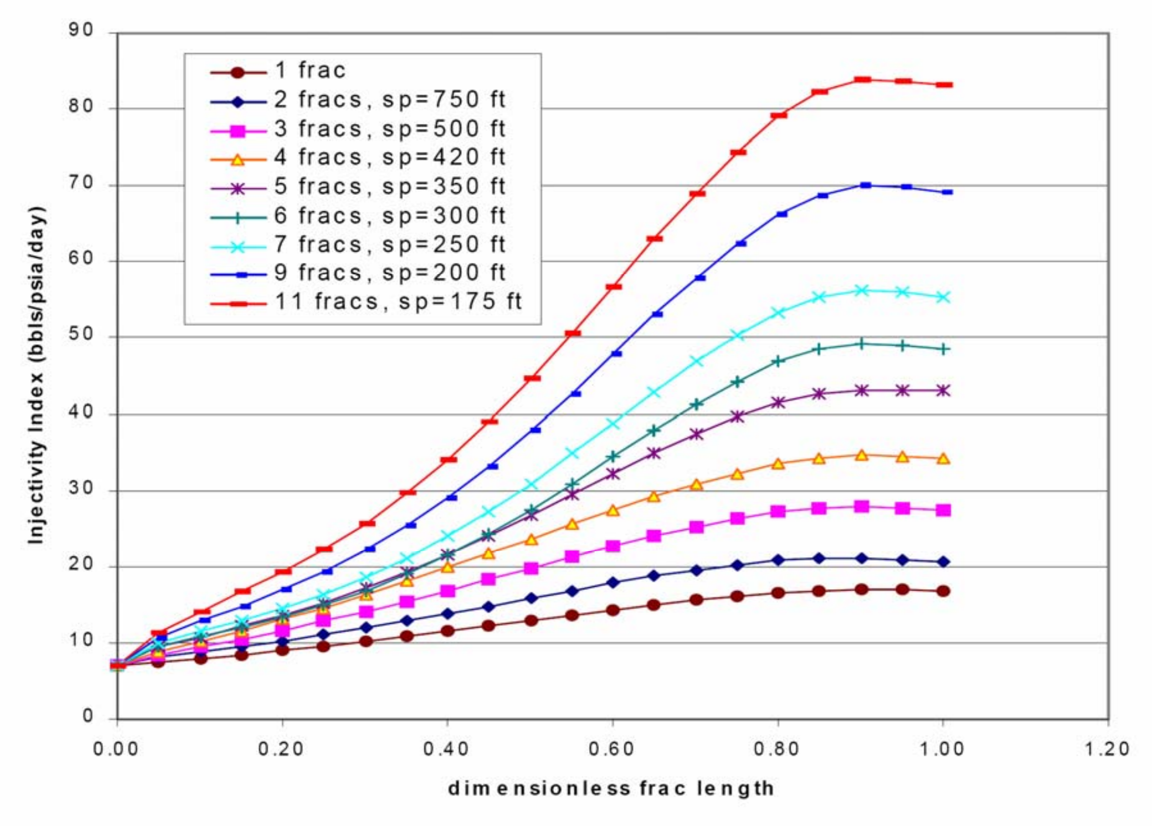

Figure 4.4.11: Number of fractures effect on injectivity.

The need for calculation or prediction of injectivity in horizontal injectors arises from need for predicting the injector performance and the operation economics. The tools and methods available for predicting the performance of horizontal injectors, without considering chemical reactions, are reviewed and summarized. Equations for a single fracture and multiple fractures perpendicular to a horizontal well have been implemented for parametric studies and for estimating injector performance and economics, under the condition that the horizontal permeability is the same as the vertical permeability. Numerical results are also given to show permeability anisotropy effect on injectivity and fracture interaction.

Although it is difficult to provide specific recommendation for each case from this limited case study, some of the guidelines are:

- Be careful with analytical methods - some analytical solutions can have large errors
- In design, use the simplest possible method which will be sufficient to provide realistic answers
- If the method used is not adequate, consider simulation analysis

Task 5.1 Optimize proposed number of wells and surface equipment

A number of different sources were searched in order to select formation suitable for CO_2 sequestration. The data availability and quality is different for different formations. The major goal of the data evaluation process was to select formations that have most data needed for modeling transport of CO_2 in the super-critical state. The critical data for this modeling are the formation depth, thickness, continuity, pressure, temperature, chemical composition of the formation water, and mineral composition of the formation rocks. Also of importance are the existence and continuity of the seal overlaying the formation and the presence of both, carbonate and sandstone deposits suitable for the injection.

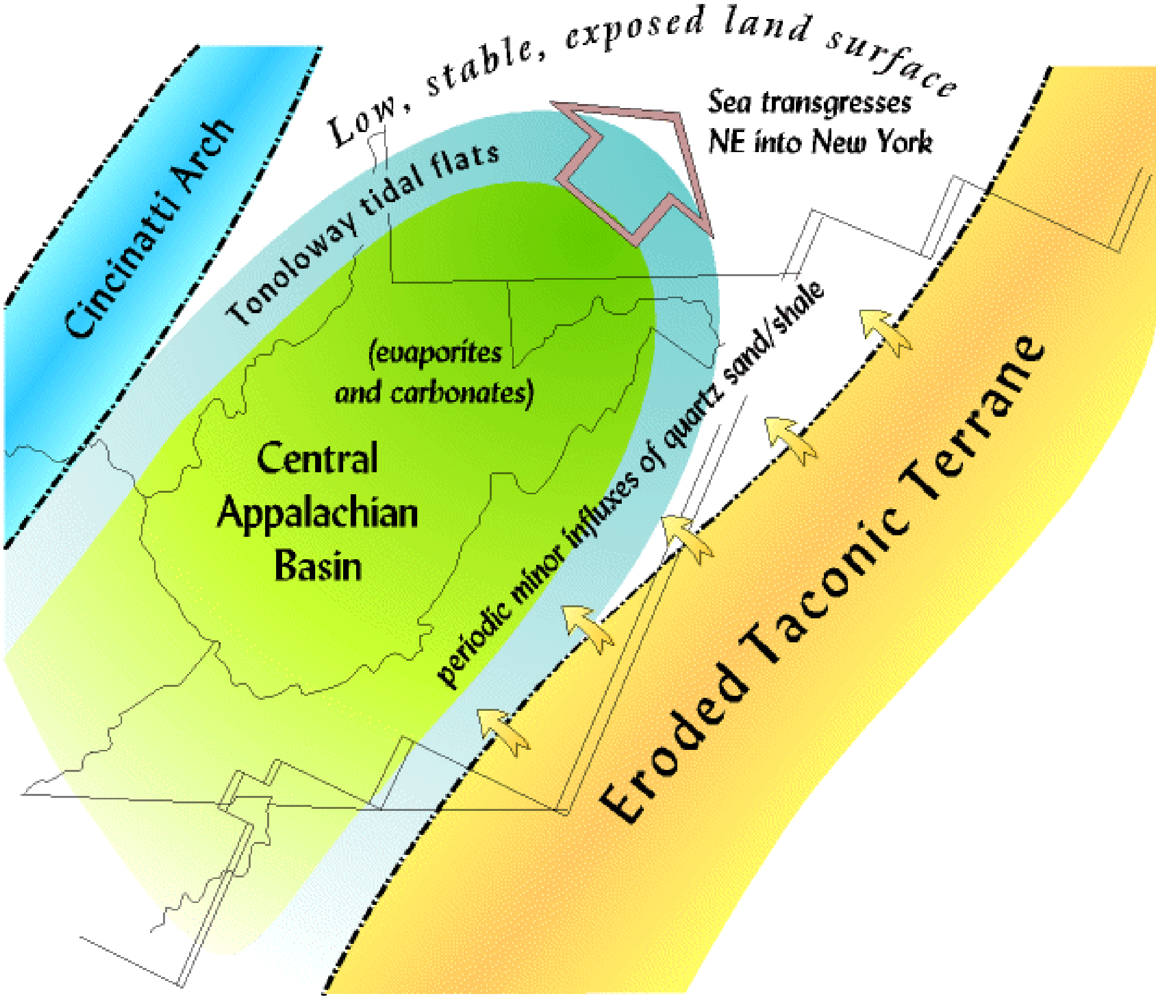

Figure 5.1.1: Central Appalachian Basin

One formation that meets all the criteria is Oriskany formation (sandstone) underlain by the Helderberg Group (carbonates) located in the Appalachian basin of western Pennsylvania, eastern Ohayo, and eastern Kentucky. Besides the availability of the data needed, there are a large number of the potential sources of CO_2 located within this basin (including Pittsburgh/Morgantown/Cleveland vicinity with a large concentration of CO_2-

producing power plants). The Oriskany also has been the principal horizon for brine disposal in western Pennsylvania and it is a proven reservoir for subsurface disposal.

The map of the basin is shown in Figure 5.1.1. The stratygraphic cross-section is shown on Figure 5.1.2.

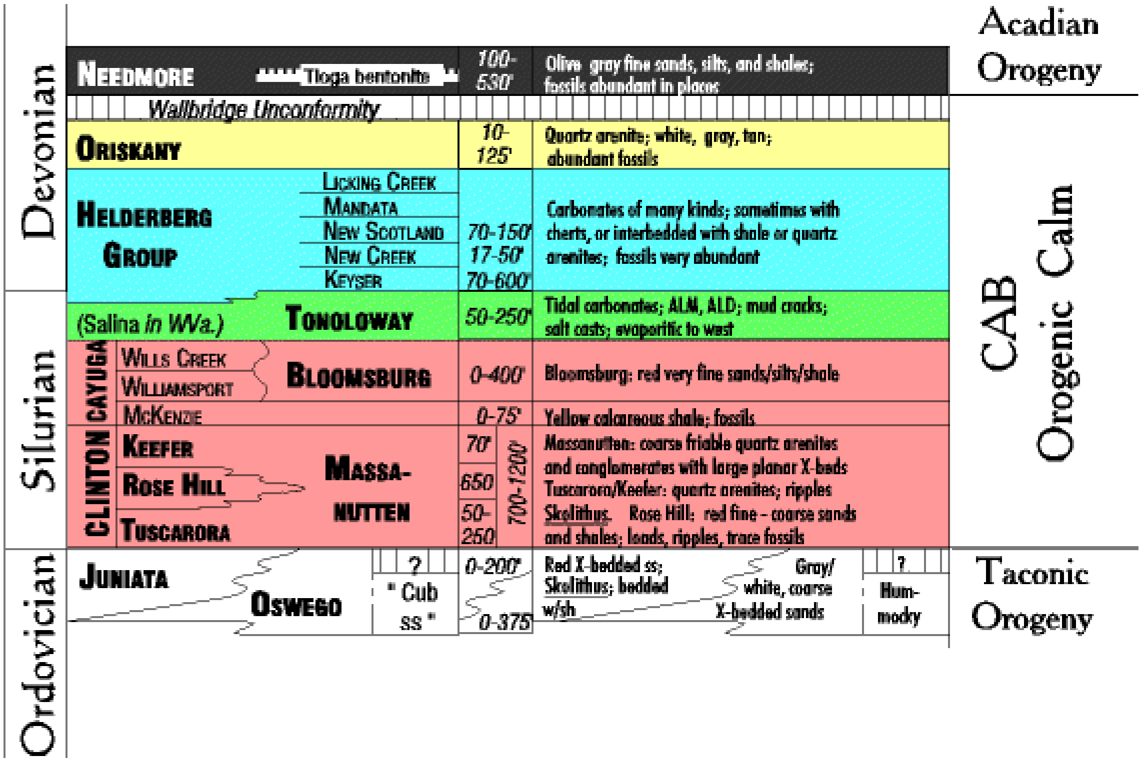

Figure 5.1.2: Stratygraphic Cross Section of the Appalachian Basin

The Oriskany formation depth is more than 800 m within the most of the basin area, except the western edge of it and some patches along its eastern boundary. The hydraulic conductivity of the formation is within an acceptable range within the most of the basin. There are many geophysical logs available for the Oriskany Sandstone interval from which formation permeability can be calculated. The formation thickness is in acceptable range within the central and eastern portions of the basin. In most areas, the formation is of good continuity.

The Oriskany Sandstone is overlain by cherty Onadaga Limestone and/or the Needmore Shale. This interval is somewhat effective as a top seal, but it may be permeable in areas because of fracturing. However, the Onadaga Limestone/Needmore Shale interval is overlain by a thick section of Middle Devonian black shale, which makes an excellent regional confining layer. The top seal has the thickness greater than 100 m within the most of the basin. The most of the production wells are in the western portion of the basin.

The fluid residence times are thought to be very long, on the order of millions of years. The lower geologic section is unable to receive fresh water as recharge or to readily discharge entrapped fluids such as brine. The flow is thought to be negligible in the Oriskany formation.

The temperature versus depth data for the Oriskany Sandstone of the central Appalachian Basin form a definite gradient, such that 63 + 0.0092 Depth = formation temperature (in °F). The temperature is above the super-critical temperature of CO_2 (31.1°C) in the large area of the basin. The pressures follow the hydrostatic gradient of 0.44 psi/ft. As it can be seen from the map, the pressure is above the super-critical pressure of CO_2 (1069.4 psi) in the large area of the basin. The salinity range is from 73 to 354 g/L. The samples were taken from 40 wells located in the central part of the basin.

Porosity ranges from less than 2 to 12 percent. Within the large area of the basin, the porosity range is from 7 to 12%. This may provide acceptable injectivity, especially when combined with fracturing. The chemical analyses are available for 40 well located in the central part of the basin. This includes the following measurements: conductivity; density; Eh; pH; Li; Na; K; Mg; Sr; Ba; Mn; Fe; Cu; Zn; Pb; alkalinity; SO4; F; and Cl.

The Oriskany is typically composed primarily of quartz (~85 percent), with 11 percent calcareous minerals and shell and about 4 percent (or less) plagioclase, orthoclase, and microcline. Heavy minerals typically compose 0.2 percent of samples analyzed

The mineralogical composition is available for 94 wells located mostly along the eastern boundary of the basin. The minerals presented are: quartz; plagioclase; orthoclase; microcline; chert; tourmaline; zircon; leucoxene; limonite; rutile;pyrite; chlorite; amphibole; hypersthen; garnet; kyamite; ilmenite; biotite; and Celestine.

The location of the potential site was searched based on the critical pressure and temperature needed to maintain CO_2 in super-critical state under the ambient formation conditions. The critical with regard to the pressure depth is 741 m and the critical with regard to the temperature depth is 827 m. Consequently, the critical depth is 827 m.
The other search criteria were: formation continuity; the formation thickness (greater than 25 m); the top seal continuity; suitable permeability and porosity; distant location from the hydrocarbon production areas. Based on this analysis, the central eastern area was selected (Figure 5.1.3).

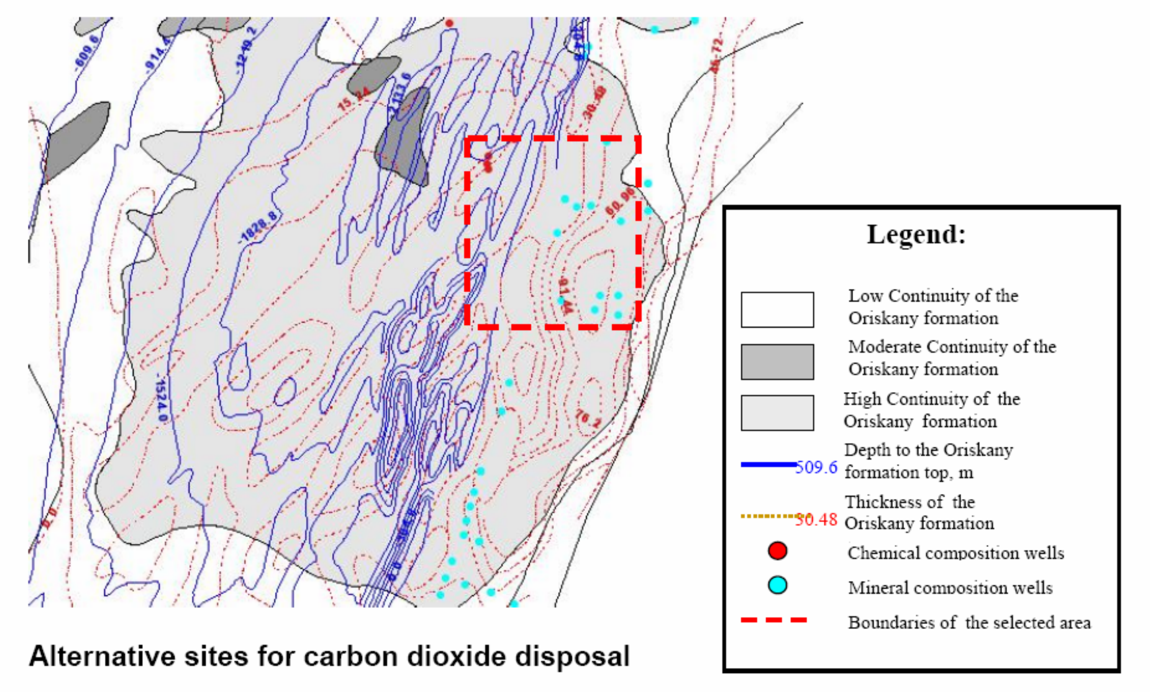

Figure 5.1.3: Location of the central eastern area suitable for co sequestration within the central part of the Appalachian basin

The potential site proposed for carbon dioxide disposal above was located in the middle part of the Appalachian Basin. This site has a number of advantages associated with it. One of these advantages is the high density of the carbon dioxide emitting sources in the close vicinity of the site (Figure 5.1.4). The disadvantages of this site are that it is located in the highly populated East Cost area and within the very complex political, economic, and regulatory framework. Two alternative sites were identified to overcome these disadvantages. The first alternative site is located in San Juan Basin and the second site is located in Palo Duro Basin (Figure 5.1.4). The short description of these alternative sites is provided below.

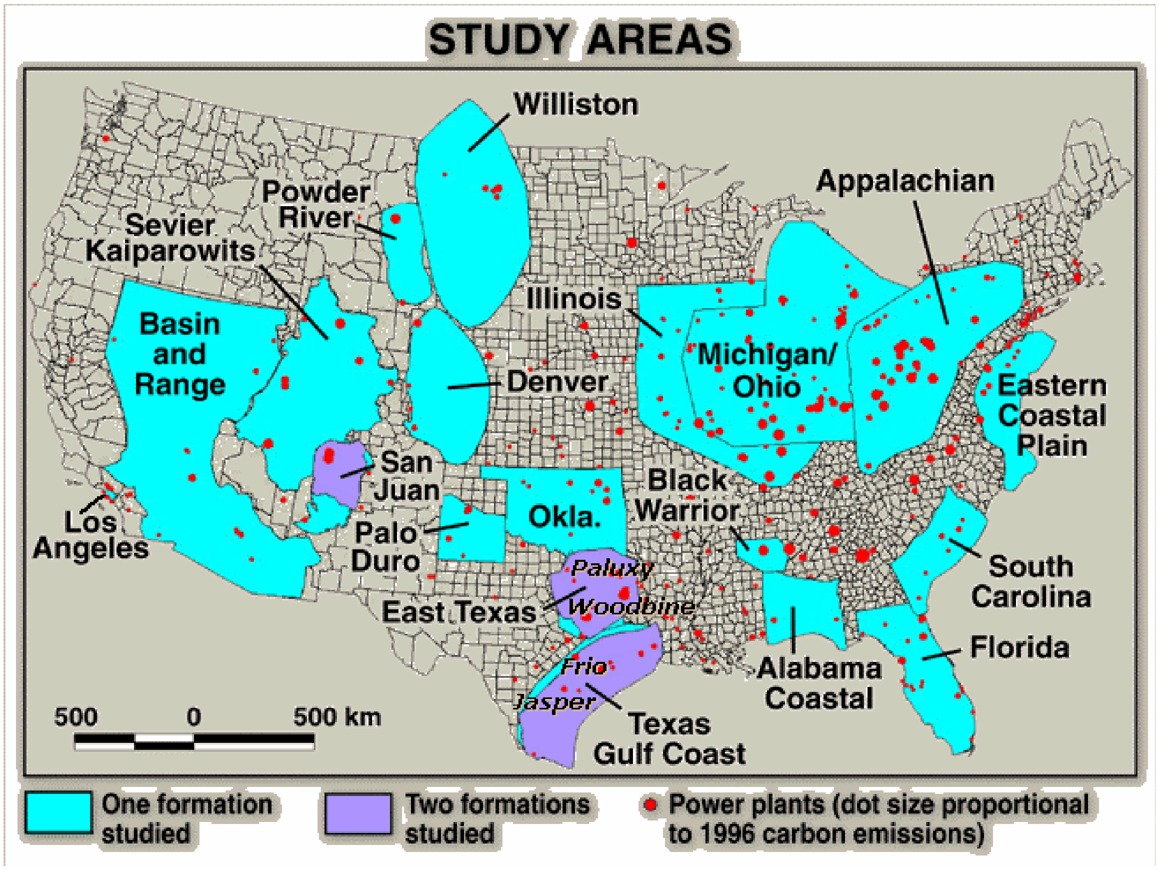

Figure 5.1.4: Location of the basins suitable for carbon dioxide disposal and carbon dioxide emitting sources

The San Juan basin is located mostly in New Mexico (northwest corner). Two carbon dioxide emitting sources are located in the northwest area of the basin (Figure 5.1.4). A formation defined as a suitable formation for carbon dioxide disposal is sandstone Morrison formation. It is possible that a carbonate formation (such as a Bridge Creek limestone formation) may be suitable for disposal as well. However, this subject was not studied yet. The map and cross section of the San Juan basin are shown in the Figures 5.1.5 and 5.1.6.

The sandstones of the Morrison formation are characterized as immature reactive sandstones. This makes the Morrison formation a good target for carbon dioxide disposal. A confined aquifer is associated with the lower portion of the Morrison formation. The formation is overlain by the low permeable tuffaceous mudstone.

The formation depth is greater than 800 m within the most of the basin area. The maximum formation depth is 3200 m in some localized areas in the eastern part of the basin. The hydraulic conductivity was estimated at a number of locations along the western edge of the basin. The range of the formation permeability is from 5 to 500 mdarcy
The formation thickness is from 200 to 300 m within the most basin. It is from 300 to 400 m within the central part of the basin and from 100 m to 200 m along the south edge. The information on the top seal thickness available from the database concerns only a small

area located in the southern part of the basin. The flow in the Morrison formation aquifer is from the recharge areas rimming the San Juan Basin toward the center of the basin. The temperature is in the range from 20° to 50° C within the most of the basin. In some areas it is up 80° C.

No data is available from the database on the formation pressures. The salinity range is from 0.5 to 10 g/L. Mean porosity is 13.5 percents. The water is of calcium bicarbonate type where concentrations are less than 2 g/L.

The coarser grained sandstone consists mostly of quartz, microcline, sodium plagioclase, and lithic fragments of various types. The finer grained beds often consist of fine-grained sandstone, mudstone, and rare limestone nodules and lenses, but locally they are greenish-gray smectitic.

The cap seal has similar lithology, but the ratio of coarse-grained beds versus finer grained material is significantly lower. Also, tuff beds containing a variety of authigenic minerals constitute a significant fraction of the cap seal. These authigenic minerals include mixed-layer illite-smectite, clinoptilolite, analcime, potassium feldspar, albite, and silica in the form of quartz and chalcedony, and calcite. Much of the mudstone in the cap seal is bentonitic

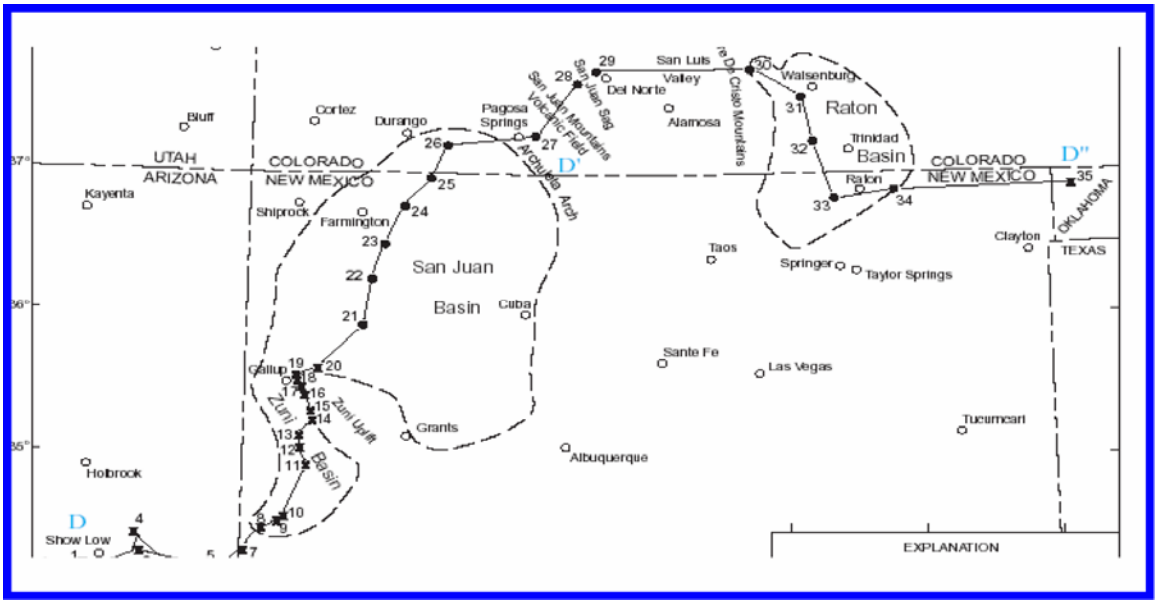

Figure 5.1.6: Cross Section through the Sun Juan Basin

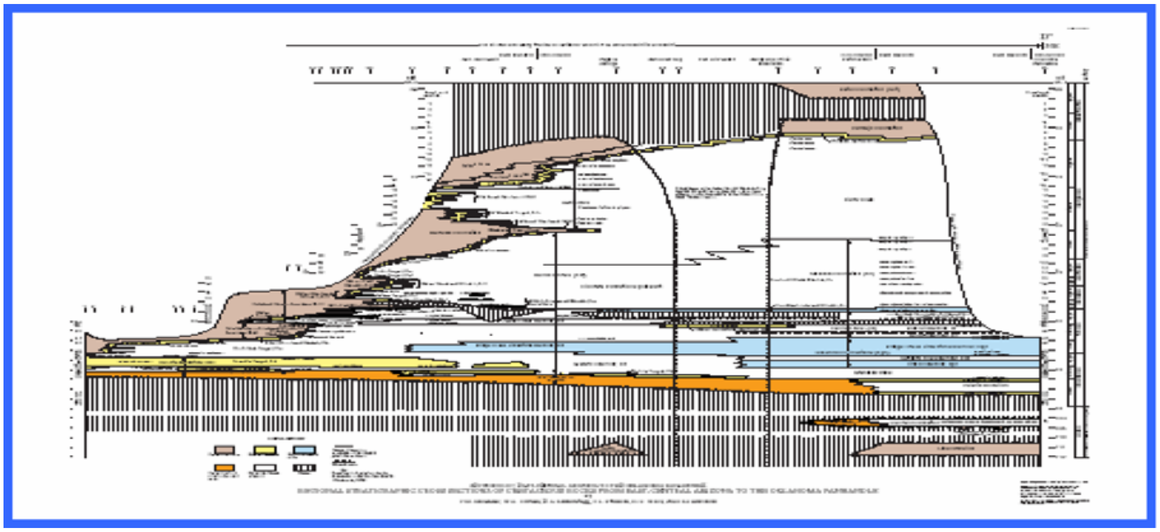

Figure 5.1.7: Location of the San Juan Basin

The eastern part of the Palo Duro basin is located in New Mexico and the western part is located in Texas. Three carbon dioxide emitting sources are located in the basin (Figure 5.1.8). A formation defined as a suitable formation for carbon dioxide disposal is sandstone Granite Wash formation. It is possible that a carbonate formation overlaying the Granite wash formation and a carbonate formation underlying it may be suitable for disposal as well. However, this subject was not studied yet. The cross-section of the Palo Duro basin is shown in the Figure 5.1.8.

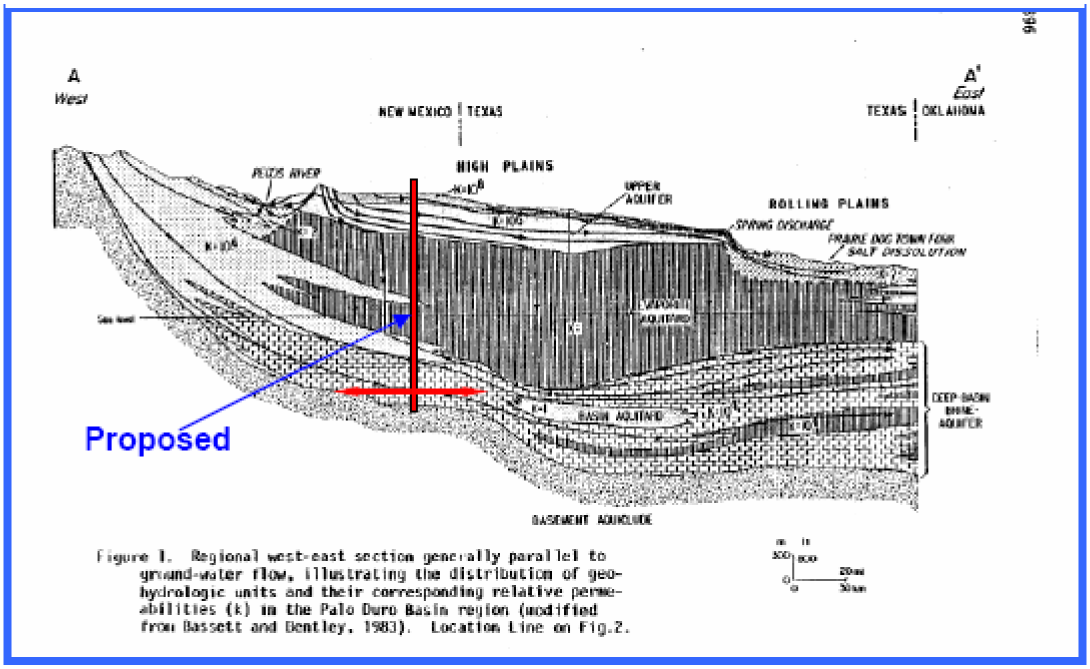

Figure 1. Regional west-east section generally parallel to ground-water flow, illustrating the distribution of geohydrologic units and their corresponding relative permeabilities (k) in the Palo Duro Basin region (modified from Bassett and Bentley, 1983). Location line on Fig. 2.

Figure 5.1.8: Cross Section through Palo Duro Basin

The sandstones of the Granite Wash formation are characterized as arkosic sandstones. A confined aquifer is associated with two carbonate formations and sandstone (Granite

Wash) formation. The formation is overlain by the thick evaporates that represents the regional aquitard.

The formation depth is greater than 800 m within the most of the basin area. The maximum formation depth is 3200 m in the southwest part of the basin. The hydraulic conductivity was estimated in a few locations. The range of the formation permeability is from 1 to 150 mdarcy. The formation thickness is from 500 to 1000 m within the most basin. It is greater than 1000 m within the southeast corner of the basin. It is smaller than 500 m in some localized areas along the basin edges.

The top seal thickness is from 200 to 500m within the most of the basin. It is less than that along the eastern basin edge. The flow in the deep brine aquifer is from west-southwest to east-northeast. Estimated travel times from the westernmost recharge area in New Mexico to the eastern boundary range from 1.2 to 4 Ma, depending on the flow path and average porosity of the different units.

The temperature data are not available from the database. The 0.403 psi/ft characterizes the slope of the pressure function for the deep brine aquifer. The salinity range is from 100 to 200 g/L. Little data are available on porosity from the database. The data on water chemistry are not available from the database.

Most of the Granite Wash falls into the categories of arkose or lithic arkose, with smaller percentages being feldspathic litharenite and minor amounts of subarkose. These immature and tuffaceous sandstones have the potential to react with high-CO2 brine. The mean value for the Morrison is near 13.5 percent calcium bicarbonate type where concentrations are less than 2000 mg/L. Depth in most areas is 200-300m. In central part it is 300-400 m, while on the southwest edge it is 100-200m. Depth to the top is in most places more than 800 m. The comparison of the two alternative sites is provided below (Table 5.1).

The comparison of the CO_2 emitting sources located in San Juan and Palo Duro basins is provided in Table 5.2. These data are from the BEG database and reflect the CO_2 emissions in 1996. 656 sources are described in the database. The minimum emission rate was 22 tons/yr in 1996. The maximum emission rate was 5,570,270 tons/yr. The mean emission was $7.57*10^5$ tons/yr. The probability of exceeding the annual CO_2 emission rates is shown in Figure 5.8. The median emission in 1996 was $3.58*10^5$ tons/yr.

Comparison	San Juan	Palo Duro
Advantages	Located in New Mexico The aquifer has low salinity and greater potential to dissolve CO2 The sandstone is highly reactive There are significant sources of CO2 located next to each other	The cap seal has great continuity and thickness within the most of the basin The carbonate formations are suitable for CO2 disposal The sandstone and carbonate formations are well defined
Disadvantages	The cap seal is not well defined within the basin. The suitability of the carbonate formations is not clear. The geology of the basin is complex	The major part of the basin (suitable for the disposal) is located in Texas. The deep aquifer has high salinity – lower ability to dissolve CO2 The sources of CO2 are spread in the different part of the basin. The sandstones have moderate reactive capability

Table 5.1.1: Alternative Site Comparison

Basin	Plant Name	Plant Location	Emission, tons/yr	Probability of Exceeding, %
San Juan	San Juan	NM	3215180	4
	Four Corners	NM	3437603	3
	Escalante	NM	304296	54
Palo Duro basin	Moore County	TX	11336	94
	Tolk State	TX	1801290	15
	Holly Ave	TX	94649	7
Total			496474187	

Table 5.1.2: Comparison of Carbon Dioxide Sources

Two plants located in San Juan basin are very large sources (only 3-4% of all the sources are larger). One plant located in San Juan basin is close to the average source. Two plants located in Palo Duro basin are small sources (75-94% of all the sources are larger). One plant located in Palo Duro basin is relatively large. All the plants in Palo Duro basin are located in Texas. Only Talk State plant (large source) is located in the close vicinity to the boundary between New Mexico and Texas (thus, the source is in Texas and the injection may be in New Mexico).

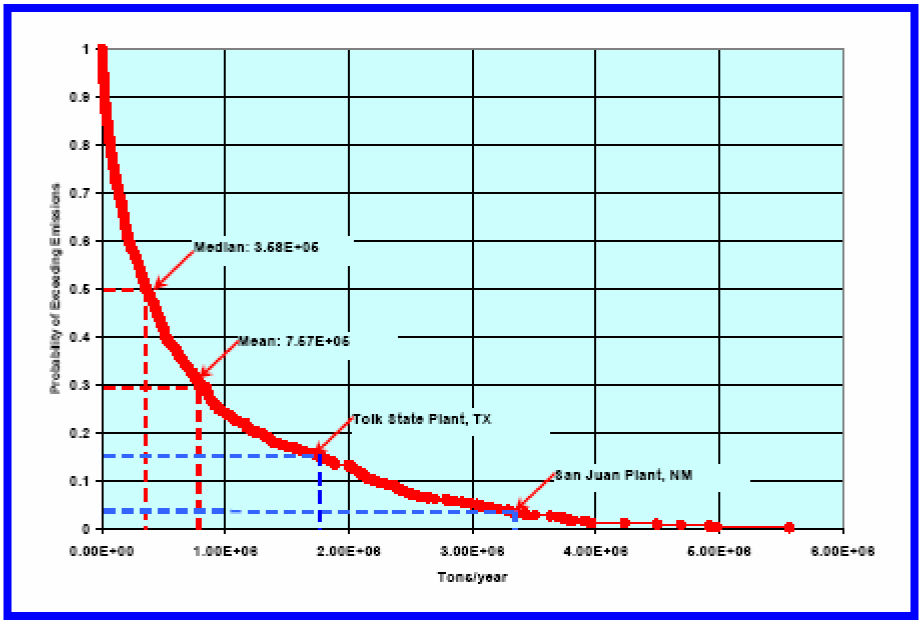

Figure 5.1.9: Probability of Exceeding of the Annual Emission Rates of Carbon Dioxide

For a given injection rate of 12,600 m^3/day as required by a 800 MW power plant, an analysis was performed to determine the number of required injection wells depending on process. In the analysis we consider the existence of an impermeable stress barrier, hence the CO_2 will only flow through the sequestration zone and the bottom-hole injection pressure is limited by the minimum horizontal stress of the barrier. The required number of wells was determined from either radial flow equations or flow equations of fractured injectors. The drilling cost, capital expenditure, is considered as a lump sum that is accounted for in the first year only, a more thorough analysis would take into account both the tangible and intangible value of the asset and spread it over a given number of years but for our purposes the calculation as it stands should suffice. Both the maintenance and man power costs, operating expenditure, are considered to be fixed amounts that are deducted on a yearly basis. At the end of a well life an abandonment cost is considered, capital expenditure. Another operating expenditure associated with the process is power, this makes up the largest part of the operating costs. Finally in cases where a hydraulic fracturing stimulation is required an extra cost is added to the drilling cost for the fracture job, this again comes under capital expenditure. Finally all the costs are summed across there respective years and a discount rate considered to establish the Net Present Value of the option.

In the first scenario we consider the viability of using a vertical well operating under matrix conditions. The initial skin in this case is present due to formation damage from the drilling process and the type of completion used and has an adverse effect on the injection process. It was found that a minimum of four wells were required to completely dispose of the CO_2 generated from an 800 MW power plant. Furthermore it was found that wells could only operate under these conditions for five years at which point another four wells would be drilled, at another remote location, requiring a new compressor and pipeline connections. With eight wells now operational the both maintenance and man power costs are increased, but the injection rate can be decreased significantly among the eight wells hence they would last for another seven years at which point another four wells would be added, and the process is repeated. No further wells would need to be added for the twenty year period of analysis.

In the second scenario we consider the case of a vertical well that has initially been stimulated using a hydraulic fracturing technique. The effect on the injection is prominent, the previously adverse skin effect is overcome by the fracturing and the well's daily capacity is significantly increased for the same injection pressure. In this case only two wells are needed and the wells will operate for the duration of the twenty years.

Several cases were considered for the horizontal injector although a complete economic analysis was not carried out. From an engineering point of view horizontal injectors would improve injection dramatically, and in most cases only one horizontal well with fractures is required. Consequently, this can greatly improve the economics of CO_2 sequestration.

Operation	**Value**	**Unit**
Drilling	2.00	mm$
Hydraulic Fracturing	0.30	mm$
Abandonment	0.40	mm$
Compressor	3.00	mm$
Retrofit	0.30	mm$
Pipeline	1.00	mm$/mile
Distance	2	mile
Power	10.00	cents/KWhr
Maintenance	0.05	mm$/year/well
Labor	0.12	mm$/person/well

Table 5.1.3 Model Input Parameters

Table 5.1.3 shows the input parameters considered for the model. All dollar values are in millions of dollars (mm$).

Figure 5.1.3 shows the yearly expenditure for both the matrix injection in red and the fractured injection in blue. Note that for the matrix expenditure there are several spikes denoting the repeated drilling phases discussed earlier and that the final abandonment cost is much greater than that for fractured injection since the number of wells to be disposed of is considerably larger. Note the increase in operating costs for the matrix injection after each set of new wells is drilled this is caused by the increase in both man power and maintenance costs for the added wells. The figure also shows the Net Present Value of each option, note the net present value of the matrix injection is twice that of the fractured injection and that the value is negative hence fractured injection proves a more economically viable option.

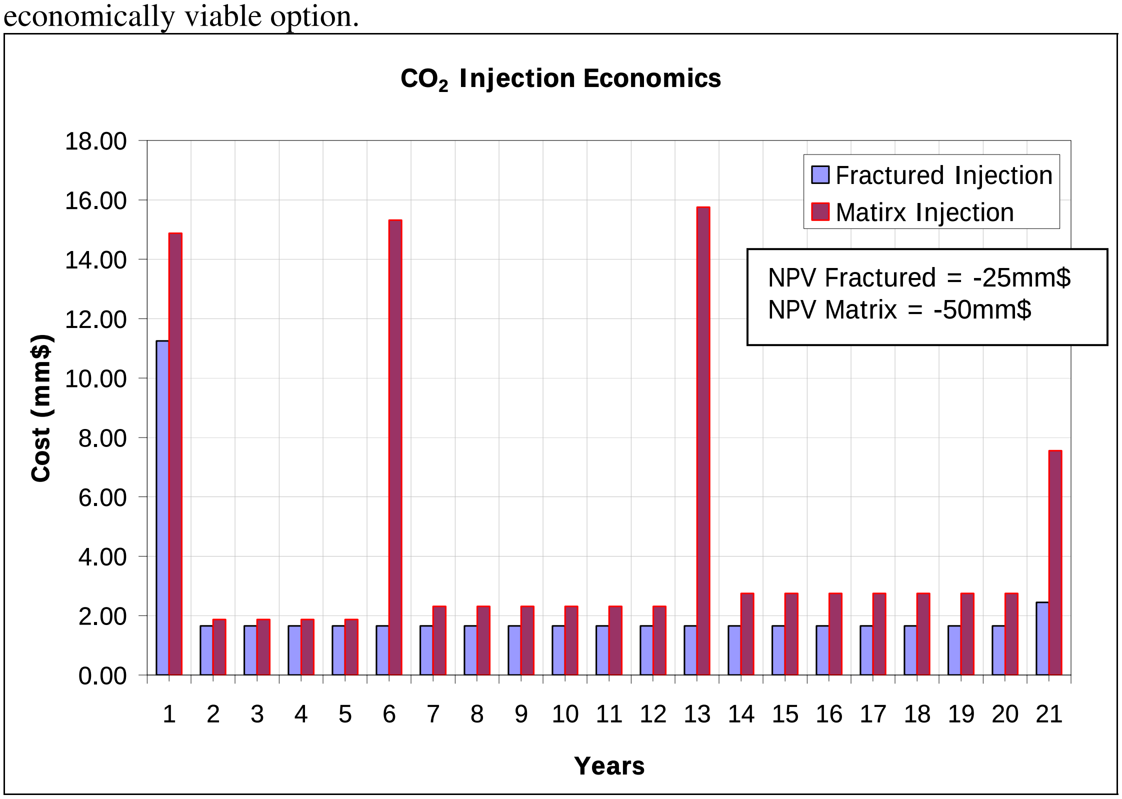

Fig.5.1.10 yearly expenditure

Table 5.1.4 and 5.1.5 show the cost of each option, per year and per ton respectively. Again the cost of matrix injection is twice that of fractured injection.

	Cost (mm$)/Year	
	Fractured	**Matrix**
Drilling	0.2	1.2
Fracture Job	0.03	0
Abandonment	0.04	0.24
Compressor	0.15	0.45
Pipeline	0.10	0.3
Power	1.5	1.5
Maintenance	0.11	0.46
Man Power	0.13	0.55

Total	2.25	4.71

Table 5.1.4: Cost Per Year

	Cost (cents/ton)	
	Fractured	**Matrix**
Drilling	4	22
Fracture Job	1	0
Abandonment	1	4
Compressor	3	8
Pipeline	2	5
Power	27	27
Maintenance	2	8
Man Power	2	10
Total	41	86

Table 5.1.5: Cost per Injected Ton

Table 5.1.6 shows the injection rate and pressure for a single well of each of the listed types. The figure also shows the number of wells needed. The total disposal volume is 12600 m^3/day and the injection pressure cannot exceed 6895 kPa.

Injector		**Number Needed**	**Rate (m^3/day)**	**Pressure (kPa)**
	Matrix	4	3595	6895
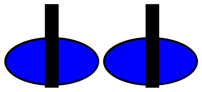	Fractured	3	9241	6895
	Horizontal (1219m No fracture)	1	12600	6827

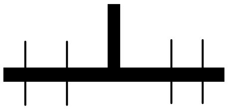	Horizontal (1219m fracture 4)	1	12600	2177
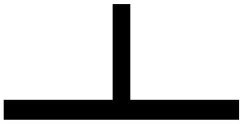	Horizontal (610m No fracture)	2	10456	6895
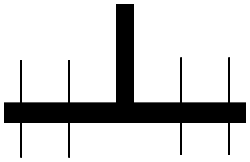	Horizontal (610m 4 fractures)	1	12600	2315

Table 5.1.6: Injection Rates and Pressures

Task 5.2 Preliminary cost estimate for a complete installation

The role of injection well costs for sequestration of CO_2 was briefly explored, starting with base-case data from the Battelle report (Smith et al 2001) on sequestration economics. The following table summarizes the results.

Summary of costs associated with injection wells and injection site compressors (\$/ton of CO_2)	
Battelle base case	\$1.60
Battelle base case at 12% interest instead of 4.1%	\$1.71
Well costs reduced to 60% of initial assumptions	\$1.50
Well costs reduced to 10% of initial assumption	\$1.25
Zero well costs	\$1.20

The following assumptions were made:

- 800 MWe coal fired plant producing 7.27 million tons per year of CO_2
- 10 million dollar cost for injection wells - 10 wells at 1 million each
- Project life 30 years
- DCF interest rate 12%, no taxes
- Wells replaced at year 10 and 20 with 5%/yr inflation on purchase costs
- No salvage value or site closure costs
- CO_2 delivered to well site at 1000 psia and then compressed to 3000 psia, an assumption in the Battelle report
- 10 million dollar compressor costs, with compressor replacement at year 15, with 5%/yr inflation on purchase cost.
- 5¢/Kw-hr electric power for compressor
- 15%/yr of investment cost for maintenance and labor.

This above calculation indicates that incremental cost for CO_2 sequestration costs associated with injection well and fracturing costs is relatively small compared to other costs associated with CO_2 sequestration from conventional coal fired power plants.

Task 5.3 Review cost of proposed technologies to increase the injectivity of CO_2 sequestration in relation to other technologies

As has been reported earlier, the estimated costs for CO2 sequestration by injection into geological formations are $0.41-0.86/ton**.** A variety of other techniques (Heddle et al 2003, Murray 2000) have been proposed for sequestration of carbon from reforestation to injection to deep sea aquifer and production of methane from coal mines. The costs of these techniques can vary widely for the same method depending upon the assumptions used. What is reported here for comparison is the average and best values based on optimistic assumptions for several types of carbon sequestration.

Technique	Average Cost/Ton	Best
Fractured well	0.41	N/a
Matrix of wells	0.86	N/a
Reforestation*	35	1
Deep saline aquifer	2.93	1.14
Methane production	(5.59)	(25.72)
Enhanced Oil Recovery	(12.21)	(91.26)
Ocean pipeline	5.53	2.90
Depleted oil reservoir	3.82	1.21
Depleted gas reservoir	4.87	1.20

As can be seen from the above table, the method presented in this study performs better than all other techniques that do not produce a sellable product. The relatively low cost of reforestation or other biomass sequestration techniques are limited by their low capacity and increase rapidly as required sequestration capacity increases. The economics of techniques that produce sellable produces depend strongly upon market price of the produces produced, and under worst case scenarios result in costs higher than those predicted for the methods presented in this study.

A limitation of cost analysis in this study is that the analysis is based on current costs and does not try and account for variations in future costs. However, the assumptions used to predict future economics have a large impact on the results and seem relatively arbitrary, so that level of analysis was not performed.

Summary and Conclusions

Based on the two-phase numerical model described in Task 1.2, it is hypothesized that:

- Results indicate that, as a CO_2 sequestration site screen criterion, the suitable geological formation should have a large permeability, preferably over 100 mD.
- For low permeability formations, hydraulic fracturing is necessary to achieve reasonable sequestration rate. Appropriate fracture length depends on formation permeability. The effectiveness of vertical fractures in enhancing gas injectivity increases as the reservoir absolute permeability decreases.
- There must be a minimum fracture length required to significantly enhance gas injectivity above which the improvement will be limited.
- As a CO_2 sequestration site screen criterion, it is advantageous to choose aquifers with low water salinity for CO_2 sequestration operations.

In Tasks 1.4, 1.6 and 1.9 significant improvements were made to the simulations. These improvements allowed for better modeling of viscous fingering, leak-off rates and reduction/improvements in permeability caused by movement of fines and/or proppant materials. By validating these models with experiments like those performed in Tasks 1.7 and 2.3, the results of both continuum-level (Task 1.10) and mesoscale (Task 2.1) simulation codes were improved. These advances should allow for a better understanding of the complex interactions between fluid and formation properties, both during the initial fracturing and during CO_2 injection. Work still needs to be done on incorporating the chemical composition changes which would occur during injection.

Using NMR techniques developed as part of Tasks 3.2, 4.2 and 4.3, the T_2 responses of the shales studied showed that the petrophysical properties of the geological formations could be determined using fairly standard NMR well bore instrumentation. These procedures allow both the initial evaluations of a formation's suitability in terms of storage capacity and seal integrity, and the property changes caused to permeability and porosity as CO_2 is injected into the formation. The dynamic property can be determined from laboratory experiments performed on core samples gathered during the initial well drilling, and the initial properties can be gathered as part of a standard well logging. These additional costs are small compared with the cost of drilling the wells and those associated with the CO_2 sequestration operations as shown in Task 5.2.

Finally, the cost analysis showed that the cost of CO_2 sequestration was \$0.41-0.86/ton, which is considerable less than the target of \$10/ton. These techniques would be most economical if used to sequester CO_2 at the point of generation before it is released into the atmosphere. This means that it best location would be at or near power plants. Costs increase dramatically if the CO_2 has to be extracted from the atmosphere, but this is a common problem with many sequestration methods.

One major problem with all the simulations was a lack of resolution in 3-d simulations. As computer systems keep improving, it should be possible to solve these problems at sufficient resolution within the next three to six years.

Besides increases in computing capability, better understanding of the chemical dynamics that occur during CO_2 injections in shales and the complex dynamics of dissolution and precipitation on porosity and permeability are areas that could use further study. Finally incorporating these into existing reservoir simulations would greatly improve the ability to effectively use this method in addition to providing benefits to traditional uses like enhanced oil recovery.

REFERENCE LIST

Akkurt, R., and R. Cherry, 2000, NMR well logging. OGCI, Houston, p212.

Amyx, J.A., D.M. Bass Jr., and R.L. Whiting, 1960, *Petroleum reservoir engineering*. McGraw-Hill Book Company, Inc., New York, p610.

Babu, D.K. and Odeh, A.S., 1989 "Productivity of a Horizontal Well," SPE 18298, SPE Reservoir Engineering.

Bachu, S., Gunter, W.D., and Perkins E.H. 1994. "Aquifer disposal of CO_2: hydrodynamic and mineral trapping" *Energy Conversion and Management*, **35** 269-279.

Basan, P.B., B.D. Lowden, P.R. Whattle, and J.J. Attard, 1997, "Pore-size data in petrophysics: a perspective on the measurement of pore geometry" In M.A. Lovell and P.K. Harvey (eds.), *Developments in petrophysics*, Geological Society, London, Special Publication, **122**, 47-67.

Bower, K. and Shuler, P.J.:1989 "Carbon Dioxide Injection and Resultant Alteration of Weber Sandstone ((Pennsylvania-Permian), Rangely Field Colorado," paper SPE 19875 presented at the 64th Annual Technical Conference and Exhibition of the Society of Petroleum Engineers held in San Antonio, TX.

Brindley, G.W., and G. Brown (eds.), 1984, *Crystal structures of clay minerals and their X-ray identification*. Mineralogical Society, London, p495.

Buijse, M.A., 2000 "Understanding wormholing mechanisms can improve acid treatments in carbonate formations," *SPE Prod. & Facilities*, 168-175, August.

Carbon Sequestration: A Better Alternative for Climate Change?, Maryland School of Public Affairs, 1999 (http://www.puaf.umd.edu/faculty/papers/nelson/carbseq/pdf/)

Capuano, R.M. 1990. "Hydrochemical Constraints on Fluid Mineral Equlibria during Compaction Diagenesis of Kerogen-rich Geopressured Sediments" *Geochim et Cosmochim. Acta* **54**, 1283-1299.

Coates, G.R., L. Xiao, and M.G. Prammer, 1999, NMR logging principles and applications. Halliburton Energy Services, Houston. p234.

Corey, A.T.: "The Interpretation between Gas and Oil Relative Permeability," *Producers Monthly*, 38-41 (November 1954).

Czernichowski-Lauriot, L., Sanjuan, B. Rochelle. C., Bateman, K., Pearce, J. and Blackwell, P. 1996 Inorganic geochemistry. In: Holloway, S. (ed) The Underground Disposal of Carbon Dioxide. Final Report of Joule II Project Number CT92-0031, Chapter 7.

Davis, L.A., 2003, Personal communication. Pseudo-intrusion model, porosity density functions. IDL routine, and Excel files.

Davis, L.A., Graham, A.L., Parker, H.W., Ingber, M.S., Mammoli, A.A., Mondy, L.A., Guo, Q. and Abou-Sayed, A.S.: 2001 "Maximizing Storage Rate and Capacity and Insuring the Environmental Integrity of Carbon Dioxide Sequestration in Geological Reservoirs," Progress Report, June.

Downey, M.W., 1994, "Hydrocarbon seal rocks" In L.B. Magoon and W. G. Dow (eds.), The petroleum system – from source to trap. *AAP, Memoir* **60**, p. 159-64.

Fang, Z., Mammoli A. A., Brady, J., Ingber, M. S., Mondy, L. A., and Graham, A. L. 2002 "Flow-aligned tensor models for suspension flows," *International Journal of Multiphase Flow*, **28** 137-166.

Goode, P.A. and Kuchuk, F.J., 1991 "Inflow Performance of Horizontal Wells," SPE 21460.

Gunter, W.D., Perkins, E.H. and Hutcheon, I. 2000. "Aquifer Disposal of Acid Gases: Modeling of Water-rock Reaction for Trapping of Acid Wastes" *Applied Geochemistry*, **15**, 1085-1095.

Gunter, W.D., Perkins, E.H. and McCann,T.J. 1993. "Aquifer Disposal of CO_2 Rich-Gases: Reaction Design for Added Capacity" *Energy Conversion and Management*, **34**, 941-948.

Gunter, W.D., Wiwchar, B and Perkins, E.H. 1996. "Aquifer Disposal of CO_2 –rich Greenhouse Gases: Extension of the Time Scale of Experiment for CO Sequestering Reactions by Geochemistry Modeling" *Mineralogy and Petrology*, **59**, 121-140.

Hadavinia H., Advani S.G., Fenner R.T., 1995 "The evolution of radial fingering in a Hele-Shaw cell using C-1 continuous Overhauser boundary element method", *Engineering Analysis with Boundary Elements*, **16**, p.p. 183-195.

Harris**,** P.C., and Pippin, P.M., 2000, "High-Rate Foam Fracturing: Fluid Friction and Perforation Erosion", SPE 60841.

Heddle, B., H. Herzog & M. Klett, 2003 *The Economics of CO2 Storage*, MIT LFEE 2003-003 report, (http://sequestration.mit.edu/pdf/LFEE_2003-003_RP.pdf)

Henry, R.L., Feather, G.L., Smith, L.R. and Fussel, D.D.: 1984 "Utilization of Composition Observation Wells In A West Texas CO_2 Pilot Flood," paper SPE 9786 presented at the 64th Annual Technical Conference and Exhibition of the Society of Petroleum Engineers held in San Antonio, TX October 8-11.

Hsiao, S.-C., A. A. Mammoli and M. S. Ingber, 2003 "The evaluation of domain integrals on complex multiply-connected three-dimensional geometries for boundary element methods", *Comp. Mech.*, **32**, 226-233.

Hutcheon, I., Shevalier, M., and Abercrombie, H.J.1993. pH Buffering by Metastable Mineral-Fluid Equilibria and Evolution of Carbon Dioxide Fugacity during Burial Diagenesis . *Geochimica et Cosmochimica Acta* **57**, 1017-1027.

Ikoku, C.U.1980: Natural Gas Engineering, PennWell Books, Tulsa, OK, 1980.

Ingber, M. S., A. A. Mammoli, M. J. Brown, 2001 "A comparison of domain integral evaluation techniques for boundary element methods", *Int, J. Numer. Meths. Engrg.* **52**, 417-432.

Janda, N. B., P. W. Morrison, B. Z. Saylor, & G. Matisoff, 2001 "A methodology for measuring the rate of reaction of CO2 with Brine-Rock Mixtures," First National Conference on Carbon Sequestration, Washington, DC, May 14-17.

Johnson, J. W., E. H. Oelkers, and H.C. Helgeson, 1992 "SUPCRT92: A software package for calculating the standard molal thermodynamic properties of minerals, gases, aqueous species, and reactions from 1 to 5000 bars and 0 to 1000 C," *Computers and Geosciences*, **18**, pp 899-947.

Joshi, S.D., 1988 "Augmentation of Well Productivity with Slant and Horizontal wells," PSE 15375, *Journal of Petroleum Technology*, **40** No. 6, pp. 729-739.

Katz et al.: 1959 *Handbook of Natural Gas Engineering*, McGraw-Hill Book Company, New York.

Kenyon, W.E., 1997, “Petrophysical principles of applications of NMR logging” *The Log Analyst*, March-April, p. 21-43.

Kenyon, B., R. Kleinberg, C. Straley, G. Gubelin, C. Morris, 1995, *Nuclear magnetic resonance imaging*, Technology of the 21st century. Schlumberger, SMP-5183, p33.

Kharaka, Y.K.,Law, L.M., Carothers, W.W. and Georlitz, D.F. 1986. “Role of Organic Species Dissolved in Formation Waters From Sedimentary basins in Mineral Diagenesis. Roles of Organic Matter In Sedimentary Diagenesis” Edited by Donald L. Gautier. US. Geological Survey, *Society of Economic Paleontologist and Mineralogist Special Publication* No. 38. 111-121.

Kleinberg, R.L., 1996a, “Well logging.” *Encyclopedia of Nuclear Magnetic Resonance*, **8**, p. 4960-4969.

Kleinberg, R.L., 1996b, “Utility of NMR T_2 distributions, connection with capillary pressure, clay effect, and determination of the surface relaxivity parameter ρ_2” *Magnetic Resonance Imaging*, **14** nos. 7/8, p. 761-767.

Krushin, J.T., 1997, “Seal capacity of nonsmectite shale. In R.C. Surdam (ed.), Seals, traps, and the petroleum system” *AAPG Memoir* **67**, Chapter 3, p. 31-47.

Kuppe, F. and Settari, A.: 1998 “Productivity of Fractured Horizontal Wells”, *J. Can. Petrol. Technol.*, **37**, No. 10, Oct., 68-81.

Larsen, L., and Hegre, T.M.: 1991 "Pressure Transient Behaviour of Horizontal Wells with Finite-Conductivity Vertical Fractures," SPE 22076, paper presented at the International Arctic Technology Conference, Anchorage, May.

Liu, X. and Ortovela, P. 1996 “A Couple Reaction and Transport for Assessing the Injection, Migration and Fate of waste Fluids,” paper SPE 36640 presented at the Annual Technical Conference and Exhibition held in Denver.

Leighton, D. and Acrivos, A. 1987 “The Shear-Induced Migration of Particles in Concentrated Suspensions.” *J. Fluid Mech*. **181**, 415-439.

Lundegard, P.D., and Land, L.S. 1986. Carbon Dioxide and Organic Acids: Their Role in Porosity Enhancement and Cementation, Paleogene of the Gulf Coast. Roles of Organic Matter In Sedimentary Diagenesis. Edited by Donald L. Gautier. US. Geological Survey, Society of Economic Paleontologist and Mineralogist Special Publication No. 38. 129-146.

Mammoli, A. A.2002 “Solution of non-linear boundary integral equations in complex geometries with auxiliary domain subtraction”, *Int, J. Numer. Meths. Engrg.* **55**, 1115-1128.

Mathis, R.L., and Sears, S.O.: 1984 “Effects of CO_2 Flooding on Dolomite Reservoir Rock, Denver Unit, Wasson (San Andres) Field, TX,” paper SPE 13132 presented at the 59thAnnual Technical Conference and Exhibition held in Houston, TX.

Meshri, I.D. 1986. On the Reactivity of Carbonic and Organic Acids and Generation of Secondary Porosity. Roles of Organic Matter In Sedimentary Diagenesis. Edited by Donald L. Gautier. US. Geological Survey, Society of Economic Paleontologist and Mineralogist Special Publication No. 38. 123-128.

Morris, J. F. and Boulay, F. 1999 *J. Rheol.*, **43**, 1213.

Morris, J. F. 2003 personal communication

Murray, B., 2000 “Evaluating Forest Carbon Sequestration Potential in the U.S. with an Economic Model of the Forest and Agricultural Sectors”, presented at *Advances in Terrestrial Ecosystem Carbon Inventory, Measurements and Monitoring*

Nott, P. R. and Brady, J. F. 1994 “Pressure-Driven Flow of Suspensions: Simulation and Theory.” *J. Fluid Mech.* **275**, 157-199.

Omole, O., and Osoba, J. S.: 1983 “Carbon Dioxide-dolomite Rock Interaction during CO_2 Flooding Process,” presented at the annual meeting of the Petroleum Society of the Canadian Institute of Mining and Metallurgy, paper 83-34-17.

Paige, R.W., Murray, L.R. and Roberts, J.D.M., 1993, “Field Application of Hydraulic Impedance Testing for Fracture Measurement,” SPE 26525.

Paige, R.W., Roberts, J.D.M., Murray, L.R. and Mellor, D.W., 1992, “Fracture Measurement Using Hydraulic Impedance Testing,” SPE 24824

Patton, J. .T., and Phelan, P. F.: 1980 “Investigation of Possible Mechanisms by Which Carbon Dioxide Might Damage Oil Reservoirs,” Department of chemical engineering and DOE, DE-AC21-79MC10865.

Pearce, E.H., Holloway, S., Wacker, H., Nellis, M.K., Rochelle, C. A. and Bateman, K. 1996. “Natural Occurrences as Analogues for the Geological Disposal of Carbon Dioxide”. *Energy Conversion and Management*, 37, 1123-1128.

Phillips, R. J., Armstrong, R. C., Brown, R. A., Graham, A. L., and Abbott, J. R., 1992 “A constitutive equation for concentrated suspension that accounts for shear-induced particle migration,” *Phys. Fluids A*, **4,** 30-40.

Power, H. and Wrobel, L. C., 1995 “Boundary Integral Methods in Fluid Mechanics”, *Computational Mechanics Publications*, Southampton – Boston.

Pruess, K., Xu, T. and Garcia, J.: 2001 "Numerical Modeling of Aquifer Disposal of CO_2,” paper SPE 66537 presented at the 2001 SPE/EPA/DOE Exploration and Production Environmental Conference, San Antonio, Texas, February 26-28.

Rao, R. R., Mondy, L. A., Baer, T. A., Altobelli, S. A., and Stephens, T. S., 2002 "NMR measurements and simulations of particle migration in non-Newtonian fluids," *Chem. Eng. Comm.* **189**, 1-22

Rau, G. H., K, Caldeira, K. G. Knauss, B. Downs, and H. Sarv, 2001 “Enhanced carbonate dissolution as a means of capturing and sequestering carbon dioxide,” First National Conference on Carbon Sequestration, Washington, DC May 14-17.

Reidenbach, V.G., Harris, P.C., Lee, Y.N, and Lord D.L., 1986, "Rheological Study of Foam Fracturing Fluids Using Nitrogen and Carbon Dioxide", SPE 12026.

Ross, G. D., A. C. Todd, J. A. Tweedie, and A. G. S. Will, 1982“The dissolution effects of CO2-brine systems on the permeability of U.K. and North Sea Calcareous Sandstones,” SPE/DOE Paper 10685, Proceedings 3rd Joint SPE/DOE Symposium on Enhanced Oil Recovery, Tulsa, OK, April 4-7.

Sayegh, S.G., Krause, F.F., Girard. M., and Debree, C.: 1990 “Rock/Fluid Interactions of Carbonated brines in a sandstone reservoir: Pembina Cardium, Alberta Canada,” paper SPE 19392 presented at SPE Formation Evaluation.

Schlömer, S. and B.M. Krooss, 1997, Experimental characterisation of the hydrocarbon sealing efficiency of cap rocks. Marine and Petroleum Geology, v. 4, p. 565-580.

Schowalter, T.T., 1979, Mechanics of secondary hydrocarbon migration and entrapment. *AAPG Bulletin*, **63**, no. 5, p. 723-760.

Shuler, P.J., Freitas, E.A. and Bower, K.A.: 1991 “Selection And Application of $BaSO_4$ Scale Inhibitors for a CO_2 Flood, Rangely Weber San Unit, Colorado,” paper SPE 18973 presented at SPE production Engineering.

Smith. L., N. Gupta, B. Sass & T. Bubenik, 2001 “Carbon Dioxide Sequestration in Saline Formations – Engineering and Economic Assessment Final Technical Report,” PRDA#: DE-RAC26-98FT35008. Project#: DE-RA26-98FT40418 MOD 005, Gattelle, Columbus. OH, July 9.

Sneider**,** R.M., J.S. Sneider, G.W. Bolger, and J.W. Neasham, 1997, Comparison of seal capacity determinations: Conventional cores vs cuttings. In R.C. Surdam (ed.), Seals, traps, and the petroleum system. AAPG, Memoir 67, p. 1–12.

Straley, C., D. Rossini, H. Vinegar, P. Tutunijan, and C. Morris, 1997, “Core analysis by low-field NMR.” *The Log Analyst*, March-April, p. 84-94.

Warpinski, N.R., P.T. Branagan, R.E. Peterson, S.L. Wolhart and J.E. Uhl, 1998, “Mapping Hydraulic Fracture Growth and Geometry Using Microseismic Events Detected by a Wireline Retrievable Accelerometer Array”, SPE 40014, *Proc. SPE Gas Technology Symposium*, Calgary, AB, Canada: 335-346.

Watts, N.L., 1987, “Theoretical aspects of cap-rock and fault seals for single- and two-phase hydrocarbon column” *Marine and Petroleum Geology*, **4**, November, p. 274-307.

Wright**,** C.A., E.J. Davis, G. Wang, and L. Weijers, 1999 “Downhole Tiltmeter Fracture Mapping: A New Tool for Direct Measurement of Hydraulic Fracture Growth”, presented at the 37th U.S. Rock Mechanics Symposium, Vail, CO.

Zhang, K. and Acrivos, A. 1994 "Viscous Resuspension in Fully Developed Laminar Pipe Flows" *Int. J. Multiphase Flow* **20**, 579.

APPENDIX A
SAMPLE COMPOSITION FROM X-RAY DIFFRACTION

Table A.1: Relative abundances of minerals for the CH core.

Sample	Q[1] (%)	Pl[2] (%)	KF[3] (%)	Cal[4] (%)	Dol[5] (%)	Sid[6] (%)	Py[7] (%)	Illite (%)	K[8] (%)	Chl[9] (%)
8075	14	4	--	6	2	--	8	34	5	27
8098.5	17	5	--	2	1	--	7	57	1	10
8122.5	16	6	1	2	2	1	4	31	3	34
8155	16	4	1	3	1	--	5	43	8	20
8162.5	21	7	1	--	3	1	3	29	3	33
8168	25	6	--	+	3	2	3	15	6	40
8187.5	23	6	--	+	3	2	2	37	1	27

[1]Q: quartz; [2]Pl: plagioclase; [3]KF: K-feldspars; [4]Cal: calcite; [5]Dol: dolomite; [6]Sid: siderite; [7]Py: pyrite; [8]K: kaolinite; [9]Chl: chlorite.

Table A.2: Relative abundances of minerals for the PH core.

Sample	Q[1] (%)	Pl[2] (%)	KF[3] (%)	Dol[4] (%)	Sid[5] (%)	Anh[6] (%)	Py[7] (%)	Illite (%)	K[8] (%)	Chl[9] (%)
7647.55	45	5	+	2	1	--	1	43	2	1
7649.8	16	2	--	--	39	--	--	40	4	--
7652.5	58	6	1	2	3	--	1	26	2	2
7660.45	48	3	--	2	2	+	1	41	2	1
7666.4	51	5	1	1	4	--	1	35	3	--
7674.5	79	4	1	1	2	--	--	11	2	+
7685.45	67	2	--	1	1	--	--	24	3	2
7692.45	73	3	+	2	2	--	--	18	1	1
7695	26	1	--	2	54	--	--	18	+	--
7700.15	79	--	--	--	--	+	1	16	3	--
7702.35	46	--	2	16	7	--	5	19	5	1

[1]Q: quartz; [2]Pl: plagioclase; [3]KF: K-feldspars; [4]Dol: dolomite; [5]Sid: siderite; [6]Anh: anhydrite; [7]Py: pyrite; [8]K: kaolinite; [9]Chl: chlorite

Table A.3: Relative abundances of minerals for the CSM core.

Sample	Q[1] (%)	Pl[2] (%)	KF[3] (%)	Cal[4] (%)	Dol[5] (%)	Sid[6] (%)	Gyp[7] (%)	Py[8] (%)	Illite (%)	Sm[9] (%)	K[10] (%)	Chl[11] (%)
295.9	27	10	--	2	4	1	--	1	37	4	1	14
307.6	27	8	1	1	5	1	--	2	33	12	1	8
319	29	11	1	2	5	1	--	--	32	--	2	16
433.3	24	10	1	2	9	1	--	--	9	39	1	4
440.1	33	15	1	2	8	1	--	1	6	30	+	3
447.2	27	8	1	1	4	2	--	2	15	33	--	8
450	25	8	1	2	7	1	--	1	6	44	1	5
915.5	25	2	4	3	6	1	+	4	10	35	1	8
918.3	19	4	1	1	4	1	+	4	36	--	1	29
920.9	18	5	1	2	1	2	+	5	42	--	1	24
924.7	18	5	--	2	3	1	+	3	24	--	2	41
927.6	20	6	--	1	5	1	+	4	4	53	1	7
930.2	21	10	1	2	3	1	--	3	12	45	--	2
930.4	23	16	1	1	4	1	+	4	4	41	--	5
931.7	27	12	2	3	3	1	+	3	5	42	--	2
932.7	18	5	--	2	4	1	--	4	9	52	1	4
932.9	18	6	--	1	4	1	+	5	5	55	--	4
934.1	23	6	1	2	6	1	--	4	2	52	--	2
1589	2	23	--	2	--	6	--	3	1	63	--	1
1605.8	18	5	0.5	2	2	1	--	4	3	60	--	4
1621.5	19	6	--	2	2	--	--	2	1	65	--	1

[1]Q: quartz; [2]Pl: plagioclase; [3]KF: K-feldspars;[4]Cal: calcite; [5]Dol: dolomite; [6]Sid: siderite; [7]Gyp: gypsum; [8]Py: pyrite; [9] Sm: smectite; [10]K: kaolinite; [11]Chl: chlorite

APPENDIX B
BULK VOLUME

Table B.1: Bulk volume of samples of the Lewis Shale (CH core).

Sample	Bulk Volume (cm^3)
8075	8.92
8098.5	18.24
8122.5	15.83
8112.5	3.50
8131.6	8.69
8155	15.64
8162.5	14.48
8168	16.99
8187.5	10.55

Table B.2: Bulk volume of samples of the pebble shale unit (PH core).

Sample	Bulk Volume (cm^3)
7647.55	13.75
7649.8	21.55
7652.5	20.34
7660.45	20.07
7666.4	17.97
7674.5	18.55
7685.45	17.72
7692.45	19.31
7695	19.34
7700.15	21.12
7702.35	20.09

Table B.3: Bulk volume of samples of the Lewis Shale (CSM core).

Sample	Bulk Volume (cm^3)
295.9	11.19
307.6	9.58
319	15.75
433.3	13.91
440.1	7.54
447.2	11.31
450	9.32
915.5	19.75
918.3	11.16
920.9	9.18
924.7	4.09
927.6	7.14
930.2	15.05
930.4	17.99
931.7	12.67
932.7	5.14
932.9	4.38
934.1	18.36
1589	9.73
1605.8	6.40
1621.5	5.81

APPENDIX C
NMR RESULTS

Table C.1: Magnetizations and T_{2ML} of the samples of the Lewis Shale (CH core). The M_0 and T_{2ML} correspond to each saturation state.

Sample	Undersaturated		Desaturated		Saturated	
	M_0	T_{2ML} (ms)	M_0	T_{2ML} (ms)	M_0	T_{2ML} (ms)
8075	8.314	1.959	3.547	1.959	187.821	0.408
8098.5	12.710	3.785	8.760	5.262	405.255	0.338
8112.5	8.338	1.749	5.430	4.935	67.507	0.606
8122.5	12.394	2.661	10.905	2.176	367.820	0.360
8131.6	9.024	3.177	10.580	1.919	186.634	0.374
8155	15.125	1.988	9.592	3.602	468.701	0.301
8162.5	9.679	3.711	11.222	2.265	361.736	0.330
8168	10.311	3.624	11.624	2.400	542.215	0.297
8187.5	10.944	2.809	6.706	4.086	241.023	0.367

Table C.2: Magnetizations and T_{2ML} of the samples of the PH core. The M_0 and T_{2ML} of the pebble shale unit correspond to each saturation state.

Sample	Undersaturated		Desaturated		Saturated	
	M_0	T_{2ML} (ms)	M_0	T_{2ML} (ms)	M_0	T_{2ML} (ms)
7647.55	7.417	7.100	6.654	7.367	302.767	0.649
7649.8	15.781	2.200	10.851	3.159	204.731	0.494
7652.5	18.932	2.124	6.201	13.963	592.226	1.127
7660.45	9.677	7.469	9.608	5.896	592.604	1.247
7666.4	15.589	2.914	9.801	6.572	389.155	0.953
7674.5	23.017	3.413	9.969	8.534	265.075	1.728
7685.45	39.726	1.668	16.519	3.581	260.192	1.320
7692.45	38.112	1.701	6.957	16.332	360.401	1.613
7695	48.770	2.441	21.603	3.022	177.487	1.646
7700.15	46.007	2.988	9.001	6.572	232.256	5.318
7702.35	8.799	9.618	8.673	7.919	486.409	1.163

Table C.3: Magnetizations and T_{2ML} of the samples of the Lewis Shale (CSM core). The M_0 and T_{2ML} correspond to each saturation state.

Sample	Undersaturated		Desaturated		Saturated	
	M_0	T_{2ML} (ms)	M_0	T_{2ML} (ms)	M_0	T_{2ML} (ms)
295.9	48.828	0.496	8.593	2.804	528.608	1.372
307.6	15.851	1.173	7.016	4.039	517.181	0.992
319	60.702	0.620	8.258	4.202	467.673	0.616
433.3	NA*	NA*	7.222	5.820	571.514	2.180
440.1	57.089	0.424	7.031	3.785	422.256	1.304
447.2	12.378	1.257	8.598	2.984	493.394	0.989
450	11.978	2.468	9.638	3.628	596.616	0.473
915.5	16.200	1.916	12.478	2.250	1154.303	0.981
918.3	13.009	2.412	3.438	9.773	545.411	0.808
920.9	11.185	1.693	9.515	2.549	339.977	0.543
924.7	5.004	6.352	6.856	3.123	NA*	NA*
927.6	13.616	2.235	8.938	2.318	326.922	0.442
930.2	11.954	2.985	8.128	5.284	665.033	0.738
930.4	108.018	0.322	6.054	8.090	973.897	1.053
931.7	58.857	0.538	7.495	4.969	551.829	1.019
932.7	13.103	1.578	5.655	4.582	213.793	0.492
932.9	5.330	5.160	8.027	2.933	201.643	0.472
934.1	14.921	1.832	7.057	4.463	896.822	0.455
1589	11.011	2.544	9.789	2.155	556.318	0.254
1605.8	9.884	3.280	8.476	2.298	324.197	0.421
1621.5	13.691	3.984	7.200	3.027	286.911	0.413

*NA: not available

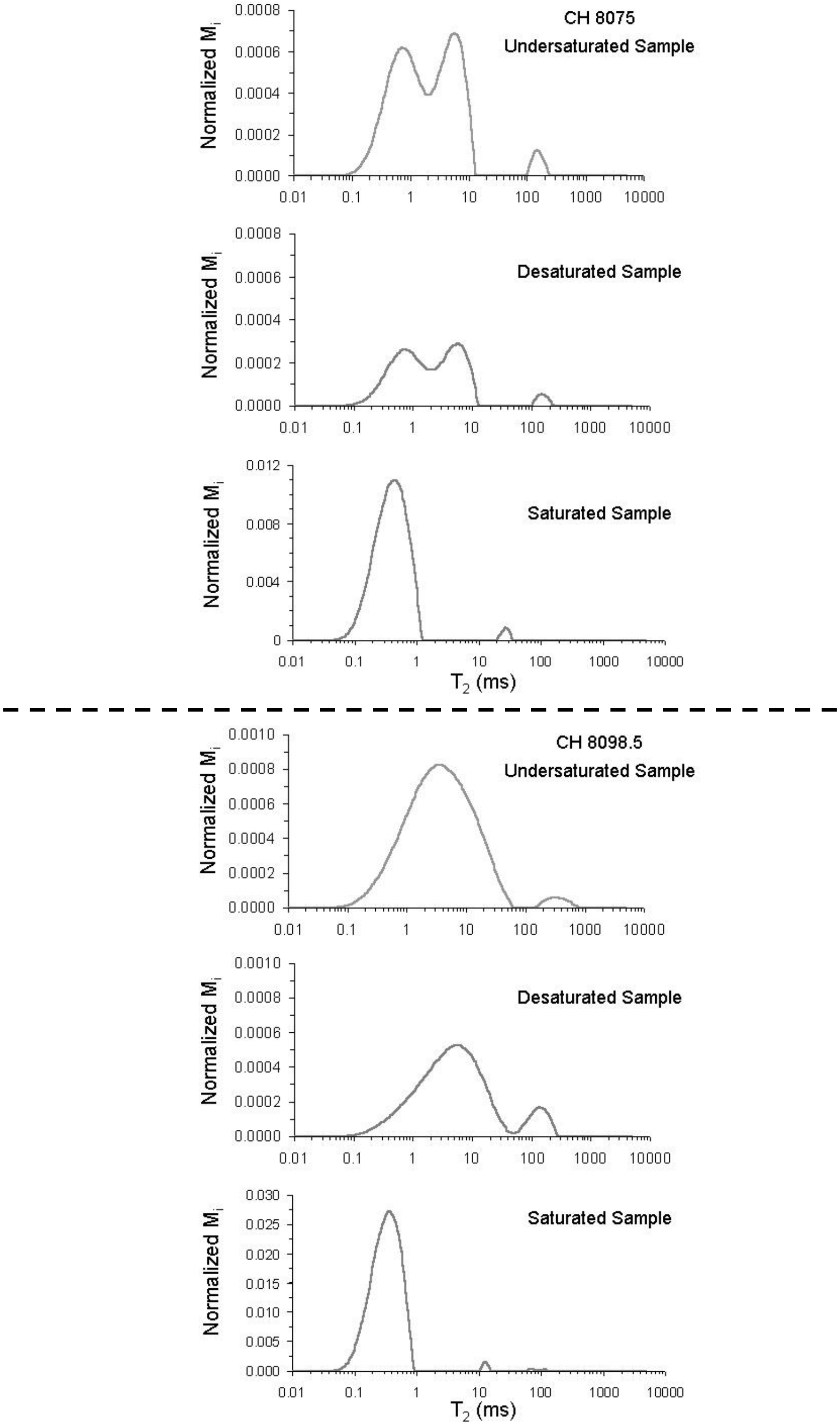

Figure C.1: T_2 distributions of the Lewis Shale, CH core. Each saturation state is represented. The sample name is located at the top right corner of the T_2 distribution of the undersaturated sample.

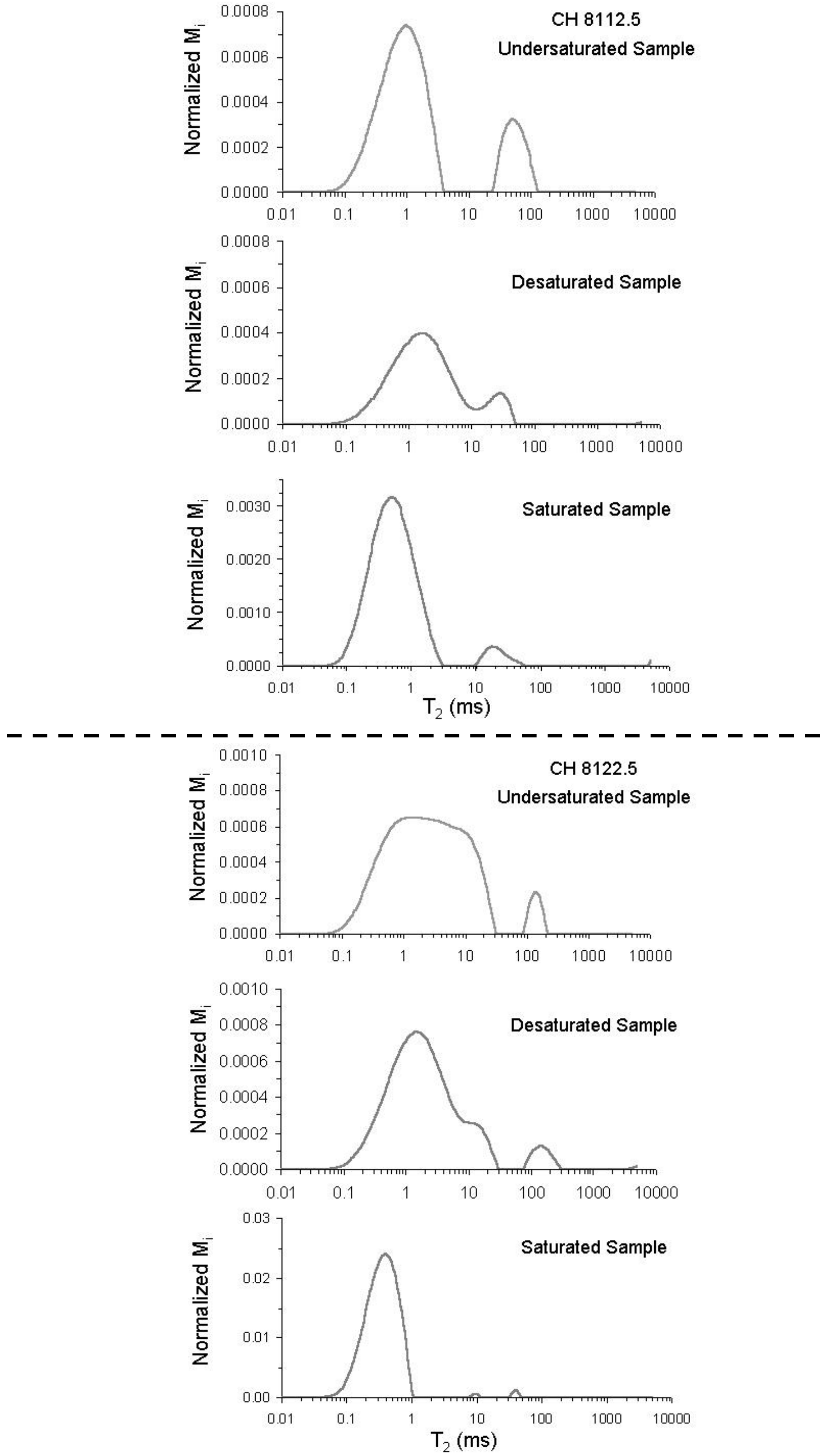

Figure C.1: Continued.

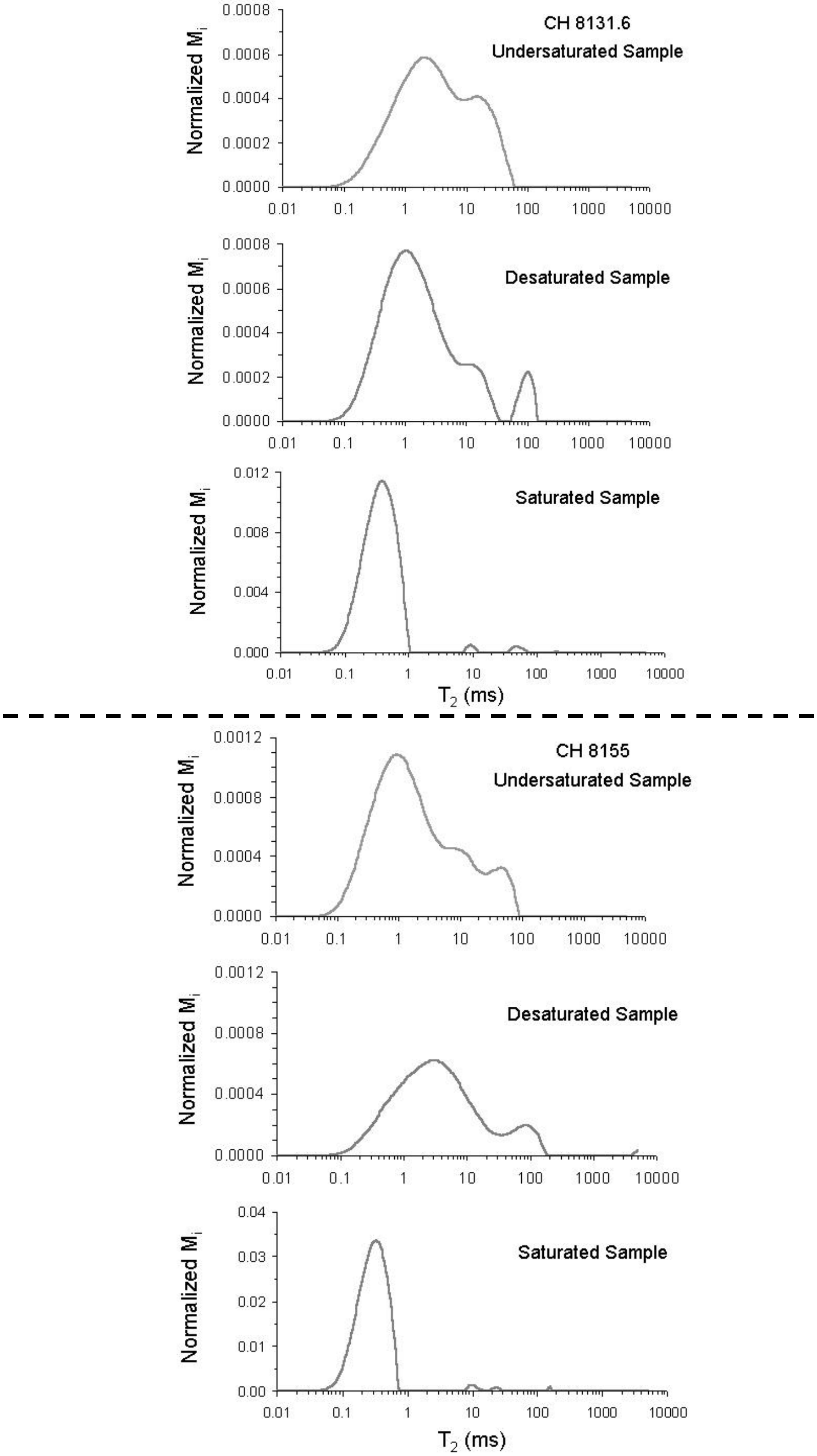

Figure C.1: Continued.

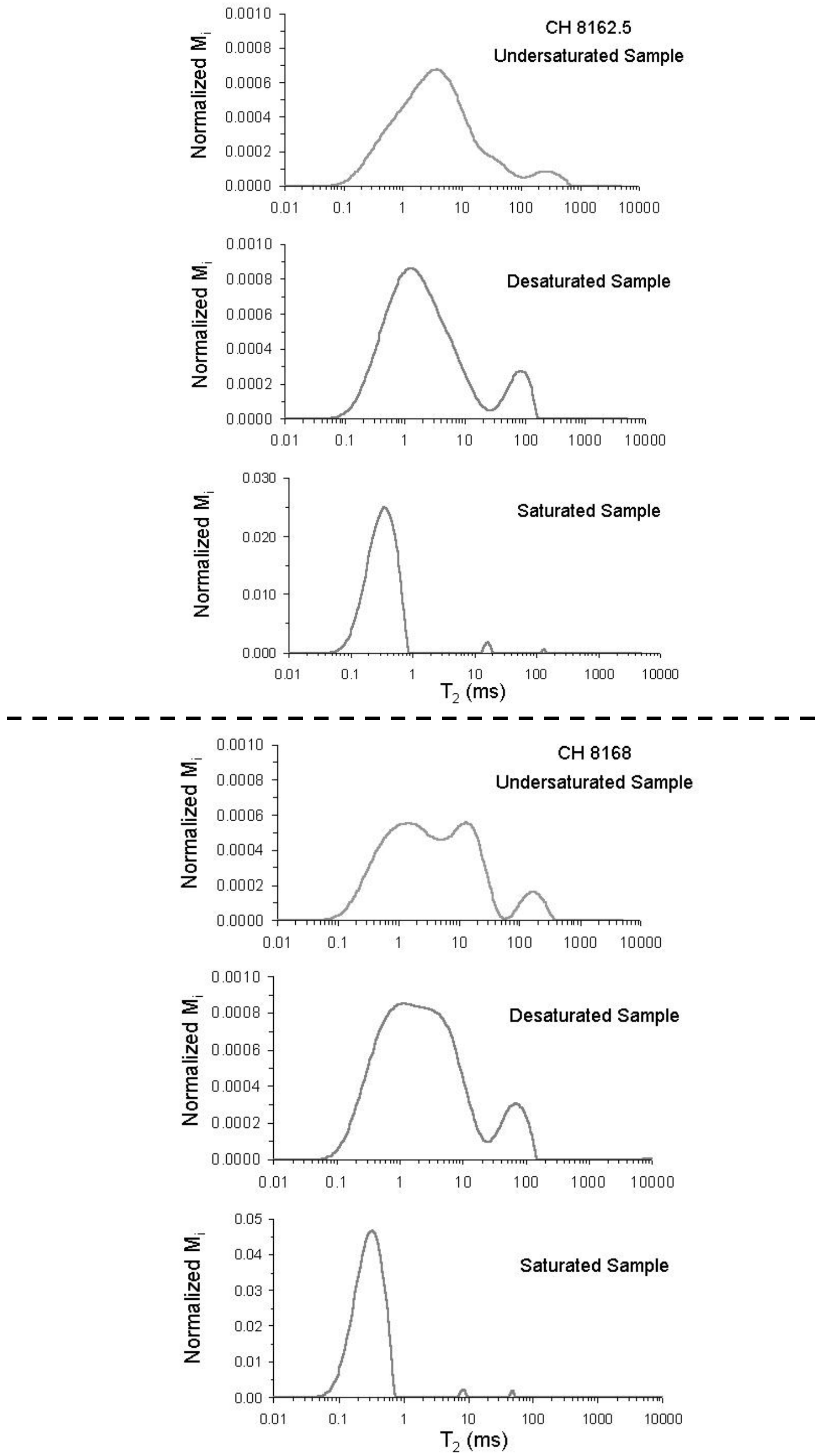

Figure C.1: Continued.

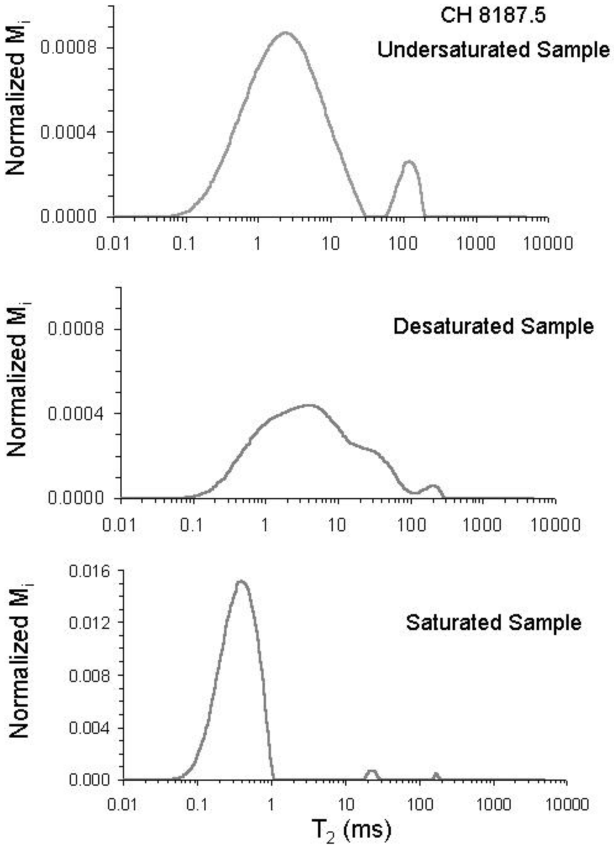

Figure C.1: Continued.

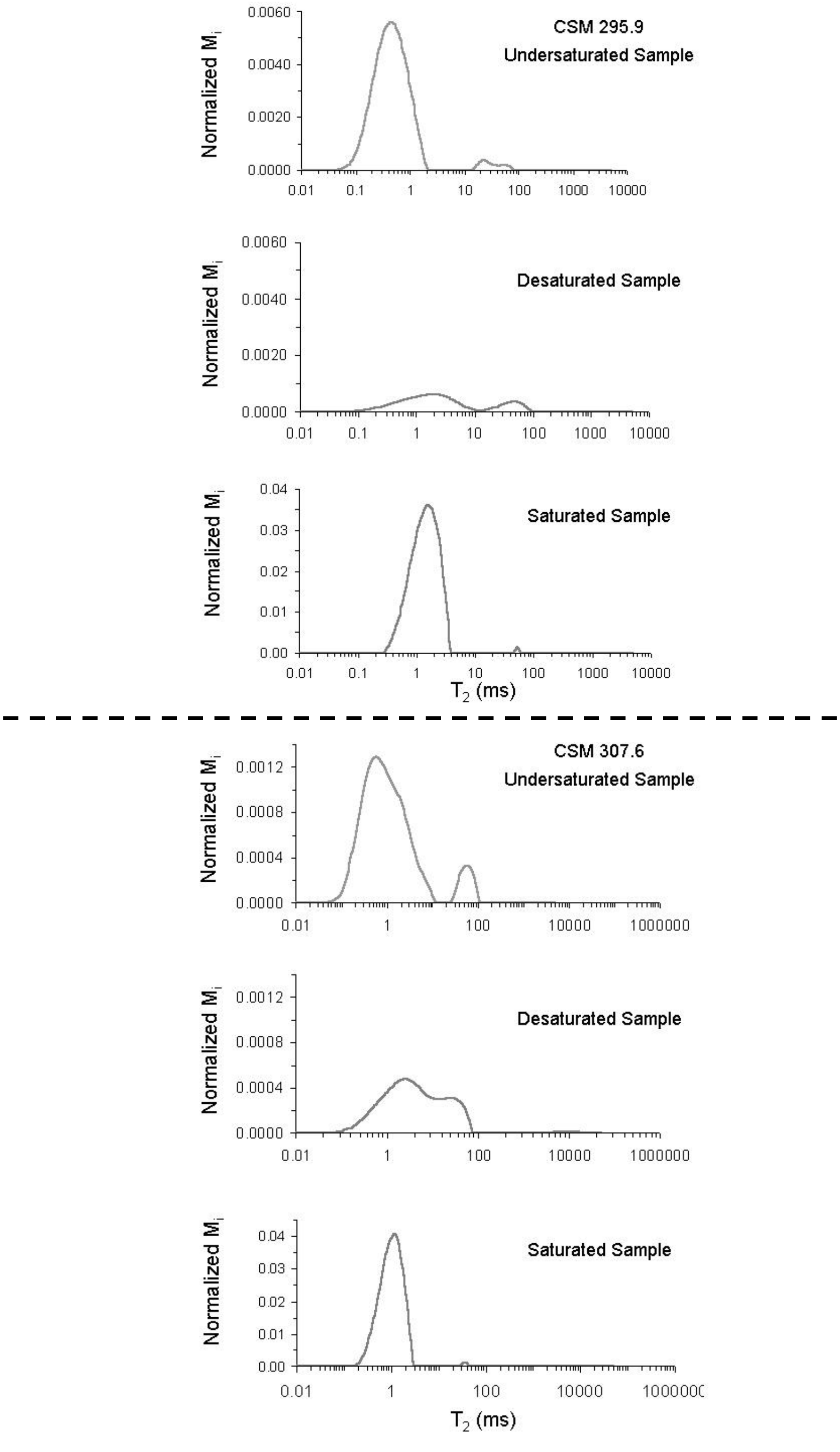

Figure C.2: T_2 distributions of the Lewis Shale, CSM core. Each saturation state is represented. The sample name is located at the top right corner of the T_2 distribution of the undersaturated sample.

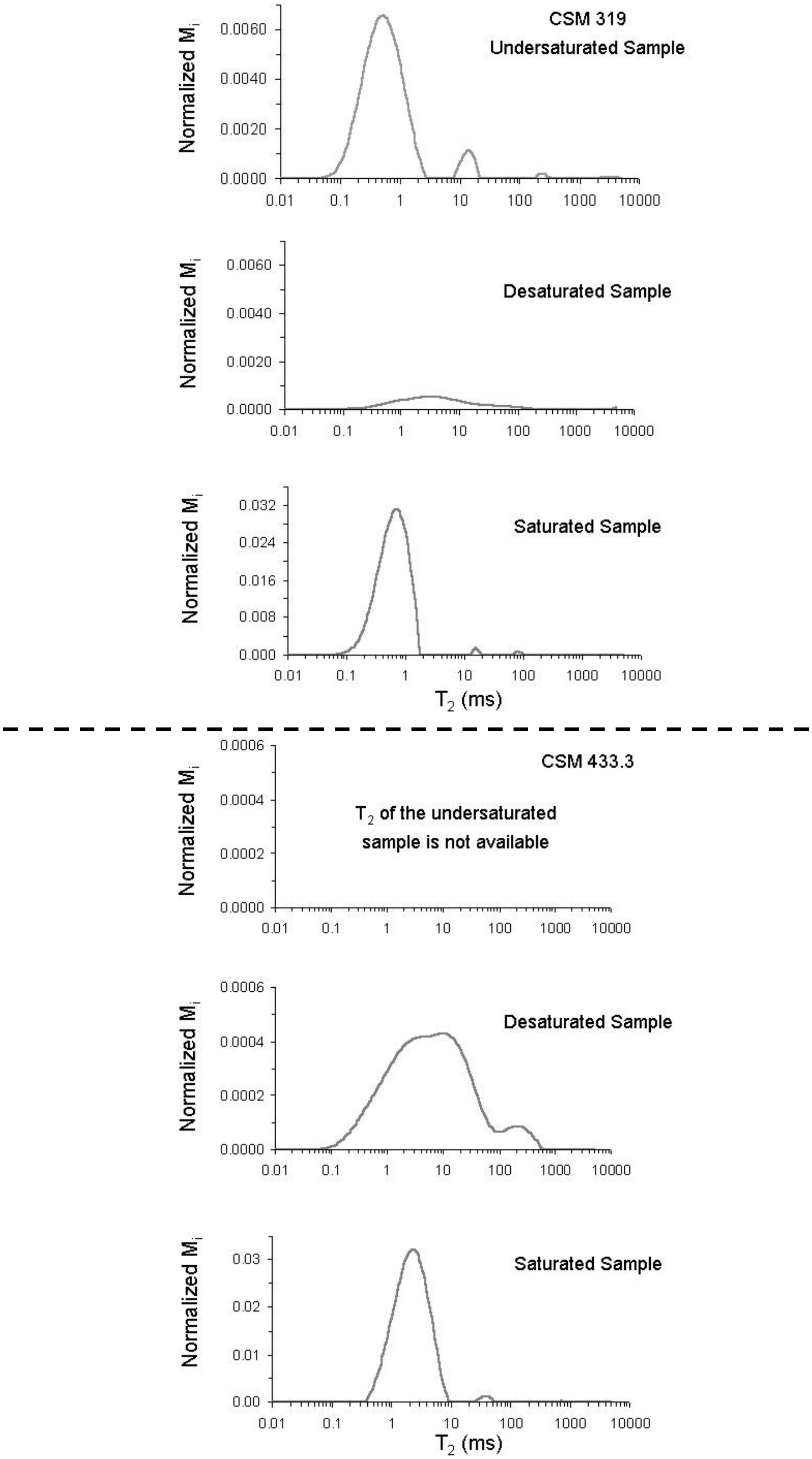

Figure C.2: Continued.

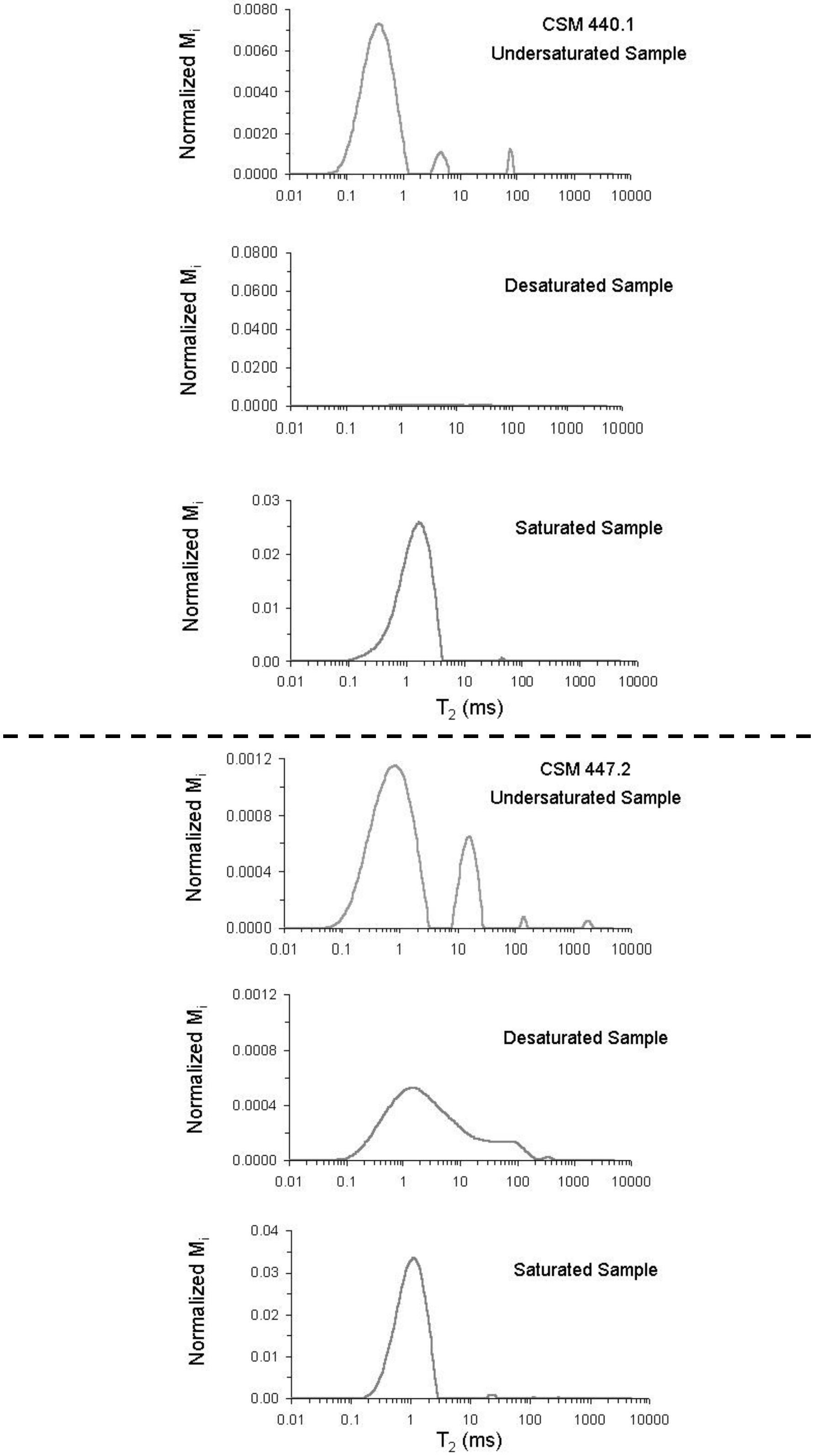

Figure C.2: Continued.

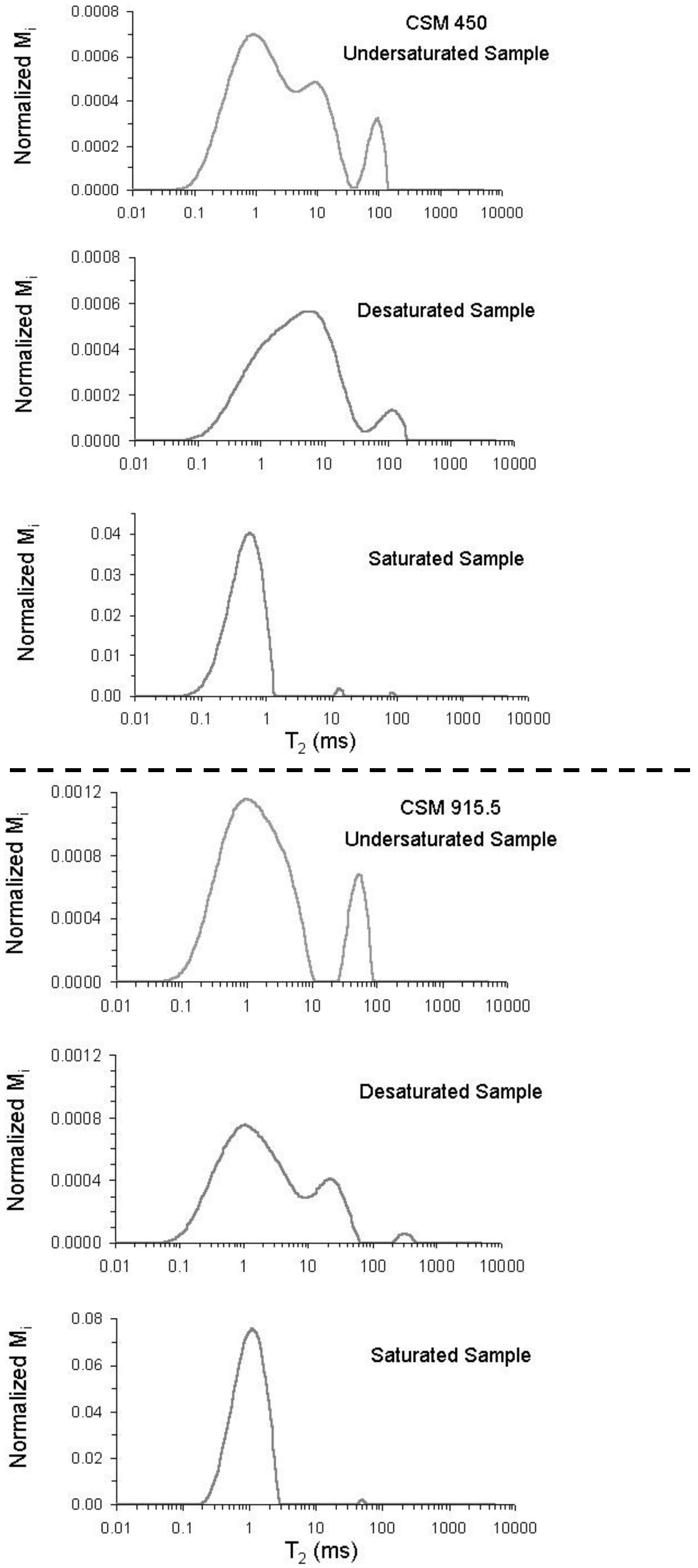

Figure C.2: Continued.

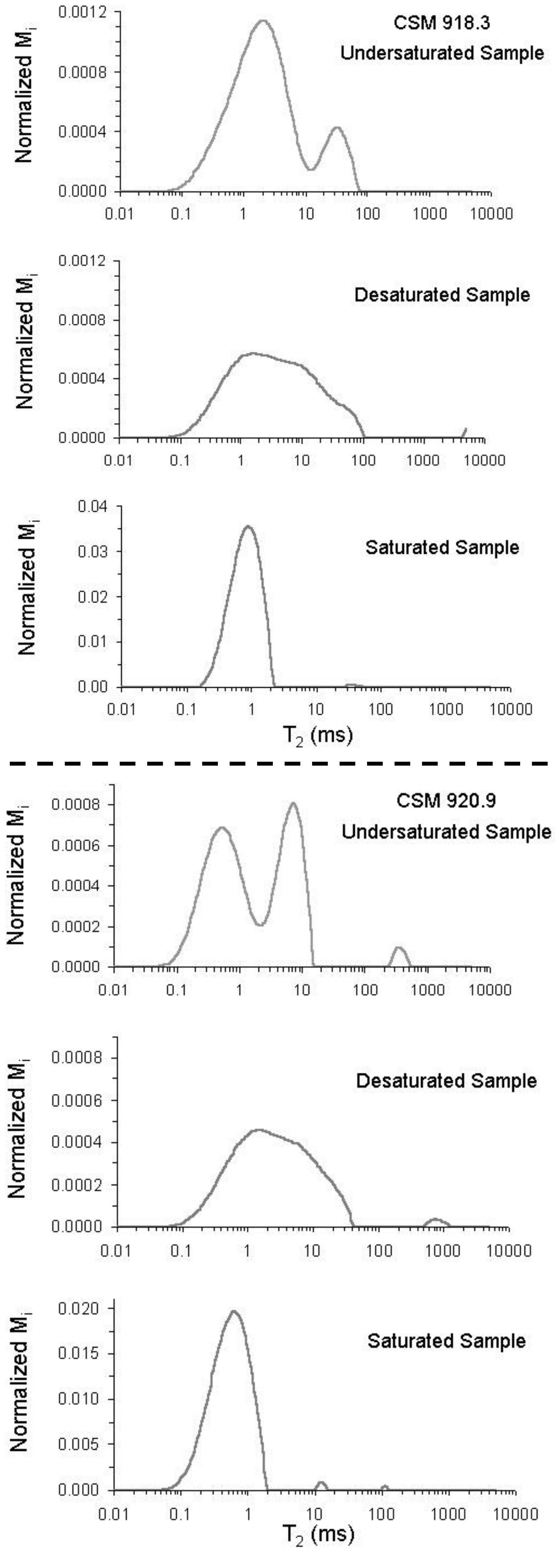

Figure C.2: Continued.

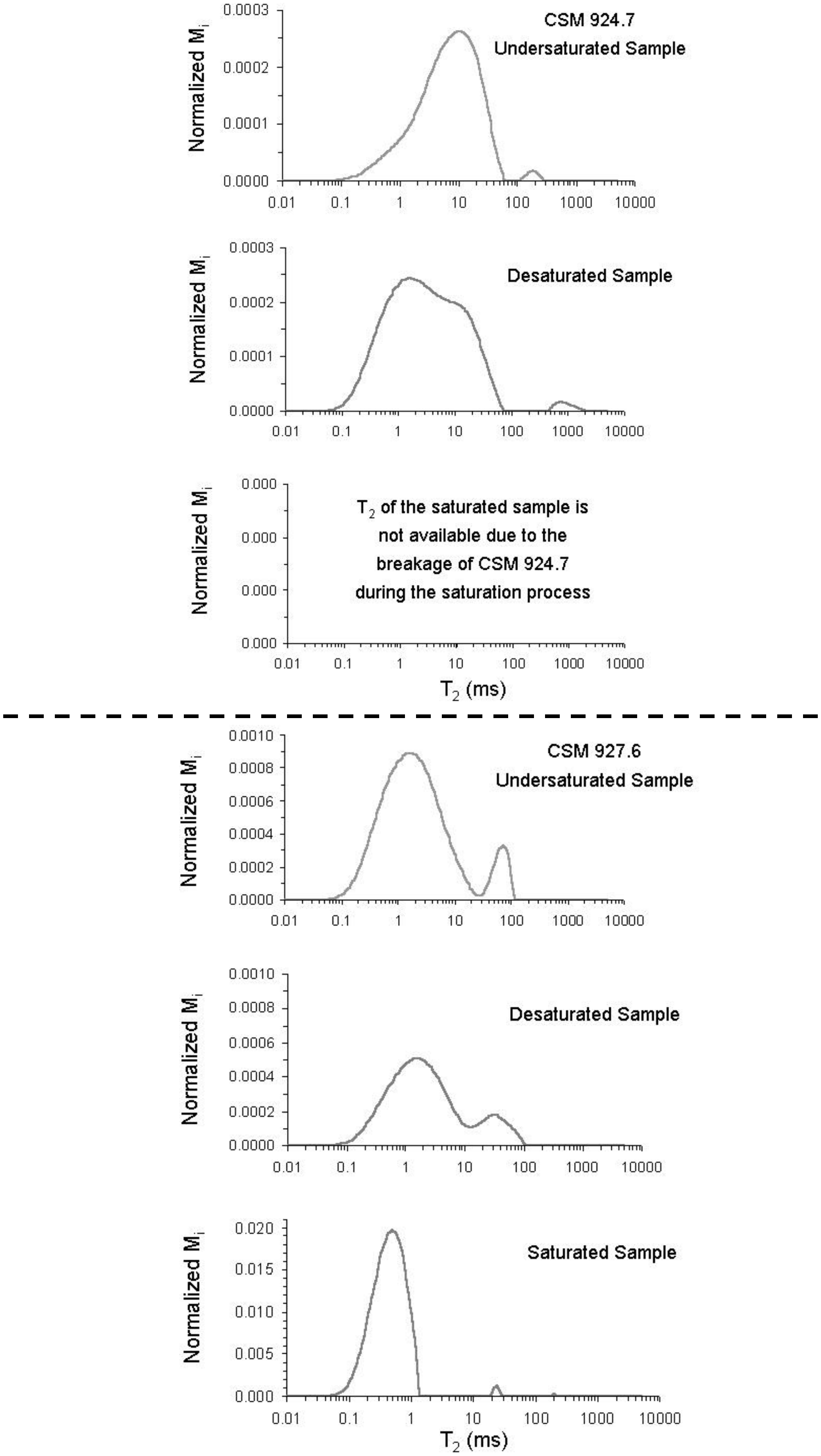

Figure C.2: Continued.

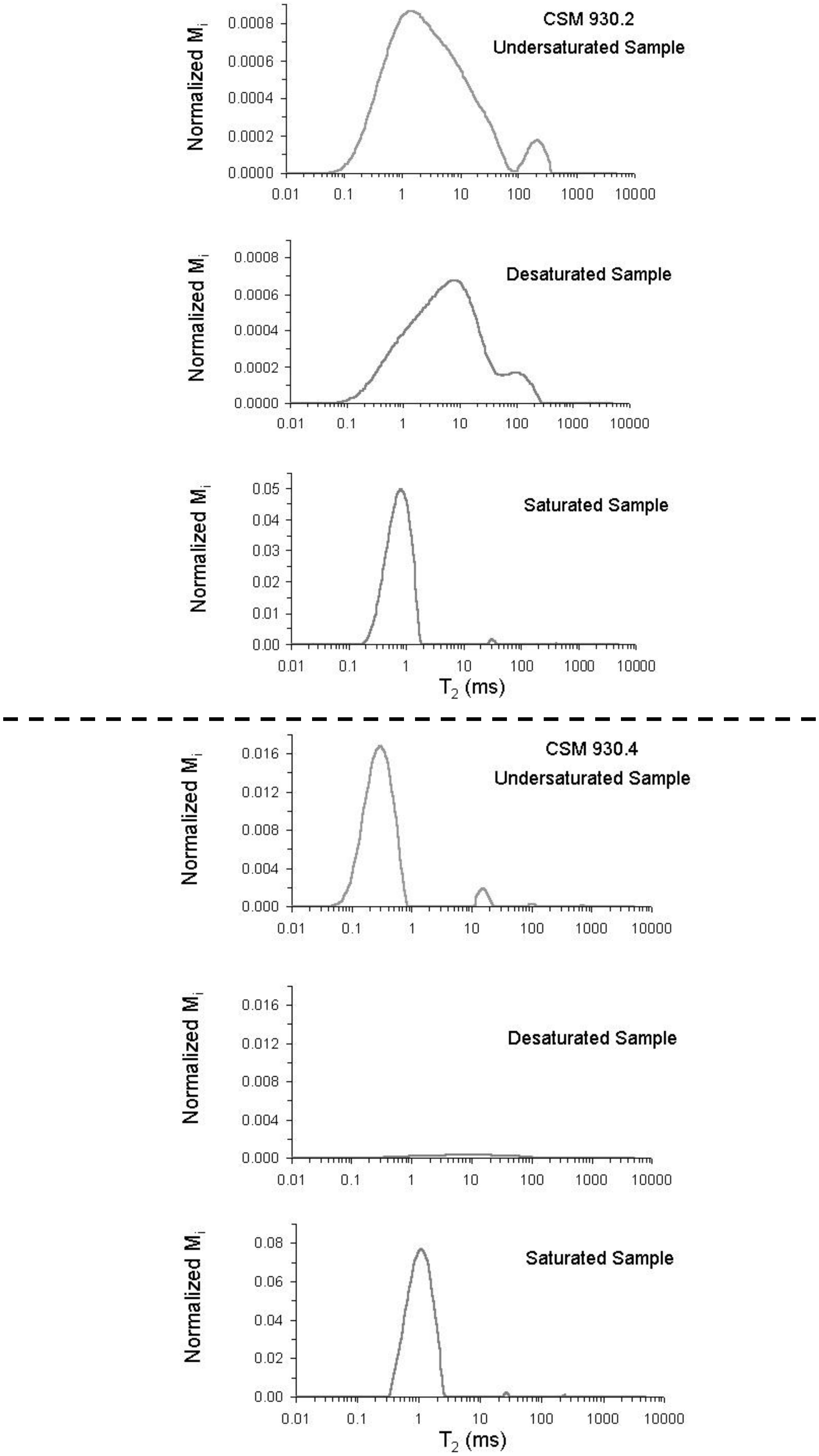

Figure C.2: Continued.

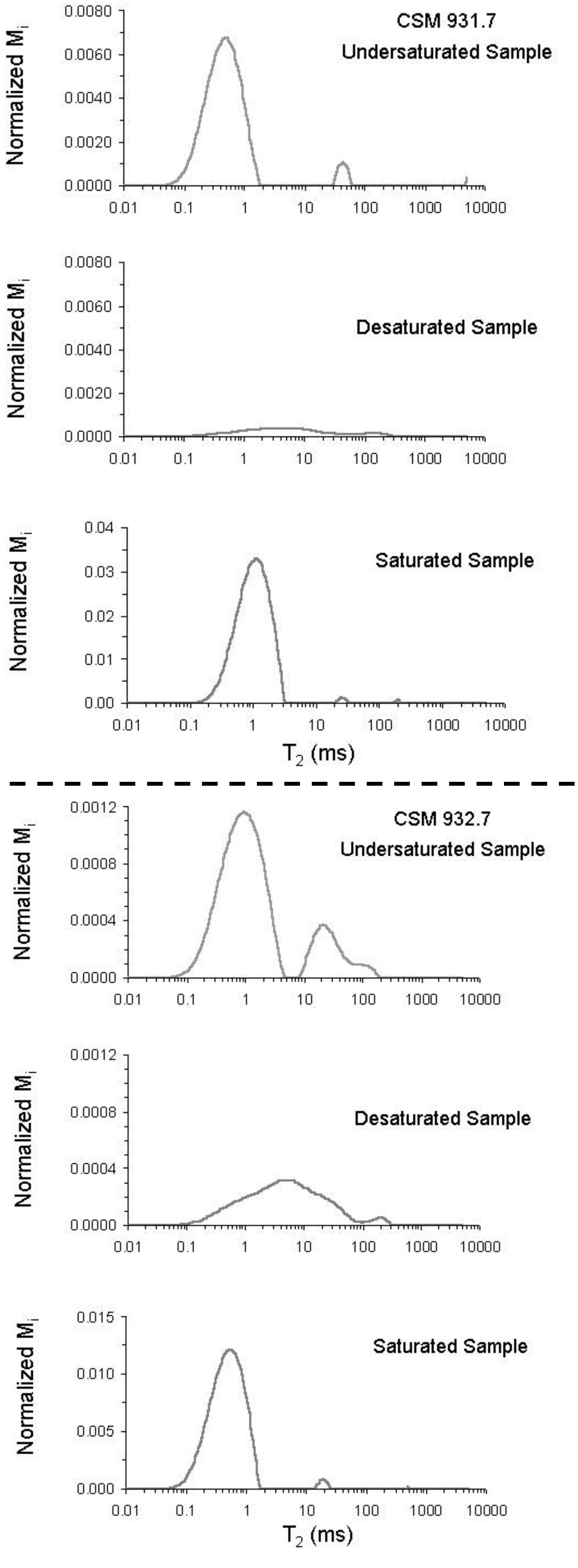

Figure C.2: Continued.

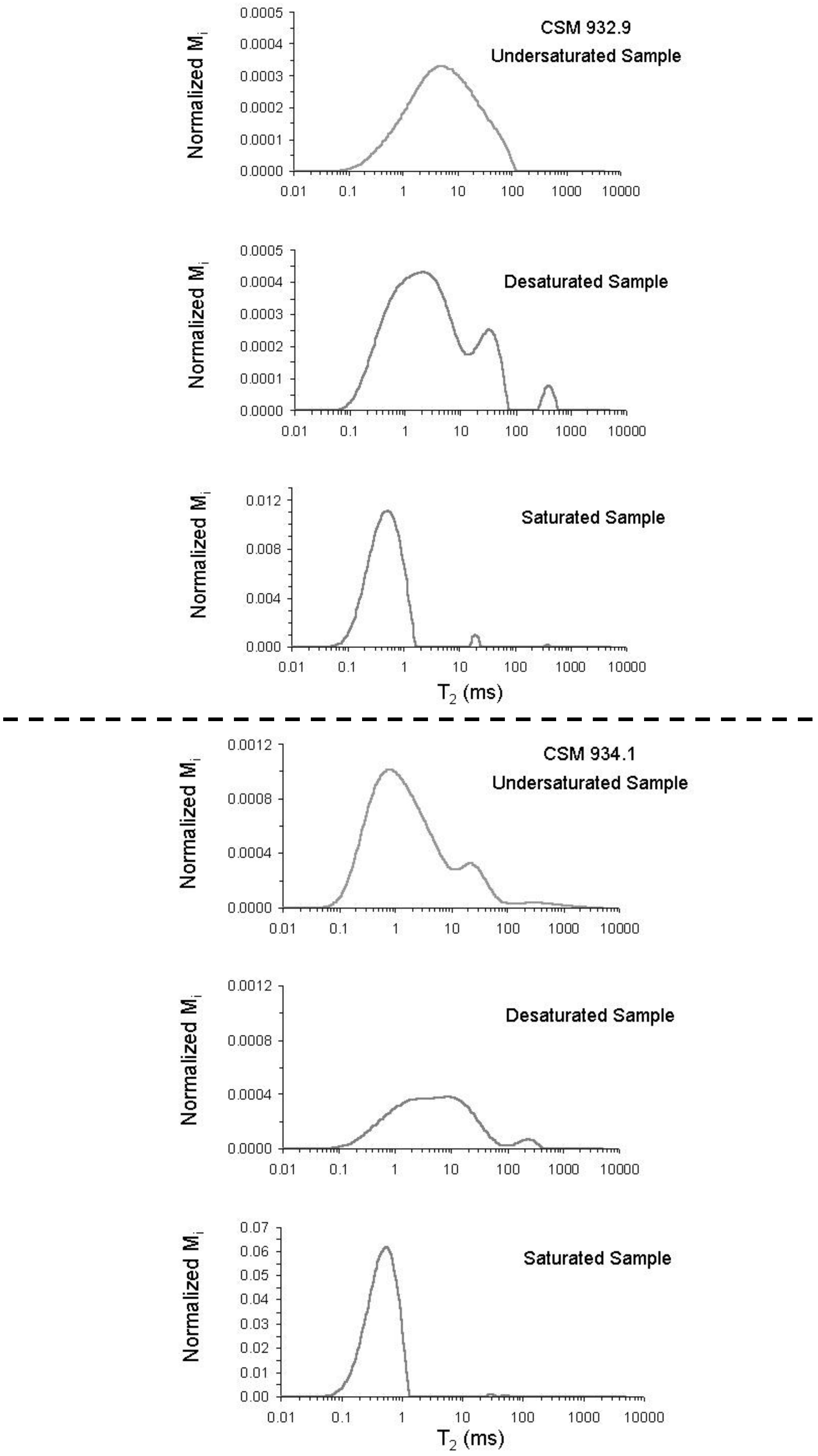

Figure C.2: Continued.

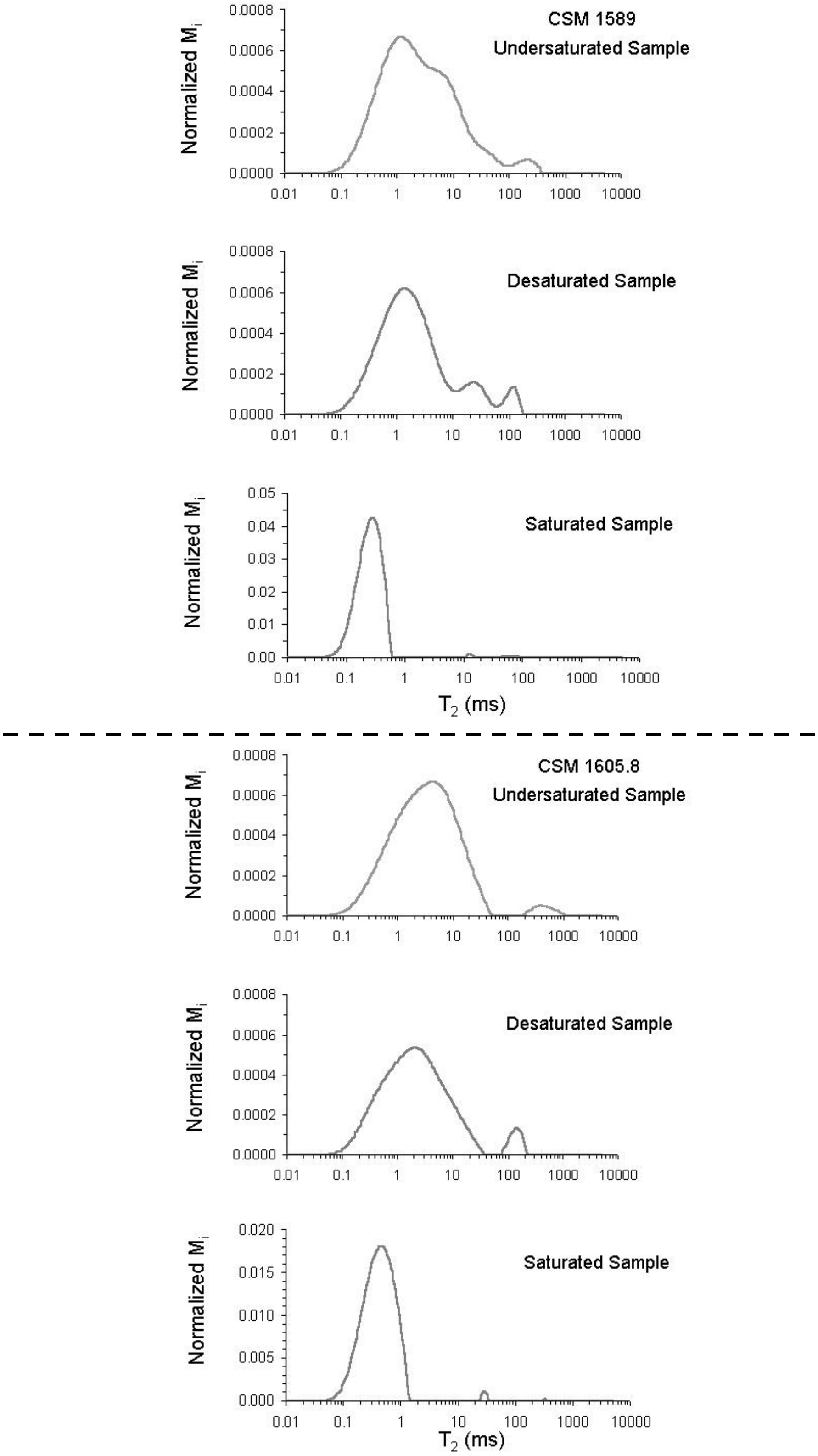

Figure C.2: Continued

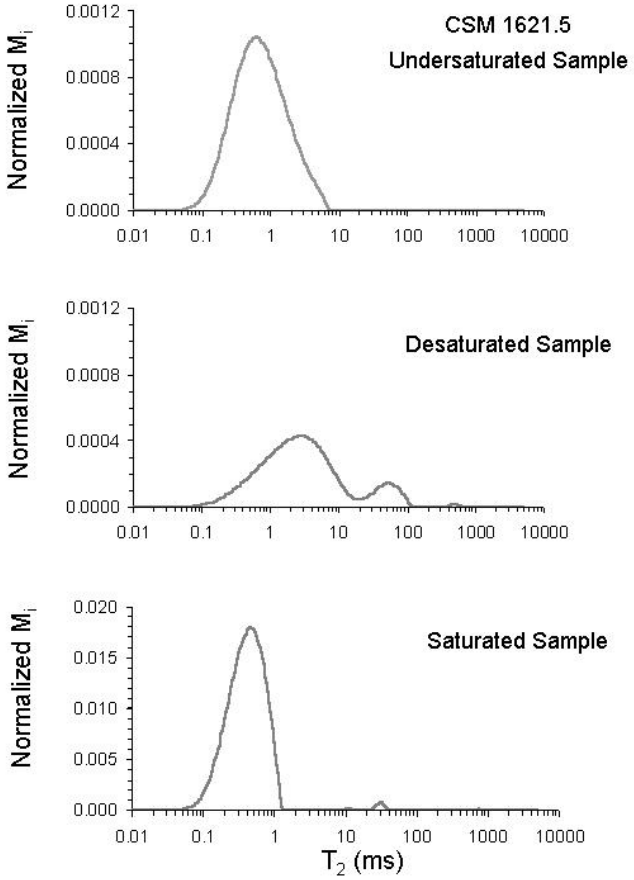

Figure C.2: Continued

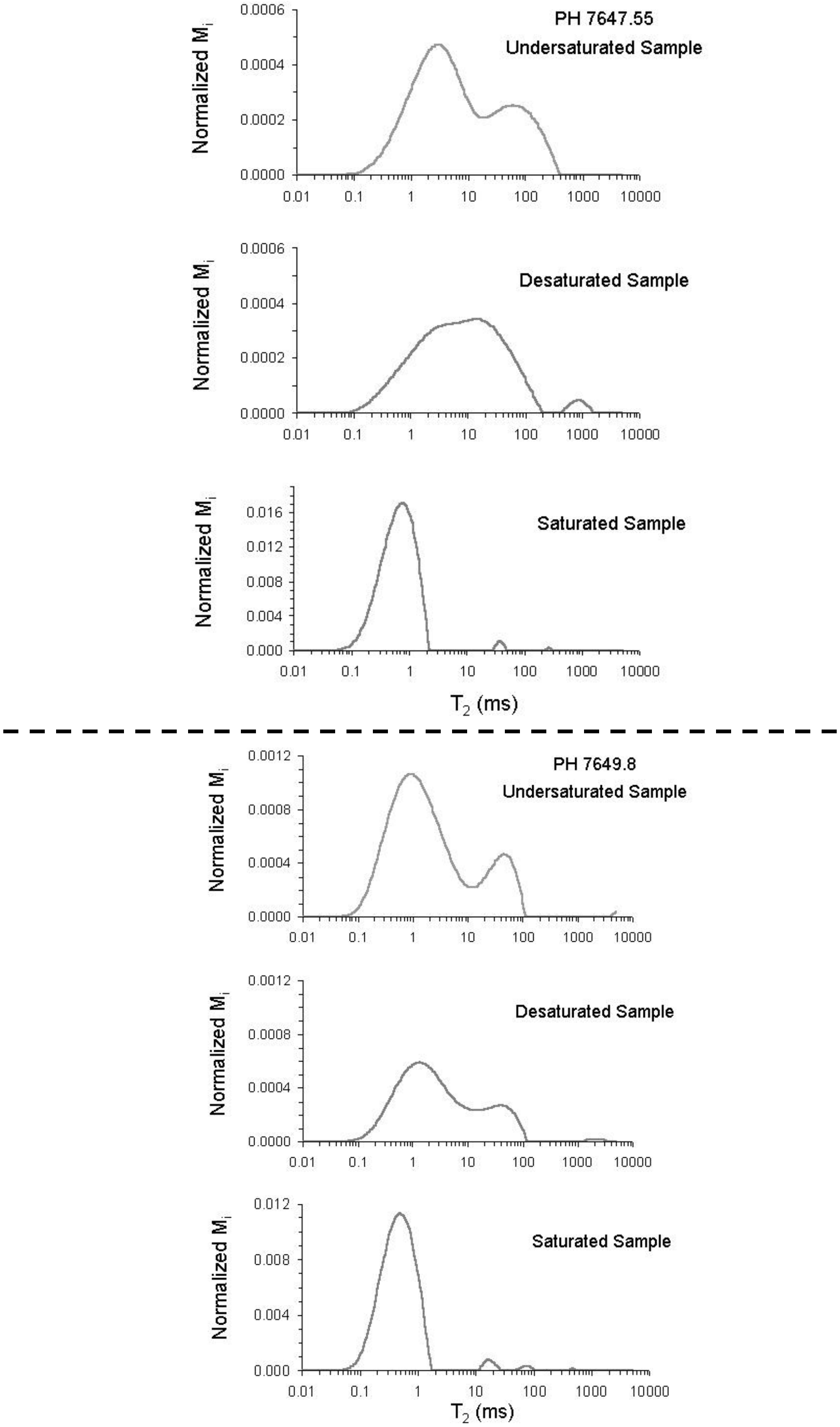

Figure C.3: T_2 distributions of the pebble shale unit, PH core. Each saturation state is represented. The sample name is located at the top right corner of the T_2 distribution of the undersaturated sample.

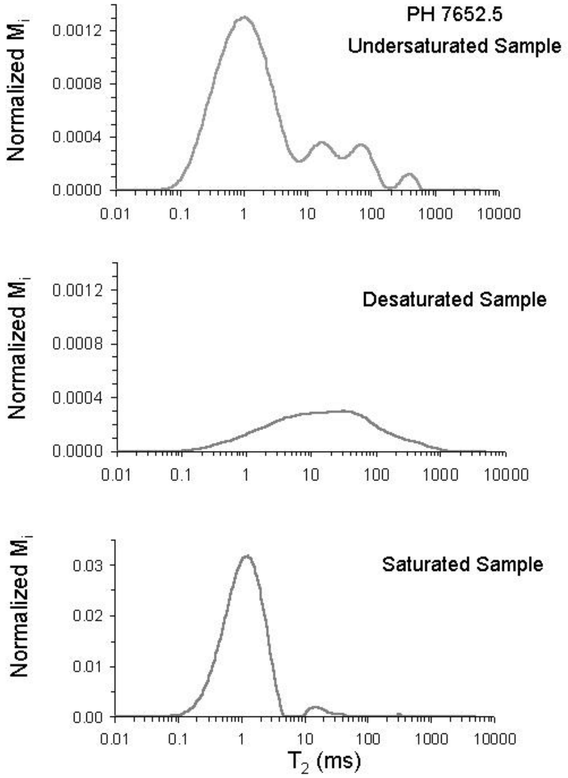

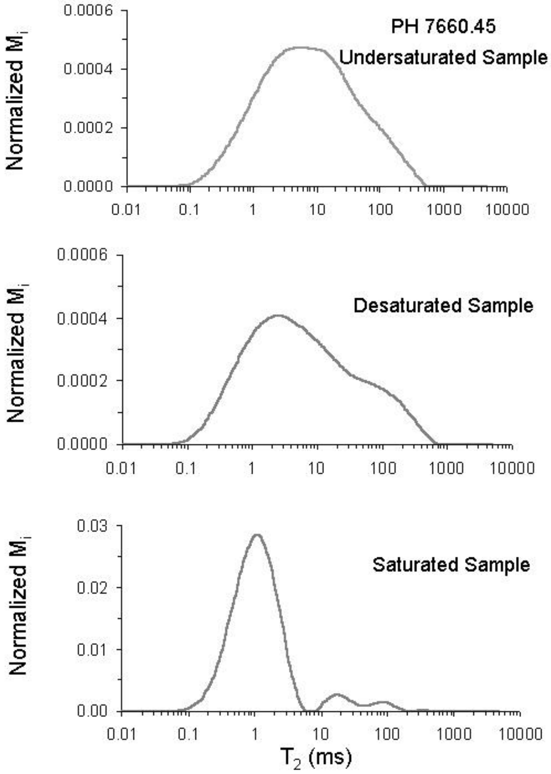

Figure C.3: Continued.

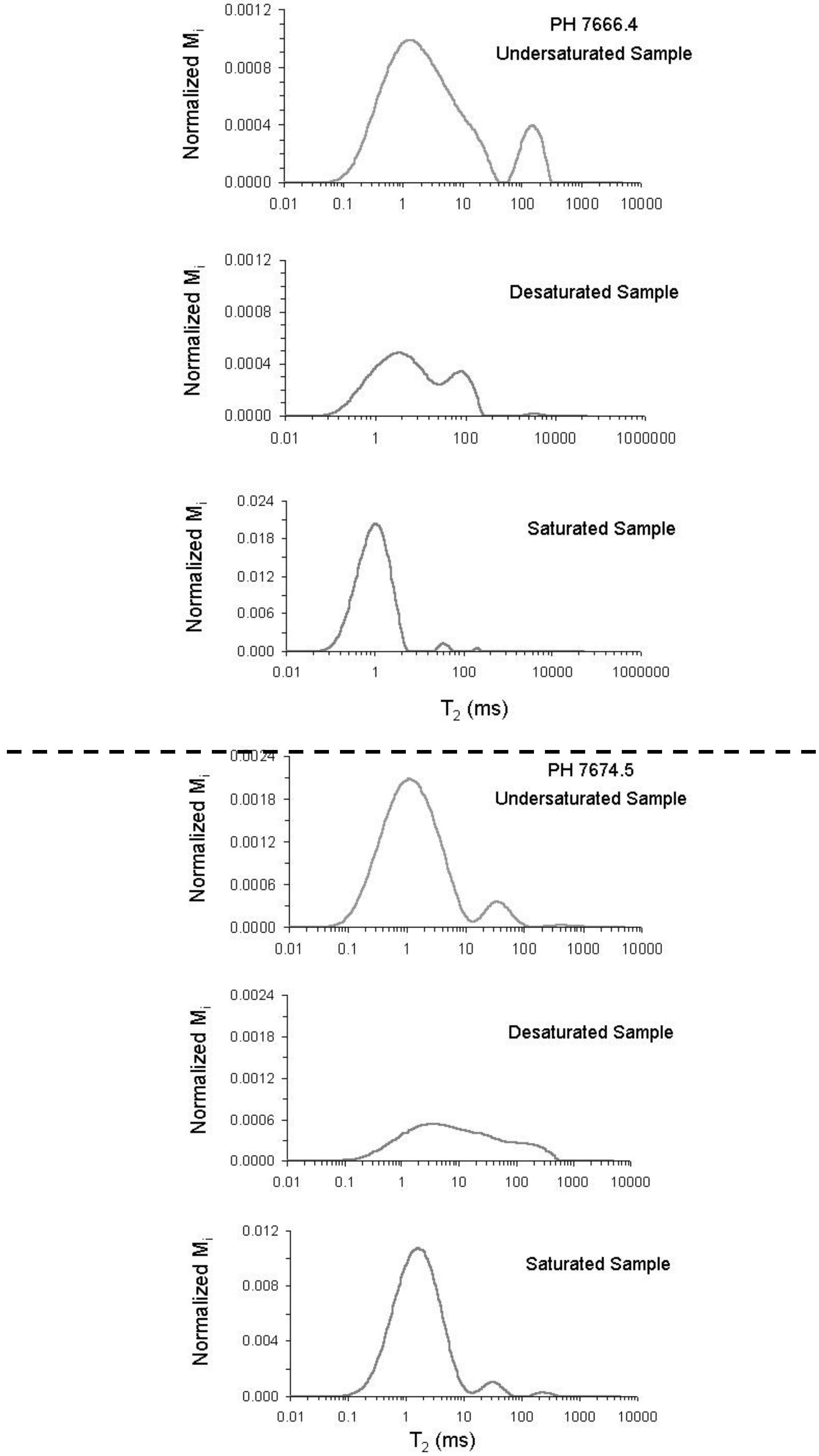

Figure C.3: Continued.

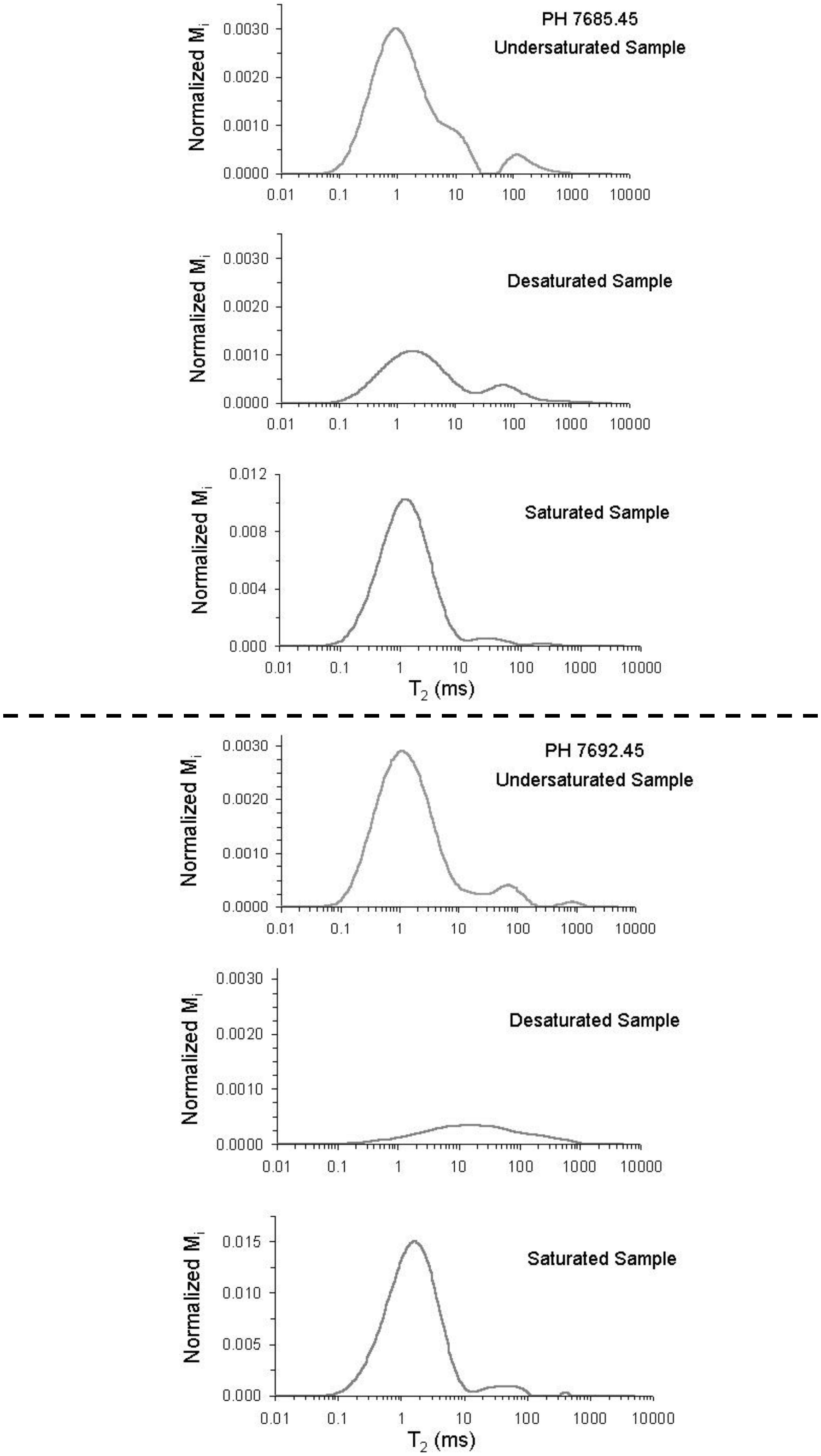

Figure C.3: Continued.

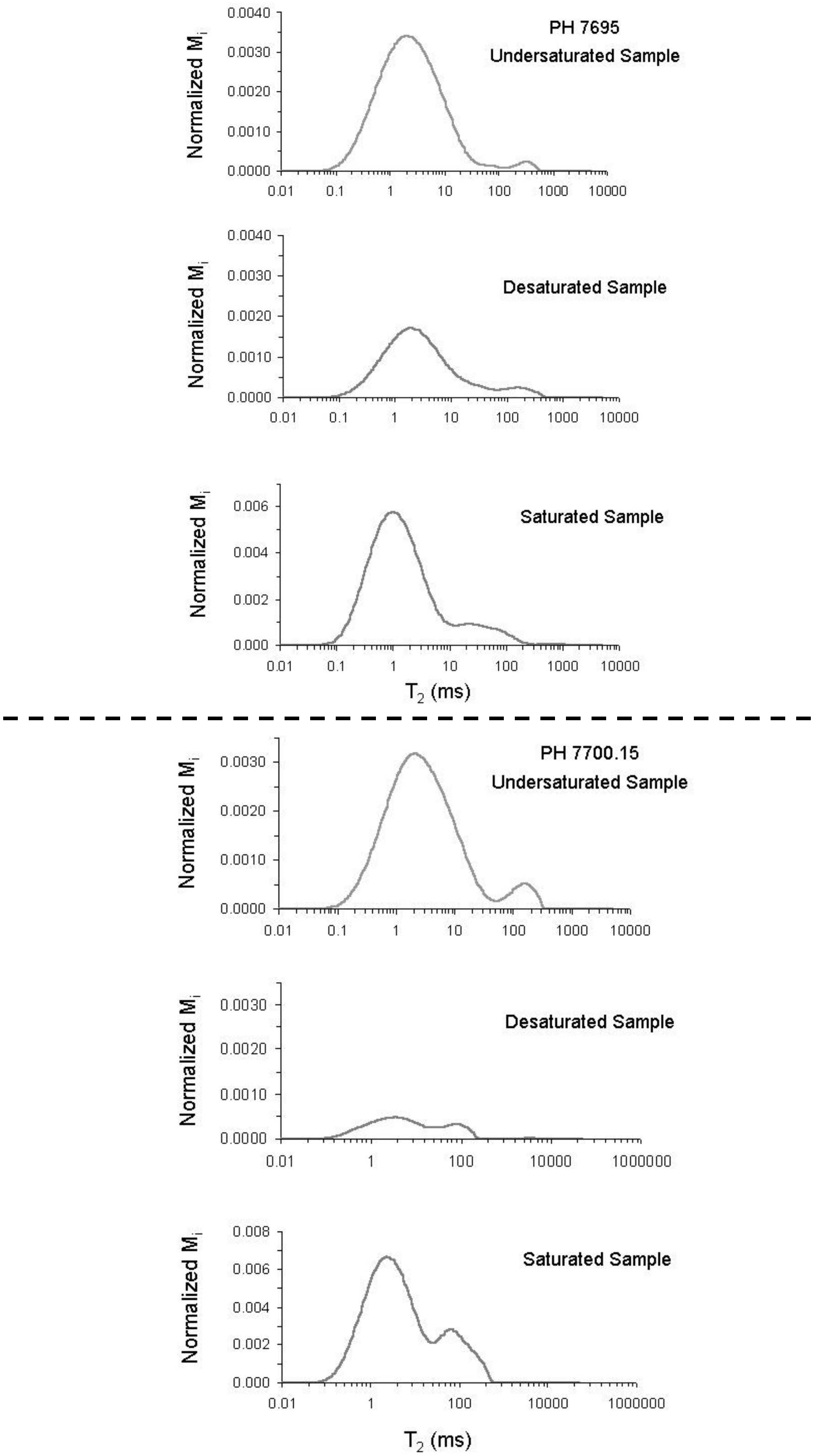

Figure C.3: Continued.

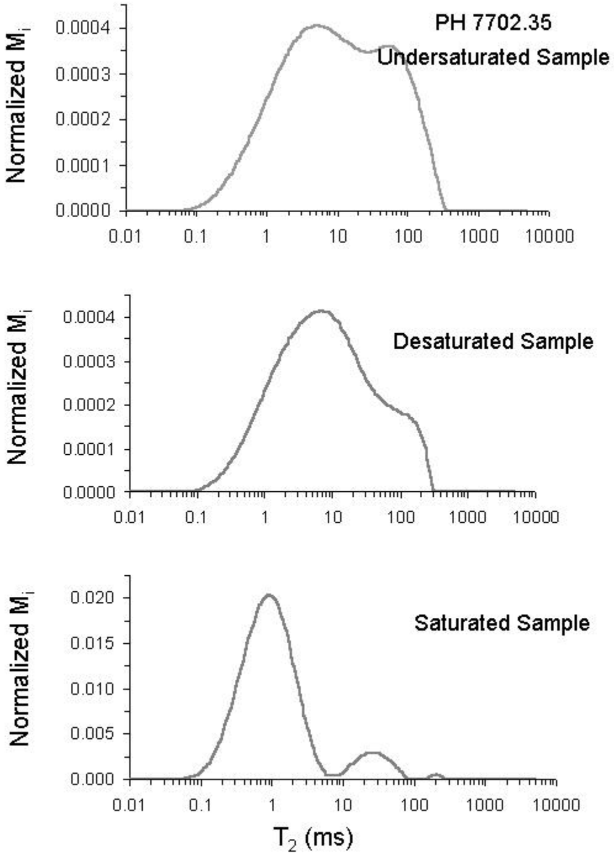

Figure C.3: Continued.

Table C.4: Permeabilities of the samples of the Lewis Shale (CH core).

Sample	SDR permeability		Coates-Timur permeabiliy		Air permeability	MIP permeability
	Original (md)	Recalc.* (md)	Original (md)	Recalc.** (md)	(md)	(md)
8075	0.000025	0.000016	0.0000002	0.0000003	< 0.0010	0.00003
8098.5	0.000024	0.000015	0.0000096	0.0000145	0.0010	0.00003
8112.5	0.000046	0.000028	0.0000191	0.0000288	< 0.0001	0.00004
8122.5	0.000035	0.000021	0.0000394	0.0000596	0.0010	0.00060
8131.6	0.000023	0.000014	0.0000529	0.0000800	0.0010	0.00003
8155	0.000063	0.000039	0.0000047	0.0000071	0.0210	0.00004
8162.5	0.000037	0.000023	0.0000047	0.0000072	0.0060	0.00004
8168	0.000079	0.000049	0.0000467	0.0000706	0.0050	0.00006
8187.5	0.000028	0.000018	0.0000042	0.0000064	0.0020	0.00005

* Recalculated SDR permeability and the C parameter of Table 3.11

** Recalculated SDR permeability with equation [3.7] and the C parameter of Table 3.11

Table C.5: Permeabilities of the samples of the Alaskan PH core.

Sample	SDR permeability	Coates-Timur permeabiliy	Air permeability	MIP permeability

	Original (md)	Recalc.* (md)	Original (md)	Recalc.** (md)	(md)	(md)
7647.55	0.000099	0.000097	0.000076	0.000077	0.05	0.000200
7649.8	0.000002	0.000002	0.000001	0.000001	0.02	0.000001
7652.5	0.000901	0.000877	0.000042	0.000043	0.05	0.000300
7660.45	0.001166	0.001135	0.001464	0.001500	0.03	0.000200
7666.4	0.000114	0.000111	0.000050	0.000052	0.02	0.002500
7674.5	0.000108	0.000105	0.000051	0.000052	0.28	0.000700
7685.45	0.000071	0.000069	0.000044	0.000045	Not available	Not available
7692.45	0.000312	0.000303	0.000216	0.000222	Not available	Not available
7695	0.000017	0.000017	0.000067	0.000068	5.5	15.600000
7700.15	0.000408	0.000397	0.001971	0.002019	6	0.471000
7702.35	0.000421	0.000410	0.000893	0.000915	0.01	0.000200

* and ** references are in Table C.4.

Table C.6: Permeabilities of the samples of the Lewis Shale (CSM core).

Sample	SDR permeability		Coates-Timur permeabiliy		Air permeability	MIP permeability
	Original (md)	Recalc.* (md)	Original (md)	Recalc.** (md)	(md)	(md)
295.9	0.00720	0.00104	0.000180	0.000678	0.008	0.017
307.6	0.00743	0.00104	0.000356	0.00163	0.012	0.015
319	0.00030	0.00004	0.000023	0.00011	0.024	0.032
433.3	0.00974	0.00163	0.000458	0.00205	0.034	0.248
440.1	0.01164	0.00202	0.000227	0.00103	0.476	0.017
447.2	0.00315	0.00044	0.000007	0.00003	0.030	0.013
450	0.00377	0.00053	0.000232	0.00106	0.010	0.013
915.5	0.00880	0.00123	0.000283	0.00129	0.090	0.007
918.3	0.00266	0.00037	0.000140	0.00064	Not available	0.005
920.9	0.00056	0.00008	0.000033	0.00015	Not available	0.006
927.6	0.00077	0.00011	0.000005	0.00002	0.005	0.006
930.2	0.00148	0.00021	0.000031	0.00014	0.005	0.006
930.4	0.00846	0.00118	0.000012	0.00006	0.007	0.005
931.7	0.00293	0.00041	0.000034	0.00016	Not available	0.005
932.7	0.00067	0.00009	0.000002	0.00001	Not available	0.005
932.9	0.00090	0.00013	0.000017	0.00008	Not available	0.005
934.1	0.00118	0.00017	0.000048	0.00022	0.011	0.006
1589	0.00054	0.00008	0.000198	0.00090	0.628	0.013
1605.8	0.00091	0.00013	0.000010	0.00004	0.007	0.002
1621.5	0.00091	0.00013	0.000096	0.00044	0.001	0.003

* and ** references are in Table C.4.

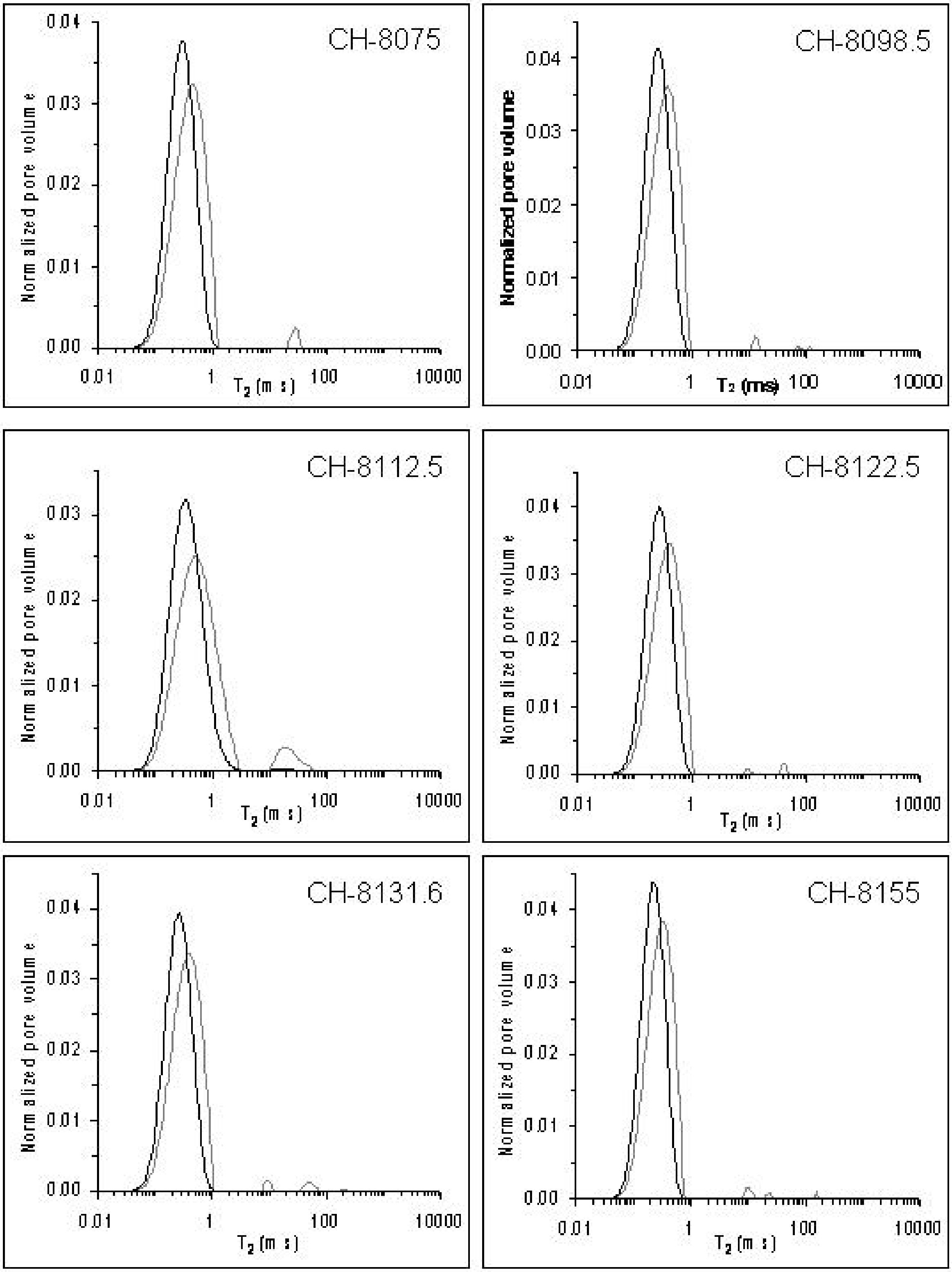

Figure C.4: Comparison of T_2 distributions and pseudo-intrusion distributions. The gray line identifies the T_2 distributions and the solid black line represents the pseudo-intrusion distributions.

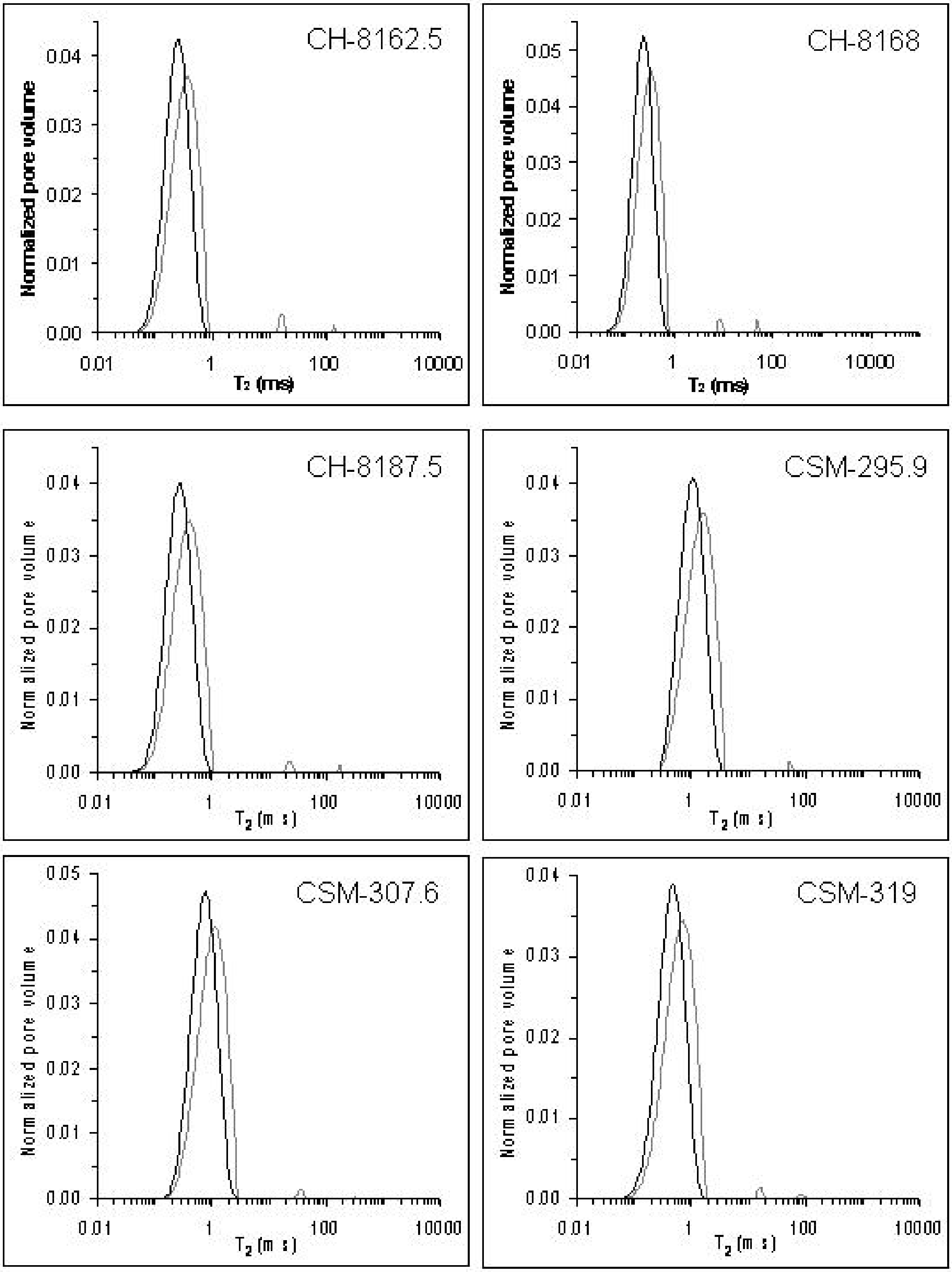

Figure C.4: Continued.

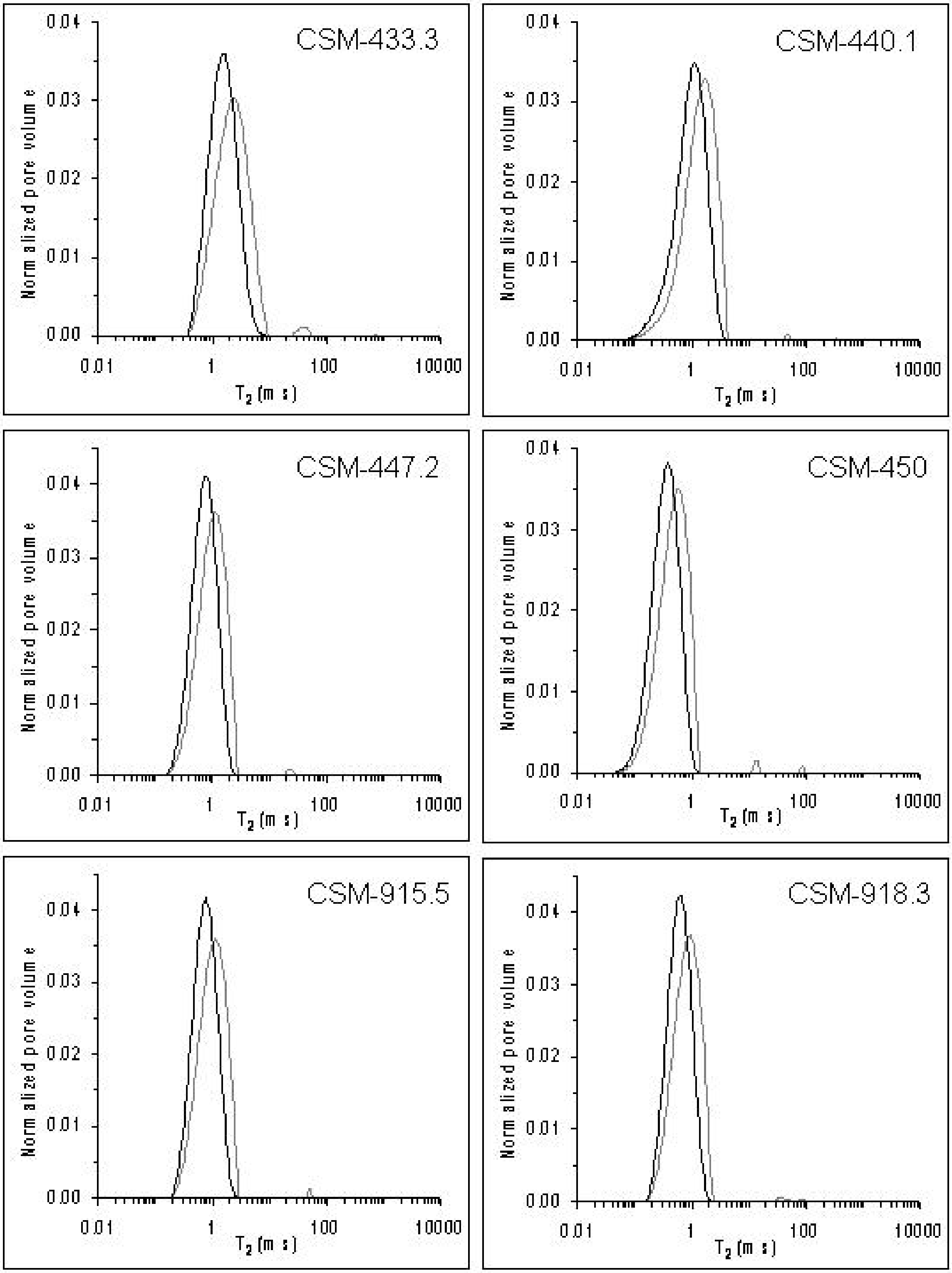

Figure C.4: Continued.

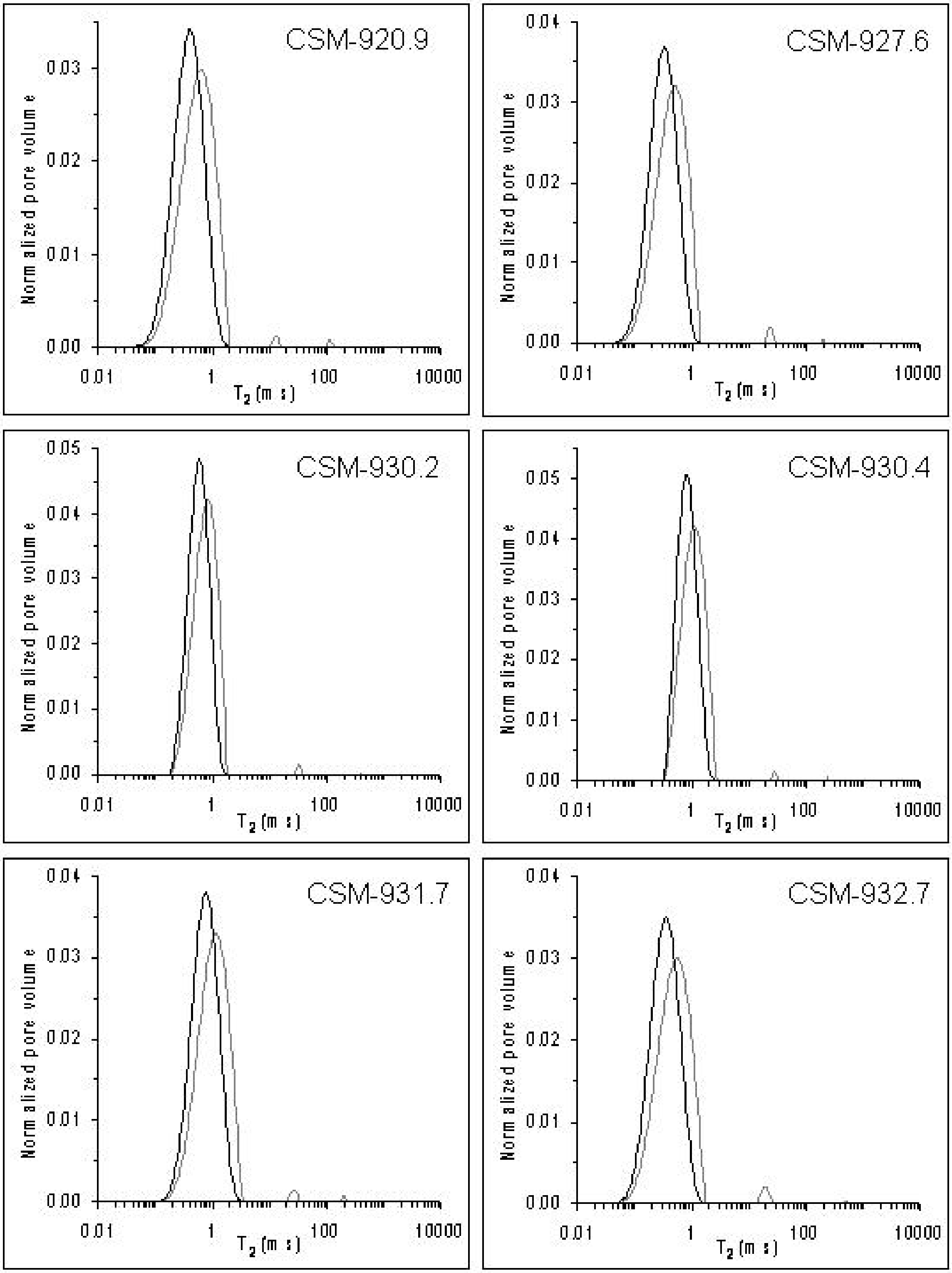

Figure C.4: Continued.

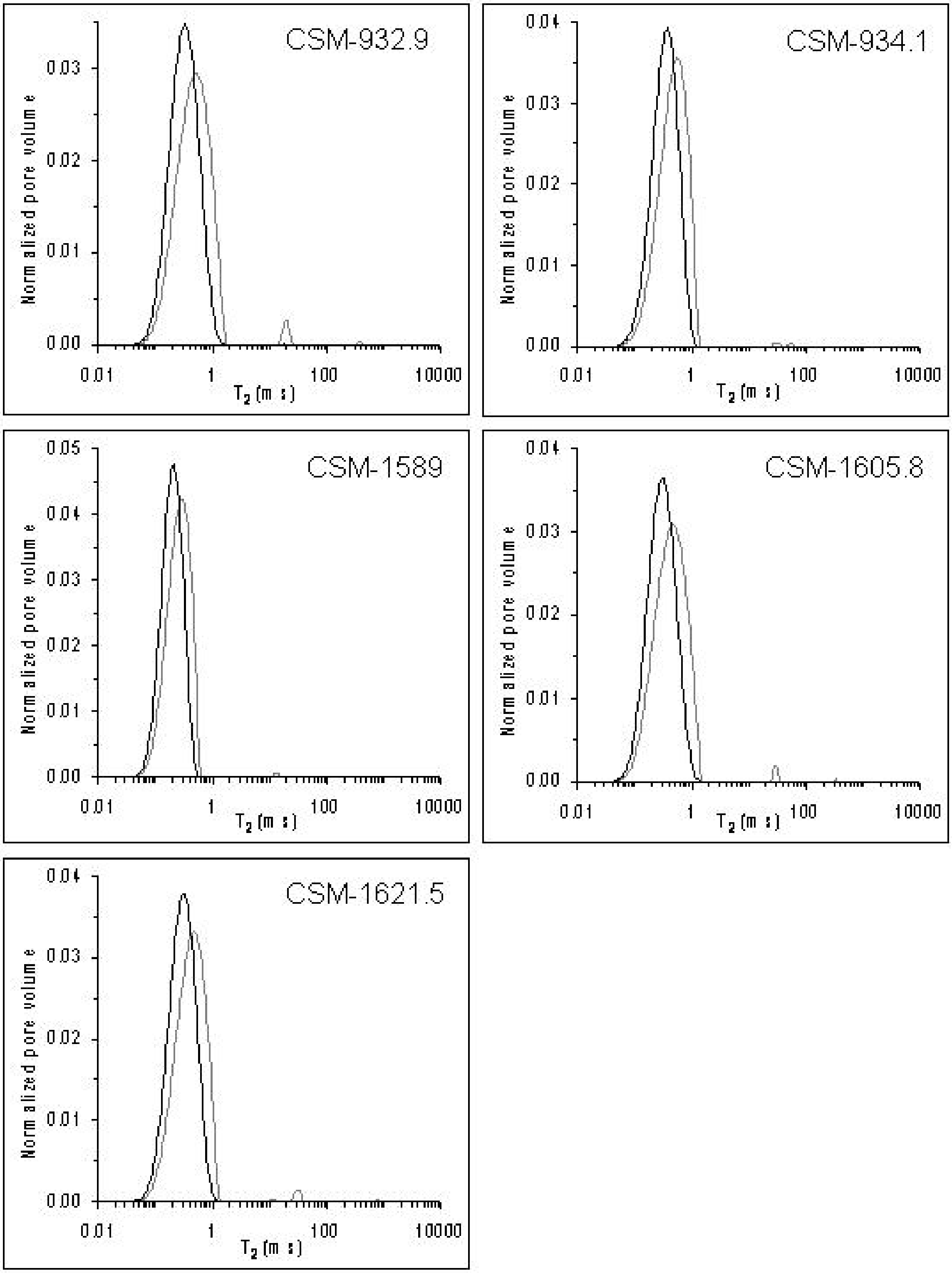

Figure C.4: Continued.

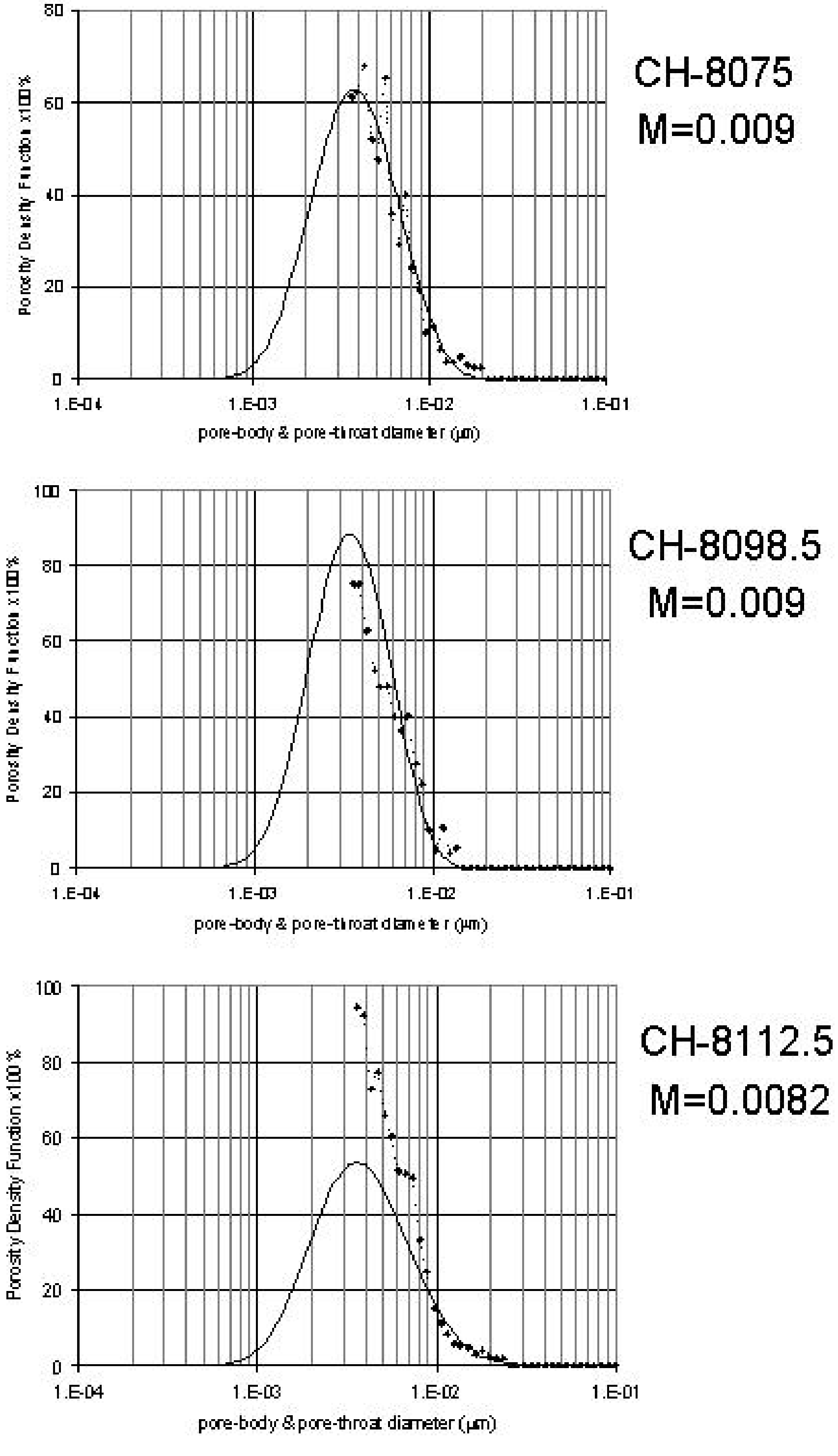

Figure C.5: Porosity probability functions of the CH samples. The solid black line represents the NMR pseudo-intrusion porosity density function, and the dashed black line is the mercury pore-throat porosity density function. The used scaling factor (M) between the functions is indicated together with the sample name.

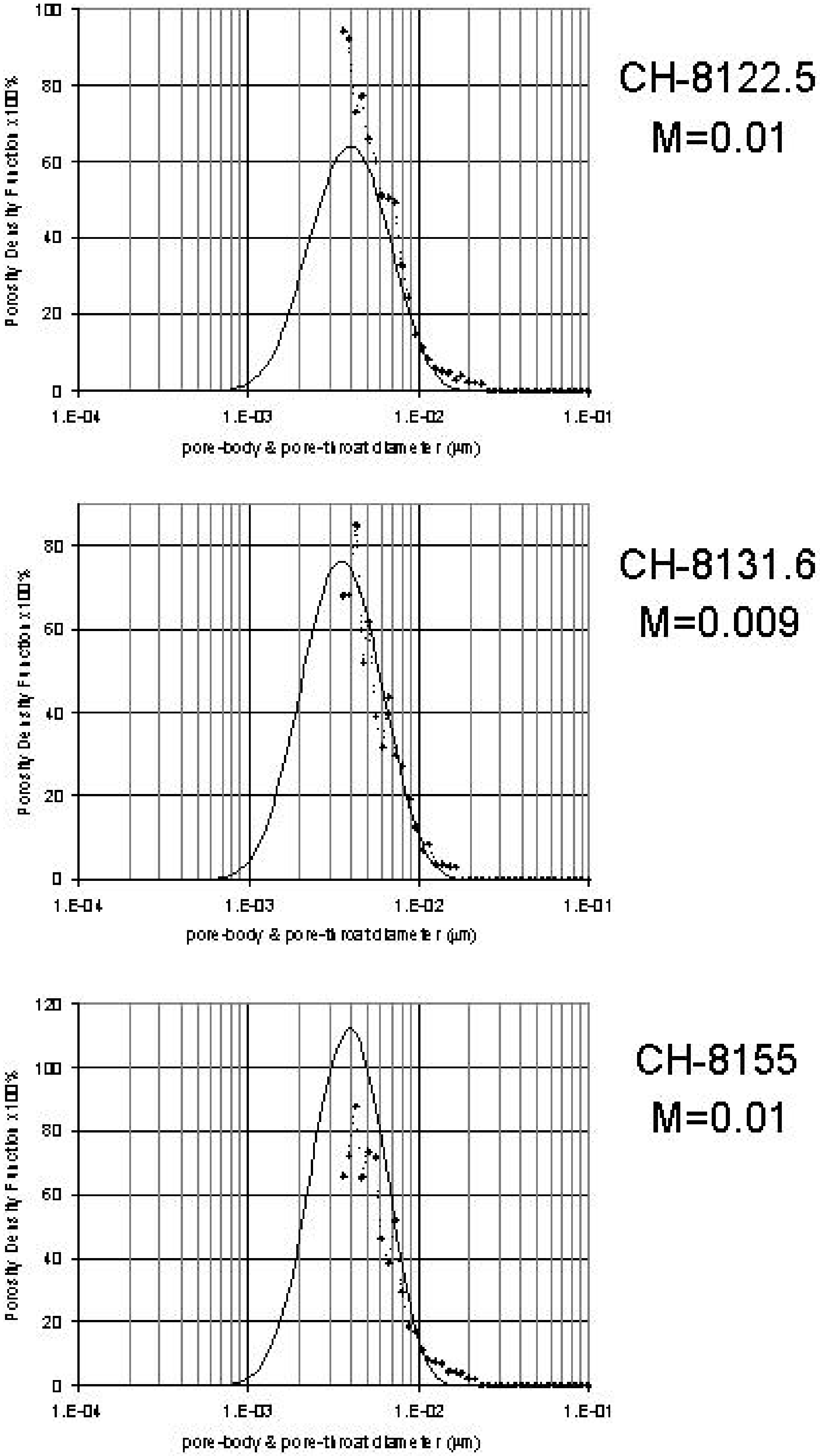

Figure C.5: Continued.

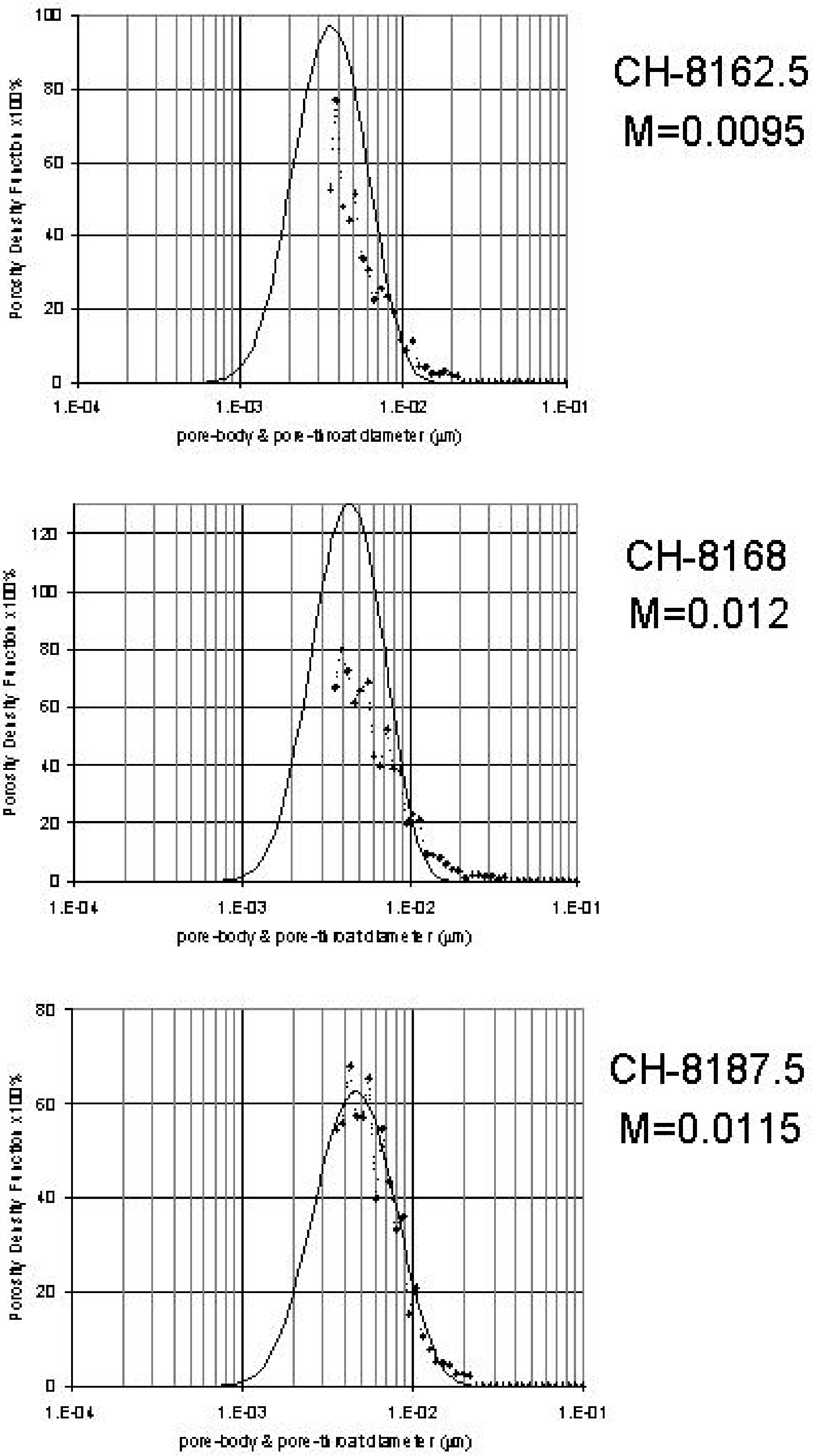

Figure C.5: Continued.

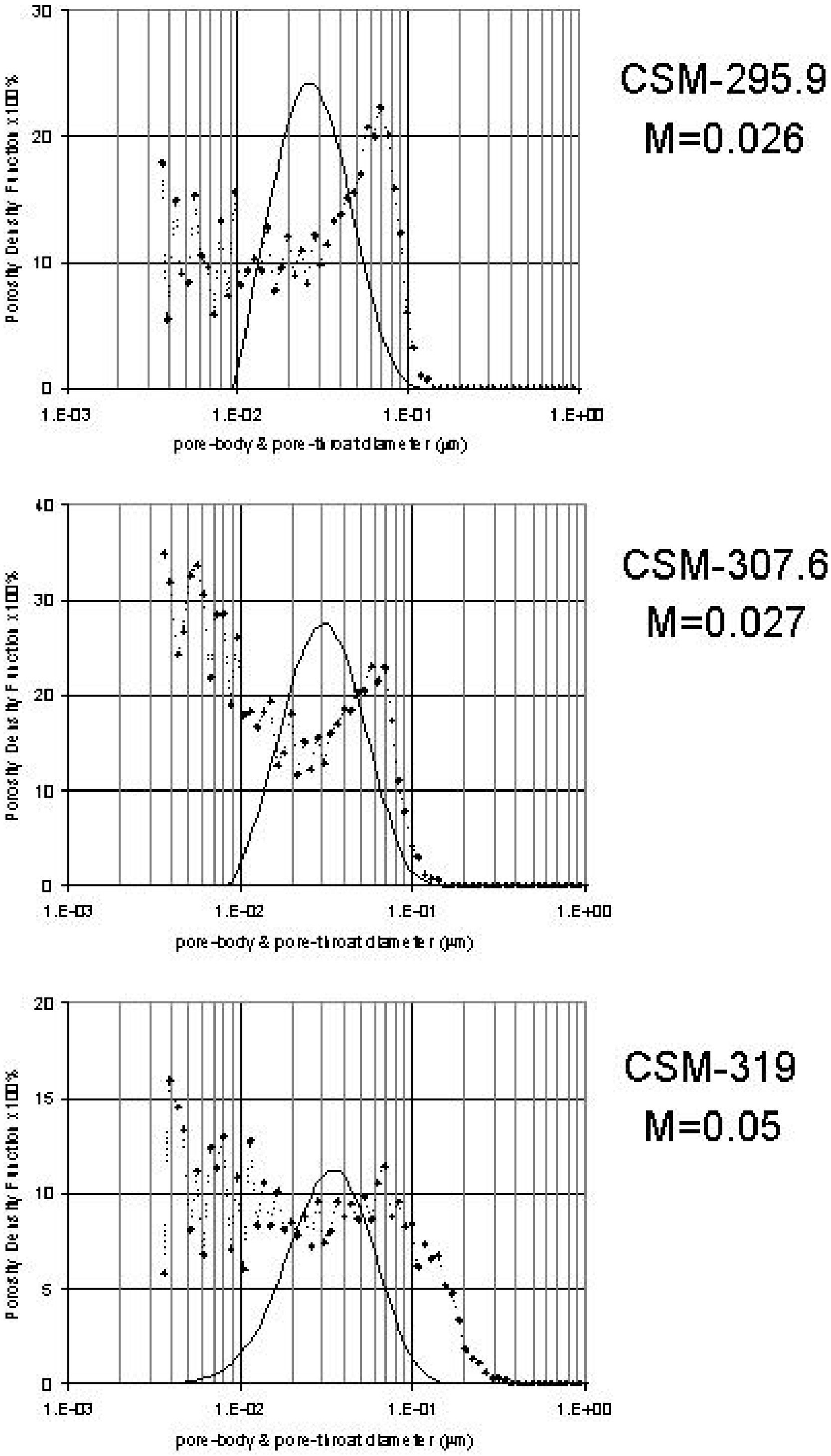

Figure C.6: Porosity probability functions of the CSM samples. The solid black line represents the NMR pseudo-intrusion porosity density function, and the dashed black line is the mercury pore-throat porosity density function. The used scaling factor (M) between the functions is indicated together with the sample name.

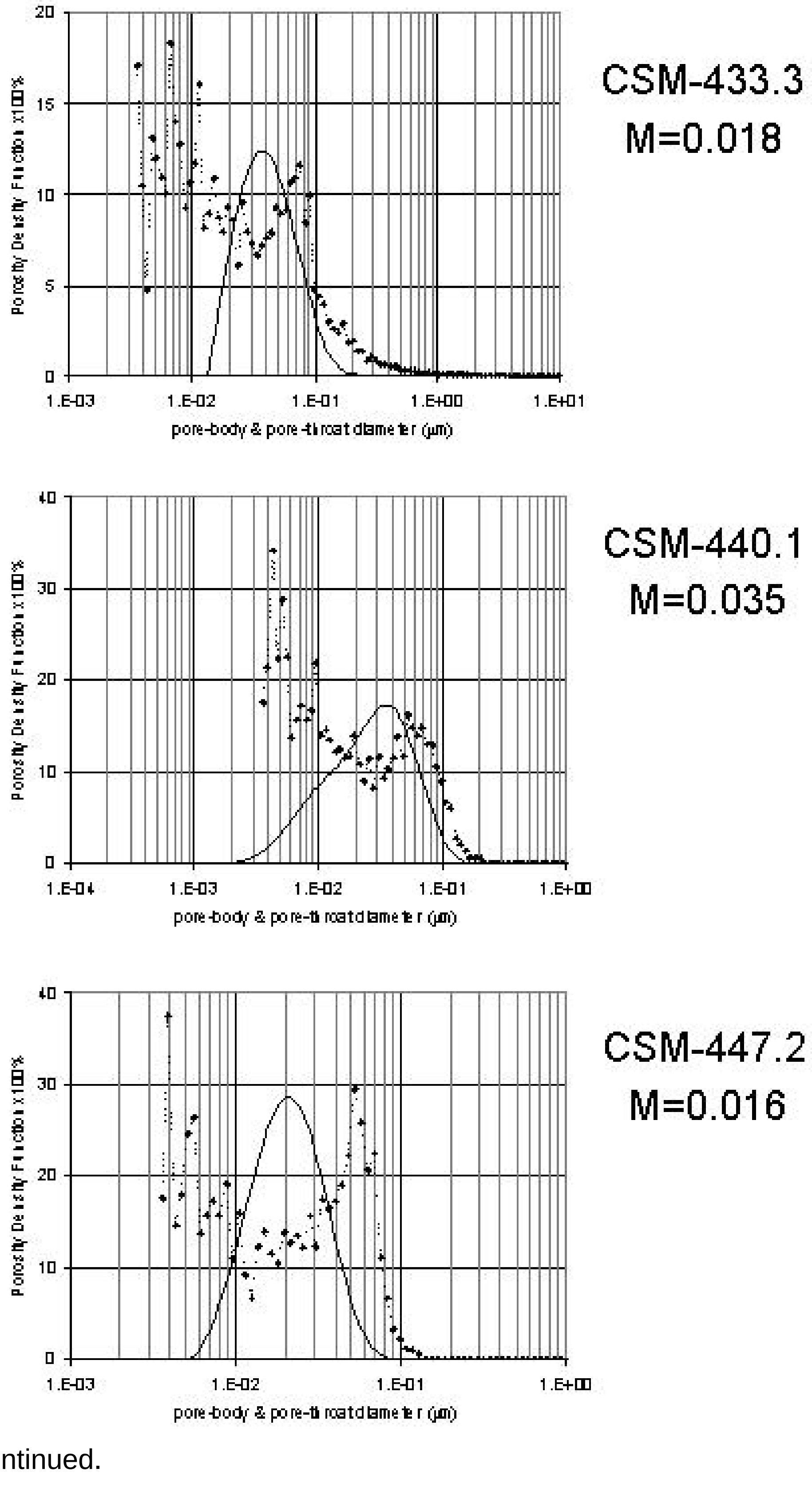

Figure C.6: Continued.

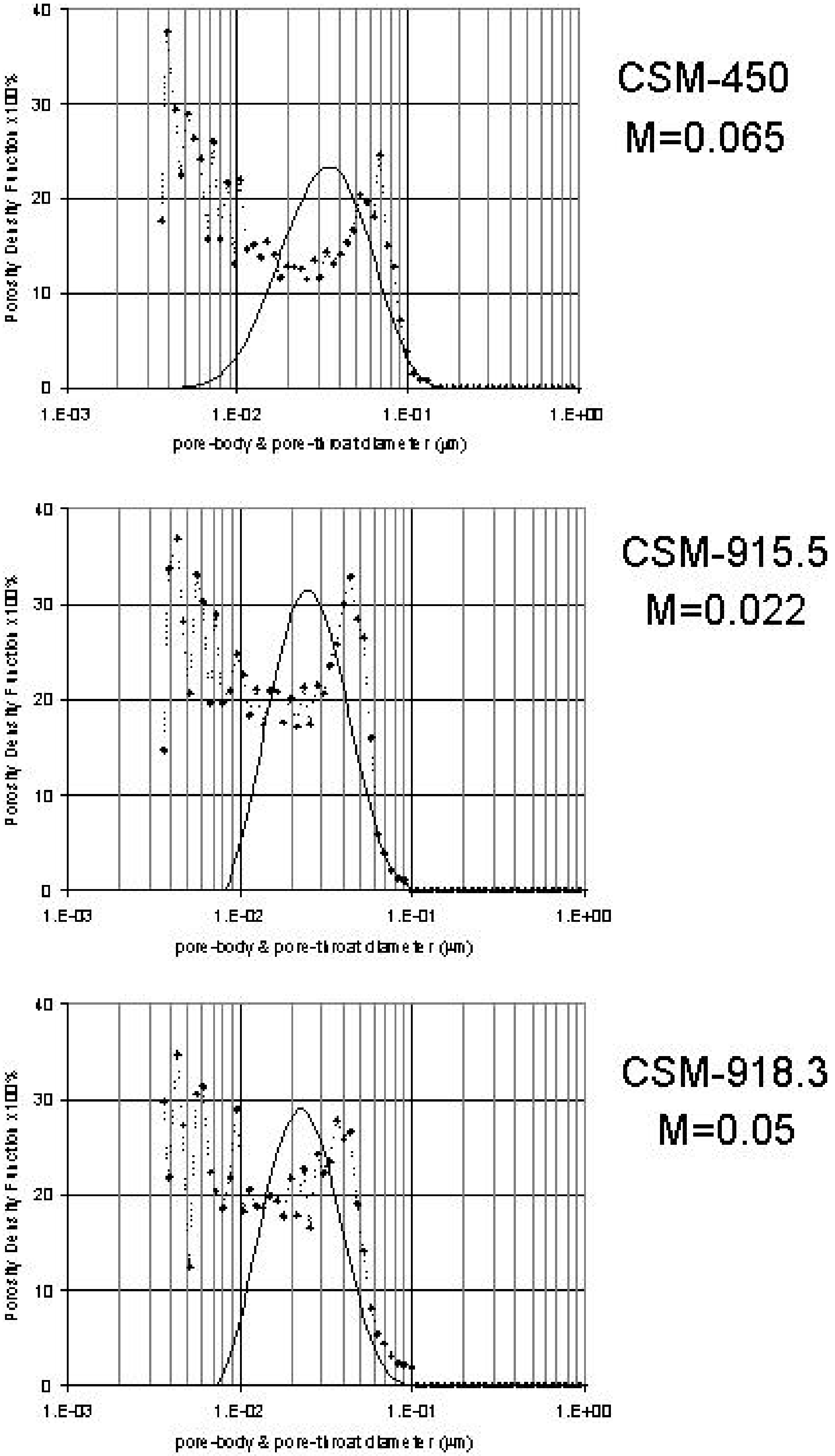

Figure C.6: Continued.

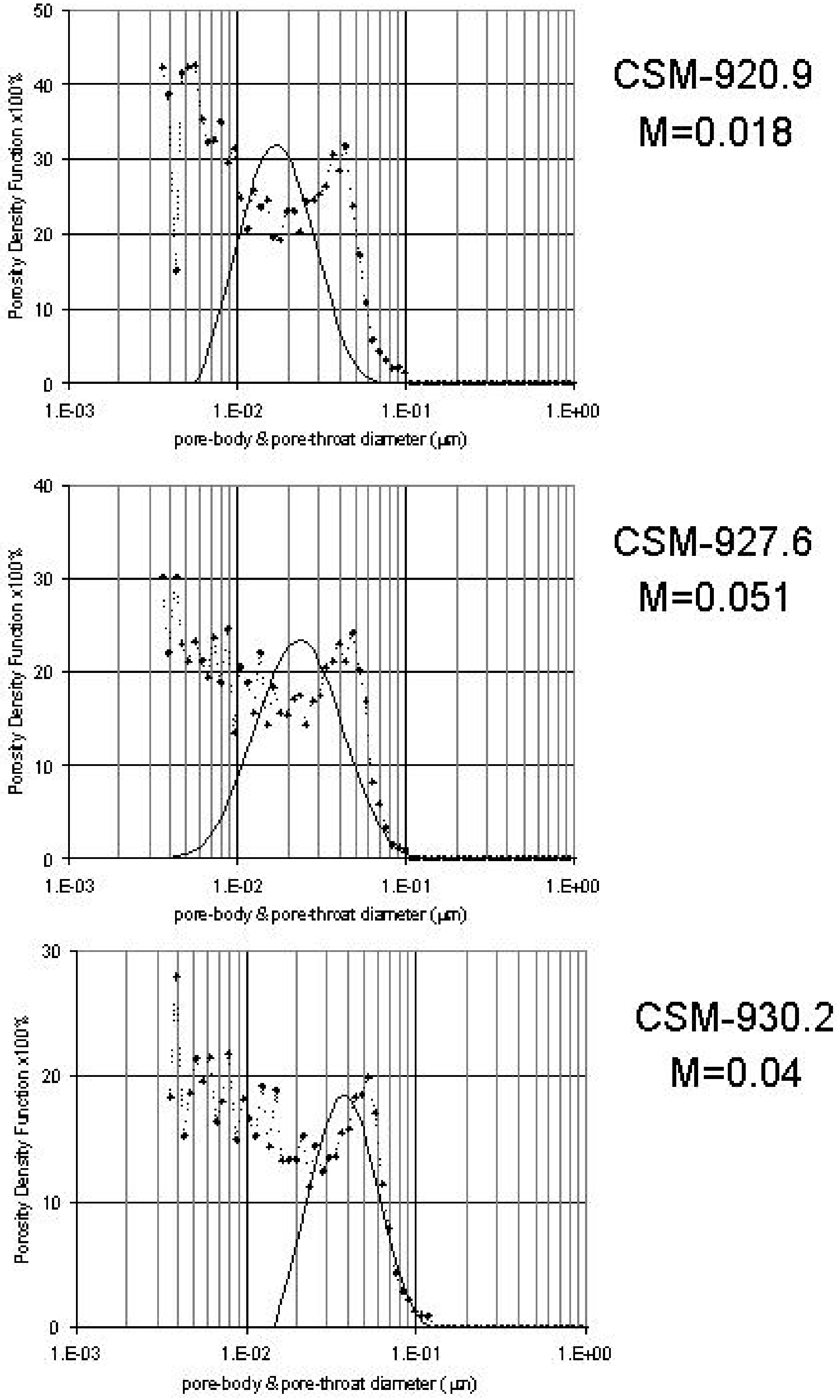

Figure C.6: Continued.

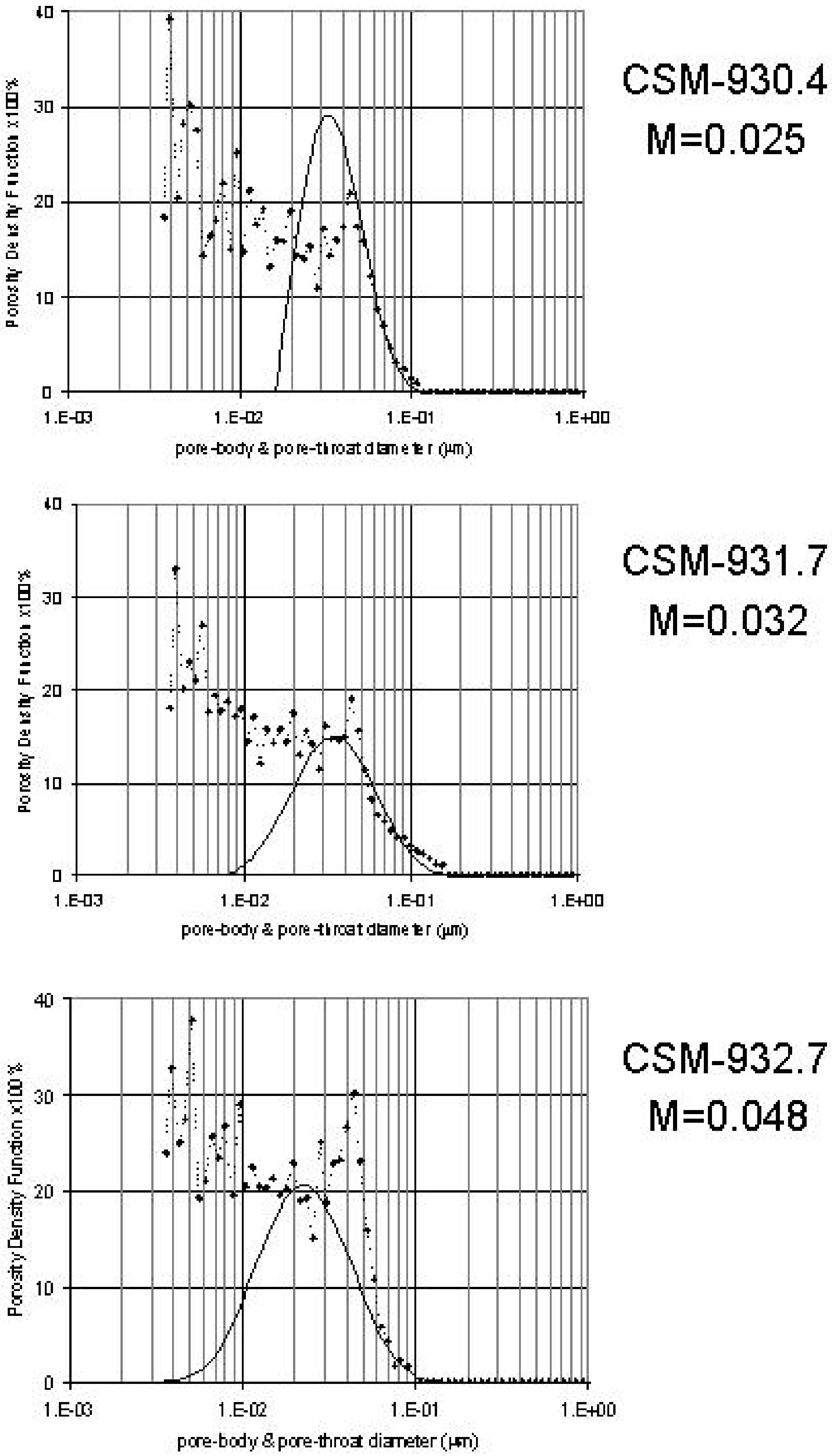

Figure C.6: Continued.

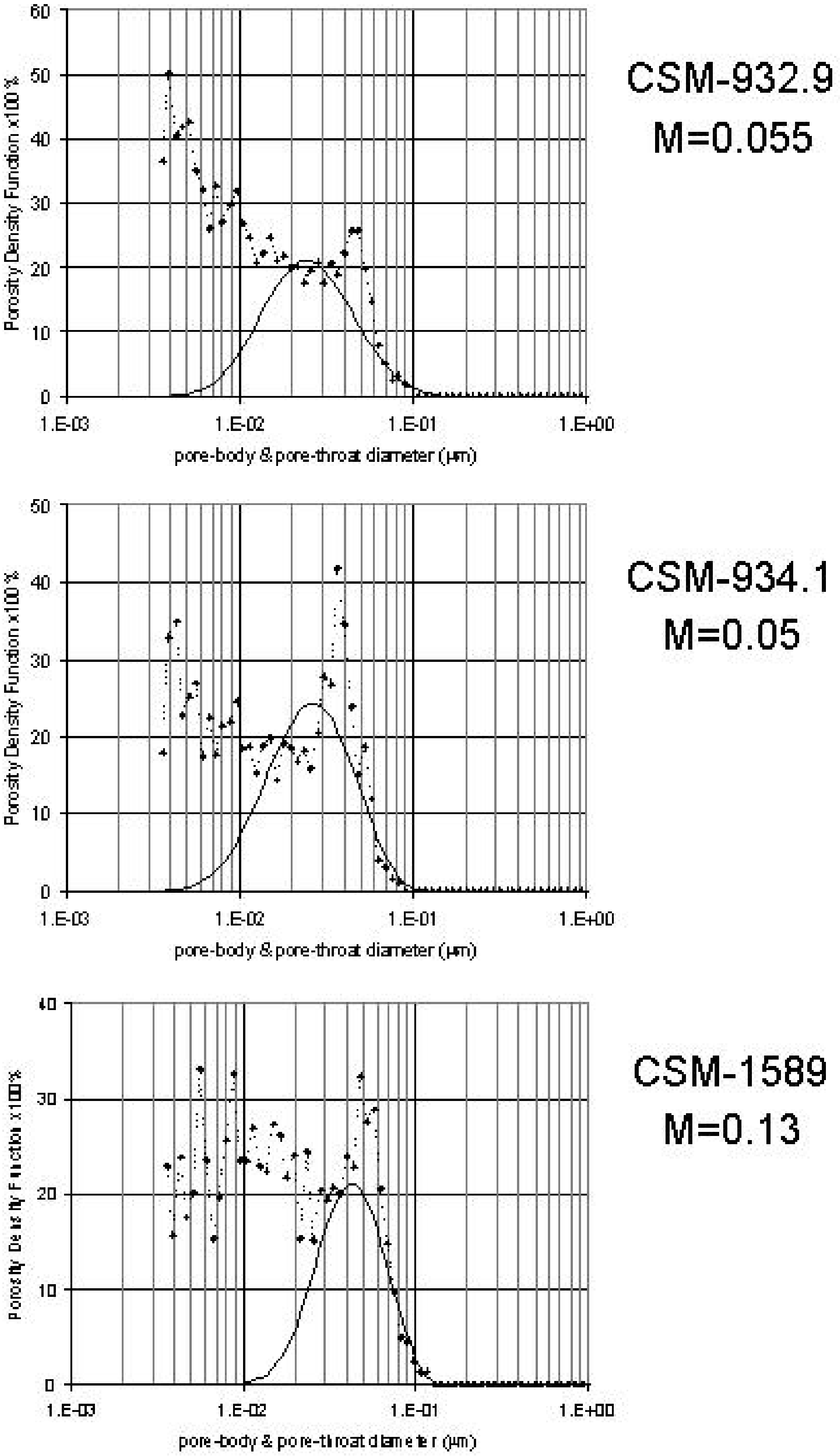

Figure C.6: Continued.

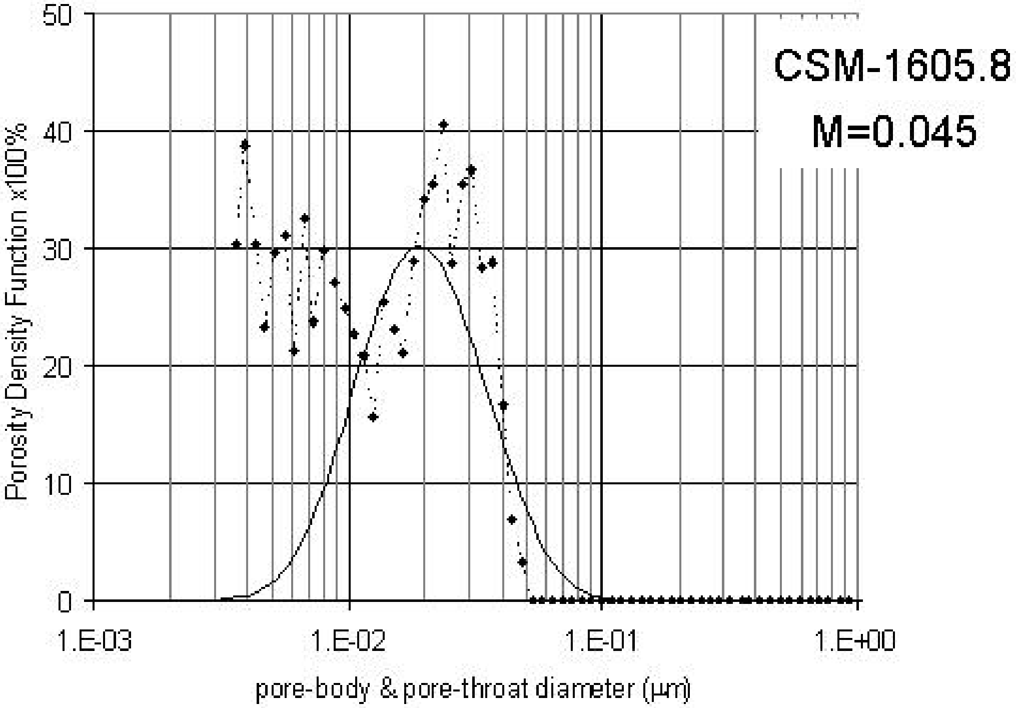

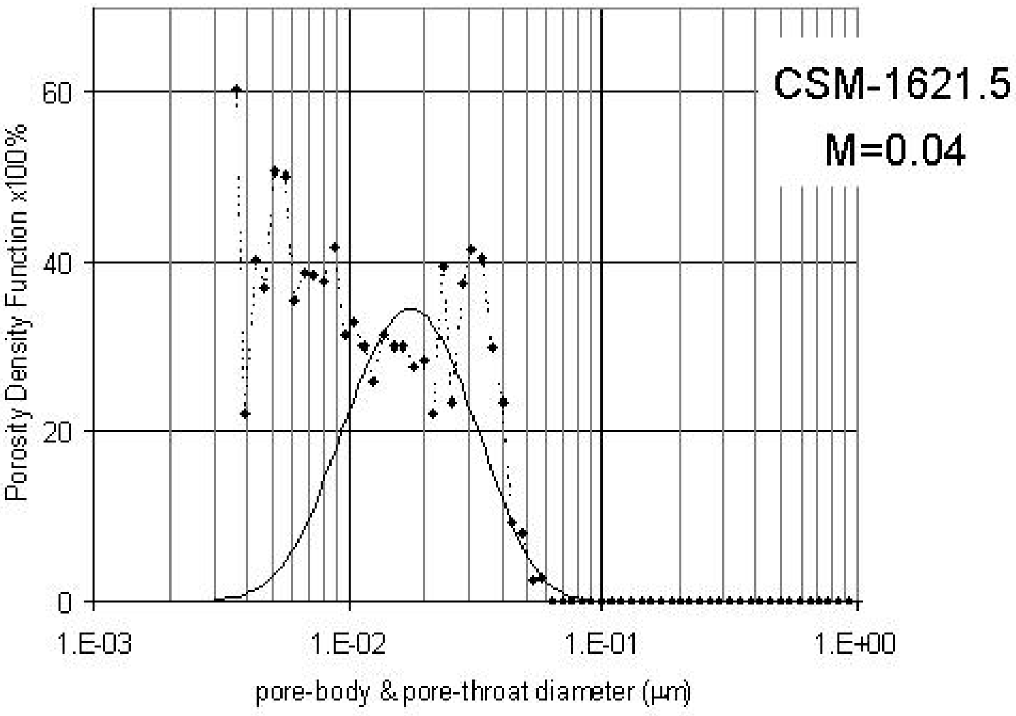

Figure C.6: Continued.

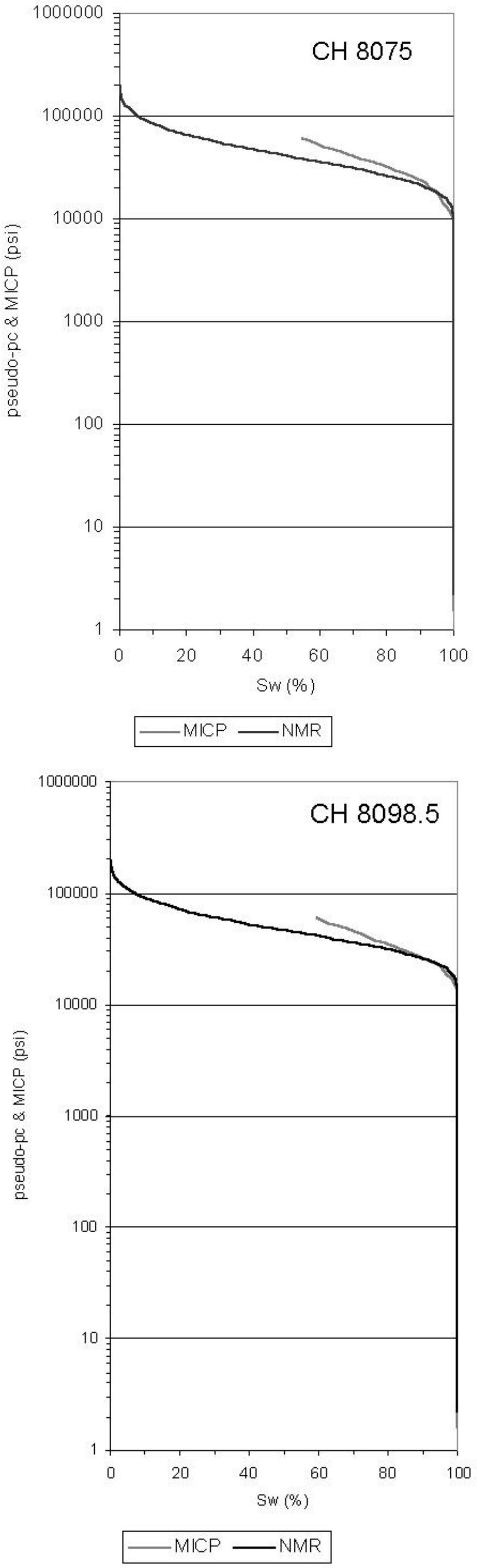

Figure C.7: MICP and NMR pseudo-capillary pressure curves of the CH core.

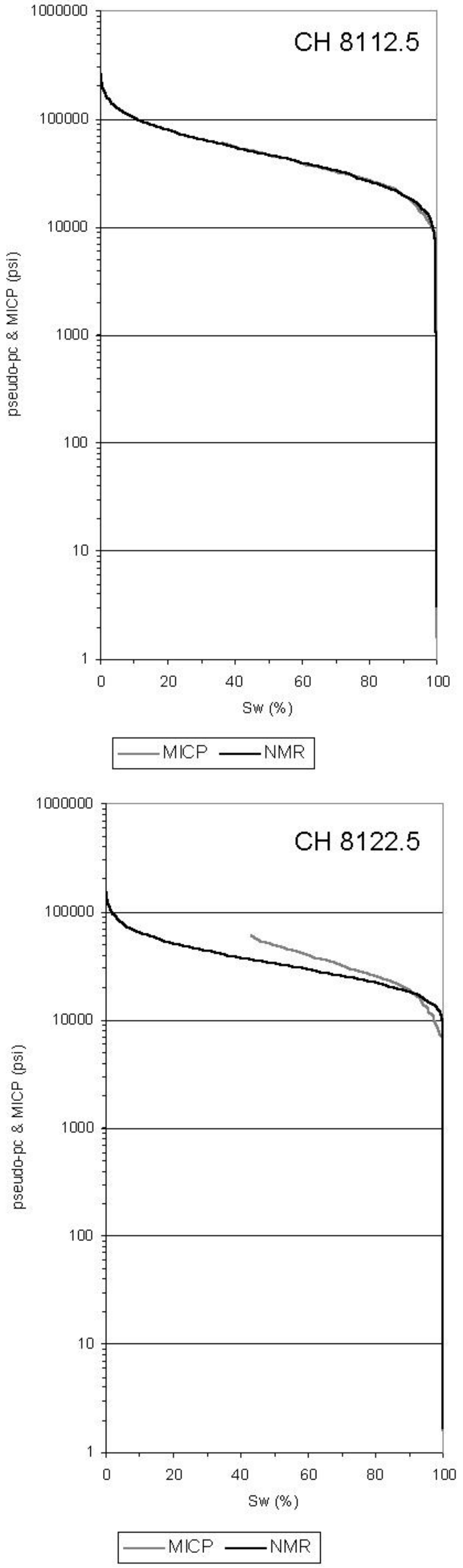

Figure C.7: Continued.

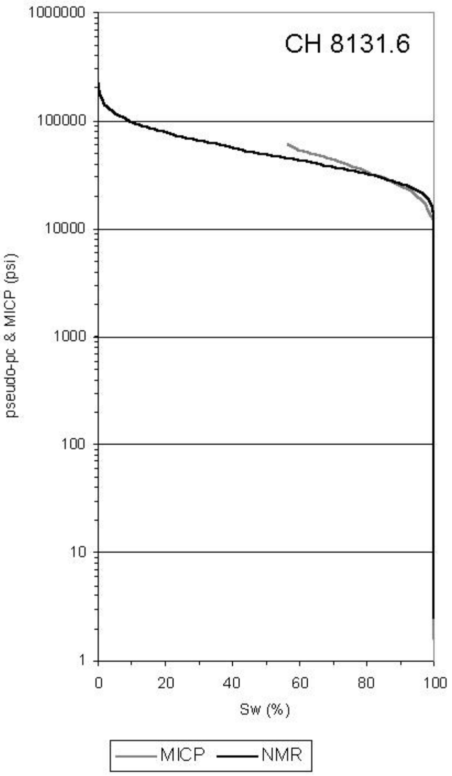

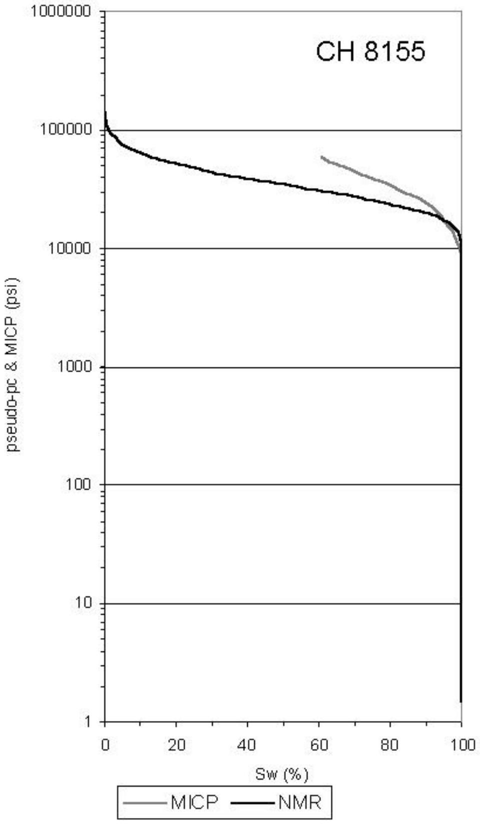

Figure C.7: Continued.

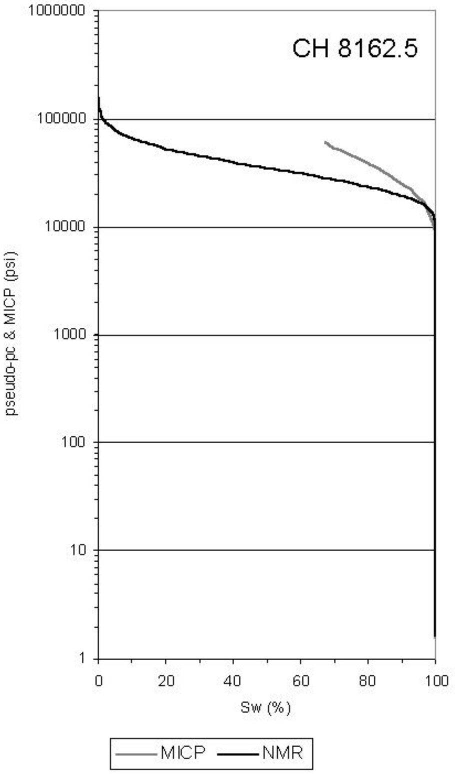

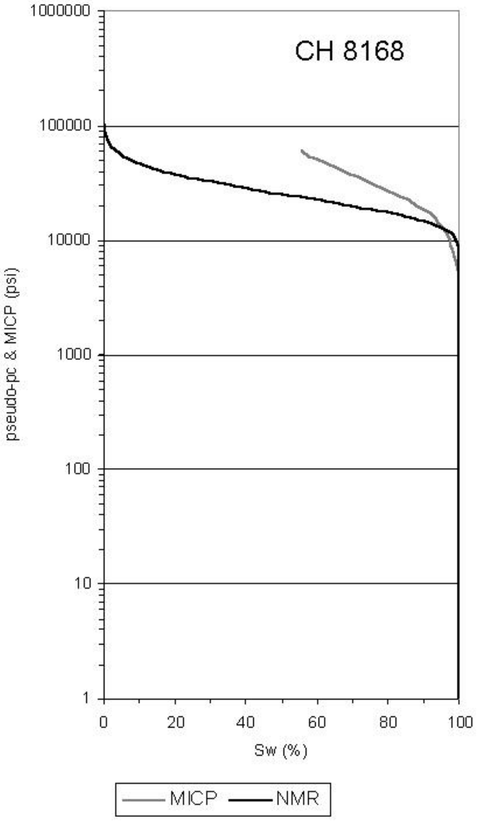

Figure C.7: Continued.

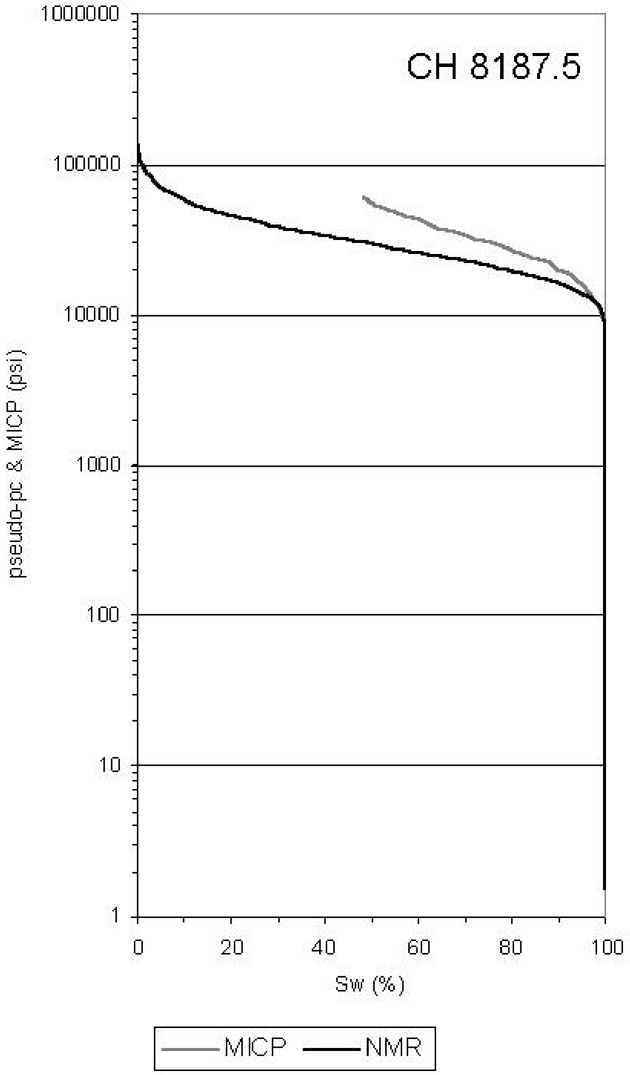

Figure C.7: Continued.

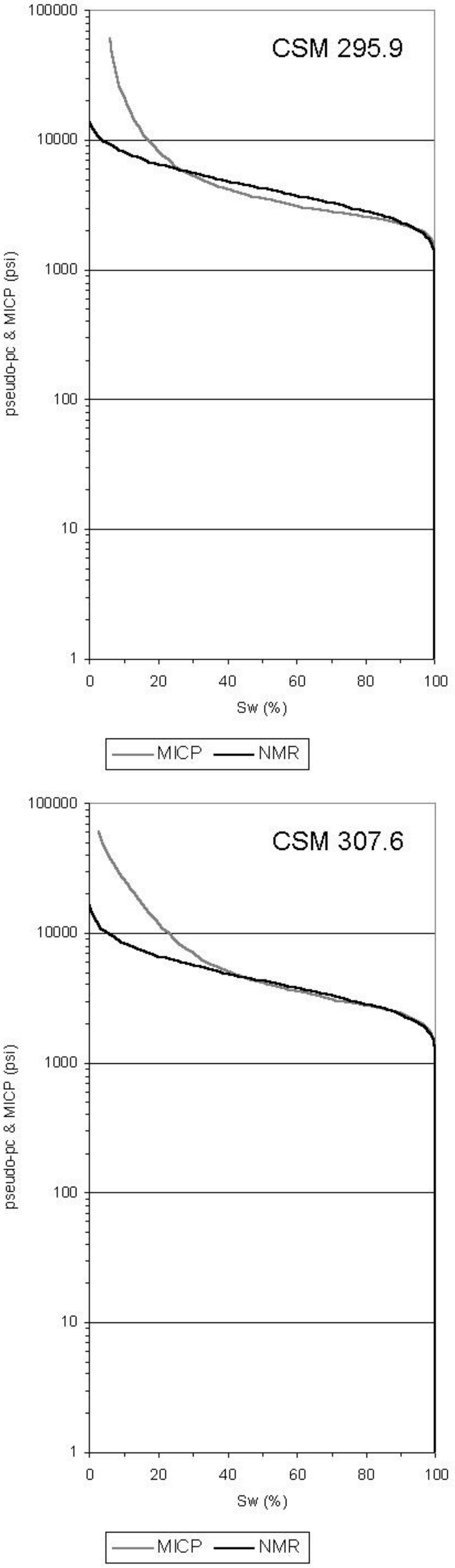

Figure C.8: MICP and NMR pseudo-capillary pressure curves of the CSM core.

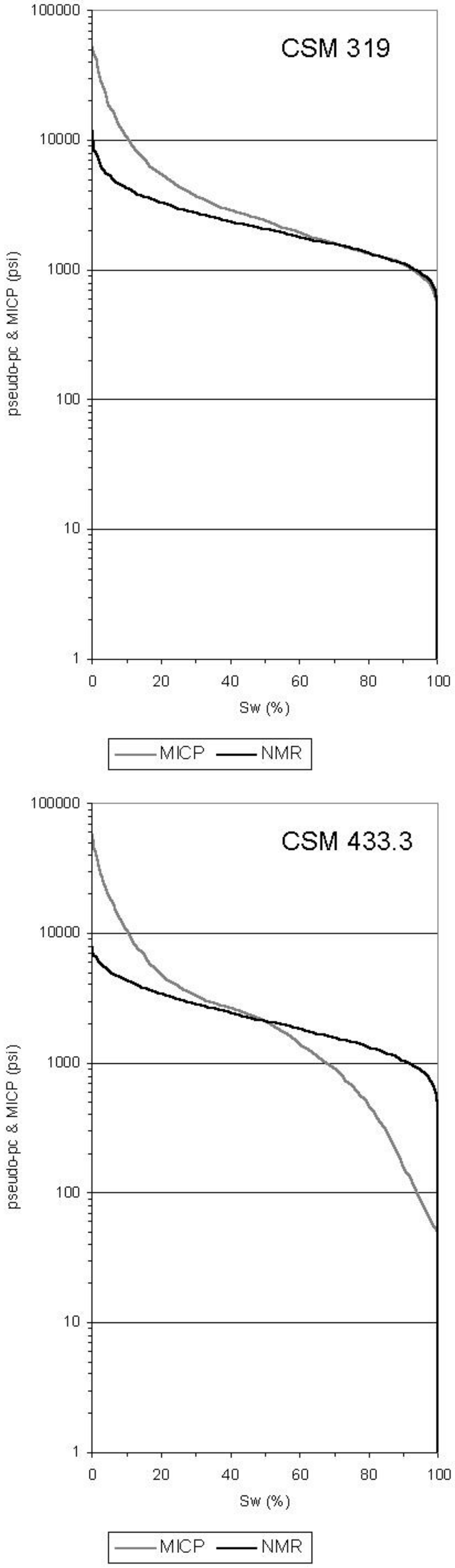

Figure C.8: Continued.

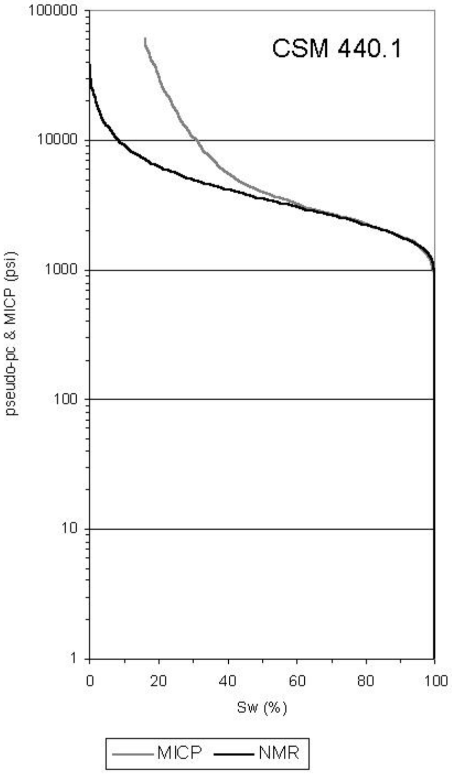

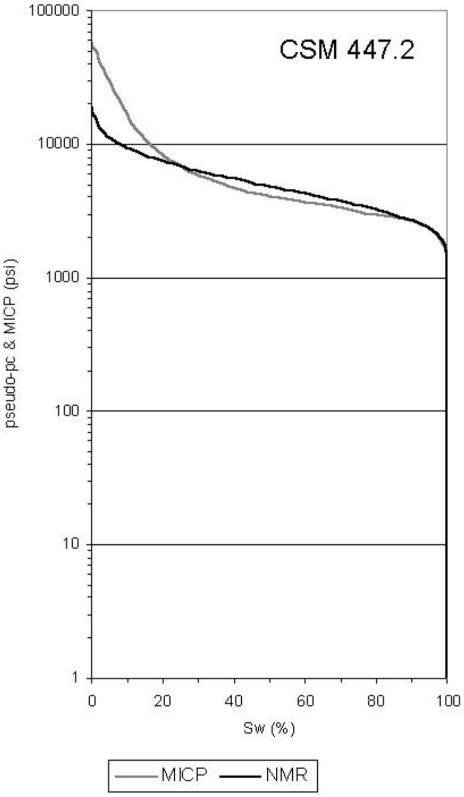

Figure C.8: Continued.

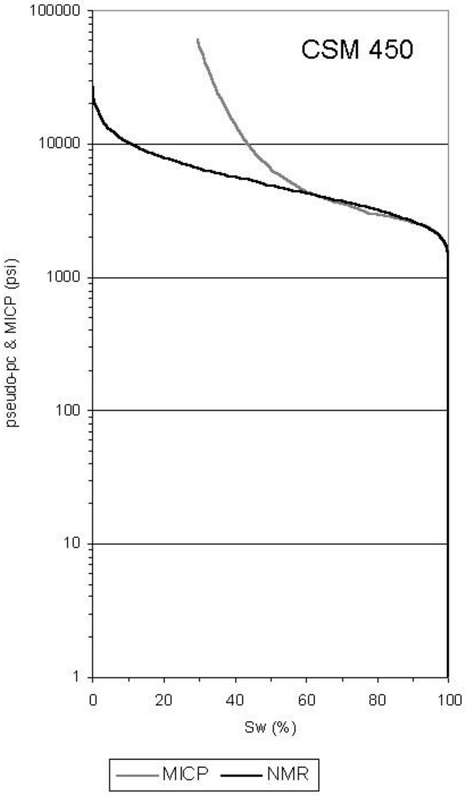

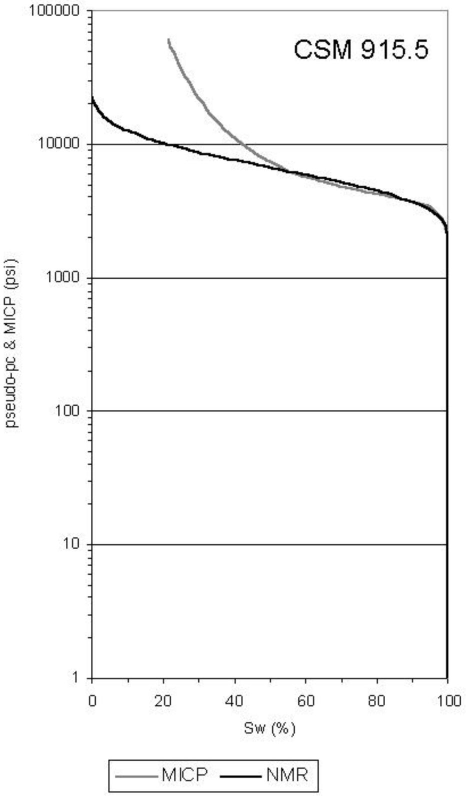

Figure C.8: Continued.

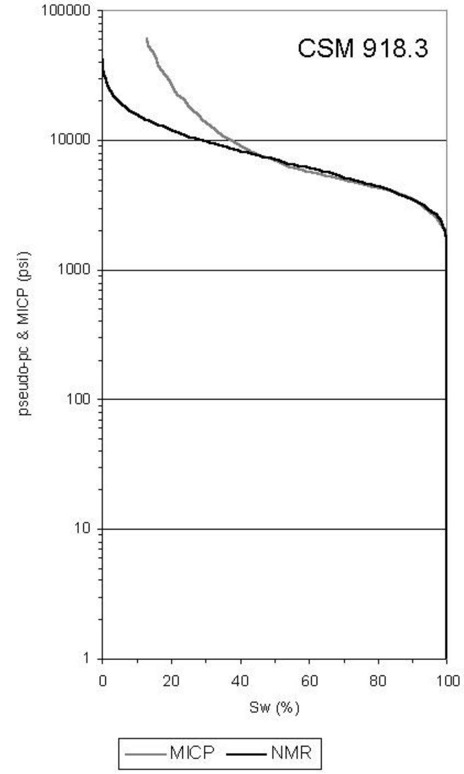

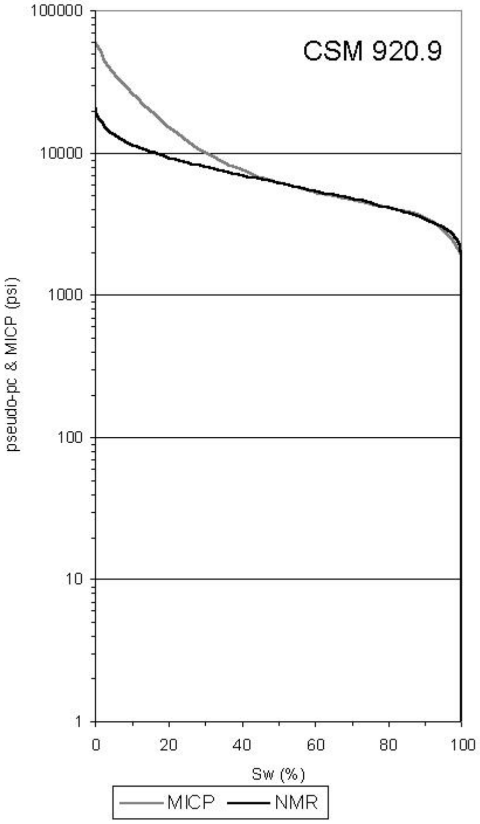

Figure C.8: Continued.

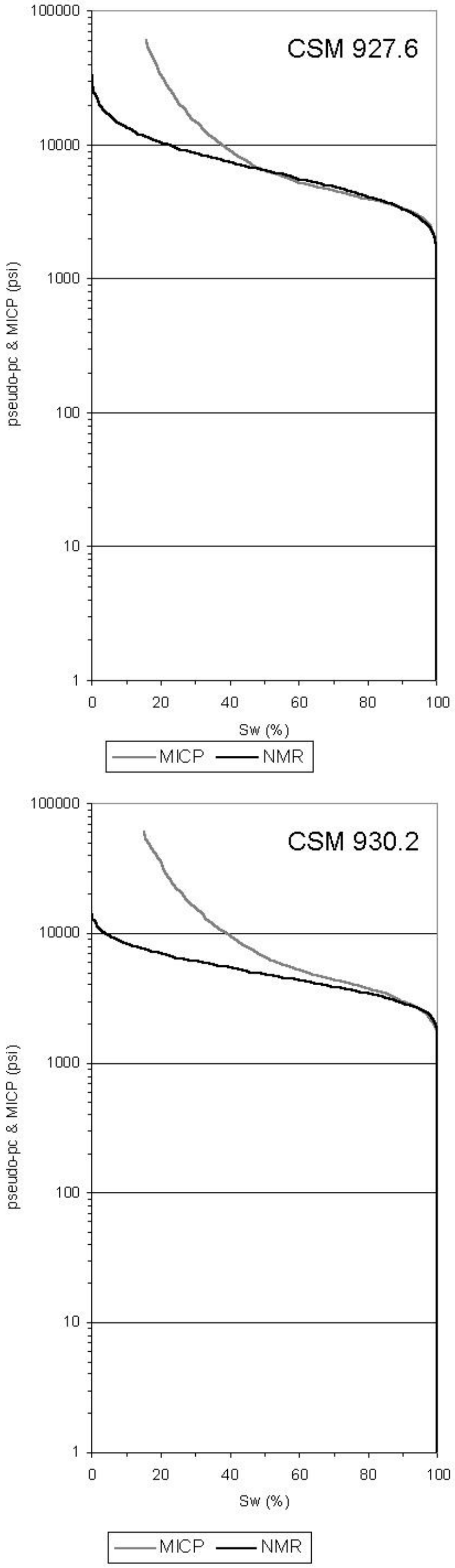

Figure C.8: Continued.

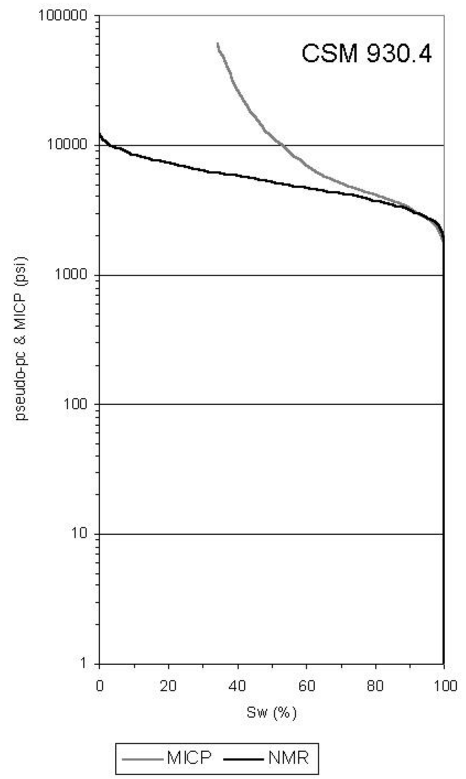

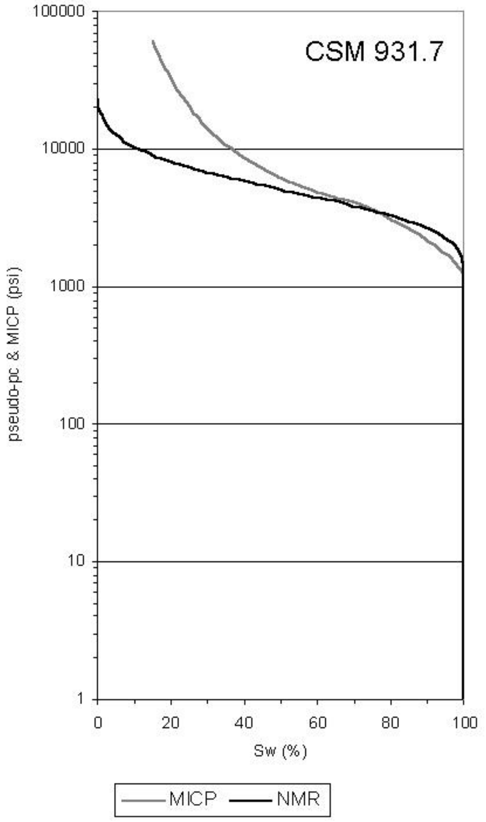

Figure C.8: Continued.

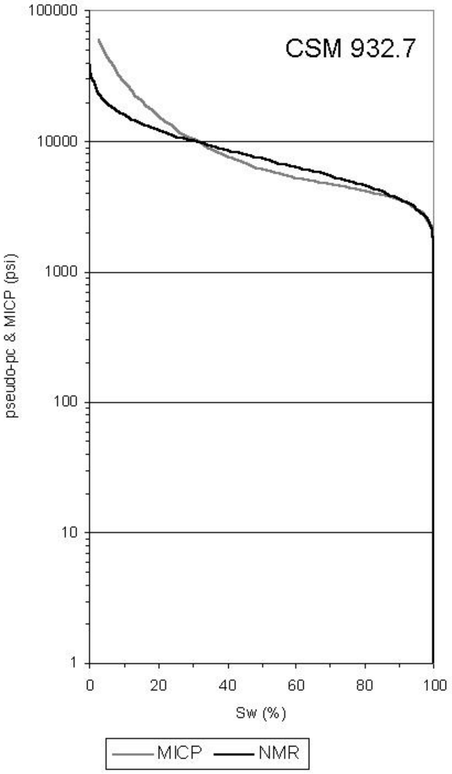

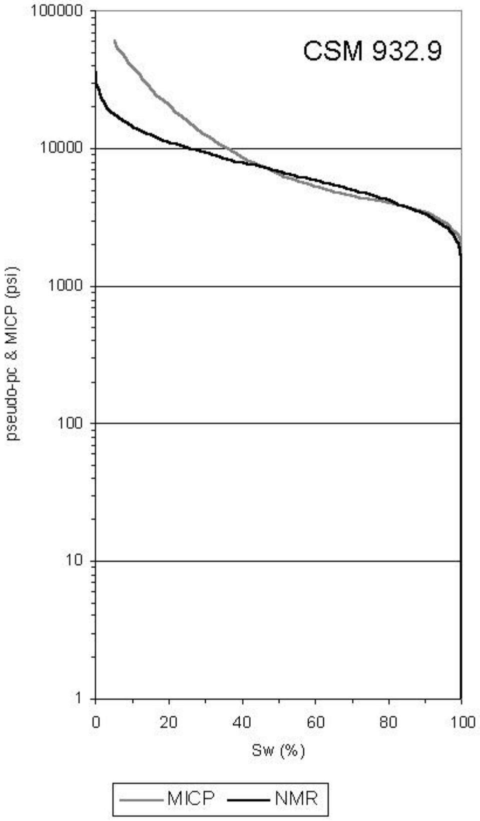

Figure C.8: Continued.

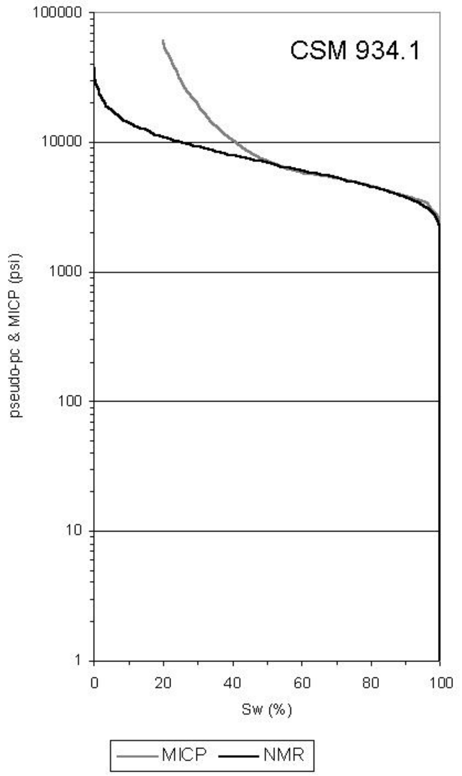

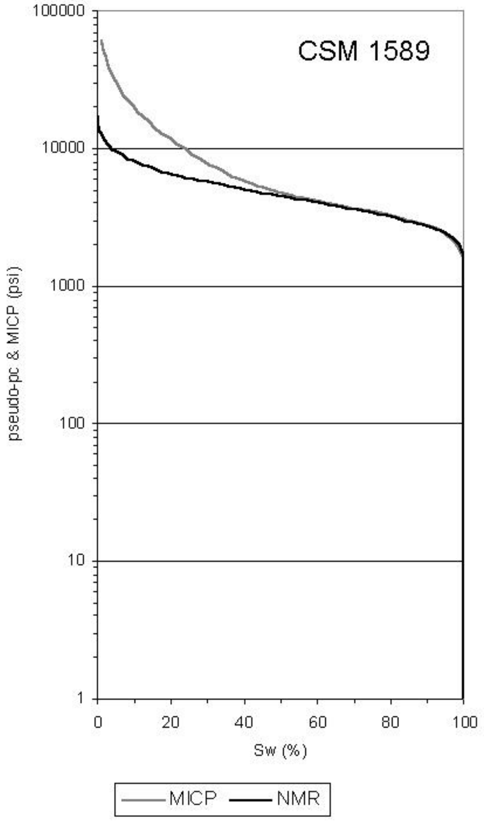

Figure C.8: Continued.

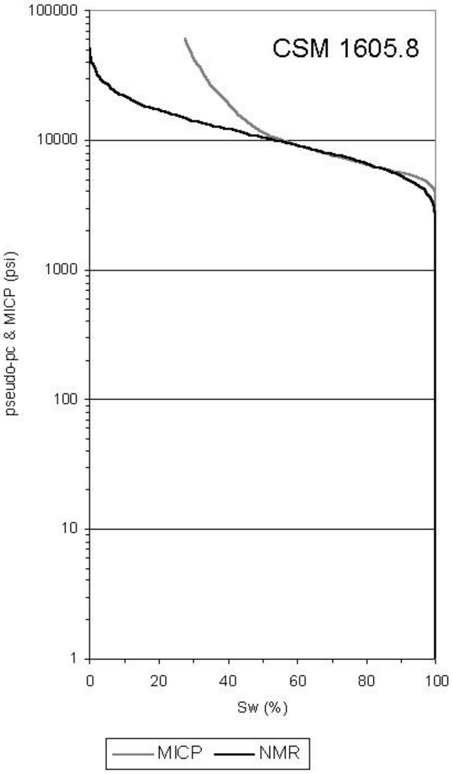

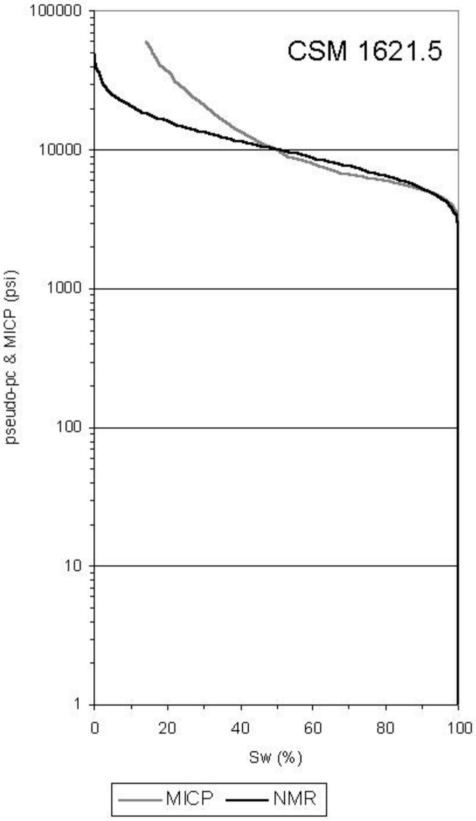

Figure C.8: Continued.